

Swansea University E-Theses

Integral equations applied to electromagnetic scattering in the resonance region.

Takawira, Isaac

How to cite:

Takawira, Isaac (2003) *Integral equations applied to electromagnetic scattering in the resonance region..* thesis, Swansea University.
<http://cronfa.swan.ac.uk/Record/cronfa42381>

Use policy:

This item is brought to you by Swansea University. Any person downloading material is agreeing to abide by the terms of the repository licence: copies of full text items may be used or reproduced in any format or medium, without prior permission for personal research or study, educational or non-commercial purposes only. The copyright for any work remains with the original author unless otherwise specified. The full-text must not be sold in any format or medium without the formal permission of the copyright holder. Permission for multiple reproductions should be obtained from the original author.

Authors are personally responsible for adhering to copyright and publisher restrictions when uploading content to the repository.

Please link to the metadata record in the Swansea University repository, Cronfa (link given in the citation reference above.)

<http://www.swansea.ac.uk/library/researchsupport/ris-support/>

DEPARTMENT OF ELECTRICAL AND ELECTRONIC
ENGINEERING



UNIVERSITY OF WALES SWANSEA

**Integral equations Applied to Electromagnetic
Scattering In The Resonance Region**

ISAAC TAKAWIRA

Thesis submitted to the University of Wales in candidature for the degree of
Doctor of Philosophy

JUNE 2003

ProQuest Number: 10798089

All rights reserved

INFORMATION TO ALL USERS

The quality of this reproduction is dependent upon the quality of the copy submitted.

In the unlikely event that the author did not send a complete manuscript and there are missing pages, these will be noted. Also, if material had to be removed, a note will indicate the deletion.



ProQuest 10798089

Published by ProQuest LLC (2018). Copyright of the Dissertation is held by the Author.

All rights reserved.

This work is protected against unauthorized copying under Title 17, United States Code
Microform Edition © ProQuest LLC.

ProQuest LLC.
789 East Eisenhower Parkway
P.O. Box 1346
Ann Arbor, MI 48106 – 1346



The University of Wales

Integral equations Applied to Electromagnetic Scattering In The Resonance Region

ISAAC TAKAWIRA

Thesis submitted in candidature for the degree of
Doctor of Philosophy

Department of Electrical & Electronic Engineering
University of Wales Swansea

June 2003

Declaration

This work has not previously been accepted in substance for any degree and
is not currently submitted in candidature for any degree elsewhere.

Signed:

(Candidate)

Date:

✓ 17/9/2003

Statement 1

This thesis is the result of my own investigations, except where otherwise stated. Materials from other sources are acknowledged by explicit references. These are listed in the reference section at the end of the thesis.

Signed:

(Candidate)

Date:

u 17/9/2003

Statement 2

I hereby give consent for my thesis, if accepted, to be available for photocopying and for inter-library loan, and for the title and summary to be made available to outside organisations.

Signed:

(Candidate)

Date:

' 17/9/2003

Contents

| | |
|----------------------------|-----|
| Title page | i |
| Declaration and Statements | ii |
| Contents | iv |
| Acknowledgement | ix |
| Abstract | x |
| Symbols and Constants | xii |

1 INTRODUCTION

| | | |
|-------|--|----|
| 1.1 | Introduction | 2 |
| 1.2 | Survey of electromagnetic analytic methods | 2 |
| 1.2.1 | Finite difference time domain | 3 |
| 1.2.2 | Finite element method | 6 |
| 1.2.3 | Method of Moments | 7 |
| 1.2.4 | Hybrid Methods | 11 |
| 1.3 | The Problem | 12 |
| 1.4 | Organisation of the thesis | 13 |

2 RAO-WILTON- GLISSON FORMULATION FOR ELECTROMAGNETIC SCATTERING FROM SURFACES

| | | |
|-------|--|----|
| 2.1 | Introduction | 16 |
| 2.2 | Maxwell's equation and their solutions | 18 |
| 2.3 | The RWG Basis Functions | 22 |
| 2.3.1 | Current Approximation | 25 |

| | | |
|-------|---|----|
| 2.3.2 | Testing Procedure | 26 |
| 2.4 | Formulation For Conducting Bodies | 28 |
| 2.4.1 | Electric Field Integral Equation | 28 |
| 2.4.2 | Testing of the EFIE | 30 |
| 2.4.3 | Evaluation of the Impedance Matrix Elements | 32 |
| 2.5 | Comment On The Evaluation Of Integrals | 34 |
| 2.6 | Formulation For Dielectric Bodies | 36 |
| 2.6.1 | Formulation of the CFIE | 36 |
| 2.6.2 | Testing of the CFIE | 40 |
| 2.7 | Formulation For Conducting and Dielectric Objects | 43 |
| 2.8 | Concluding Remarks | 49 |

3 FOUR-SI FORMULATION FOR ELECTROMAGNETIC SCATTERING FROM PERFECTLY CONDUCTING OBJECTS

| | | |
|---------|---|----|
| 3.1 | Introduction | 52 |
| 3.2 | Four-SI formulation for perfectly conducting bodies | 53 |
| 3.2.1 | Area Coordinates | 56 |
| 3.2.2 | Numerical Solution of the tested EFIE | 60 |
| 3.2.2 | Evaluation of the tested electric scalar potential | 67 |
| 3.2.3 | Evaluation of the tested incident field | 68 |
| 3.3 | Impedance Matrix Calculations | 69 |
| 3.3.1 | Calculation of the Impedance Elements | 69 |
| 3.3.2 | Optimum number of Gaussian points | 70 |
| 3.3.2.1 | Introduction | 70 |

| | | |
|---------|--|-----|
| 3.3.2.2 | Optimisation of number of Gaussian Points | 72 |
| 3.3.2.2 | Singularity Extraction | 81 |
| 3.4 | Matrix Equation Solver | 83 |
| 3.5 | Numerical Results and Discussions | 83 |
| 3.5.1 | Introduction | 83 |
| 3.5.2 | Scattering from a Sphere | 84 |
| 3.5.3 | Scattering from a metallic disc at oblique incidence | 89 |
| 3.5.4 | Scattering from a metallic plate at nearly grazing incidence | 93 |
| 3.5.5 | Scattering from a metallic rectangular Trihedral | 96 |
| 3.5.6 | Scattering from a cavity | 100 |
| 3.6 | Conclusion | 106 |

4 FOUR-SI FORMULATION FOR ELECTROMAGNETIC SCATTERING FROM DIELECTRIC OBJECTS

| | | |
|-------|---|-----|
| 4.1 | Introduction | 110 |
| 4.2 | 4-SI Formulation For Dielectric Objects | 112 |
| 4.2.1 | Introduction | 112 |
| 4.2.2 | CFIE Matrix Equation | 121 |
| 4.2.3 | Optimisation of the number of Gaussian Points for the $1/R^3$ | 125 |
| 4.2.4 | Numerical Implementation | 134 |
| 4.3 | Results and Discussions | 135 |
| 4.3.1 | Scattering by dielectric spheres | 136 |
| 4.3.2 | Scattering by a dielectric cylinder | 142 |
| 4.3.3 | Scattering by a dielectric box | 144 |
| 4.3.4 | Scattering by a dielectric plate | 150 |

| | | |
|-------|---------------------------------|-----|
| 4.3.4 | Scattering by a dielectric disc | 153 |
| 4.4 | Concluding Remarks | 160 |

5 FOUR-SI FORMULATION FOR ELECTROMAGNETIC SCATTERING FROM CONDUCTING/ DIELECTRIC COMPOSITE OBJECTS

| | | |
|-------|--|-----|
| 5.1 | Introduction | 163 |
| 5.2. | 4-SI Formulation for Composite problems | 165 |
| 5.2.1 | Integral Equations | 165 |
| 5.2.2 | Testing of the Integral Equations | 167 |
| 5.3 | Results | 171 |
| 5.3.1 | Scattering by a metallic plate coated with a dielectric | 172 |
| 5.3.2 | Scattering by a prism with multiple metallic and dielectric regions | 178 |
| 5.3.3 | Scattering by a dielectric disc coated with conducting material at both ends | 181 |
| 5.4 | Concluding Remarks | 183 |

6 SUMMARY AND CONCLUSIONS

| | | |
|-----|-------------------------|-----|
| 6.0 | Summary and conclusions | 186 |
| 6.1 | Introduction | 186 |
| 6.2 | Chapter summaries | 186 |
| 6.3 | Future Work | 190 |

7 APPENDICES

| | | |
|------------|--|-----|
| Appendix A | A Normalized Local Area Coordinate System and numerical integration over a triangle | 193 |
| Appendix B | Definition of Scattering Angles | 197 |
| | REFERENCES | 199 |

ACKNOWLEDGMENTS

I am most grateful and indebted to my supervisor Dr. A. McCowen for his patient advice and guidance, encouragement and fruitful suggestions throughout this work.

I also extend my gratitude to the staff members of the Department of Electrical and Electronic Engineering's Computer Lab for providing the computing systems technical support.

I would also like to thank Dr. W. S. Wissam and Mr. E. P. Stevens for always expressing an interest in my work and offering encouragement.

I am also very thankful to Dr. G. Thomas and his wife for their hospitality when my family arrived in Swansea.

Finally, I would like to give my deepest thanks to my wife, Isabel, for her moral support. I am also grateful to my wife, my twin-sons, Tanaka and Takudzwa, and Gwendolin for their patience and understanding of my frequent absence.

ABSTRACT

In the application of an integral method to the problem of electromagnetic scattering by three-dimensional objects, the electromagnetic problem is formulated in terms of an electric field integral equation for conducting bodies and a combined field integral equation for dielectric or composite objects. The electric and magnetic fields are related to the unknown surface currents by the Green's functions for the scalar and vector potentials. Triangular patches are used to model the scatterer's surface and the basis functions proposed by Rao, Wilton and Glisson, represent the surface current on the scatterer's surface.

The application of the method of moments for the solution of the integral equations results in double surface integrals, which are computationally very expensive. Rao, Wilton and Glisson avoided the computation of a double surface integral by approximating the surface integral over the observation triangle by evaluating the integral at the centre of each observation point using a one point Gaussian quadrature scheme. This approach has also been adopted by other workers as it is relatively straightforward to implement since it only requires the field evaluation over the source triangle. In addition, the edge lengths of the triangle patches should be of the order of one-tenth of a wavelength if good results are to be obtained. This simplifies the computational task and it was believed that it decreases the computation time. For electrically large objects, many patches are needed and the order of the system matrices derived from the discretisation of the integral equations becomes large. This thesis investigates whether the approximation used to compute the impedance terms in the reported schemes lead to a computationally efficient scheme.

In this thesis, a comparison is made between the use of the EFIE and the CFIE with the full double surface integrals and the original EFIE and the CFIE schemes with the associated approximation. The integrals over the observation and source triangles are both evaluated. The equations of the discretised integral equations for conducting, dielectric and composite objects are derived to enable the impedance terms to be computed efficiently. A method is described of how to minimise the computing time for the evaluation of the double surface integrals and a criterion is presented for obtaining a good compromise between accuracy and total computing time.

The proposed formulation has been developed for the EFIE, for scattering by perfect electric conductors only; for the CFIE, for both dielectric/magnetic materials only and also the CFIE for mixed perfect electric conductors and dielectric materials. The scheme has been used to calculate the radar cross-section of conducting, dielectric and mixed objects and the results compared with those based on the RWG formulation and from the literature. The basis of comparison with the RWG formulation is based on accuracy, total computation time and computer memory required. The proposed formulation's results for conducting objects compare well with results from the literature and clearly demonstrate significant computational advantage over the original RWG formulation. For dielectric objects, the proposed formulation shows only some computational advantage over the RWG formulation whereas there is a no improvement with the mixed objects.

Symbols & Constants

| | |
|-------------------------|---|
| A | Magnetic vector potential |
| <i>a</i> | Constant |
| B, B | Magnetic flux density, T; Wb m ² |
| <i>b</i> | Constant |
| <i>c</i> | Constant |
| D, D | Electric flux density, C m ⁻² |
| dB | decibel |
| E, E | Electric field intensity, V m ⁻¹ |
| E^{inc} | Incident electric field, V m ⁻¹ |
| E_{tan} | Tangential component of electric field, V m ⁻¹ |
| E^s | Scattered electric field intensity, V m ⁻¹ |
| <i>e</i> | Electric charge |
| <i>e</i> | Base of natural logarithm, 2.718281828 |
| F | Electric vector potential, V m ⁻¹ |
| <i>F, f</i> | Function |
| f_n(r) | Basis function |
| <i>f_m</i> | Weighting function |
| G(r, r') | Green's function |
| H, H | Magnetic field, A m ⁻¹ |
| H^{inc} | Incident magnetic field, A m ⁻¹ |
| H_{tan} | Tangential component of magnetic field, A m ⁻¹ |
| H^s | Scattered magnetic field, A m ⁻¹ |
| I | Integral |
| <i>I, i</i> | Current, A |
| J | Electric surface current, A |

| | |
|---------------------|---|
| \mathbf{J}_c | Electric surface current on conductor, A |
| \mathbf{J}_d | Electric surface current on dielectric, A |
| \mathbf{J}_σ | Conduction current, A |
| \mathbf{J}_n | Current coefficients |
| j | $\sqrt{-1}$ |
| k | wavenumber, rad m ⁻¹ |
| k_d | wavenumber in a dielectric, rad m ⁻¹ |
| k_o | free space wavenumber, rad m ⁻¹ |
| L, l | Length; linear dimension |
| l_{mn} | Length of the n th edge |
| \mathbf{M} | Magnetic surface current, A |
| \mathbf{M}_d | Magnetic surface current on dielectric, A |
| N | Number of non-boundary edges |
| \mathbf{n} | Surface normal |
| \mathbf{O} | Global origin |
| R | Distance between source point and observation point |
| \mathbf{r}^o | Position vector of observation point, m |
| \mathbf{r}' | Position vector of source point, m |
| $\mathbf{r}^{c\pm}$ | Position vector of centroid of triangle point, m |
| S | Surface element, m ² |
| S_c | Surface boundary of conducting object |
| S_d | Surface boundary of dielectric object |
| T | Triangular surface patch element |
| V | Voltage, v |
| V_m | Element of the excitation voltage column vector |
| w | Weighting functions |
| Z_{mn} | Element of the impedance matrix |
| α | Constant |

| | |
|------------------------|--|
| α_n | Coefficients |
| β | Wave number |
| γ | Propagation constant |
| ε | Permittivity, F m ⁻¹ |
| ε_0 | Permittivity of free space, 8.854187 pF m ⁻¹ |
| ε_r | Relative permittivity |
| λ | Wavelength, m |
| λ_d | Wavelength in a dielectric, m |
| λ_0 | Free space wavelength, m |
| μ | Permeability, H m ⁻¹ |
| μ_r | Relative permeability |
| μ_0 | Permeability of free space, 400 π nH m ⁻¹ |
| ρ^c | Position vector of centroid, local coordinates |
| ρ^n | Position vector of basis function, local coordinates |
| ρ_e | Electric charge density, C m ⁻³ |
| ρ_m | Magnetic charge density, C m ⁻³ |
| σ | Conductivity, S m ⁻¹ |
| Φ, ϕ | Electric scalar potential, v |
| Ψ | Magnetic scalar potential, A m ⁻¹ |
| ∇, ∇_s | Surface divergence operator |
| $\langle f, g \rangle$ | Inner product |

CHAPTER 1

INTRODUCTION

| | | |
|------------|---|----|
| 1.1 | Introduction | 2 |
| 1.2 | Survey of electromagnetic analytic methods | 2 |
| 1.2.1 | Finite difference time domain | 3 |
| 1.2.2 | Finite element method | 6 |
| 1.2.3 | Method of Moments | 7 |
| 1.2.4 | Hybrid Methods | 11 |
| 1.3 | The Problem | 12 |
| 1.4 | Organisation of the thesis | 13 |

1.1 Introduction

More complex electromagnetic scattering and radiation problems can be solved nowadays than before thanks to the rapid increase in more efficient and accurate numerical algorithms and the accompanying rapid development in computer hardware. Numerical simulations in electromagnetics, like in other fields, are nowadays an indispensable part in the design and construction phases of various passive and electronic equipment. These have applications in many areas, such as in communications, the prediction of the radar cross section (RCS) of complex objects like aircraft, antenna and radar analysis and design, electromagnetic compatibility and microwave imaging. Practical measurements are often very expensive and time consuming. These are usually done at the end of numerical simulations to validate the simulated results.

The numerical techniques for solving electromagnetic scattering and radiation problems involve either solving partial-differential equations with the Finite-Difference Time Domain (FDTD) method [1,2] or the Finite-Element Method (FEM) [3,4] which result in sparse matrices, or integral equations which are transformed to dense matrix equations using the Method of Moments (MoM) [5,6]. The FEM and the MoM are predominantly frequency domain methods though time dependent formulations have been reported [7-11].

1.2 Survey of electromagnetic analytic methods

Over the past forty years, various computational techniques have been developed to solve electromagnetic related problems that are very difficult, if not impossible, to solve using analytical solutions or exact methods.

Electromagnetic problems can be cast either as partial differential equations or as integral equations. The most common numerical methods for the solution of electromagnetic scattering and radiation field problems are reviewed in this section. These are the FDTD, the FEM and the MoM. Each numerical method has its own advantages and disadvantages and each is best suited for a certain class of problems. The following sections give an overview of some of the most common numerical methods. There is yet no single method that can tackle all types of electromagnetic problems.

The mathematical formulation of scattering problems relies on Maxwell's equations. There are generally two distinct approaches to solving Maxwell's equations. These are either based on differential equation or integral equation methods.

1.2.1 Finite difference time domain

The FDTD [12-14] is one of the most direct methods to solve Maxwell's time-dependent curl equations in differential form. In this method both time and space are discretised and the solution algorithm is iterative. The FDTD has broad applicability to the study of three-dimensional objects [15]. The scatterers can be closed, open, conducting, dielectric, inhomogeneous or anisotropic.

This is one of the most popular method for analysing transient and frequency-domain electromagnetic problems. Its results are in the time-domain and these can easily be Fourier-transformed to the frequency domain, thus giving information over a wide frequency range.

This method presents a direct way to introduce a numerical method for the solution of Maxwell's equations. In FDTD, the starting point is the Maxwell's equations in differential form. The equations are modified to central-difference equations and then discretised. The electric field and magnetic field are alternately solved for given instants in time in a computational space set up with the aid of the boundary conditions.

Initially, a computational domain or space must be set up with boundary conditions to compute Maxwell's differential form equations. The grid material of each cell within the domain must be specified. Any material can be modelled as long as its permeability, permittivity, and conductivity are specified within each cell.

The literature on FDTD is very extensive and a comprehensive literature survey on FDTD can be found in [13]. The method was originally developed by Yee [1] and was extended by Umashankar, Taflove, and Morris [16,17)]. The derivation of the FDTD formulation from Maxwell's equations is based on mathematical methods of approximating derivatives by finite differences and the integrals are approximated by summations. The problem of solving large systems of linear equations needed in many other numerical techniques is avoided because of the time-iterative solution process.

The FDTD is based on solving the electromagnetic scattering problem in the time-domain by discretising Maxwell's curl equations in time and space and solving them numerically as an initial value problem. The entire computational volume of the problem is discretised. For the scheme proposed by Yee [1], central-difference approximations are applied to the time and space derivatives in Maxwell's curl equations. The sampling points for the electromagnetic fields are chosen so that the discretisation error stays within some previously fixed bounds. The discretisations in space and time are not independent but have to

satisfy the stability-condition for numerical stability and least numerical dispersion. Also, the components of the electric and magnetic fields are interleaved in time and space so as to be able to fulfil the appropriate boundary conditions at media interfaces. There is no need for setting up or solving a set of linear equations. The computer storage and running time are proportional to the computational volume and time interval.

The main advantages of FDTD-based techniques for solving electromagnetic problems are its simplicity and ability to handle inhomogeneous objects. The FDTD is a well-tested method that has been applied to such diverse applications as absorption in tissue [18], analysis of microstrip circuits [19] and antenna scattering [20].

Some of the drawbacks of FDTD include the requirement to perform computations over a spatial domain that is larger than the object. This is in contrast to either the volume or surface integral equation methods. For electrically large objects, this requires more computer memory storage space. The other disadvantage of the FDTD is the staircase approximation of oblique boundaries, and this often gives poor accuracy. The FDTD is not well suited to geometries that exhibit variations in shape that are small with respect to the wavelength. Another disadvantage of this method is that calculations on resonant structures lead to prohibitively long computation times [21].

Several researchers have used the FDTD to evaluate the scattering by metallic objects [22-26], dielectric objects [27,28] and composite objects comprising metallic and dielectric objects [21-31].

1.2.2 Finite element method

The FEM [32-35] is based on solving the electromagnetic scattering problem in the frequency-domain by discretising the Helmholtz equation [36], which is an elliptic differential equation, in space and solving it numerically as a boundary value problem.

As in the FDTD, one chooses a finite spatial computational domain containing the object discretised by means of a suitable mesh. Discretising Helmholtz equation and enforcing the boundary conditions on the object's surface as well as continuity conditions across neighbouring grid mesh cells yields a system of linear equations that can be solved numerically for the field values at the node points of the grid cells. The system of equation can either be solved by Gaussian elimination or an iterative method such as the conjugate gradient method.

Since the solution has to satisfy the radiation boundary condition at infinity [37], ways have to be found to ensure that the FEM-solution computed in the finite computational domain satisfies the radiation condition at infinity [33,38]. The FEM can be applied to arbitrarily shaped and inhomogeneous objects. The coefficient matrix is banded which is an advantage over surface or volume-integral equation methods. One of the disadvantages of the FEM is that computations need to be done over a computational domain that is larger than the object as opposed to integral equation methods.

The finite element method (FEM) is the oldest numerical technique applied to engineering problems. FEM itself is not rigorous, but when combined with integral equation techniques it can yield rigorous formulations. Some of the advantages of FEM are:

(i) Sparse matrices result (as opposed to MoM for which dense matrices result).

Sparse matrices allow the application of a wide range of fast matrix solvers.

- (ii) Its application involves discretisation of the computational domain, and therefore is adaptable to a wide range of geometries and material variations.

Although the FEM has been extensively used to solve complex electromagnetic field problems, its application to the open domain problems remains limited. This is due to the fact that the use of FEM in wave scattering problems requires a discretisation of the exterior and the introduction of absorbing boundary conditions [39] set on the outer boundary terminating the FEM mesh. It is for this reason that hybrid numerical schemes are usually preferred instead of the FEM. These schemes are usually based on the coupling of the FEM, which discretises the interior of the computational domain, and an integral equation method over the surface of the computational domain. Such applications of the method to EM scattering problems can be found in the works of AngeAlini *et al.* [40].

The FEM has been used to analyse the electromagnetic scattering from a wide range of objects including [41-44].

1.2.3 Method of Moments

The method of moments (MoM) [5] is one of the most popular methods to compute the scattering of electromagnetic waves by conducting bodies. The MoM is a mathematical procedure for converting an integral equation formulation of an electromagnetic field problem into a matrix form that can then be solved numerically. The use of the MoM became popular due to the work of Harrington [5]. The method has since been applied to a wide variety of electromagnetic

problems ranging from radiation from thin-wire antennas to scattering from three-dimensional objects [45-48]. Compared with other numerical methods, the MoM is very versatile in its application and highly accurate. It can be used to a wide range of objects such as wires, three-dimensional conducting and dielectric objects or composite objects.

The procedure for applying the MoM to electromagnetic scattering involves deriving an appropriate integral equation, discretisation of the integral equation into matrix equation, computation of the matrix elements and solving the matrix equation.

The MoM is based on solving complex integral equations by reducing them to a system of linear equations. The equation solved by MoM generally has the form of an electric field integral equation (EFIE), a magnetic field integral equation (MFIE) or a combined field integral (CFIE) [49,50]. The EFIE or the MFIE formulations are used when dealing with problems involving conductors [6,51,52]. Rao *et al.* [6] were the first to report the solution of electromagnetic scattering in the resonance region via the time-independent EFIE using triangular basis functions. When only the conductors are present the electric field integral equation technique is used to solve for the electric current distribution on the conductor's surface. When the dielectric is present, the CFIE is used. Umashankar *et al.* [53] developed the CFIE for lossy-dielectric scatterers using the triangular basis developed by Rao *et al.* [6]. The use of the CFIE increases the size of the problem as additional two sets of unknown surface currents, the dielectric and magnetic currents surface currents have to be solved for. Hence the CFIE formulation is more complex than either the EFIE or the MFIE formulations. Unlike the EFIE or the MFIE formulations, the CFIE demands tremendous computer storage space and computational demands when applied to electrically large scatterers [53]. Although the MoM can be applied in the time

domain, much of the published work is based on time-independent integral equation formulations [6,51,53,54].

Two approaches can be defined in deriving an integral equation for a scatterer. An integral equation can be derived for the induced currents in the scatterer or for the equivalent currents on the scatterer. When the unknowns are surface currents on the scatterer the integral equation is called the surface integral equation and if the unknowns are volume currents inside the scatterer then the integral equation is called the volume integral. The integral equation is transformed into a matrix equation by discretising the unknown currents. Only the surface integral approach is used in this thesis. The integral equation formulation for computational electromagnetics is made easier by the use of the electromagnetic equivalence principle [5].

As with the FDTD and the FEM, the major problems with the MoM are the very large computer memory requirements and the long computation times when dealing with electrically large problems [55]. Several schemes have been devised to lessen these shortcomings. Techniques have been devised to compress the impedance matrix so as to reduce the computer memory storage requirement [56-58]. Preconditioners have been coupled to iterative solvers so as to accelerate the numerical solution of the matrix equations [59-60]. Basis functions with special properties [61-63] lead to sparse matrices with substantially reduced memory requirements.

The MoM requires $O(N^3)$ floating operations if Gaussian elimination is used to solve N linear equations, or $O(N^2)$ operations per iteration if the conjugate gradient (CG) method is used. The MoM can be applied in both time domain and frequency domain. The main differences in applying the method of moments in the two domains are primarily in the formulation and solution steps. In the time

domain, the unknown equivalent current or field must be discretised in both time and space.

The required characteristics of the scatterer determine when to use the time or frequency domain calculations. For instance, non-linear characteristics are easier to model in the time domain whereas dispersive characteristics of a material are modelled more easily in the frequency domain than in the time domain. The work in this thesis is done in the frequency domain.

With the MoM method, the scatterer's surface is divided into a number of connected triangular patches. The surface electric current is then approximately represented by the basis functions for triangular patches developed by Rao *et al.* [6].

The RWG functions represent the current passing through the edges of a triangular patch as a constant. Small triangular patches, typically with edge lengths of the order of one-tenth of a wavelength have to be used to yield a sufficiently accurate approximation of the surface current. For geometries with complicated shapes, the mesh density is higher. Application of the MoM to the surface integral equations results in a full system of linear equations which form dense matrix equations. This leads to a large number of unknowns for a large scatterer.

The MoM has been used by many authors in the study of electromagnetic scattering by conducting and dielectric objects [5,6,51,64-66]. Only a few references are cited here.

1.2.4 Hybrid Methods

Many hybrid techniques have been developed in an attempt to overcome the intrinsic limitations of the major computational methods. For electrically large objects, the moment method becomes computationally very expensive in terms of both memory and computation times, even for resonant scatterers. One way around this difficulty is to employ hybrid techniques [67-69].

However, the accuracy of these hybrid techniques have been found to be limited [68] and this has led to the development of new methods which combine the MoM and other techniques such as the impedance matrix localization method (IML) [61,70], the fast multipole method (FMM) [71,72], the complex multipole beam approach (CMBA) [73]. The fast multipole method is an efficient way to perform matrix-vector multiplications whereby the field at each point due to every other source point is calculated for all points in a group of N points. Normally this would require $O(N^2)$ calculations. The fast multipole method reduces this to $O(N^{1.5})$ [71,74,75]. Recently, McCowen [54] has analysed the scattering from three-dimensional dielectric objects by applying a far-field approximation to the CFIE. The results show significant savings in matrix fill-time and storage from the original CFIE formulation.

The FMM accomplishes its speed by using an indirect fast computation of the matrix vector product. As the matrix size increases, the matrix conditioning deteriorates such that precondition becomes necessary [75].

Other hybrid techniques mentioned below have been developed to solve complex problems. Finite-difference time-domain-physical optics (FDTD-PO) [76] techniques, MoM-FDTD [77], hybrid ray-FDTD [78,79] techniques have been proposed to reduce the memory requirements and computation times.

There are also several hybrid formulations which combine the MOM with the FEM to solve electromagnetic radiation/scattering problems from structures consisting of inhomogeneous dielectric bodies of arbitrary shapes attached to one or more perfectly conducting bodies [80-84]. While either method alone fails to model these structures efficiently, a combination of both finite element and moment methods provides an excellent way to solve these problems. The FEM is employed to handle the interior domain of inhomogeneous dielectric bodies and the MoM is used to develop surface integrals that relate the field quantities on boundary surfaces with the equivalent surface currents.

1.3 The Problem

Rao, Wilton and Glisson [6] were the first to solve the EFIE using the MoM technique and the triangular basis functions. Umashankar *et al.* [53] later extended the application of the MoM using the RWG basis functions to the analysis of the electromagnetic scattering by arbitrary shaped three-dimensional homogeneous dielectric objects based on the CFIE. The geometry of the scatterer's surface is approximated by triangular patches. The testing process of the EFIE or the CFIE results in double surface integrals that are required for the calculation of the matrices [6,52]. Rao *et. al* [6] evaluated the double surface integrals by performing first an accurate integration over the source triangle, followed by an approximation of the integrand over the observation triangle, which was performed by sampling the integrand at a single point, the centroid of the observation triangle. This approach was taken to avoid the costly evaluation of the two double surface integrals resulting in a fast and accurate algorithm. This is the approach that has since been used by many researchers [53,54,58].

The approach taken in this thesis avoids the approximation of the double surface integrals of the tested EFIE or the CFIE for computing the elements of the impedance matrix using the MoM [5]. With this method, the two surface integrals are evaluated more accurately. This is done in such a way that a balance is struck between accuracy and the computation time. This approach is in contrast to the existing approach RWG formulation which approximates the integrals but nevertheless, produce good results. However, for electrically large objects the latter approach requires a large number of unknowns resulting in the requirement for more computer memory and CPU-time. The main motivation in devising the proposed formulation was to produce a scheme that goes a long way in addressing the shortcomings of the existing approach, which is hereafter referred to as the RWG formulation, particularly for electrically larger problems. The proposed formulation has been incorporated into the Swansea's MoM 3-D code for evaluation. The differences between these two approaches will be pointed out in chapters 3 and 4.

The scattering by the arbitrary shaped three dimensional (3-D) objects is analysed by solving the integral equation where the unknowns are the surface currents on the scatterer's surface. The surface of the object is approximated by flat triangular surface patches [6].

1.4 Organisation of the thesis

This thesis is organised as follows. The triangular patch model of the moment method formulation for the EFIE as derived by Rao *et al.* [6] for scattering by perfectly conducting objects and for the CFIE as derived in [53] for scattering by three dimensional dielectric objects is reviewed in chapter 2.

The proposed modification to the EFIE formulation as proposed in [6] for conducting bodies is presented in chapter 3. The surface integrals present in the tested EFIE are computationally more expensive to compute than in the original scheme, so emphasis in the chapter is on an efficient algorithm and procedure to compute the matrix terms efficiently. The analytical RCS results for conducting bodies are presented and compared with the results from the literature.

The RCS problems [36] are used as the basis for comparison between the formulation proposed in this thesis and other computation schemes, including the RWG formulation. This comparison is used to assess the performance and efficiency of the proposed formulation.

The application of the proposed scheme is extended to dielectric objects in chapter 4. In this chapter, the modification to the CFIE formulation as derived in [53] is performed. In the case of the CFIE, the expressions for the impedance matrix terms for the modified formulation are more complex than those of the EFIE formulation and are therefore more computationally demanding to evaluate. Analytical RCS results for dielectric objects are presented and compared with the results from the literature.

Chapter 5 extends the modified CFIE formulation to incorporate mixed conducting materials and lossless/lossy dielectric materials and the corresponding RCS results are presented. Chapter 6 presents the overall conclusions for the thesis.

CHAPTER 2

RAO-WILTON- GLISSON FORMULATION FOR ELECTROMAGNETIC SCATTERING FROM SURFACES

| | | |
|------------|--|-----------|
| 2.1 | INTRODUCTION | 16 |
| 2.2 | MAXWELL'S EQUATIONS AND THEIR SOLUTIONS | 18 |
| 2.3 | THE RWG BASIS FUNCTIONS | 22 |
| 2.3.1 | Current Approximation | 25 |
| 2.3.2 | Testing Procedure | 26 |
| 2.4 | FORMULATION FOR CONDUCTING BODIES | 28 |
| 2.4.1 | Electric Field Integral Equation | 28 |
| 2.4.2 | Testing of the EFIE | 30 |
| 2.4.3 | Evaluation of the Impedance Matrix Elements | 32 |
| 2.5 | COMMENT ON THE EVALUATION OF THE INTEGRALS | 34 |
| 2.6 | FORMULATION FOR DIELECTRIC BODIES | 36 |
| 2.6.1 | Formulation of the CFIE | 36 |
| 2.6.2 | Testing of the CFIE | 40 |
| 2.7 | FORMULATION FOR CONDUCTING AND DIELECTRIC OBJECTS | 43 |
| 2.8 | CONCLUDING REMARKS | 49 |

2.1 Introduction

This Chapter discusses the essence of the Rao-Wilton-Glisson basis function set introduced in [85]. The solution of computational electromagnetic problems that are based on surface integral equations depend on the representation of the unknown functions in terms of some known basis functions. The most commonly used subdomain basis functions used in the numerical solution of the surface integral equations are the “rooftops” basis functions [85] and the triangular basis functions [6]. The rooftop basis functions are defined on rectangular sub-domains and the triangular basis functions are defined on triangular sub-domains or patches. The triangular basis functions were developed by Rao, Wilton and Glisson [6] and are used in this work.

This chapter reviews in detail the basis functions introduced by Glisson [86] and from the work developed by Rao *et al.* [6]. The linear triangle basis function presented in [6] will be referred to in this thesis as the RWG basis function. This will lay the groundwork for the formulation proposed in this thesis in subsequent chapters. As will be discussed in Chapter 3, the difference between the proposed formulation and the RWG formulation lies in the way the impedance matrix elements are calculated.

In the surface integral equations that are considered in this work, the problems are discretised by the Method of Moments (MoM) using the Rao-Wilton-Glisson (RWG) basis functions [6]. With this method, a mesh of connected flat triangular patches approximates the geometry of the scatterer. The triangular patches have several advantages [87]. They have the ability to conform to any geometrical surface or boundary; they allow easy descriptions of the patch scheme to the computer and may be used with greater densities on those areas of the surface where greater resolution is required. The number of triangular patches of the problem is directly proportional to the

electrical size used since the basis functions used in the discretisation of the surface integral equation are defined on the triangular patches.

These triangular-patch basis functions have been widely used in electromagnetic scattering problems to model arbitrary surfaces [6], [50], [88-94]. Besides the triangular surface patch model, other approaches to the flat surface patch model have been reported in the literature, such as the rectangular patches [85,95] and polygonal patches [96,97].

Several researchers have also investigated the use of curved patches to describe the geometry of arbitrary shapes [98-101]. Wilkes and Cha [98] extended the flat triangular patch model developed by Rao, Wilton and Glisson [6] to the curved triangular patch. Zhu and Lanstorfer [99] reported the application of curved parametric triangular and quadrilateral edge elements as basis functions in the moment method solution of the electric field integral equation. They concluded that a combination of the basis functions defined on curved patches to model an arbitrarily shaped surface produced more accurate results than with conventional planar patches. Brown and Prata [100] developed a quadrilateral roof-top type of basis function for analysing electromagnetic scattering on curved surfaces. Their results were shown to agree very well with an analytic solution.

In the case where an object of curvature is of interest, the use of flat triangular patches creates unnecessary geometry modelling errors in the solution. Such errors can be important, for example, in near-field calculations. Wilkes and Cha [98] demonstrate, by analysing a metallic sphere, that parametrically defined curved patches in place of flat triangular patches and with specifically designed basis functions produce fewer number of unknowns. Wei *et. al* [101] have also demonstrated that the use of curved triangular and quadrilateral basis functions can reduce the total of number of unknowns when analysing curved surfaces.

2.2 Maxwell's Equations and their solutions

The mathematical formulation of electromagnetic scattering problems relies on Maxwell's equations. These were originally introduced by James Maxwell in 1864 [102]. These equations are:

$$\nabla \times \mathbf{H} = \mathbf{J} + j\omega\epsilon\mathbf{E} \quad (2.1)$$

$$\nabla \times \mathbf{E} = -j\omega\mu\mathbf{H} - \mathbf{M} \quad (2.2)$$

$$\nabla \cdot \mathbf{D} = \rho_e \quad (2.3)$$

$$\nabla \cdot \mathbf{B} = \rho_m \quad (2.4)$$

where \mathbf{E} is the electric field, \mathbf{H} is the magnetic field, \mathbf{B} is the magnetic flux density and \mathbf{D} is the electric flux density, \mathbf{J} is the electric current density, \mathbf{M} is the magnetic current density, ρ_e is the electric surface charge density and ρ_m is the magnetic surface charge density. The four fields \mathbf{E} , \mathbf{D} , \mathbf{H} and \mathbf{B} describe the total electromagnetic field. All the quantities in Maxwell's equations are assumed to have harmonic time dependency.

The angular frequency is given by $\omega = k/\sqrt{\mu\epsilon} = (2\pi/\lambda)/\sqrt{\mu\epsilon}$, where k is the wave number and λ is the wavelength of the incident electromagnetic wave. There is an additional equation that involves the current density \mathbf{J} and the charge density ρ_e . These are related through the continuity equation that expresses the conservation of charge:

$$\nabla \cdot \mathbf{J} = -j\omega\rho_e \quad (2.5)$$

A corresponding equation for the magnetic current and the magnetic charge density is given by

$$\nabla \cdot \mathbf{M} = -j\omega\rho_m \quad (2.6)$$

In an isotropic conductor, the current density \mathbf{J} is related to the electric field by:

$$\mathbf{J} = \sigma\mathbf{E} \quad (2.7)$$

where σ is called the electric conductivity. For $\sigma \neq 0$, the medium is a conductor and whereas for $\sigma = 0$, the medium is called a dielectric. In a linear isotropic medium, the relations between \mathbf{D} and \mathbf{E} , \mathbf{B} and \mathbf{H} are:

$$\mathbf{D} = \varepsilon\mathbf{E} \quad (2.8)$$

and, for a linear magnetic material

$$\mathbf{B} = \mu\mathbf{H} \quad (2.9)$$

where ε and μ are the electric permittivity and the magnetic permeability respectively.

The magnetic field \mathbf{H} is related to the magnetic vector potential \mathbf{A} in the presence of an electric current and electric charge only, by the equation

$$\mathbf{H} = \frac{1}{\mu} \nabla \times \mathbf{A} \quad (2.10)$$

It can easily be shown that the electric field is related to the magnetic vector potential \mathbf{A} and the scalar potential by:

$$\mathbf{E} = -j\omega\mathbf{A} - \nabla\phi \quad (2.11)$$

where ϕ is the electric scalar potential.

The corresponding equations for \mathbf{H} and \mathbf{E} in the presence of magnetic current and magnetic charge only are:

$$\mathbf{E} = -\frac{1}{\varepsilon} \nabla \times \mathbf{F} \quad (2.12)$$

$$\mathbf{H} = -j\omega\mathbf{F} - \nabla\Psi \quad (2.13)$$

where \mathbf{F} and Ψ are the electric vector potential and magnetic scalar potential respectively.

The equation relating the magnetic vector potential \mathbf{A} and the electric surface current density \mathbf{J} is given by:

$$\nabla^2\mathbf{A} + k^2\mathbf{A} = -\mu\mathbf{J} \quad (2.14)$$

The electric scalar potential ϕ is related to the electric surface charge density by the equation

$$\nabla^2\phi + k^2\phi = -\frac{\rho_e}{\varepsilon} \quad (2.15)$$

Similarly, the equations that relate the electric vector potential \mathbf{F} and the magnetic scalar potential Ψ to the magnetic surface current \mathbf{M} and magnetic surface charge density are:

$$\nabla^2\mathbf{F} + k^2\mathbf{F} = -\varepsilon\mathbf{M} \quad (2.16)$$

$$\nabla^2\Psi + k^2\Psi = -\frac{\rho_m}{\mu} \quad (2.17)$$

The solutions for the vector potentials $\mathbf{A}(\mathbf{r})$ and $\mathbf{F}(\mathbf{r})$ in equations (2.14) and (2.16) are given by:

$$\mathbf{A}(\mathbf{r}) = \frac{\mu}{4\pi} \iint_S \mathbf{J}(\mathbf{r}') \frac{e^{-jkR}}{R} dS(\mathbf{r}') \quad (2.18)$$

$$\mathbf{F}(\mathbf{r}) = \frac{\varepsilon}{4\pi} \iint_S \mathbf{M}(\mathbf{r}') \frac{e^{-jkR}}{R} dS(\mathbf{r}') \quad (2.19)$$

Also, the solutions for the scalar potentials $\phi(\mathbf{r})$ and $\Psi(\mathbf{r})$ in equations (2.15) and (2.17) are given by:

$$\phi(\mathbf{r}) = -\frac{1}{4\pi j\omega\varepsilon} \iint_S \nabla'_s \cdot \mathbf{J}(\mathbf{r}') \frac{e^{-jkR}}{R} dS(\mathbf{r}') \quad (2.20)$$

$$\Psi(\mathbf{r}) = \frac{-1}{4\pi j\omega\mu} \iint_S \nabla'_s \cdot \mathbf{M}(\mathbf{r}') \frac{e^{-jkR}}{R} dS(\mathbf{r}') \quad (2.21)$$

where $R = |\mathbf{r}' - \mathbf{r}|$, with \mathbf{r} being the observation point and \mathbf{r}' the source point and ∇'_s is the surface divergence operator on the primed coordinates, i.e. source points. Both points are located at the surface S of the object.

The expressions for the scattered fields in terms of the vector and scalar potentials, if both electric and magnetic currents are present, are given by

$$\mathbf{E}^s = -j\omega\mathbf{A} - \nabla\phi - \frac{1}{\varepsilon} \nabla \times \mathbf{F} \quad (2.22)$$

$$\mathbf{H}^s = -j\omega\mathbf{F} - \nabla\Psi + \frac{1}{\mu} \nabla \times \mathbf{A} \quad (2.23)$$

Boundary conditions are associated with Maxwell's equations to describe different physical situations. For scattering from perfect conductors, the electric field vanishes inside the object and the total tangential electric field on the surface of the scatterer is zero. In the case of dielectric scatterers, there is continuity of the tangential electric or magnetic field across the interface.

Using the boundary conditions, Maxwell's equations are then rewritten in the form of integral equations which relate the electric and magnetic fields \mathbf{E} and \mathbf{H} to the equivalent electric and magnetic currents \mathbf{J} and \mathbf{M} on the surface of the object. Enforcing boundary conditions on the scatterer's surface enables the Maxwell's equations to be solved for the currents \mathbf{J} and \mathbf{M} , assuming that the incident fields are known.

The next section discusses the RWG basis functions used to represent the current in the moment method.

2.3 The RWG Basis Functions

The RWG basis function is one of the most commonly used basis functions. It models the current density on a triangular patch as the superposition of three non-orthogonal current densities [6].

These were originally proposed by Glisson [86] and later developed by Rao *et. al.* [6] These basis functions are suitable for use with the EFIE, MFIE, the CFIE and triangular patch modelling. It is assumed that the body's surface S is accurately approximated by triangular patches on which the RWG basis functions are defined. The basis function proposed by Rao, Wilton and Glisson [6] is illustrated in Figure 2.1.

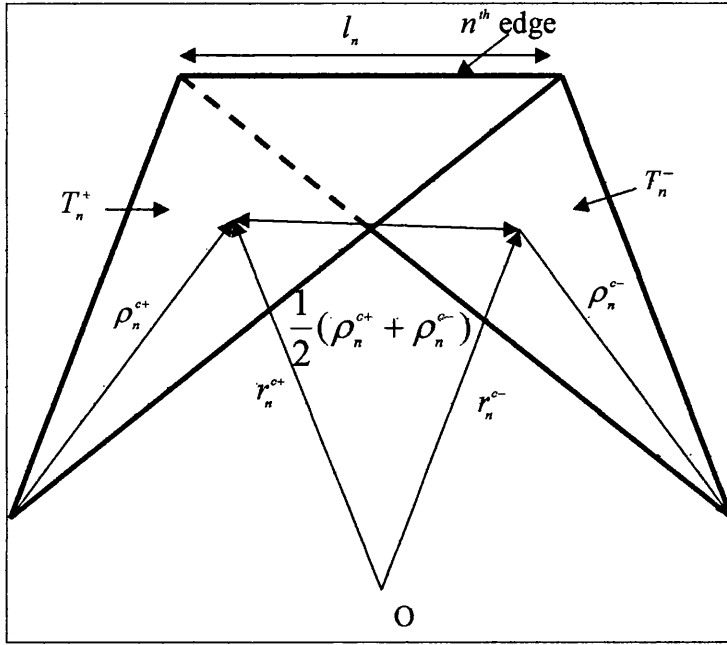


Figure 2.1 Domain for the RWG surface basis functions

Figure 2.1 shows two triangles T_n^+ and T_n^- associated with the n th edge of a triangle-meshed surface of the scatterer. Points in T_n^+ may be specified either by the position vector \mathbf{r} , defined with respect to the global origin O , or by the position vector ρ_n^+ , which is defined with respect to the free vertex of T_n^+ . The same is true for the position vector ρ_n^- except that it is directed toward the free vertex of T_n^- . The plus or minus designations of the triangles are chosen such that the positive current reference direction associated with the n th edge is from T_n^+ to T_n^- . The vector basis functions associated with the n th edge are defined as

$$\mathbf{f}_n(\mathbf{r}) = \begin{cases} \frac{l_n \rho_n^+}{2A_n^+} & \text{for all } \mathbf{r} \text{ in } T_n^+, \\ \frac{l_n \rho_n^-}{2A_n^-} & \text{for all } \mathbf{r} \text{ in } T_n^-, \\ 0 & \text{otherwise} \end{cases} \quad (2.24)$$

where l_n is the length of the common edge and A_n^\pm is the area of the triangle T_n^\pm . The subscripts refer to the edges and the superscripts refer to faces of the triangular meshes.

Some of the properties that make the basis function ideally suited to represent the current on the scatterer's surface are:

(i) Within each triangle, the current density is the sum of three basis functions that are associated with the three edges. The superposition of the basis functions within a triangle represents a distribution of surface density current flowing within the triangle.

(ii) At each edge except the n th edge (common edge of T_n^+ and T_n^-), $\mathbf{f}_n(\mathbf{r})$ has no component normal to that edge. The component of $\mathbf{f}_n(\mathbf{r})$ normal to the n th edge is constant and continuous across the edge, because the normal component of ρ_n^\pm along the n th edge is just the height of T_n^\pm with the n th edge as the base and the height expressed as $2A_n^\pm/l_n$. This avoids the presence of spurious line charges in the numerical model.

(iii) The surface divergence of the basis function is

$$\nabla_s \cdot \mathbf{f}_n(\mathbf{r}) = \begin{cases} \frac{l_n}{A_n^+} & \text{for } \mathbf{r} \text{ in } T_n^+, \\ \frac{-l_n}{A_n^-} & \text{for } \mathbf{r} \text{ in } T_n^-, \\ 0 & \text{otherwise} \end{cases} \quad (2.25)$$

where the surface divergence in T_n^\pm is $(\pm 1/\rho_n^\pm) \partial(\rho_n^\pm f_n)/\partial \rho_n^\pm$ (with f_n being the component of \mathbf{f}_n in the direction of ρ_n). Thus from equation (2.5) charge density is constant throughout the interior of the each triangle.

(iv) The surface integral of the basis function over T_n^+ and T_n^- , which is needed later in the discretisation of equations detailed later is

$$\iint_{T_n^+ + T_n^-} \mathbf{f}_n(\mathbf{r}) dS = \frac{l_n}{2} (\rho_n^{c+} + \rho_n^{c-}) = l_n (\mathbf{r}_n^{c-} - \mathbf{r}_n^{c+}) \quad (2.26)$$

where $\rho_n^{c\pm}$ is defined between the free vertex and the centroid of T_n^\pm with ρ_n^{c+} directed away from the vertex and ρ_n^{c-} directed toward the vertex, as shown in Figure 2.1 and $\mathbf{r}_n^{c\pm}$ is the vector from the global origin O to the centroid of T_n^\pm .

2.3.1 Current Approximation

The first step in the method of moments solution process is to expand the current as a finite sum of expansion functions. Except for the boundary edges, a basis function \mathbf{f}_n is associated with each edge of the triangulated

structure. The current on the scatterer's surface may now be approximated in terms of \mathbf{f}_n by

$$\mathbf{J} = \sum_{n=1}^N I_n \mathbf{f}_n(\mathbf{r}) \quad (2.27)$$

where N is the number of edges not on a surface boundary. As a basis function is associated with each non-boundary edge, up to three non-zero basis functions may therefore exist within each triangular face. At each edge, only the basis function associated with that edge might have a component of current normal to the edge. Since the normal component of \mathbf{f}_n at the n th edge is unity, each component I_n in (2.27) may be interpreted as the normal component of current density flowing past the n th edge. Equation (2.27) includes only contributions from non-boundary edges since the normal component of current at a surface boundary must vanish. The superposition of the basis functions inside one triangle results in a suitable current distribution throughout the patch.

2.3.2 Testing Procedure

In order to obtain a linear system of equations from the integral equations and to solve for the unknown electric and magnetic current coefficients, the equations are tested by suitable testing functions.

The general form of the EFIE and the MFIE integral equations are:

$$\mathbf{E}^{inc} = L_e(\mathbf{J}) \quad (2.28)$$

$$\mathbf{H}^{inc} = L_m(\mathbf{J}) \quad (2.29)$$

where \mathbf{E}^{inc} and \mathbf{H}^{inc} are the incident electric and magnetic fields respectively, L_e and L_m are the surface integral operators for the EFIE and MFIE respectively, and \mathbf{J} is the induced current (electric or magnetic).

The next stage in the solution process requires the definition of a set of m linearly independent testing (or weighting) functions, w_j , to be defined. An inner product of each weighting function is formed with both sides of the integral equation being solved.

In the case of the EFIE equation, the testing process results in a set of m independent equations of the form

$$\langle \mathbf{E}^{inc}, \mathbf{w}_j \rangle = \langle L_e(\mathbf{J}), \mathbf{w}_j \rangle \quad j = 1, 2, \dots, m \quad (2.30)$$

By expanding \mathbf{J} using equation (2.27), a set of equations $N \times N$ simultaneous equations with the current constants, I_n , as the unknowns. In the Galerkin method, the weight functions w_j are chosen to be the basis functions themselves, f_j .

$$\langle \mathbf{E}^{inc}, \mathbf{f}_m \rangle = \langle L_e \left[\sum_{n=1}^N I_n \mathbf{f}_n \right], \mathbf{f}_m \rangle \quad j = 1, 2, \dots, N \quad (2.31)$$

Equation (2.31) maybe written in matrix form as

$$[\mathbf{E}^{inc}] = [\mathbf{Z}][\mathbf{J}] \quad (2.32)$$

where: $Z_{ij} = \langle L_e(\mathbf{f}_j), \mathbf{f}_i \rangle$ and $\mathbf{E}_j^{inc} = \langle \mathbf{E}^{inc}, \mathbf{f}_j \rangle$

The vector \mathbf{E}^{inc} contains the known incident field quantities and the terms of the Z-matrix are functions of the geometry. The unknown current coefficients

are the terms of the \mathbf{J} vector. These values are obtained by solving the system of equations.

The next section reviews the EFIE formulation for problems of electromagnetic scattering by perfectly conducting objects.

2.4 Formulation for Conducting Bodies

The integro-differential equation for the current distribution based on the electric field operator is called the electric field integral equation (EFIE). In this section, the derivation of the integral equation for the surface current induced on a conducting scatterer is reviewed. The use of the RWG basis functions in applying the method of moments is covered next. The computation procedure for the evaluation of the impedance matrix elements as done by RWG is then discussed.

2.4.1 Electric Field Integral Equation

This section focuses on the case where the perfect electric conductors are the only materials present in the electromagnetic scattering problem. This means the conductors have infinite conductivity, the electric and magnetic fields do not penetrate the surface of the metallic objects more than a thin boundary layer, which in practice is considered to be of zero thickness. Another effect of the infinite conductivity condition is that no tangential electric fields can exist on the surface of the metallic conductors, otherwise the infinite conductivity would lead to infinite currents, which is not practical.

In the case of perfect electric conductors, the electromagnetic scattering problem is considered in terms of electric currents induced on the surface of

the conducting object. Consider a perfectly conducting scatterer with a surface S , which is either open or closed. The incident electric field \mathbf{E}^{inc} is due to an impressed source in the absence of the scatterer. Induced surface currents \mathbf{J} flow on S .

The scattered electric field \mathbf{E}^s due to the surface current is given by

$$\mathbf{E}^s = -j\omega\mathbf{A} - \nabla\phi \quad (2.33)$$

where the magnetic vector potential and the scalar potential are defined in (2.18) and (2.20) respectively.

The continuity equation relates the surface charge density ρ to the surface divergence of the current density:

$$\nabla_s \cdot \mathbf{J} = -j\omega\rho_e \quad (2.34)$$

where ∇_s is the surface divergence operator.

Applying the boundary condition that the sum of the incident, \mathbf{E}^{inc} , and the scattered, \mathbf{E}^s , electric fields has no tangential component on the perfectly conducting surface, i.e.,

$$\hat{n} \times (\mathbf{E}^{inc} + \mathbf{E}^s) = 0 \text{ on surface } S \quad (2.35)$$

leads to the following integro-differential equation for the surface current density \mathbf{J} ,

$$\mathbf{E}_{tan}^{inc} = (j\omega\mathbf{A} + \nabla\phi)_{tan}, \text{ } \mathbf{r} \text{ on } S. \quad (2.36)$$

The subscript “tan” denotes the components tangential to the surface of S. With \mathbf{A} and ϕ given by the equations (2.18) and (2.20) respectively, equation (2.36) represents the so-called electric field integral equation.

2.4.2 Testing of the EFIE

The next step in solving for the current coefficients when applying the method of moments is to implement the testing procedure. The expansion functions chosen are the same as the RWG basis functions which were reviewed in section 2.3.2. Considering the tangential components only, the electric field equation (2.36) is tested with the basis function \mathbf{f}_m according to the inner product defined in (2.30):

$$\langle \mathbf{E}^{inc}, \mathbf{f}_m \rangle = j\omega \langle \mathbf{A}, \mathbf{f}_m \rangle + \langle \nabla \phi, \mathbf{f}_m \rangle \quad (2.37)$$

Making use of a surface calculus identity [103], the last term on right hand side in (2.37) can be rewritten as

$$\langle \nabla \phi, \mathbf{f}_m \rangle = - \iint_S \phi \nabla_s \cdot \mathbf{f}_m dS \quad (2.38)$$

where use has been made of the fact that \mathbf{f}_m has no normal component to any part of the boundary of S.

Using equation (2.25), the integral in equation (2.38) is approximated as:

$$\iint_S \phi \nabla_s \cdot \mathbf{f}_m dS = l_m \left(\frac{1}{A_m^+} \iint_{T^+} \phi dS - \frac{1}{A_m^-} \iint_{T^-} \phi dS \right) \quad (2.39)$$

$$\approx l_m \left[\phi(\mathbf{r}_m^{c+}) - \phi(\mathbf{r}_m^{c-}) \right]$$

where the two averages of ϕ over the triangles T_m^+ and T_m^- have been approximated by the corresponding values of ϕ at the centroids of the triangles.

The integration of the magnetic vector potential and the incident field terms in equation (2.37) are similarly approximated.

The tested incident field terms are given by:

$$\begin{aligned} \langle \mathbf{E}^{inc}, \mathbf{f}_m \rangle &= l_m \left[\frac{1}{2A_m^+} \iint_{T_m^+} \mathbf{E}^{inc} \cdot \boldsymbol{\rho}_m^+ dS + \frac{1}{2A_m^-} \iint_{T_m^-} \mathbf{E}^{inc} \cdot \boldsymbol{\rho}_m^- dS \right] \\ &\simeq \frac{l_m}{2} \left[\mathbf{E}^{inc}(\mathbf{r}_m^{c+}) \cdot \boldsymbol{\rho}_m^{c+} + \mathbf{E}^{inc}(\mathbf{r}_m^{c-}) \cdot \boldsymbol{\rho}_m^{c-} \right] \end{aligned} \quad (2.40)$$

and the tested magnetic vector potential is approximated by

$$\begin{aligned} \langle \mathbf{A}, \mathbf{f}_m \rangle &= l_m \left[\frac{1}{2A_m^+} \iint_{T_m^+} \mathbf{A} \cdot \boldsymbol{\rho}_m^+ dS + \frac{1}{2A_m^-} \iint_{T_m^-} \mathbf{A} \cdot \boldsymbol{\rho}_m^- dS \right] \\ &\simeq \frac{l_m}{2} \left[\mathbf{A}(\mathbf{r}_m^{c+}) \cdot \boldsymbol{\rho}_m^{c+} + \mathbf{A}(\mathbf{r}_m^{c-}) \cdot \boldsymbol{\rho}_m^{c-} \right] \end{aligned} \quad (2.41)$$

The integrals in equations (2.40) and (2.41) are solved by approximating \mathbf{E}^{inc} and \mathbf{A} with their values at the centroid of each triangle and then carrying out integrations similar to those used to obtain equation (2.26).

From equations (2.38) - (2.41), the tested electric field integral equation (2.37) becomes:

$$\begin{aligned}
& l_m \left[\mathbf{E}^{inc}(\mathbf{r}_m^{c+}) \cdot \frac{\rho_m^{c+}}{2} + \mathbf{E}^{inc}(\mathbf{r}_m^{c-}) \cdot \frac{\rho_m^{c-}}{2} \right] \\
& = j\omega l_m \left[\mathbf{A}(\mathbf{r}_m^{c+}) \cdot \frac{\rho_m^{c+}}{2} + \mathbf{A}(\mathbf{r}_m^{c-}) \cdot \frac{\rho_m^{c-}}{2} \right] - l_m [\phi(\mathbf{r}_m^{c+}) - \phi(\mathbf{r}_m^{c-})]
\end{aligned} \tag{2.42}$$

Equation (2.42) is solved for the current coefficients by enforcing the boundary conditions at each triangle edge, $m = 1, 2, \dots, N$.

2.4.3 Evaluation of the Impedance Matrix Elements

By making use of the expression for the current expansion given by equation (2.27) in (2.42) an $N \times N$ system of linear equations is obtained which may be written in matrix form as

$$[\mathbf{V}_m] = [\mathbf{Z}_{mn}][\mathbf{I}_n] \tag{2.43}$$

where $[\mathbf{V}_m]$ is a column vector of length N , $[\mathbf{Z}_{mn}]$ is an $N \times N$ matrix and $[\mathbf{I}_n]$ is a column vector of length N . The elements of \mathbf{Z} and \mathbf{V} are given by

$$Z_{mn} = l_m \left[j\omega \left(\mathbf{A}_{mn}^+ \cdot \frac{\rho_m^{c+}}{2} + \mathbf{A}_{mn}^- \cdot \frac{\rho_m^{c-}}{2} \right) - (\phi_{mn}^+ - \phi_{mn}^-) \right] \tag{2.44}$$

$$V_m = l_m \left(\mathbf{E}^{inc+}(\mathbf{r}_m^{c+}) \cdot \frac{\rho_m^{c+}}{2} + \mathbf{E}^{inc-}(\mathbf{r}_m^{c-}) \cdot \frac{\rho_m^{c-}}{2} \right) \tag{2.45}$$

where

$$\mathbf{A}_{mn}^{\pm} = \frac{\mu}{4\pi} \iint_S \mathbf{f}_n(\mathbf{r}') \frac{e^{-jkR_m^{\pm}}}{R_m^{\pm}} dS' \quad (2.46)$$

$$\phi_{mn}^{\pm} = -\frac{1}{4\pi j\omega\epsilon} \iint_S \nabla_s' \cdot \mathbf{f}_n(\mathbf{r}') \frac{e^{-jkR_m^{\pm}}}{R_m^{\pm}} dS' \quad (2.47)$$

$$R_m^{\pm} = |\mathbf{r}_m^{c\pm} - \mathbf{r}'| \quad (2.48)$$

Each matrix element Z_{mn} is associated with the pair of edges m , for the observation triangle and n , for the source triangle. Hence each integral in Z_{mn} is related to two source triangles attached to edge n and with two observation points at the centroids of the two triangle attached to edge m .

The impedance matrix can be obtained directly by calculating the matrix elements directly for each pair of source and observation RWG basis functions. However, this direct approach is more time consuming, because the same value of vector and scalar potentials could appear in 3 different pairs of basis functions. This is because a triangular patch can have a maximum of 3 non-boundary edges, with each edge being an independent basis function. Hence, for the same observation point, the scalar and vector potentials in each triangular patch could be involved in up to 3 different pairs of basis functions. The vector and scalar potentials are calculated for each pair of triangular patches, instead of for each pair of basis function. This is a much more efficient approach of computing the impedance matrix elements.

The integrations in (2.46) and (2.47) are performed over the source triangular patches. This implies that in the computer implementation, the calculated potential values and the patches' coordinates should be saved and recalled when required during the computation of matrix elements. This approach guarantees that the integrals in the vector and scalar potential for each observation point are evaluated only once. Since each triangular patch can have up to 3 basis functions and noting that there are 3 field components,

using this approach computation could be made as much as 9 times faster in comparison to the direct approach, which does the computations edge by edge.

Once the matrices of Z and V of equation (2.43) are determined, the system of linear equations for the current coefficients I_n may be solved.

2.5 Comment on the evaluation of the integrals

The purpose of approximations used by Rao *et al.* [6] used in equations (2.39), (2.40) and (2.41) is to avoid the computation of the surface integrals over the observation triangles so that only the surface integral involving the function \mathbf{A} over the source triangles T_n^\pm is performed. In other words, the integrals in (2.46) and (2.47) are evaluated by integrating from the centroid of T_m^+ to the middle of the edge l_m and then to the centroid of T_m^- . The incident field and the vector potential quantities \mathbf{A} are approximated by their values at the centroid. The integrals of the gradients of the scalar potential quantities reduce to the differences of the scalar potentials at the centroids. Hence the integrations of the tested quantities over each triangular patch are reduced to the area of the triangular patch multiplied by the integrand evaluated at the centroid of the triangular patch. This avoids the expensive computation of two surface integrals to fill the impedance matrix. This results in a numerically efficient procedure that avoids the computation of integrations over the testing triangular domains.

The task of evaluating the double integrals can be quite difficult and time consuming. To overcome the difficulties of large memory requirement and high computation time, Rao *et al.* [6] introduced the approximations described in sections 2.4.2 and 2.4.3.

Since the introduction of the RWG basis functions, a number of researchers have implemented the approximations pointed out in equations (2.39), (2.40) and (2.41) in analysing scattering from conducting objects and have demonstrated that accurate results can be obtained by employing the same approximations [51, 94, 104-111].

Chaowei and Sarkar [94] used the triangular patch vector basis functions developed by Rao et al., [6], for expansion and testing functions in the conventional method of moments for the analysis of scattering from perfectly conducting plates.

Cai-Cheng Lu *et. al* [105] utilized the RWG basis functions and the approximations in equations (2.39), (2.40) and (2.41) to analyse scattering from thin metallic sheets and a perfectly conducting sphere. They obtained good comparison with respect to the analytical Mie series solution. Sendur and Gurel [106] analysed the scattering of electromagnetic waves of a Hertzian dipole in the presence of a perfectly conducting sphere using the RWG basis functions. Their results were in good agreement with the analytical solution obtained by Harrington [104]. Leat *et. al* [91] used the RWG triangular-basis-function method of moments to model the impedance and field patterns of bowtie antennas in free space. Their results agree with those of the experimental paper by Brown and Woodward [107]. McCowen and Salman [51,108] implemented the RWG basis functions when analysing the scattering problems from metallic surfaces using the method of moments with the far field approximation technique that increased the computational efficiency of the original method of moments approach. Rossi *et. al* [109] employed the use of the RWG basis functions to represent the surface current induced on the conducting scatterer in the analysis of electromagnetic-wave scattering by arbitrarily shaped objects using a three-dimensional multilevel fast far-field approximation method. Song and Chew [110] solved the scattering problem of a very large conducting sphere (diameter of 120λ) using the method of moments, where the RWG basis functions were used, in

conjunction with the multilevel fast multipole algorithm. Their numerical results compared well with the analytical Mie series results. Carr *et. al* [111] have again analysed the scattering problems of a sphere and a cube in free space using the RWG basis functions.

The next section considers the scattering of electromagnetic waves from dielectrics.

2.6 Formulation for Dielectric Bodies

2.6.1 Formulation of the CFIE

In this section, the derivation of the CFIE [112] and its MoM solution for scattering by 3-D dielectric bodies is discussed. For a homogeneous dielectric body, the boundary conditions are the continuity of the tangential electric and magnetic fields across the interface. Continuity of each field provides one equation. By combining the resultant EFIE and MFIE the CFIE is obtained.

This section deals with the electromagnetic scattering from dielectric bodies immersed in free space. The formulation of the CFIE is discussed. For the dielectric media, the adopted procedure is to solve a pair of coupled integral equations for the equivalent electric (J) and magnetic (M) currents on the surface S of the dielectric [53]. The equivalent surface current densities J and M are expanded using the RWG triangular-patch basis functions and the CFIE is then solved by the method of moments.

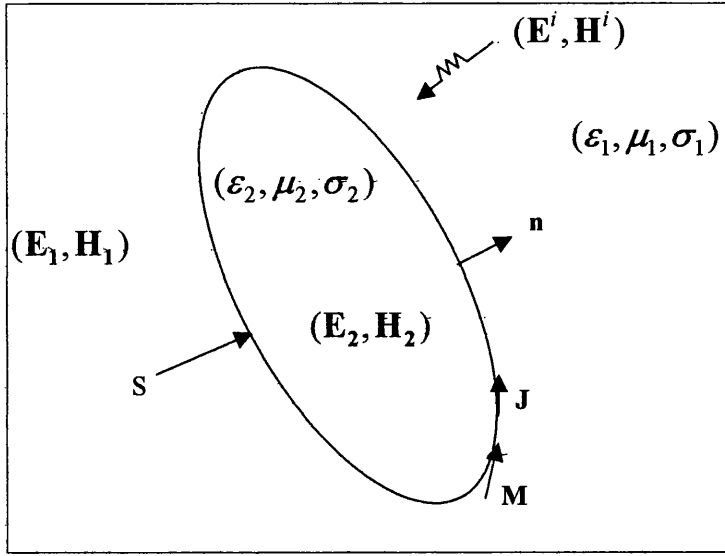


Figure 2.2 Homogeneous dielectric object embedded in a homogeneous medium (free space), \mathbf{J} and \mathbf{M} are the equivalent currents for the exterior.

Referring to Figure 2.2, S denotes the surface of a three dimensional homogeneous dielectric object illuminated by an incident plane wave. The regions exterior and interior to the object are characterized by material parameters $(\epsilon_1, \mu_1, \sigma_1)$ and $(\epsilon_2, \mu_2, \sigma_2)$, respectively. The total fields $(\mathbf{E}_1, \mathbf{H}_1)$ in the exterior region are given by the sums of the incident fields $(\mathbf{E}^{inc}, \mathbf{H}^{inc})$ and the fields radiated by a set of equivalent currents (\mathbf{J}, \mathbf{M}) on the surface S . Hence

$$\mathbf{E}_1 = \mathbf{E}^{inc} + \mathbf{E}_1^s(\mathbf{J}, \mathbf{M}) \text{ outside surface } S \quad (2.49)$$

$$\mathbf{H}_1 = \mathbf{H}^{inc} + \mathbf{H}_1^s(\mathbf{J}, \mathbf{M}) \text{ outside surface } S \quad (2.50)$$

where \mathbf{E}_1^s and \mathbf{H}_1^s are integral operators for the exterior region.

By the equivalence principle, the equivalent currents are related to the total tangential fields on the surface S by:

$$\mathbf{J} = \mathbf{n} \times \mathbf{H}_1 \quad \text{just outside surface } S \quad (2.51)$$

$$\mathbf{M} = -\mathbf{n} \times \mathbf{E}_1 \quad \text{just outside surface } S \quad (2.52)$$

where \mathbf{n} is the unit normal to surface S pointing out of the object.

Now, because of the discontinuous behaviour of \mathbf{E}_1^s and \mathbf{H}_1^s across surface S , equations (2.51) and (2.52) imply that equations (2.49) and (2.50) are zero everywhere inside the dielectric object, i.e.

$$\mathbf{E}^{inc} + \mathbf{E}_1^s(\mathbf{J}, \mathbf{M})|_{\text{inside } S} = 0 \quad (2.53)$$

$$\mathbf{H}^{inc} + \mathbf{H}_1^s(\mathbf{J}, \mathbf{M})|_{\text{inside } S} = 0 \quad (2.54)$$

The fields $(\mathbf{E}_2, \mathbf{H}_2)$ in the interior region are expressed in terms of the same pair of equivalent currents (\mathbf{J}, \mathbf{M}) , but with the opposite sign [53]:

$$\mathbf{E}_2 - \mathbf{E}_2^s(-\mathbf{J}, -\mathbf{M})|_{\text{inside } S} = 0 \quad (2.55)$$

$$\mathbf{H}_2 - \mathbf{H}_2^s(-\mathbf{J}, -\mathbf{M})|_{\text{inside } S} = 0 \quad (2.56)$$

From equations (2.22), (2.23) and (2.53) - (2.56), the electric and magnetic scattered fields can be expressed in terms of their sources, \mathbf{J} and \mathbf{M} , through the electric and magnetic vector potentials and using the continuity of the tangential components of the electric and magnetic fields:

$$\mathbf{E}^{inc}(\mathbf{r}) = j\omega [\mathbf{A}_1(\mathbf{r}) + \mathbf{A}_2(\mathbf{r})] + [\nabla\phi_1(\mathbf{r}) + \nabla\phi_2(\mathbf{r})] + \nabla \times \left[\frac{1}{\epsilon_1} \mathbf{F}_1(\mathbf{r}) + \frac{1}{\epsilon_2} \mathbf{F}_2(\mathbf{r}) \right] \quad (2.57)$$

$$\mathbf{H}^{inc}(\mathbf{r}) = j\omega [\mathbf{F}_1(\mathbf{r}) + \mathbf{F}_2(\mathbf{r})] + [\nabla\Psi_1(\mathbf{r}) + \nabla\Psi_2(\mathbf{r})] - \nabla \times \left[\frac{1}{\mu_1} \mathbf{A}_1(\mathbf{r}) + \frac{1}{\mu_2} \mathbf{A}_2(\mathbf{r}) \right] \quad (2.58)$$

Equations (2.57) and (2.58) are the combined field integral equations (CFIE). In this particular case, there are two regions, hence the expressions for the potentials, become, for $i = 1, 2$:

$$\mathbf{A}_i(\mathbf{r}) = \frac{\mu_i}{4\pi} \iint_S \mathbf{J}(\mathbf{r}') G_i(\mathbf{r}, \mathbf{r}') dS(\mathbf{r}') \quad (2.59)$$

$$\mathbf{F}_i(\mathbf{r}) = \frac{\varepsilon_i'}{4\pi} \iint_S \mathbf{M}(\mathbf{r}') G_i(\mathbf{r}, \mathbf{r}') dS(\mathbf{r}') \quad (2.60)$$

$$\phi_i(\mathbf{r}) = \frac{1}{4\pi\varepsilon_i'} \iint_S \rho_e G_i(\mathbf{r}, \mathbf{r}') dS(\mathbf{r}') \quad (2.61)$$

$$\Psi_i(\mathbf{r}) = \frac{1}{4\pi\mu_i} \iint_S \rho_m G_i(\mathbf{r}, \mathbf{r}') dS(\mathbf{r}') \quad (2.62)$$

where the complex permittivity ε_i' is used in (2.19) and (2.20) to obtain (2.60) and (2.61) is given by

$$\varepsilon_i' = \varepsilon_i \left(1 + \frac{\sigma_i}{j\omega\varepsilon_i} \right) \quad (2.63)$$

and

$$\rho_e = \frac{-1}{j\omega} (\nabla_s' \cdot \mathbf{J}(\mathbf{r}')) \quad (2.64)$$

$$\rho_m = \frac{-1}{j\omega} (\nabla_s' \cdot \mathbf{M}(\mathbf{r}')) \quad (2.65)$$

$$G_i(\mathbf{r}, \mathbf{r}') = \frac{e^{-jkR}}{R} \quad (2.66)$$

2.6.2 Testing of the CFIE

The combined field integral equations (2.57) and (2.58) are tested so that the unknown current coefficients, and hence the unknown surface currents can be obtained. The same RWG testing functions used in testing the EFIE in section 2.4.2 are used. Testing the equations (2.57) and (2.58) on the surface of the dielectric gives:

$$\langle \mathbf{E}^{inc}, \mathbf{f}_m \rangle = \langle j\omega(\mathbf{A}_1 + \mathbf{A}_2), \mathbf{f}_m \rangle + \langle (\nabla\phi_1 + \nabla\phi_2), \mathbf{f}_m \rangle \quad (2.67)$$

$$+ \langle \nabla \times \left(\frac{\mathbf{F}_1}{\varepsilon_1} + \frac{\mathbf{F}_2}{\varepsilon_2} \right), \mathbf{f}_m \rangle$$

$$\langle \mathbf{H}^{inc}, \mathbf{f}_m \rangle = \langle j\omega(\mathbf{F}_1 + \mathbf{F}_2), \mathbf{f}_m \rangle + \langle (\nabla\Psi_1 + \nabla\Psi_2), \mathbf{f}_m \rangle \quad (2.68)$$

$$- \langle \nabla \times \left(\frac{\mathbf{A}_1}{\mu_1} + \frac{\mathbf{A}_2}{\mu_2} \right), \mathbf{f}_m \rangle$$

where the subscript m represents an edge formed by the triangles T_m^\pm , $m = 1, 2, \dots, N_d$, where N_d is the number of edges on the dielectric surface.

The first terms in equations (2.67) and (2.68) are evaluated as discussed in section 2.4.2. They are approximated by evaluating the vector potentials at the centroids of the respective triangles. The same approximation is applied to the evaluation of the second-terms in equations (2.67) and (2.68). This approximation is shown in equation (2.39).

Now consider the evaluation of the third terms in equations (2.67) and (2.68).

$$\begin{aligned}
\langle \nabla \times \mathbf{A}, \mathbf{f}_m \rangle &= \iint_S (\nabla \times \mathbf{A}) \cdot \mathbf{f}_m dS \\
&= \frac{l_m}{2A_m^+} \iint_{T_m^+} \rho_m^+ \cdot [(\nabla \times \mathbf{A})]^+ dS \\
&\quad + \frac{l_m}{2A_m^-} \iint_{T_m^-} \rho_m^- \cdot [(\nabla \times \mathbf{A})]^- dS \\
&= \frac{l_m}{2} \left[\rho_m^{c+} \cdot (\nabla \times \mathbf{A}(\mathbf{r}_m^{c+})) + \rho_m^{c-} \cdot (\nabla \times \mathbf{A}(\mathbf{r}_m^{c-})) \right]
\end{aligned} \tag{2.69}$$

Substituting the equations (2.39) and (2.69) in (2.67) and (2.68) gives

$$\begin{aligned}
&l_m \left[\frac{\rho_m^{c+}}{2} \cdot \mathbf{E}^{inc}(\mathbf{r}_m^{c+}) + \frac{\rho_m^{c-}}{2} \cdot \mathbf{E}^{inc}(\mathbf{r}_m^{c-}) \right] \\
&= j\omega l_m \left[\frac{\rho_m^{c+}}{2} \cdot \left\{ \mathbf{A}_1(\mathbf{r}_m^{c+}) + \mathbf{A}_2(\mathbf{r}_m^{c+}) \right\} + \frac{\rho_m^{c-}}{2} \cdot \left\{ \mathbf{A}_1(\mathbf{r}_m^{c-}) + \mathbf{A}_2(\mathbf{r}_m^{c-}) \right\} \right] \\
&\quad + l_m \left[\left\{ \phi_1(\mathbf{r}_m^{c-}) - \phi_1(\mathbf{r}_m^{c+}) \right\} + \left\{ \phi_2(\mathbf{r}_m^{c-}) - \phi_2(\mathbf{r}_m^{c+}) \right\} \right] \\
&\quad + \left[\left\{ \frac{\mathbf{P}_1(\mathbf{r}_m^{c+})}{\varepsilon_1} + \frac{\mathbf{P}_2(\mathbf{r}_m^{c+})}{\varepsilon_2} \right\} + \left\{ \frac{\mathbf{P}_1(\mathbf{r}_m^{c-})}{\varepsilon_1} + \frac{\mathbf{P}_2(\mathbf{r}_m^{c-})}{\varepsilon_2} \right\} \right]
\end{aligned} \tag{2.70}$$

and

$$\begin{aligned}
&l_m \left[\frac{\rho_m^{c+}}{2} \cdot \mathbf{H}^{inc}(\mathbf{r}_m^{c+}) + \frac{\rho_m^{c-}}{2} \cdot \mathbf{H}^{inc}(\mathbf{r}_m^{c-}) \right] \\
&= j\omega l_m \left[\frac{\rho_m^{c+}}{2} \cdot \left\{ \mathbf{F}_1(\mathbf{r}_m^{c+}) + \mathbf{F}_2(\mathbf{r}_m^{c+}) \right\} + \frac{\rho_m^{c-}}{2} \cdot \left\{ \mathbf{F}_1(\mathbf{r}_m^{c-}) + \mathbf{F}_2(\mathbf{r}_m^{c-}) \right\} \right] \\
&\quad + l_m \left[\left\{ \Psi_1(\mathbf{r}_m^{c-}) - \Psi_1(\mathbf{r}_m^{c+}) \right\} + \left\{ \Psi_2(\mathbf{r}_m^{c-}) - \Psi_2(\mathbf{r}_m^{c+}) \right\} \right] \\
&\quad - \left[\left\{ \frac{\mathbf{Q}_1(\mathbf{r}_m^{c+})}{\mu_1} + \frac{\mathbf{Q}_2(\mathbf{r}_m^{c+})}{\mu_2} \right\} + \left\{ \frac{\mathbf{Q}_1(\mathbf{r}_m^{c-})}{\mu_1} + \frac{\mathbf{Q}_2(\mathbf{r}_m^{c-})}{\mu_2} \right\} \right]
\end{aligned} \tag{2.71}$$

where the \mathbf{P}_i and \mathbf{Q}_i terms containing the curl operations are given by

$$\mathbf{P}_{1,2}(\mathbf{r}_m^{c\pm}) = \frac{l_m}{2} \rho_m^{c\pm} \cdot [\nabla \times \mathbf{F}_{1,2}(\mathbf{r}_m^{c\pm})] \quad (2.72)$$

$$\mathbf{Q}_{1,2}(\mathbf{r}_m^{c\pm}) = \frac{l_m}{2} \rho_m^{c\pm} \cdot [\nabla \times \mathbf{A}_{1,2}(\mathbf{r}_m^{c\pm})] \quad (2.73)$$

where

$$[\nabla \times \mathbf{F}_i(\mathbf{r})] = \frac{\epsilon'_i}{4\pi} \iint_S \mathbf{M}(\mathbf{r}') \times \nabla' G_i(\mathbf{r}, \mathbf{r}') dS(\mathbf{r}') \quad (2.74)$$

and

$$[\nabla \times \mathbf{A}_i(\mathbf{r})] = \frac{\mu}{4\pi} \iint_S \mathbf{J}(\mathbf{r}') \times \nabla' G_i(\mathbf{r}, \mathbf{r}') dS(\mathbf{r}') \quad (2.75)$$

As is the case in section 2.4.2, the integrals over the tested terms of the vector potentials are approximated by evaluating the potentials at the centroids of the respective triangles. This avoids the computation of double surface integrals, which can be computational very demanding. The same approximation is applied to the evaluation of the terms with integrals with "curl terms" in equations (2.72) and (2.73).

Several researchers have shown that the above mentioned approximations for evaluating the impedance matrix entries are sufficiently accurate to represent numerically the electromagnetic scattering by arbitrary shaped dielectric objects. Umashankar *et al.* [53] used a method based on the method of moments and the CFIE to analyse electromagnetic scattering by arbitrary

shaped 3-D homogeneous lossy and lossless objects. They employed the RWG functions as both expansion and testing functions. The comparisons of the numerical results against the analytical results for the sphere and a finite circular cylinder were good. Sarkar *et al.* [113] compared the far-field results computed from the surface integral formulation and the volume formulation for the problem of electromagnetic scattering from dielectric objects analysis of scattering problems. The results from the approaches were in good agreement, thereby validating both the approaches for the analysis of scattering problems. For the surface formulation, the Sarkar *et al.* [113] adopted triangle-patch modelling developed by Rao [6].

Opp *et al.* [114] applied the triangular surface patch technique to homogeneous dielectric bodies using the combined field integral equation and validated the surface currents against analytic expressions for the surface fields for a homogeneous dielectric sphere. Their MoM generated results agreed very well with the predicted analytical results. The reason for performing the surface current validation was that the far field computation would wash out many of the numerical errors present in the surface currents. Sheng *et al.* [115] presented an accurate method of moments solution of the CFIE using the multilevel fast multipole algorithm for scattering by 3-D arbitrarily shaped homogeneous objects using the RWG functions as both the expansion and testing functions.

2.7 Formulation for Conducting and Dielectric Objects

This section reviews the formulation for the problem of electromagnetic scattering from objects consisting of perfectly conducting and homogeneous dielectric bodies of arbitrary shape situated in an isotropic free space medium. The system is excited by a plane wave. The surface equivalence principle [105] is used to replace the bodies by equivalent conductor surface current

\mathbf{J}_c , dielectric electric surface current \mathbf{J}_d and dielectric magnetic surface current \mathbf{M}_d , radiating into an unbounded medium. A set of coupled integral equations, involving the surface currents, is obtained by enforcing the boundary conditions on the tangential components of the total electric and magnetic fields. The method of moments is used to solve the integral equations. The following formulation is based on the work in [6] and [53].

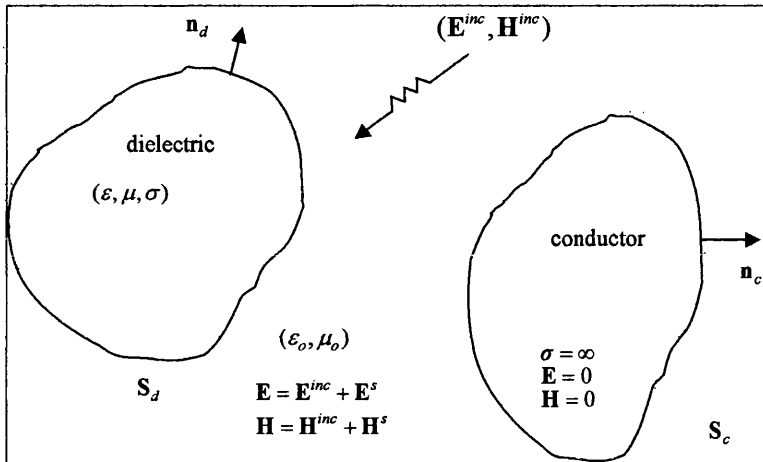


Figure 2.3 The original conductor-dielectric problem

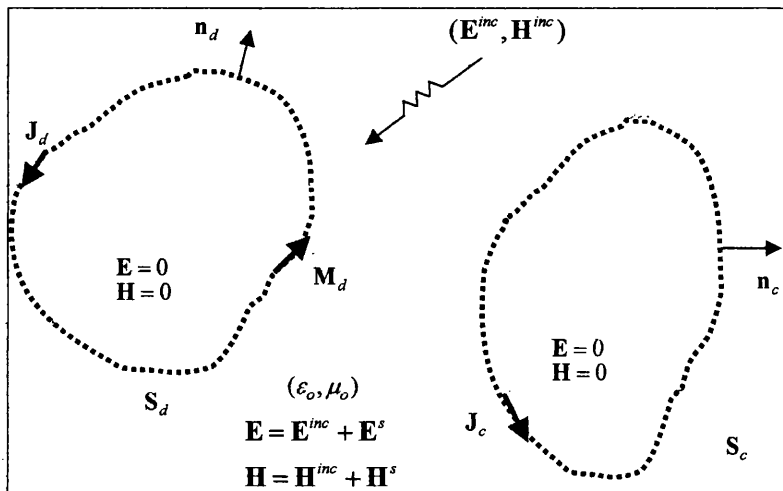


Figure 2.4 The external equivalence problem

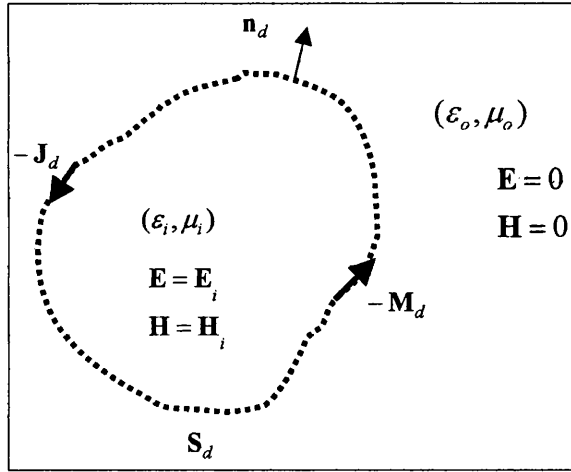


Figure 2.5 The internal equivalence problem for the fields in the dielectric

The two-body configuration comprising a conducting object and a dielectric object shown in Figure 2.3, will be used to illustrate the formulation for the mixed problem. Although only two objects are shown for simplicity, the formulation can be extended to multiple conducting and dielectric objects. In Figure 2.3, S_c and S_d denote the surfaces of a perfectly conducting and a homogeneous body of arbitrary shape immersed in a homogeneous medium whose medium parameters are (ϵ_o, μ_o) . S_c can either be open or closed but S_d can not be open. The objects are excited by external impressed sources that produce the field $(\mathbf{E}^{inc}, \mathbf{H}^{inc})$ in the absence of the objects. The objective is to obtain the total fields (\mathbf{E}, \mathbf{H}) at any arbitrary point outside the two objects. This total field is the sum of the incident field and the scattered field. Using the equivalence principle [105], the scattered field can be produced by equivalent surface currents of proper magnitude direction flowing on surfaces S_c and S_d and radiating into an unbounded medium. Applying the boundary conditions on the tangential components of the total fields results in a set of coupled integral equations for these surface currents.

Using the equivalence principle, the problem of Figure 2.3 can be solved by considering the external equivalent problem shown in Figure 2.4 and the

internal equivalent problem shown in Figure 2.5. In the external equivalent problem, the conducting body is replaced by an electric current, \mathbf{J}_c , flowing on surface S_c and the dielectric body of Figure 2.3 is replaced by equivalent electric and magnetic surface currents \mathbf{J}_d and \mathbf{M}_d flowing on surface S_d . The material parameters of the whole space are now (ϵ_o, μ_o) and the impressed sources are still the same as in the original problem of Figure 2.3. The total field (\mathbf{E}, \mathbf{H}) at external points to the bodies is the sum of the incident field and the field produced by the surface currents \mathbf{J}_c , \mathbf{J}_d and \mathbf{M}_d radiating in the unbounded medium characterised by (ϵ_o, μ_o) as shown in Figure 2.4. Inside the bodies, the scattered field cancels the incident field.

Hence we can have,

$$\mathbf{E}^s(\mathbf{J}_c)_{\text{tan}} = -\mathbf{E}_{\text{tan}}^{\text{inc}} \quad \text{on } S_c^- \quad (2.76)$$

$$\mathbf{H}^s(\mathbf{J}_c)_{\text{tan}} = -\mathbf{H}_{\text{tan}}^{\text{inc}} \quad \text{on } S_c^- \quad (2.77)$$

$$\mathbf{E}^s(\mathbf{J}_d, \mathbf{M}_d)_{\text{tan}} = -\mathbf{E}_{\text{tan}}^{\text{inc}} \quad \text{on } S_d^- \quad (2.78)$$

$$\mathbf{H}^s(\mathbf{J}_d, \mathbf{M}_d)_{\text{tan}} = -\mathbf{H}_{\text{tan}}^{\text{inc}} \quad \text{on } S_d^- \quad (2.79)$$

where the subscript "tan" denotes the tangential component, S_c^- and S_d^- denote the surfaces just inside S_c and S_d respectively, $\mathbf{E}^s(\mathbf{J}_c)$, $\mathbf{E}^s(\mathbf{J}_d, \mathbf{M}_d)$, $\mathbf{H}^s(\mathbf{J}_c)$ and $\mathbf{H}^s(\mathbf{J}_d, \mathbf{M}_d)$ represent the electric and magnetic fields produced by the surface currents \mathbf{J}_c , \mathbf{J}_d and \mathbf{M}_d when they radiate into the unbounded medium (ϵ_o, μ_o) .

Since the fields across S_c and S_d in Figure 2.4 are discontinuous, the currents are given by

$$\mathbf{J}_c = \mathbf{n}_c \times \mathbf{H}_c^+ \quad (2.80)$$

$$\mathbf{J}_d = \mathbf{n}_d \times \mathbf{H}_d^+ \quad (2.81)$$

$$\mathbf{M}_d = -\mathbf{n}_d \times \mathbf{E}_d^+ \quad (2.82)$$

where \mathbf{n}_c and \mathbf{n}_d represent the unit outward normal vectors to S_c and S_d respectively, \mathbf{H}_c^+ is the total magnetic field just outside S_c in Figure 2.4 and $(\mathbf{E}_d^+, \mathbf{H}_d^+)$ are the total fields outside S_d in Figure 2.4. The field inside S_d is calculated using the equivalence shown in Figure 2.5. In this case the whole space is characterised by the parameters (ϵ_i, μ_i) and the impressed sources of the original problem are replaced by equivalent surface currents $-\mathbf{J}_d$ and $-\mathbf{M}_d$. These currents produce the total field $(\mathbf{E}_i, \mathbf{H}_i)$ at any point internal to S_d . Outside S_d , the fields are zero. \mathbf{E}_i and \mathbf{H}_i are purely scattered fields calculated from the currents $-\mathbf{J}_d$ and $-\mathbf{M}_d$.

Hence

$$\mathbf{E}_i^+(-\mathbf{J}_d, -\mathbf{M}_d)_{\tan} = 0 \quad \text{on } S_d^+ \quad (2.83)$$

$$\mathbf{H}_i^+(-\mathbf{J}_d, -\mathbf{M}_d)_{\tan} = 0 \quad \text{on } S_d^+ \quad (2.84)$$

where S_d^+ is the surface just outside S_d , $\mathbf{E}_i^+(\mathbf{J}_d, \mathbf{M}_d)$ and $\mathbf{H}_i^+(\mathbf{J}_d, \mathbf{M}_d)$ are the electric and magnetic fields produced by the surface currents \mathbf{J}_d and \mathbf{M}_d at a point on S_d^+ .

Combining equations (2.76)-(2.79) and (2.83)-(2.84) gives

$$\mathbf{E}_{\tan}^{inc} = -\left[\mathbf{E}^s(\mathbf{J}_c) + \mathbf{E}^s(\mathbf{J}_d, \mathbf{M}_d)\right]_{\tan} \quad \text{on } S_c \quad (2.85)$$

$$\mathbf{E}_{\tan}^{inc} = -\left[\mathbf{E}^s(\mathbf{J}_c) + \mathbf{E}^s(\mathbf{J}_d, \mathbf{M}_d)\right]_{\tan} \quad \text{on } S_d \quad (2.86)$$

$$\mathbf{H}_{\tan}^{inc} = -\left[\mathbf{H}^s(\mathbf{J}_c) + \mathbf{H}^s(\mathbf{J}_d, \mathbf{M}_d)\right]_{\tan} \quad \text{on } S_d \quad (2.87)$$

Testing of the equations (2.85)-(2.87) with the RWG basis functions follows the same pattern as was the case of the CFIE for dielectric bodies in section 2.6.2.

Since the introduction of the RWG basis functions, several researchers have used the RWG basis functions as both the expansion and testing functions in the analysis of mixed problems. Sarkar *et. al.* [116] analysed electromagnetic scattering and radiation from finite microstrip structures using the CFIE and the MoM using the RWG basis functions. Results obtained were in good agreement with those based on the volume integral formulation. Arvas *et. al.* [117] used a solution procedure based on the CFIE and method of moments solution technique. The RWG basis functions were used for both the expansion and testing functions. Rao *et. al.* [118] used a solution procedure based on the CFIE and method of moments solution technique. The RWG basis functions were used as both the expansion and testing functions.

Salman and McCowen [119] used a MoM scheme based on the combined field integral equation (CFIE) to model planar microstrip structures using the RWG basis functions. In another paper Salman and McCowen [120] applied the MoM to solve the CFIE on mixed conducting and dielectric structures. They approximated the scattering surfaces by triangular patches and used the RWG basis functions as both the expansion and testing functions. Results obtained with this method were found to be in good agreement with those obtained using the CGFFT scheme. Ling *et al* [121] combined the adaptive integral method and the discrete complex image method to analyse large-scale microstrip structures. They discretised the mixed potential integral equation using the RWG basis functions for expansion and testing.

2.8 Concluding Remarks

The use of the RWG basis functions as both the expansion and testing functions in the use of the EFIE, MFIE and the CFIE with the moment method for treating problems of electromagnetic scattering by arbitrarily shaped objects has been reviewed. Of particular importance in this review are the approximations made in the evaluation of the tested integral equations. Considering the tested integral equations, the integrals formed by the tested vector potentials are approximated by evaluating the vector potentials at the centroids of the respective observation triangles. Similarly, the tested gradient of the scalar potentials are approximated by evaluating the scalar potentials at the respective centroids of the observation triangles. The same approximations are applied to the evaluation of the tested curl of the vector potentials.

The purpose of these approximations is to eliminate surface integrals of the potential quantities thus avoiding the expensive computation of two double surface integrals to evaluate the elements of the impedance matrix elements.

References of several published works using this method have been cited in the previous sections of this chapter.

It is the quality of these approximations and their implications in solving electrically large problems that is the subject of the work in this thesis in the following chapters. The next chapter addresses these approximations by presenting a formulation for electromagnetic scattering from perfectly conducting objects where the testing of the EFIE is not approximated but is performed numerically.

CHAPTER 3

FOUR-SI FORMULATION FOR ELECTROMAGNETIC SCATTERING FROM PERFECTLY CONDUCTING OBJECTS

| | |
|--|-----|
| 3.1 Introduction | 52 |
| 3.2 Four-SI formulation for perfectly conducting bodies | 53 |
| 3.2.1 Area Coordinates | 56 |
| 3.2.2 Numerical Solution of the tested EFIE | 60 |
| 3.2.2 Evaluation of the tested electric scalar potential | 67 |
| 3.2.3 Evaluation of the tested incident field | 68 |
| 3.3 Impedance Matrix Calculations | 69 |
| 3.3.1 Calculation of the Impedance Elements | 69 |
| 3.3.2 Optimum number of Gaussian points | 70 |
| 3.3.2.1 Introduction | 70 |
| 3.3.2.2 Optimisation of number of Gaussian Points | 72 |
| 3.3.2.2 Singularity Extraction | 81 |
| 3.4 Matrix Equation Solver | 83 |
| 3.5 Numerical Results and Discussions | 83 |
| 3.5.1 Introduction | 83 |
| 3.5.2 Scattering from a Sphere | 84 |
| 3.5.3 Scattering from a metallic disc at oblique incidence | 89 |
| 3.5.4 Scattering from a metallic plate at nearly grazing incidence | 93 |
| 3.5.5 Scattering from a metallic rectangular Trihedral | 96 |
| 3.5.6 Scattering from a cavity | 100 |
| 3.6 Conclusion | 106 |

3.1 Introduction

This chapter presents the derivation of the four surface integral (4-SI) formulation based on the EFIE for electromagnetic scattering from perfect electric conductors. The EFIE has been used extensively to analyze radiation and scattering from perfectly conducting bodies [5,6,36,47,50,85,109,122,123]. The EFIE formulation is solved using the MoM via the Galerkin method using the RWG basis functions discussed in Chapter 2.

The solutions from the proposed method offer computational advantages when analysing scattering from electrically large bodies. In the RWG formulation, as discussed in Chapter 2, the values of the terms containing the vector potential, electric scalar potentials and the incident field are approximated by their values at the centroid of the triangles when solving the tested EFIE.

With this new 4-SI scheme, a more accurate evaluation of the impedance matrix terms is performed. This is achieved by using an n -point Gaussian quadrature scheme to evaluate the integrals over the observation triangles, and a Patterson's integration method [124] over the source triangles. In the RWG formulation, there is only one testing point. With this new formulation, the RWG basis functions reviewed in Chapter 2 are used as both the expansion and testing functions. Two forms of the new scheme were implemented, namely the 2-SI and 4-SI schemes denoting integration over the source triangle only in the first instance and integration over both the source and observation triangles in the second case.

The equations arising from the tested EFIE are derived and the various terms are written in such a way as to facilitate easy coding. In adopting this new scheme, careful consideration needs to be given to the algorithms that are used to

compute each impedance matrix term. The algorithms were coded and embedded into the Swansea's MoM3D code [125].

The presentation of the 4-SI formulation for perfectly conducting objects is done in two parts. Firstly, the theory for the 4-SI formulation is presented in sections 3.2-3.3. The derived equations are left in a form suitable for numerical programming. This follows from the theory reviewed in Chapter 2.

In the second part of the chapter, the 4-SI scheme is validated through applications to a number of electromagnetic scattering problems. For validation purposes, published references are used. In cases where published data is not available, a 2 surface integral (2-SI) simulation (identical to the formulation used by Rao et al. [6]) with a fine level of discretisation is used as a reference. The 2-SI scheme used by the Swansea's Electromagnetics Research Group has been extensively validated against published works [51,90,120].

3.2 Four-SI formulation for perfectly conducting bodies

The derivation and testing of the EFIE equation using the RWG basis functions for both the expansion and testing functions was reviewed in section 2.4.1. The approximation of the tested EFIE, as first suggested by Rao *et al.* [6] was highlighted in the same section. In this work, no approximations are done in the evaluation of the integrals in the tested EFIE. Instead, the integrals of the tested EFIE are evaluated more accurately. Equation (2.37), which is the tested EFIE, is repeated here for the sake of continuity:

$$\langle \mathbf{E}^{inc}, \mathbf{f}_m \rangle = j\omega \langle \mathbf{A}, \mathbf{f}_m \rangle + \langle \nabla \phi, \mathbf{f}_m \rangle \quad (3.1)$$

where the magnetic vector potential, \mathbf{A} , and the scalar electric potential, ϕ , are given by equations (2.18) and (2.20) respectively.

The integrals in (3.1) will now be evaluated without making the approximations pointed out in Chapter 2.

Consider the first term on the right hand side of equation (3.1). This can be written as

$$\begin{aligned}
 j\omega \langle \mathbf{A}_n(\mathbf{r}'), \mathbf{f}_m(\mathbf{r}) \rangle &= j\omega \frac{l_m}{2A_m^+} \iint_{T_m^+} \mathbf{A}_n(\mathbf{r}') \cdot \rho_m^+(\mathbf{r}) dS + j\omega \frac{l_m}{2A_m^-} \iint_{T_m^-} \mathbf{A}_n(\mathbf{r}') \cdot \rho_m^-(\mathbf{r}) dS \\
 &= j\omega \frac{\mu_o}{4\pi} \frac{l_m}{2A_m^+} \frac{l_n}{2A_n^+} \iint_{T_m^+} \iint_{T_n^+} \rho_n^+(\mathbf{r}') \cdot \rho_m^+(\mathbf{r}) \frac{e^{-jkR}}{R} dS' dS \\
 &\quad + j\omega \frac{\mu_o}{4\pi} \frac{l_m}{2A_m^-} \frac{l_n}{2A_n^-} \iint_{T_m^-} \iint_{T_n^-} \rho_n^-(\mathbf{r}') \cdot \rho_m^-(\mathbf{r}) \frac{e^{-jkR}}{R} dS' dS
 \end{aligned} \tag{3.2}$$

using

$$\mathbf{A}(\mathbf{r}') = \frac{\mu_o}{4\pi} \iint_s \mathbf{J}(\mathbf{r}') \frac{e^{-jkR}}{R} dS \tag{3.3}$$

and the discretisation expression for the electric surface current given in equation (2.27), \mathbf{f}_m is the testing function and is the same as the basis function defined in equation (2.24). The integral terms in (3.2) are easily dealt with if a coordinate transformation is done such that the integrations are performed using a local coordinate system defined with respect to the triangles' vertices.

Next, the second term on the right hand side of equation (3.1) can be expanded as:

$$\begin{aligned}
\langle \nabla \Phi, \mathbf{f}_m \rangle &= - \iint_S \Phi \nabla_s \cdot \mathbf{f}_m dS \\
&= \frac{1}{4\pi j\omega\epsilon} \frac{l_m}{A_m^+} \frac{l_n}{A_n^+} \iint_{T_m^+} \iint_{T_n^+} \frac{e^{-jkR}}{R} dS' dS \\
&\quad - \frac{1}{4\pi j\omega\epsilon} \frac{l_m}{A_m^-} \frac{l_n}{A_n^-} \iint_{T_m^-} \iint_{T_n^-} \frac{e^{-jkR}}{R} dS' dS
\end{aligned} \tag{3.4}$$

where use has been made of equations (2.25), (2.35) and (2.40). Equation (3.4) also requires the evaluation of two surface integrals. One is performed over the source triangle and the other is performed over the observation triangle. Although (3.4) contains no position vector terms, the integration is most easily done using a coordinate system defined locally to each triangle.

Similarly, the tested incident field is given by

$$\langle \mathbf{E}^{inc}, \mathbf{f}_m \rangle = \frac{l_m}{A_m^+} \iint_{T_m^+} \mathbf{E}^{inc} \cdot \boldsymbol{\rho}_m^+ dS + \frac{l_m}{A_m^-} \iint_{T_m^-} \mathbf{E}^{inc} \cdot \boldsymbol{\rho}_m^- dS \tag{3.5}$$

The equations (3.2), (3.4) and (3.5) are most easily evaluated if the integrations are performed using a local system of normalised area coordinates. The next section will discuss the transformation from a global coordinate system to a local system of normalized area coordinates before integrals in (3.2), (3.4) and (3.5) are dealt with.

3.2.1 Area Coordinates

This section reviews a quadrature rule for evaluating an integral over a triangle. The integrations over the triangle are most easily conveniently evaluated after mapping the global coordinates of the triangular patches to a local system of area coordinates [126]. The surface integrals can then be evaluated by Gaussian quadrature after transforming the global Cartesian coordinates (x, y, z) to a system of local area coordinates (a, b, c) . The latter terms will be defined shortly.

The evaluation of the integrals in equations (3.2)-(3.5) involves the computation of the integrals over the observation triangles using an n-point Gaussian quadrature. The optimum number of "n-point" will be determined in Section 3.3.2. The integration over the source triangle is computed using Patterson's rule [124]. Area coordinates simplify the representation and calculation of the terms containing the scalar and vector integrals in the tested integral equations [127,128]. This is achieved by locating an arbitrary point P inside the source triangle, T^q , or observation triangle, T^p , such that the normalised area coordinates are given by

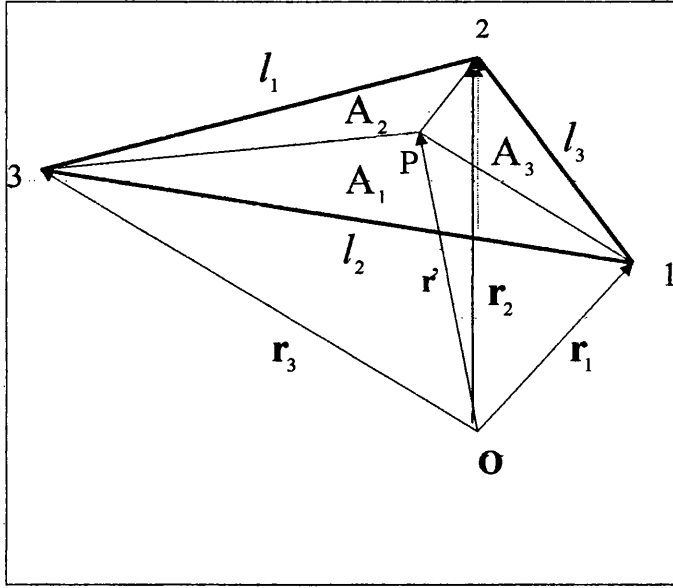


Figure 3.1 Triangle patch showing the partitioning that defines the area coordinates

$$a = \frac{A_1}{A}, \quad b = \frac{A_2}{A}, \quad c = \frac{A_3}{A} \quad (3.6)$$

where point P divides the triangle into areas A_1 , A_2 , A_3 and A is the area of the triangle. This is illustrated in Figure 3.1. O is the global origin and in this particular case, a source triangle is shown with its vertices numbered 1, 2 and 3. The lengths of the sides are l_1 , l_2 and l_3 . For the source triangle, the vertices have position vectors \mathbf{r}_1 , \mathbf{r}_2 and \mathbf{r}_3 , which are defined with respect to the global origin O . From (3.6), it is apparent that the normalized area coordinates are coupled by the equation

$$a + b + c = 1 \quad (3.7)$$

Each point within a given triangle can therefore be represented in terms of the normalised area coordinates and the position vectors of its vertices. For the source triangle, the global position vector for any point P inside the triangle is given by

$$\mathbf{r}' = a\mathbf{r}'_1 + b\mathbf{r}'_2 + c\mathbf{r}'_3 = a\mathbf{r}'_1 + b\mathbf{r}'_2 + (1-a-b)\mathbf{r}'_3 \quad (3.8)$$

The corresponding expression for case where P is inside the observation triangle is

$$\mathbf{r}^o = a\mathbf{r}^o_1 + b\mathbf{r}^o_2 + c\mathbf{r}^o_3 = a\mathbf{r}^o_1 + b\mathbf{r}^o_2 + (1-a-b)\mathbf{r}^o_3 \quad (3.9)$$

Here the superscript " ' " denotes source point and the superscript " o " denotes an observation point.

Equations (3.8) and (3.9) can be written in matrix form as:

$$\begin{bmatrix} \mathbf{r}'_x \\ \mathbf{r}'_y \\ \mathbf{r}'_z \end{bmatrix} = \begin{bmatrix} \mathbf{r}'_{1x} & \mathbf{r}'_{2x} & \mathbf{r}'_{3x} \\ \mathbf{r}'_{1y} & \mathbf{r}'_{2y} & \mathbf{r}'_{3y} \\ \mathbf{r}'_{1z} & \mathbf{r}'_{2z} & \mathbf{r}'_{3z} \end{bmatrix} \begin{bmatrix} a \\ b \\ c \end{bmatrix} \quad (3.10)$$

and

$$\begin{bmatrix} \mathbf{r}^o_x \\ \mathbf{r}^o_y \\ \mathbf{r}^o_z \end{bmatrix} = \begin{bmatrix} \mathbf{r}^o_{1x} & \mathbf{r}^o_{2x} & \mathbf{r}^o_{3x} \\ \mathbf{r}^o_{1y} & \mathbf{r}^o_{2y} & \mathbf{r}^o_{3y} \\ \mathbf{r}^o_{1z} & \mathbf{r}^o_{2z} & \mathbf{r}^o_{3z} \end{bmatrix} \begin{bmatrix} a \\ b \\ c \end{bmatrix} \quad (3.11)$$

respectively.

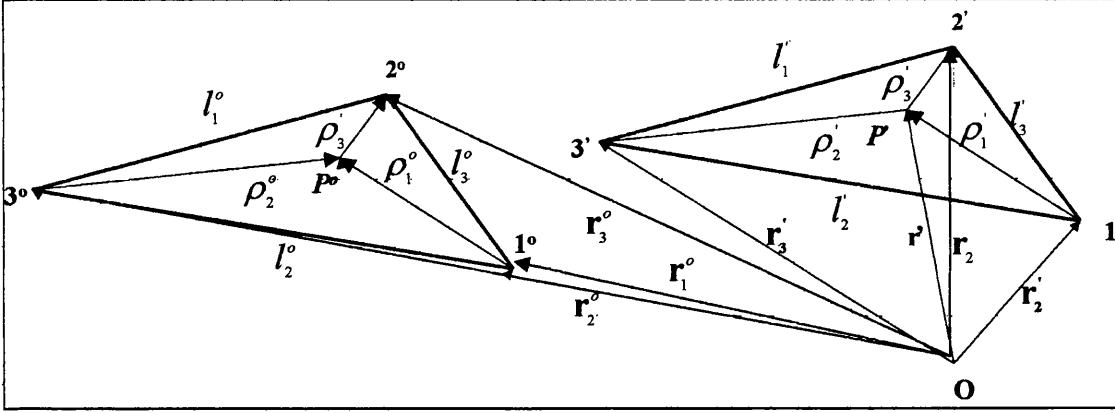


Figure 3.2 Source triangle T^q and observation triangle T^p with arbitrary located source and observation points.

The local position vectors, ρ_i' , for the source triangle, and ρ_i^o (for $i = 1, 2, 3$) for the observation triangle are defined with respect to the triangle vertices as shown in Figure 3.2. From Figure 3.2, the position vectors can be written as:

$$\rho_{i_q}' = \pm(\mathbf{r}' - \mathbf{r}_{i_q}') , \text{ for } i_q = 1, 2, 3 \quad (3.12)$$

and

$$\rho_{i_p}^o = \pm(\mathbf{r}^o - \mathbf{r}_{i_p}^o) , \text{ for } i_p = 1, 2, 3 \quad (3.13)$$

The positive sign is used if the current is flowing out of the triangle and negative if the current is flowing into the triangle.

To integrate over the source triangle, use is made of the following transformation from global coordinates to local coordinates:

$$\iint_{T^q} g(\mathbf{r}') d\mathbf{S}' = 2A \int_0^1 \int_0^{1-b} g[a\mathbf{r}'_1 + b\mathbf{r}'_2 + c\mathbf{r}'_3] da db \quad (3.14)$$

where $g(\mathbf{r}')$ is an arbitrary function over a triangle. This equation will be applied to the inner surface integral in equations (3.2), (3.4) and (3.5).

The integrations in section 3.2 can now be done in the local coordinate system, which is much simpler.

The integration over a triangle of surface of area A can be performed by using an n -point Gaussian quadrature scheme such that [128]:

$$\iint_S f(a, b, c) dS = A \sum_{i=1}^{N_g} w_i f(a_i, b_i, c_i) \quad (3.15)$$

Equation (3.15) will be used to solve the integrals over the observation triangles.

3.2.2 Numerical Solution of the tested EFIE

The transformation of global coordination system to the normalised local area coordinate system is now applied in the solution of the tested EFIE of equation (3.1).

Substituting (2.69), (3.12) and (3.13) into (3.2) gives

$$\begin{aligned}
& j\omega \langle \mathbf{A}_n(\mathbf{r}'), \mathbf{f}_m(\mathbf{r}) \rangle \\
& = (\pm) j\omega \frac{\mu_o}{4\pi} \frac{l_m}{2A_m^\pm} \frac{l_n}{2A_n^\pm} \iint_{T_m^\pm} \iint_{T_n^\pm} (\mathbf{r}' - \mathbf{r}_{i_q}) \cdot (\mathbf{r}^o - \mathbf{r}_{i_p}) G(\mathbf{r}^o, \mathbf{r}') dS' dS \\
& = (\pm) j\omega \frac{\mu_o}{4\pi} \frac{l_m l_n}{2A_m^\pm} \iint_{T_m^\pm} \left[\int_0^1 \int_0^{1-b} (a' \mathbf{r}'_1 + b' \mathbf{r}'_2 + c' \mathbf{r}'_3 - \mathbf{r}'_{i_q}) \cdot (a^o \mathbf{r}^o_1 + b^o \mathbf{r}^o_2 + c^o \mathbf{r}^o_3 - \mathbf{r}^o_{i_p}) \right. \\
& \quad \left. G(\mathbf{r}^o, \mathbf{r}') da' db' dS \right] \\
& \hspace{25em} (3.16)
\end{aligned}$$

Equation (3.14) has been applied to the inner surface integral over the source triangle T_n^\pm on the second line of equation (3.16). The inner surface integral is now to be evaluated in terms of the normalised local area coordinates. The same approach will be applied to the outer surface triangle, T_m^\pm .

By performing the dot product in equation (3.16), it can be written in the form

$$\begin{aligned}
j\omega \langle \mathbf{A}_n(\mathbf{r}'), \mathbf{f}_m(\mathbf{r}) \rangle & = (\pm) j\omega \frac{\mu_o}{4\pi} \frac{l_m l_n}{2A_m^\pm} [I_1 + I_2 + I_3 + I_4 + I_6 + I_7 + I_8 \\
& \hspace{15em} + I_9 + I_{10} + I_{11} + I_{12} + I_{13} + I_{14} + I_{15} + I_{16}] \\
& \hspace{25em} (3.17)
\end{aligned}$$

where

$$I_1 = \mathbf{r}_1^o \mathbf{r}_1' \left[\iint_{T_m^\pm} a^o \left(\int_0^1 \int_0^{1-b'} a' G(\mathbf{r}^o, \mathbf{r}') da' db' \right) \right] dS^o \quad (3.18)$$

$$= \mathbf{r}_1^o \mathbf{r}_1' A_m^\pm \sum_{i=1}^{N_g} w_i a_i^o \left(\int_0^1 \int_0^{1-b'} a' G(\mathbf{r}_i^o, \mathbf{r}') da' db' \right)$$

$$I_2 = \mathbf{r}_1^o \mathbf{r}_2' \left[\iint_{T_m^\pm} a^o \left(\int_0^1 \int_0^{1-b'} b' G(\mathbf{r}^o, \mathbf{r}') da' db' \right) \right] dS \quad (3.19)$$

$$= \mathbf{r}_1^o \mathbf{r}_2' A_m^\pm \sum_{i=1}^{N_g} w_i a_i^o \left(\int_0^1 \int_0^{1-b'} b' G(\mathbf{r}_i^o, \mathbf{r}') da' db' \right)$$

$$I_3 = \mathbf{r}_1^o \mathbf{r}_3' \left[\iint_{T_m^\pm} a^o \left(\int_0^1 \int_0^{1-b'} c' G(\mathbf{r}^o, \mathbf{r}') da' db' \right) \right] dS^o \quad (3.20)$$

$$= \mathbf{r}_1^o \mathbf{r}_3' A_m^\pm \sum_{i=1}^{N_g} w_i a_i^o \left(\int_0^1 \int_0^{1-b'} c' G(\mathbf{r}_i^o, \mathbf{r}') da' db' \right)$$

$$I_4 = -\mathbf{r}_1^o \mathbf{r}_{i_q}' \left[\iint_{T_m^\pm} a^o \left(\int_0^1 \int_0^{1-b'} G(\mathbf{r}^o, \mathbf{r}') da' db' \right) \right] dS^o \quad (3.21)$$

$$= -\mathbf{r}_1^o \mathbf{r}_{i_q}' A_m^\pm \sum_{i=1}^{N_g} w_i a_i^o \left(\int_0^1 \int_0^{1-b'} G(\mathbf{r}_i^o, \mathbf{r}') da' db' \right)$$

$$I_5 = \mathbf{r}_2^o \mathbf{r}_1' \left[\iint_{T_m^\pm} b^o \left(\int_0^1 \int_0^{1-b'} a' G(\mathbf{r}^o, \mathbf{r}') da' db' \right) \right] dS^o \quad (3.22)$$

$$= \mathbf{r}_2^o \mathbf{r}_1' A_m^\pm \sum_{i=1}^{N_g} w_i b_i^o \left(\int_0^1 \int_0^{1-b'} a' G(\mathbf{r}_i^o, \mathbf{r}') da' db' \right)$$

$$I_6 = \mathbf{r}_2^o \mathbf{r}_2' \left[\iint_{T_m^\pm} b^o \left(\int_0^1 \int_0^{1-b'} b' G(\mathbf{r}^o, \mathbf{r}') da' db' \right) \right] dS^o \quad (3.23)$$

$$= \mathbf{r}_2^o \mathbf{r}_2' A_m^\pm \sum_{i=1}^{N_g} w_i b_i^o \left(\int_0^1 \int_0^{1-b'} b' G(\mathbf{r}_i^o, \mathbf{r}') da' db' \right)$$

$$I_7 = \mathbf{r}_2^o \mathbf{r}_3' \left[\iint_{T_m^\pm} b^o \left(\int_0^1 \int_0^{1-b'} c' G(\mathbf{r}^o, \mathbf{r}') da' db' \right) \right] dS^o \quad (3.24)$$

$$= \mathbf{r}_2^o \mathbf{r}_3' A_m^\pm \sum_{i=1}^{N_g} w_i b_i^o \left(\int_0^1 \int_0^{1-b'} c' G(\mathbf{r}_i^o, \mathbf{r}') da' db' \right)$$

$$I_8 = -\mathbf{r}_2^o \mathbf{r}_{i_q}' \left[\iint_{T_m^\pm} b^o \left(\int_0^1 \int_0^{1-b'} G(\mathbf{r}^o, \mathbf{r}') da' db' \right) \right] dS^o \quad (3.25)$$

$$= -\mathbf{r}_2^o \mathbf{r}_{i_q}' A_m^\pm \sum_{i=1}^{N_g} w_i b_i^o \left(\int_0^1 \int_0^{1-b'} G(\mathbf{r}_i^o, \mathbf{r}') da' db' \right)$$

$$\begin{aligned}
I_9 &= \mathbf{r}_3^o \mathbf{r}_1' \left[\iint_{T_m^\pm} c^o \left(\int_0^1 \int_0^{1-b'} a' G(\mathbf{r}^o, \mathbf{r}') da' db' \right) \right] dS^o \\
&= \mathbf{r}_3^o \mathbf{r}_1' A_m^\pm \sum_{i=1}^{N_g} w_i c_i^o \left(\int_0^1 \int_0^{1-b'} a' G(\mathbf{r}_i^o, \mathbf{r}') da' db' \right)
\end{aligned} \tag{3.26}$$

$$\begin{aligned}
I_{10} &= \mathbf{r}_3^o \mathbf{r}_2' \left[\iint_{T^\pm} c^o \left(\int_0^1 \int_0^{1-b'} b' G(\mathbf{r}^o, \mathbf{r}') da' db' \right) \right] dS^o \\
&= \mathbf{r}_3^o \mathbf{r}_2' A_m^\pm \sum_{i=1}^{N_g} w_i c_i^o \left(\int_0^1 \int_0^{1-b'} b' G(\mathbf{r}_i^o, \mathbf{r}') da' db' \right)
\end{aligned} \tag{3.27}$$

$$\begin{aligned}
I_{11} &= \mathbf{r}_3^o \mathbf{r}_3' \left[\iint_{T_m^\pm} c^o \left(\int_0^1 \int_0^{1-b'} c' G(\mathbf{r}^o, \mathbf{r}') da' db' \right) \right] dS^o \\
&= \mathbf{r}_3^o \mathbf{r}_3' A_m^\pm \sum_{i=1}^{N_g} w_i c_i^o \left(\int_0^1 \int_0^{1-b'} c' G(\mathbf{r}_i^o, \mathbf{r}') da' db' \right)
\end{aligned} \tag{3.28}$$

$$\begin{aligned}
I_{12} &= -\mathbf{r}_3^o \mathbf{r}_{i_q}' \left[\iint_{T_m^\pm} c^o \left(\int_0^1 \int_0^{1-b'} G(\mathbf{r}^o, \mathbf{r}') da' db' \right) \right] dS^o \\
&= -\mathbf{r}_3^o \mathbf{r}_{i_q}' A_m^\pm \sum_{i=1}^{N_g} w_i c_i^o \left(\int_0^1 \int_0^{1-b'} G(\mathbf{r}_i^o, \mathbf{r}') da' db' \right)
\end{aligned} \tag{3.29}$$

$$I_{13} = -\mathbf{r}_{i_p}^o \mathbf{r}_1' \left[\iint_{T_m^\pm} \left(\int_0^1 \int_0^{1-b'} a' G(\mathbf{r}^o, \mathbf{r}') da' db' \right) \right] dS \quad (3.30)$$

$$= -\mathbf{r}_{i_p}^o \mathbf{r}_1' A_m^\pm \sum_{i=1}^{N_g} w_i \left(\int_0^1 \int_0^{1-b'} a' G(\mathbf{r}_i^o, \mathbf{r}') da' db' \right)$$

$$I_{14} = -\mathbf{r}_{i_p}^o \mathbf{r}_2' \left[\iint_{T_m^\pm} \left(\int_0^1 \int_0^{1-b'} b' G(\mathbf{r}^o, \mathbf{r}') da' db' \right) \right] dS \quad (3.31)$$

$$= -\mathbf{r}_{i_p}^o \mathbf{r}_2' A_m^\pm \sum_{i=1}^{N_g} w_i \left(\int_0^1 \int_0^{1-b'} b' G(\mathbf{r}_i^o, \mathbf{r}') da' db' \right)$$

$$I_{15} = -\mathbf{r}_{i_p}^o \mathbf{r}_3' \left[\iint_{T_m^\pm} \left(\int_0^1 \int_0^{1-b'} c' G(\mathbf{r}^o, \mathbf{r}') da' db' \right) \right] dS^o \quad (3.32)$$

$$= -\mathbf{r}_{i_p}^o \mathbf{r}_3' A_m^\pm \sum_{i=1}^{N_g} w_i \left(\int_0^1 \int_0^{1-b'} c' G(\mathbf{r}_i^o, \mathbf{r}') da' db' \right)$$

and

$$I_{16} = \mathbf{r}_{i_p}^o \mathbf{r}_{i_q}' \left[\iint_{T_m^\pm} \left(\int_0^1 \int_0^{1-b'} G(\mathbf{r}^o, \mathbf{r}') da' db' \right) \right] dS^o \quad (3.33)$$

$$= \mathbf{r}_{i_p}^o \mathbf{r}_{i_q}' A_m^\pm \sum_{i=1}^{N_g} w_i \left(\int_0^1 \int_0^{1-b'} G(\mathbf{r}_i^o, \mathbf{r}') da' db' \right)$$

where Gaussian quadrature integration, shown in (3.15), has been applied to the outer integral of (3.16). N_g is the total number of integration points on the

observation triangle T_m chosen according to the accuracy requirement and w_i is the weight associated with the i th sampling point. The procedure adopted to determine the required N_g is presented in section 3.3.2. The Gaussian quadrature is only applied as long as $T_m \neq T_n$.

For $T_m = T_n$, the integrands of both the vector and scalar potentials integrals are singular and a different integration approach is necessary.

To evaluate the elements of the impedance matrix, all four line integrals are evaluated. Hence the name four surface integrals method (4-SI) that has been given to this scheme. In this case, several observation points are placed in the observation triangle, T_m^\pm . The inner surface integral over the source triangle is evaluated for each observation point inside the triangle T_m^\pm . This approach improves the numerical accuracy when evaluating the impedance matrix elements, particularly for cases where closely coupled triangular patches are involved. However, a good compromise between accuracy in the calculation of the impedance terms and the number of Gaussian points inside the observation triangle is essential to avoid large computer computation times. Highly accurate numerical integrations lead to a substantial increase in CPU time.

From (3.18) - (3.33), it can be deduced that following relationships are true:

$$I_3 = I_4 - I_1 - I_2 \quad (3.34)$$

$$I_7 = I_8 - I_6 - I_5 \quad (3.35)$$

and

$$I_{15} = I_{16} - I_{14} - I_{13} \quad (3.36)$$

Using the relationship $c' = 1 - a' - b'$ or $c^o = 1 - a^o - b^o$, it observed that it is not necessary to evaluate integrals I_9 , I_{10} , I_{11} and I_{12} .

Hence it is only necessary to perform the integrations I_1 , I_2 , I_4 , I_5 , I_6 , I_8 , I_{13} , I_{14} and I_{16} .

In the above equations, the inner surface integrals are evaluated over the source triangles for each point located inside the observation triangle. The outer surface integral is evaluated using an n th point Gaussian quadrature rule.

3.2.2 Evaluation of the tested electric scalar potential

From equation (3.4), the tested gradient of the electric scalar potential can now be expanded to:

$$\begin{aligned}
\langle (\nabla\Phi)_n, \mathbf{f}_m \rangle &= (\pm) \frac{1}{4\pi j\omega\epsilon} \frac{l_m}{A_m^\pm} \frac{l_n}{A_n^\pm} \iint_{T_m^\pm} \iint_{T_n^\pm} \frac{e^{-jkR}}{R} dS' dS^o \\
&= (\pm) \frac{1}{4\pi j\omega\epsilon} \frac{l_m}{A_m^\pm} \frac{l_n}{1} (2) \iint_{T_m^\pm} \left[\int_0^1 \int_0^{1-b'} G(\mathbf{r}^o, \mathbf{r}') da' dh' \right] dS^o \quad (3.37) \\
&= (\pm) \frac{l_m l_n}{2\pi j\omega\epsilon} \sum_{i=1}^{N_g} w_i \left[\int_0^1 \int_0^{1-b'} G(\mathbf{r}_i^o, \mathbf{r}') da' dh' \right]
\end{aligned}$$

where use has been made of equation (3.14).

The term in square brackets in (3.37) is identical to I_{16} of the tested magnetic vector potential in equation (3.33).

3.2.3 Evaluation of the tested incident field

The tested incident electric field can now be written as

$$\begin{aligned}
\langle \mathbf{E}^{inc}, \mathbf{f}_m \rangle &= \iint_{T_m^\pm} \mathbf{E}^{inc} \cdot \mathbf{f}_m dS^o \\
&= \pm \frac{l_m}{2A_m^\pm} \iint_{T_m^\pm} \mathbf{E}^{inc} \cdot \mathbf{p}_m^\pm dS^o \quad (3.38) \\
&= \pm \frac{l_m}{2A_m^\pm} \iint_{T_m^\pm} \mathbf{E}^{inc} \cdot (\mathbf{r}^o - \mathbf{r}_{i_p}) dS^o \\
&= \pm \frac{l_m}{2} \sum_{i=1}^{N_g} E_{or}^{inc} (a_i^o r_{1or} + b_i^o r_{1or} + c_i^o r_{1or} - r_{i_p or})
\end{aligned}$$

where or can be x , y or z .

3.3 Impedance Matrix Calculations

The formulations developed in this chapter were coded and incorporated into the Swansea's MoM 3D tool [125]. The MoM 3D tool is a full-wave electromagnetic solver based on the EFIE and the MFIE, which are evaluated in the frequency domain. It can be used for arbitrary three-dimensional electromagnetic problems involving metallic structures (wires and surfaces) and piecewise homogeneous media. The surface or wire currents are computed using a method of moment technique [5].

3.3.1 Calculation of the Impedance Elements

The calculation of the impedance matrix elements follows from equations (3.16) through (3.37). Hence the impedance matrix element is in the form

$$Z_{mn} = j\omega \langle \mathbf{A}_n(\mathbf{r}'), \mathbf{f}_m(\mathbf{r}) \rangle + \langle (\nabla \Phi)_n, \mathbf{f}_m \rangle \quad (3.39)$$

where the element Z_{mn} is the contribution from testing over the observation triangle, T_m , on the electric field due to the electric current on source triangle T_n . The simplified expressions for the tested magnetic vector potential and the

electric scalar potentials are given in equations (3.17) – (3.33) and (3.37) respectively.

3.3.2 Optimum number of Gaussian points

3.3.2.1 Introduction

An important aspect of any numerical solution is the amount of computer time required to obtain the desired accuracy in the solution. The matrix fill time can be quite long because of the complexity of numerical integrations that are required to evaluate the vector and scalar potential contributions. Considerable savings in computation time are achieved by reducing the order of the numerical quadrature scheme when the integrand is slowly varying, i.e. when the source and observation points are not closely coupled. In that case, the 1-point Gaussian integration scheme is implemented. The outer integrals in equations (3.1) are only sampled at the centroid of the observation triangle.

Numerical experiments were done to investigate the performance of the 4-point, 7-point and 13-point to ascertain the optimum n-point quadrature scheme. This was done on a single edge formed by two triangles. This was a way of determining the convergence of the Green's function. Several shapes of triangles were investigated with various Gaussian quadrature integration formulae.

The objective was to adopt the lowest n-point Gaussian quadrature scheme that offers a good compromise between accuracy and total computation time. The time required for the computation of the impedance matrix elements is a substantial part of the total computing time and its essential that the order of numerical integration scheme be minimised as much as possible so as to improve the numerical efficiency of the scheme.

A singularity exists for cases where the observation and source triangles are coincident. The singularity is extracted from the integrand [50,129] and the remainder integrated using Gaussian quadrature.

The following method was used to determine the optimum number of Gaussian points needed to integrate the scattering by perfect electrical conductors accurately.

There are two critical regions of the integration process. One is when the source triangle is in the vicinity of the observation triangle. The other is when the integrand is singular. Then the kernels vary so rapidly that standard Gaussian quadrature cannot provide a suitable accurate approximation. When the source and observation triangles are closely coupled, a high number of sampling points are required in the Gaussian quadrature scheme.

The objective is to implement a different n th order Gaussian integration scheme as a function of the distance between the source and observation triangle. This is illustrated in Figure 3.3. A higher-order n_1 -point Gaussian scheme is implemented for observation triangles that are within a distance R_1 from the source triangle. For observation triangles located between R_1 and R_2 from the source triangle, a lower order n_2 -point scheme is implemented. For distance larger than R_2 , an n_3 -point scheme is used and this is a 1-point Gaussian scheme.

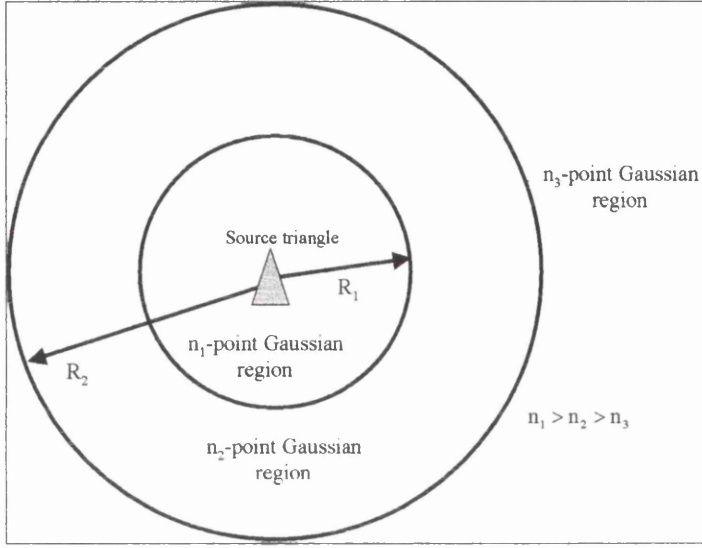


Figure 3.3 Implementation of an n -point Gaussian integration scheme as a function of distance between the source and observation triangles

The quadrature schemes used were taken from [127] and consisted of a one-point scheme, a four-point scheme, a seven-point scheme a thirteen-point scheme.

3.3.2.2 Optimisation of number of Gaussian Points

A nearness factor (NF) was introduced as a normalised parameter to specify the separation between source and observation triangles. The nearness factor is defined as

$$NF = \frac{D_{\max}}{R_{\min}} \quad (3.40)$$

where D_{\max} is the largest dimension of the source triangle and R_{\min} is the least distance from the source triangle vertices to the centroid of the observation triangle.

R_{\min} in (3.40) refers to R_1 or R_2 in Figure 3.3. Thus a higher n-point Gaussian scheme is associated with low values of R_{\min} .

Large values of NF imply that the source and observation triangles are very close, hence more accuracy is needed in computing the corresponding surface integrals. In that case, a higher order Gaussian method is needed. This implies that a large number of points equal to the order of the Gaussian integration method is needed within the observation triangle. This translates to more computation time for the evaluation of the surface integrals.

Small values of NF indicate that the source and observation triangles are far apart. Fewer points are needed for the observation triangle and a 1-point Gaussian integration point may be sufficient to achieve good integration accuracy if the separation distance is large enough.

A numerical experiment was performed by evaluating the impedance element for a particular source-observation triangle as a function of the nearness factor NF. The impedance elements were calculated using 1-point, 4-point, 7-point and 13-point Gaussian schemes and the results are plotted in Figure 3.5, Figure 3.7, Figure 3.9, Figure 11 and Figure 3.12. These were done for different triangle shapes.

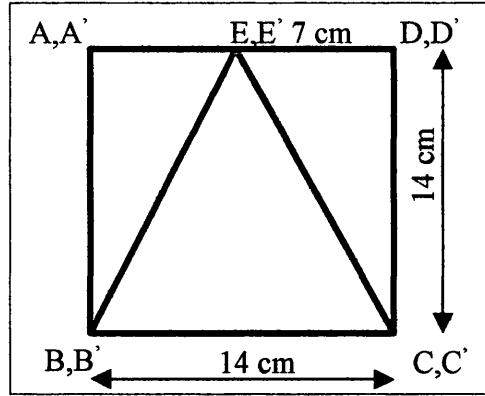


Figure 3.4 Triangles used to generate graph in Figure 3.5

Figure 3.4 shows two metallic plates, $ABCD$ and $A'B'C'D'$, each meshed into three triangles with the dimensions shown. The vertical distance between the plates is varied, with plate $ABCD$ fixed, and each time the impedance element for particular source/observation triangles is calculated using 1-point, 4-point, 7-point and 13-point Gaussian quadrature. Triangles BCE and $B'C'E'$ were used as the source and observation triangles respectively. All the dimensions shown in Figure 3.4 are in centimetres and the frequency was 300 MHz. The values for the impedance elements were plotted as a function of the nearness factor as shown in Figure 3.5.

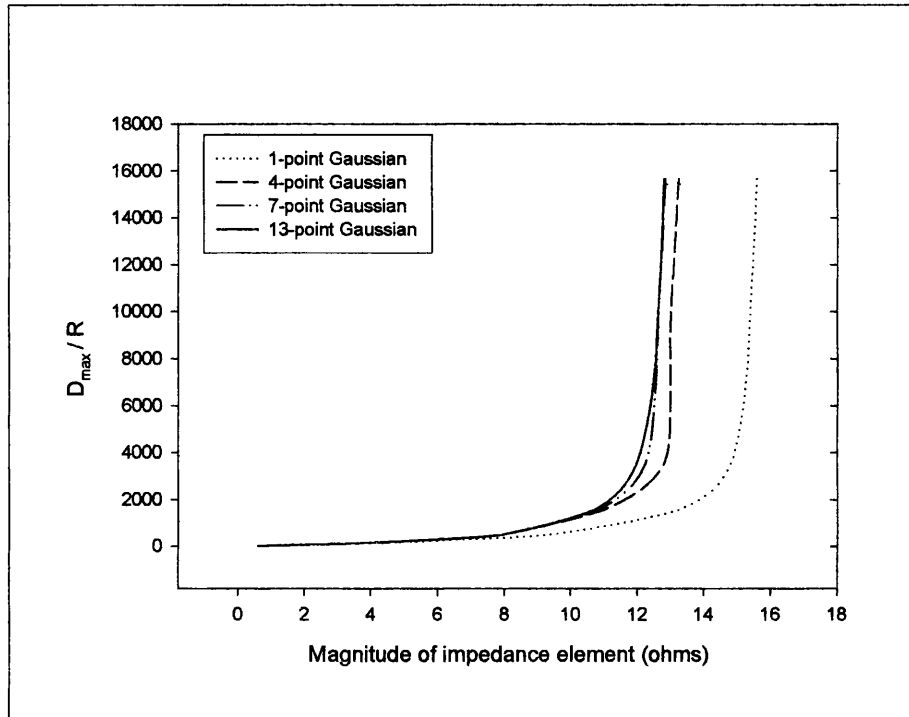


Figure 3.5 Case 1 - Variation of impedance element with nearness factor for Figure 3.4

The same procedure was repeated for three cases and the triangle shapes varied. These are shown in Figure 3.6 - Figure 3.12.

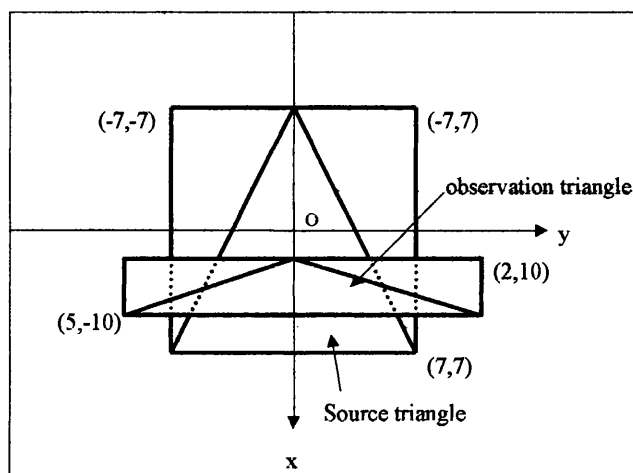


Figure 3.6 Mesh used to generate Figure 3.7

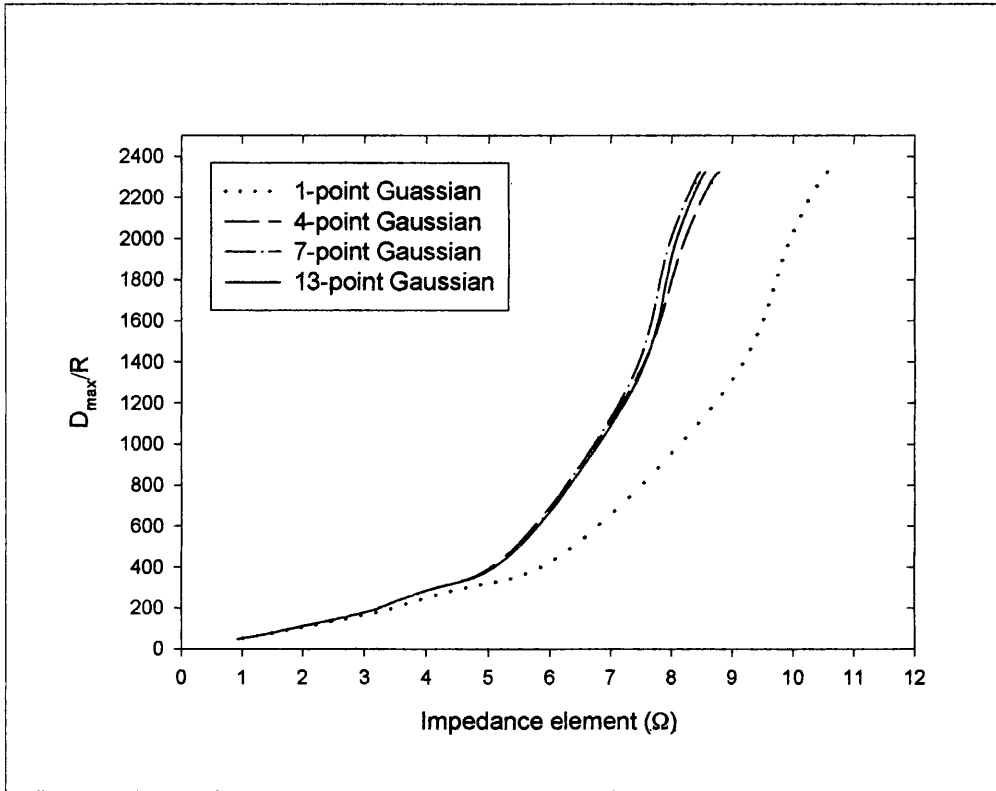


Figure 3.7 Case 2 Variation of impedance element with nearness factor for Figure 3.6

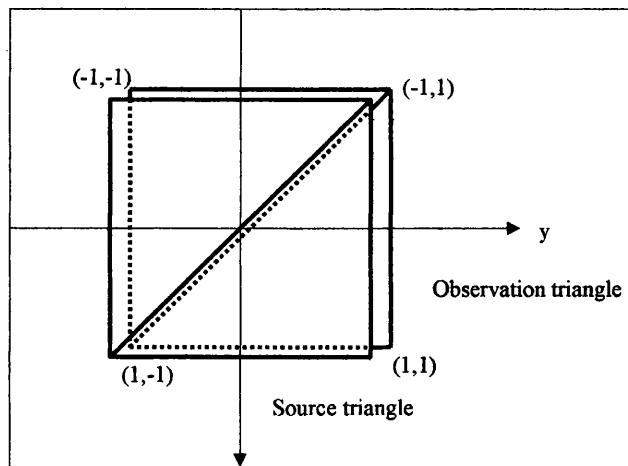


Figure 3.8 Mesh used to generate Figure 3.9

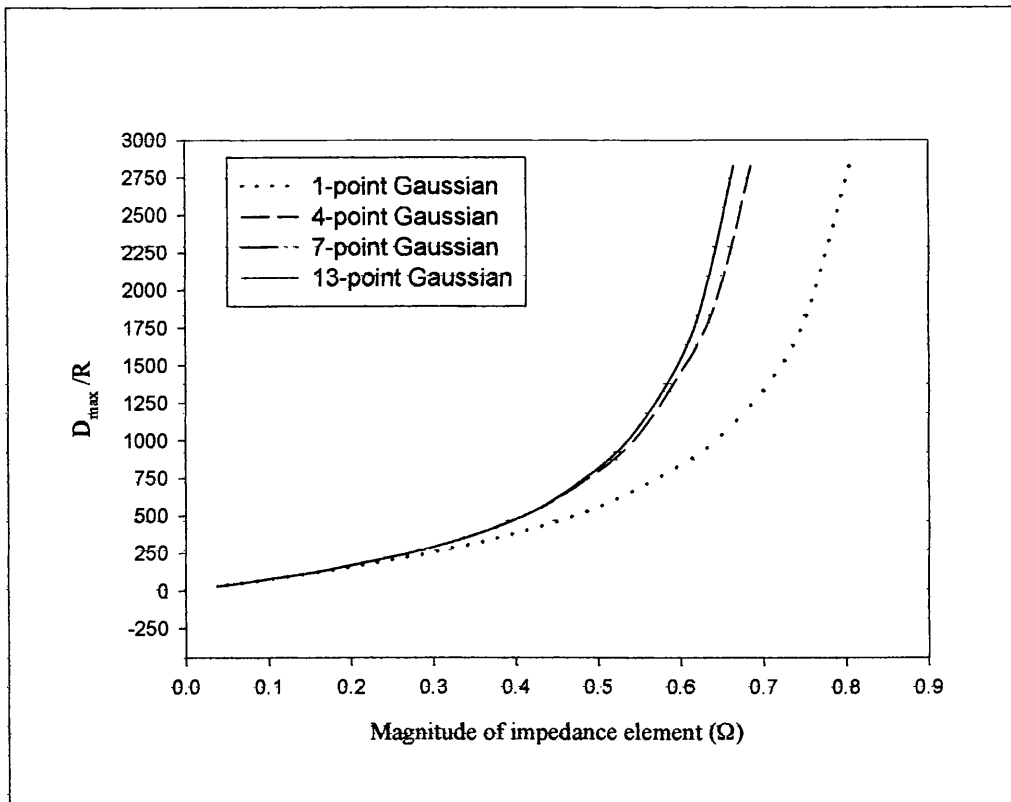


Figure 3.9 Case 3: Variation of impedance element with nearness factor for Figure 3.8

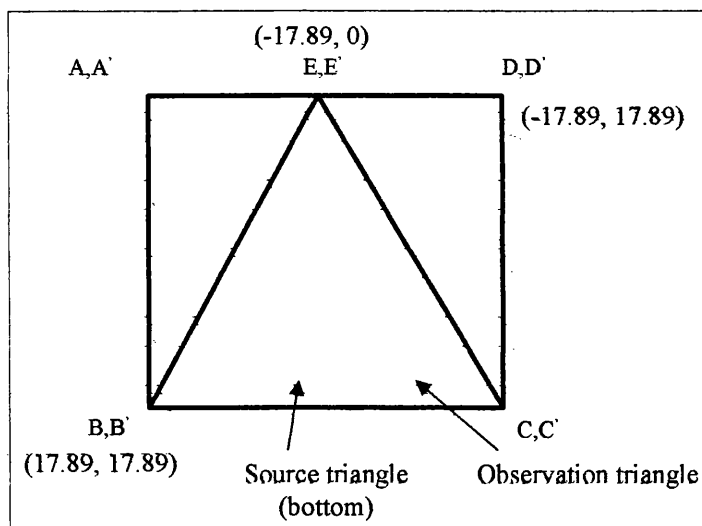


Figure 3.10 Mesh used to generate Figure 3.11

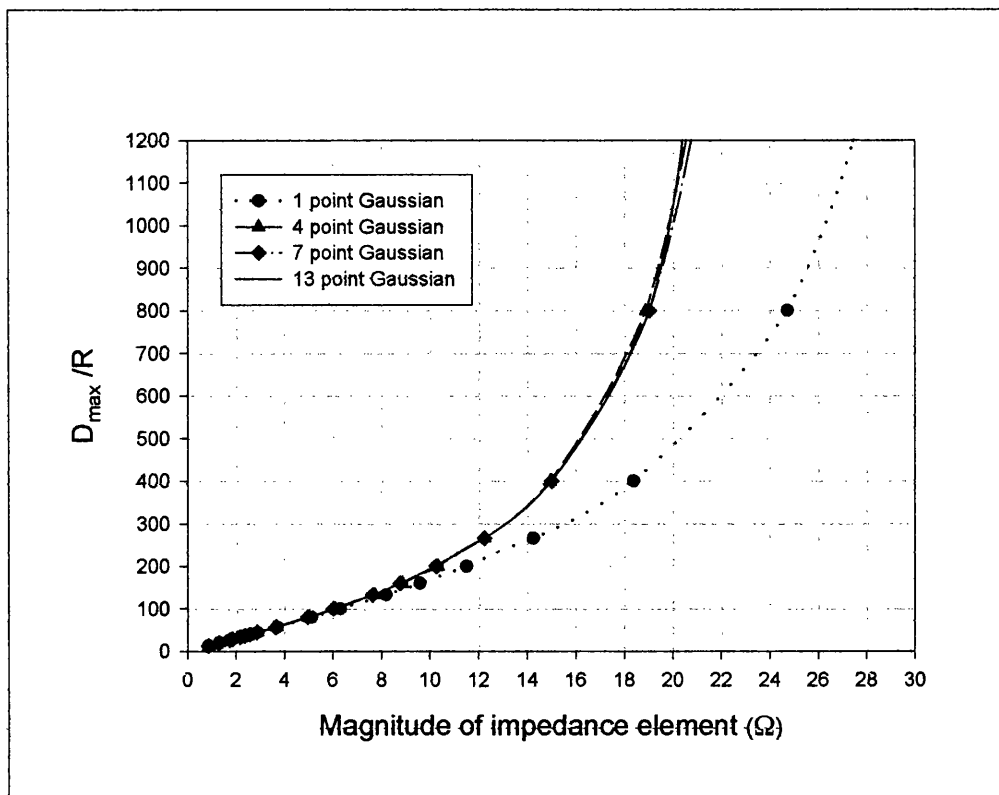


Figure 3.11 Case 4: Variation of impedance element with nearness factor for Figure 3.10

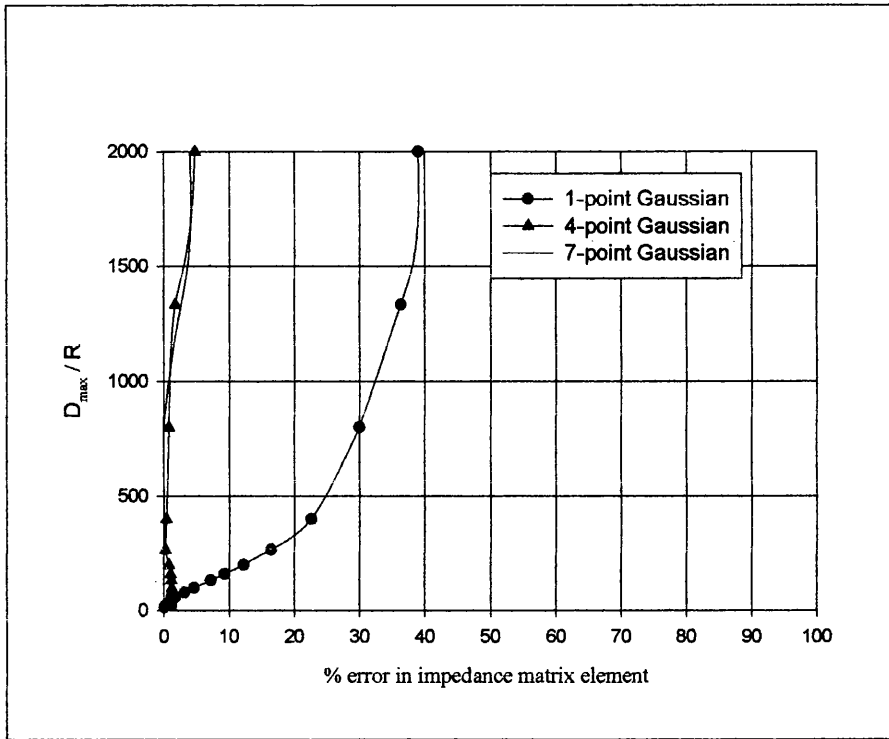


Figure 3.12 Relative error in evaluating the impedance elements for the 1-point, 4-point and 7-point Gaussian versus the nearness factor.

As Figure 3.5, Figure 3.7, Figure 3.9, Figure 3.11 and Figure 3.12 demonstrate, a distinct improvement in the impedance element calculations was observed by increasing the number of quadrature points from 1 to 13 for closely coupled face triangles. However, no appreciable improvements were observed by increasing the number of quadrature points from 7 to 13. Although it appears that the graphs for the 4-point and 7-point Gaussian appear to coincide, the actual figures for the impedance matrix terms stabilised from 7-point and higher points. It was on this basis that the 7-point Gaussian was chosen in preference to the 4-point Gaussian integration. There is a marked difference between the one-point and the higher order Gaussian schemes when the source and observation triangles are in close proximity. This proves that the higher order Gaussian schemes calculate the impedance matrix elements more accurately than the one-

point scheme. It is also observed that for large distances between the source and observation triangles, the one-point scheme is just as accurate as any higher order scheme. This happens when the nearness factor is about 20 or less. This figure was based on the calculated impedance matrix terms used to plot the graphs above, in this section. This is also the point at which all the 1-point, 4-point, 7-point and 13-point graphs converge. Hence beyond a certain separation distance between the source and observation triangles, a one-point Gaussian scheme is sufficient. This translates to very fast computation times for the evaluation of the impedance elements.

The 4-point is seen to be less accurate than the 7-point or the 13-point schemes, particularly for closely coupled triangles. However, for large edge lengths as shown in Figure 3.10, it appears that the 4-point is almost as good as the 7-point or 13-point schemes. Of particular interest is the little difference between the 7-point and the 13-point schemes. The 7-point Gaussian scheme is seen to perform as well as the 13-point scheme.

Figure 3.12 shows the relative error between the 1-point, 4-point, 7-point and the 13-point Gaussian calculated impedance values for the data taken from Figure 11. The impedance element values calculated using the 13-point Gaussian integration scheme was taken as the reference values. As Figure 3.12 illustrates, the relative error for the 1-point exceeds 10 per cent for nearness factors greater than about 200 whereas for both the 4-point and the 7-point Gaussian schemes the relative error is less than 1 per cent. However, for nearness factors less than about 200, the differences between relative errors are almost indistinguishable. Hence it has been assumed that, for values of nearness factors less than about 20, the 1-point Gaussian is just as accurate as the 7-point or 13-point Gaussian scheme.

As evident in the Figure 3.5 - Figure 3.11, the spatial resolution of the triangle meshes appear not to have had a significant effect on the trend between the nearness factor and the calculated impedance elements.

The seven-point Gaussian quadrature scheme was adopted based on the above results for closely coupled triangles, i.e. for a nearness factor greater than 190. This ensures that there is an accurate evaluation of matrix elements for nearby regions of the scatterer. For greater distances corresponding to a nearness factor of 20 and below, a 1-point Gaussian quadrature rule was implemented.

3.3.2.2 Singularity Extraction

The self-term elements describe the self-interaction, i.e. the scattered field on a triangular patch due to the current on that patch. In this case, $T_m^\pm = T_n^\pm$, hence the source and observation points coincide resulting in singularity of the integrals in (3.16) and (3.37). The singular integrand involves a highly varying function so that the Gaussian quadrature will not provide a sufficient accuracy. The accurate computation of the self-terms is important as they dominate the impedance matrix.

The singularity in (3.16) and (3.37) is of the order $1/R$, where the distance R was defined in equation (2.50). The second integral can be evaluated as the complete elliptic integral of the first kind [130].

From equations (3.16) and (3.37), it can be observed that the integrals in (3.16) and (3.37) have the form

$$I = \iiint_{T_m T_n} \frac{e^{-jkR}}{R} dS' dS \quad (3.41)$$

Equation (3.41) possesses integrable singularity problems when the Green's function becomes singular, i.e. when the distance R between the source and observation point approaches zero. In this case, an analytical integration of the singular term is necessary, since a Gaussian numerical integration is no longer adequate.

Adding and subtracting a term that has a $1/R$ singularity when R approaches zero [129] in the integrand of equation (3.41) gives

$$I = \iiint_{T_m T_n} \frac{e^{-jkR}}{R} dS' dS = \iint_{T_m} \left(\iint_{T_n} \frac{e^{-jkR} - 1}{R} dS' \right) dS + \iint_{T_m} \left(\iint_{T_n} \frac{e^{-jkR}}{R} dS' \right) dS \quad (3.42)$$

The first integral on the right-hand side of (3.42) is well-behaved throughout the source/observation triangle. The integral is bound and hence can easily be evaluated numerically with the techniques in [6,126,131]. The second integral on the right-hand side of (3.42) can be evaluated analytically in closed form with the help of formulas developed in [50] and [129].

3.4 Matrix Equation Solver

The general MoM matrix equation for the EFIE was solved using the direct solution method with Gaussian elimination or LUD decomposition using the Swansea's 3D-MoM code. With this technique, the computation time is proportional to N^3 , where N is the total number of unknowns in the impedance matrix.

There are two primary time properties of the program. The first one comprises the Green's function evaluation time and the matrix fill time. This is the primary contributor to the total solution time for electrically large complex objects for the 4-SI method. However, as the number of unknowns increases, the solve time becomes the primary contributor to the total time in the case of the 2-SI method.

3.5 Numerical Results and Discussions

3.5.1 Introduction

This section presents some numerical results computed by the Swansea's MoM 3D code based on the 2-SI and 4-SI schemes. The numerical results are also meant to provide a general idea of the accuracy, savings in computer storage and computation time obtained by using the 4-SI scheme compared to the 2-SI scheme in solving electromagnetic scattering problems for electrically large objects.

This section presents the results that were obtained using an implementation procedure described in this Chapter for electrically large perfectly conducting bodies. All the results presented in this section and in Chapters 4 and 5 were generated on a Pentium III 500MHz personal computer with 256 MB of RAM.

The radar cross section (RCS) is adopted as the main criterion for assessing the accuracy and efficiency of the 4-SI scheme and for comparing the 4-SI results with 2-SI and published results. For some problems where published results are not available, the computation is done with the 2-SI scheme using a fine mesh and then that solution is used as a reference for validating the 4-SI result. Alternatively, in some cases, the 2-SI scheme is run several times with increasingly finer meshes and the results compared against those of the 4-SI scheme. Validation is assumed if the 4-SI results progressively converge towards the 2-SI solution based on a very fine mesh structure.

3.5.2 Scattering from a Sphere

The scattering from a perfectly conducting sphere is used as the starting point for the evaluation of the 4-SI numerical scheme. This is a convenient example because it has an analytical solution and provides the code with a calculation that is not trivial. Figure 3.13 shows a triangulated patch model of a sphere. The electrical size of the sphere is given by $ka = 8.3$, where a is the radius of the sphere. The triangle corners are on the sphere so that the effective radius of the sphere is less than a . The sphere is excited by an axial incident plane wave, i.e. $\theta^i = 0^\circ$. The surface of sphere is initially defined by 5000 triangular patches, corresponding to 7500 unknowns (the maximum number allowable for the 2-SI formulation by the available computing resources), a maximum triangular edge length of $0.15\lambda_0$ and the bistatic radar cross-section calculated using the 2-SI formulation.

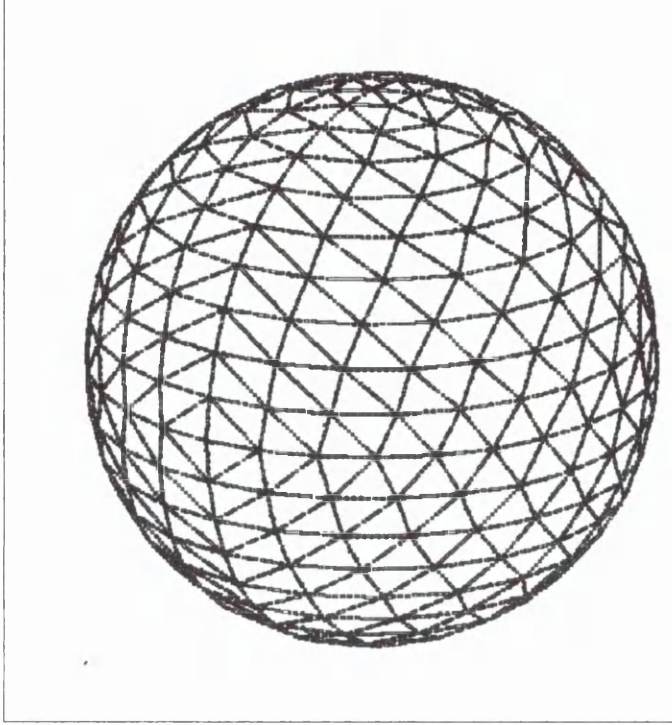


Figure 3.13 Numerical model of a sphere, subdivided into triangular meshes with $ka = 8.3$

The bistatic radar cross-section was also calculated using the 2-SI and 4-SI formulations with the sphere's surface meshed with 1692 triangles. The same calculations were repeated with the 4-SI formulation when the sphere was meshed with 1380 triangular patches, corresponding to a maximum edge length of $0.36\lambda_0$. Figure 3.14 and Figure 3.15 and Table 3.1 show the results for the bistatic radar cross-section in the plane of the incident electric field. Figure 3.15 shows the same results as Figure 3.14 but only for $90^\circ \leq \theta_i \leq 180^\circ$, to highlight the differences between the 2-SI, 4-SI and the Mie series solution. The radar cross-section is normalised with πa^2 , where a is the radius of the sphere. The agreement in Figure 3.14 between the results based on the 4-SI formulation

(graph 4-SI(b)), even with a maximum triangular edge length of $0.36\lambda_o$, and those of the Mie series solution is very good. The results for 4-SI(a) and 4-SI(b) with the maximum triangular edges of $0.36\lambda_o$ and $0.25\lambda_o$, are almost indistinguishable. Figure 3.15 shows that the agreement between the 4-SI(b) results and the Mie series solution is better than that between the 2-SI(b) results and the Mie series solution results. The maximum triangular edge in both the 2-SI and 4-SI scheme is $0.25\lambda_o$. As Figure 3.14 shows, the 2-SI formulation compares very well with both the 4-SI results and the Mie series solution when the maximum edge length of the triangular patches is $0.15\lambda_o$. This example shows that the 4-SI formulation converges to the analytic reference Mie series solution with a remarkably coarse grid when compared the 2-SI formulation.

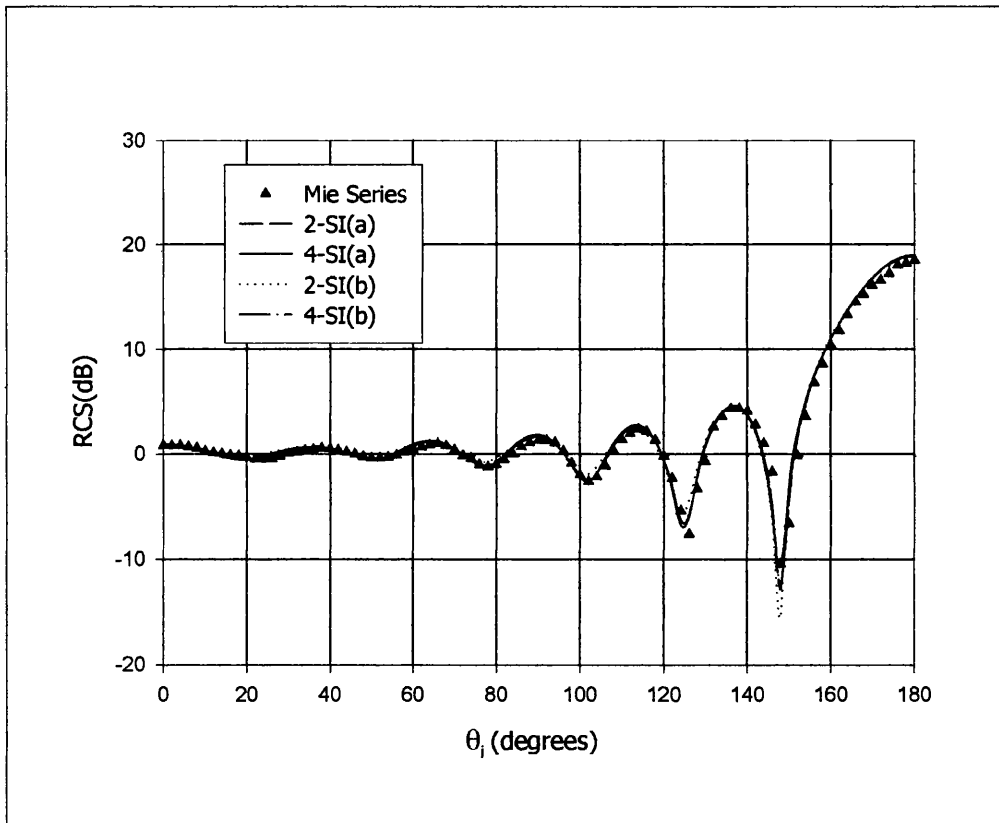


Figure 3.14 Bistatic RCS of a perfectly conducting sphere, $ka = 8.3$.

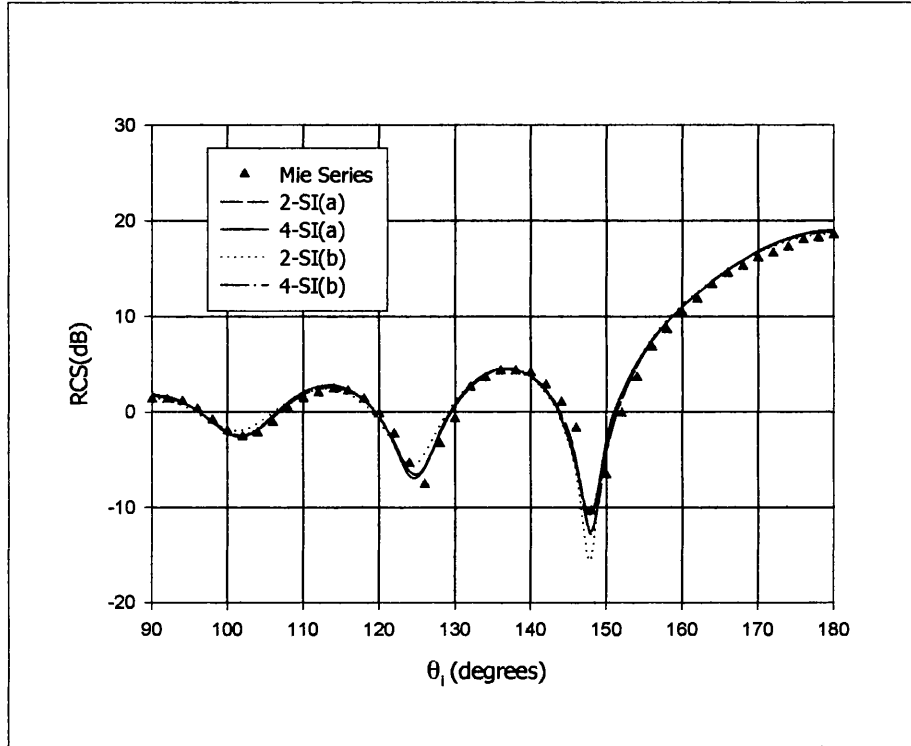


Figure 3.15 Bistatic RCS of the perfectly conducting sphere for

$$90^\circ \leq \theta_i \leq 180^\circ .$$

Memory and CPU-time requirements for the 2-SI and 4-SI schemes are given in Table 3.1. It is observed that the 4-SI reduces memory requirements by almost a factor of 7 and computation time saving is reduced by nearly a factor of six when compared to the 2-SI formulation. In the 2-SI scheme only just over half the matrix elements are stored and whereas in the case of the 4-SI scheme, all the matrix elements are stored. For the purposes of calculating the memory storage requirements, it is assumed that each impedance element is 8 bytes in size.

Table 3.1– Computation and memory requirements for a $ka = 8.3$ perfectly conducting sphere.

| Scheme | Number of patches | Number of Edges | Maximum edge length (λ_0) | Matrix fill time (sec) | Solve time (sec) | Total computation time (sec) | Memory required (MB) |
|---------|-------------------|-----------------|-------------------------------------|------------------------|------------------|------------------------------|----------------------|
| 2-SI(a) | 5000 | 7500 | 0.15 | 1493.2 | 9255.6 | 10748.9 | 216 |
| 2-SI(b) | 1692 | 2538 | 0.25 | 1040.7 | 244.6 | 1285.3 | 24.6 |
| 4-SI(a) | 1380 | 2070 | 0.36 | 1605.7 | 266.6 | 1872.3 | 33 |
| 4-SI(b) | 1692 | 2538 | 0.25 | 2280.1 | 492.9 | 2773.0 | 49.1 |

Table 3.1 shows the 2-SI scheme needs more than three times the number of unknowns to achieve the same accuracy as the 4-SI scheme. This result in the 4-SI's computation time being nearly six times faster than the 2-SI formulation. There is also memory saving of about 84 per cent.

For this particular problem, it is seen that the agreement between the 4-SI and the Mie series solution is good. This shows that the 4-SI solutions are numerically accurate despite the coarseness of the mesh. The differences between the graphs is explained by the fact the analytic Mie series uses the actual radius of the spheres whereas for the 2-SI or the 4-SI schemes, the meshing introduces an effective radius of the modelled sphere which is less than the actual radius of the sphere. The 2-SI achieves the same accuracy but the at expense of more unknowns and computation time than the 4-SI method.

The numerical modelling of the sphere using a maximum edge length of $0.36\lambda_0$ is a "crude approximation" by the usual standards and yet the 4-SI RCS prediction is very good. However, the problem with using a coarse mesh is that the curvature of the sphere is not modelled very well. To minimise this error, a

radius correction factor would have to be used. This results in a slightly larger radius used in the modelling than the actual radius such that the area of the meshed surface area is equal to the surface area of the sphere.

3.5.3 Scattering from a metallic disc at oblique incidence

This example shows the scattering by a thin perfectly conducting disc of radius $4\lambda_0$, where λ_0 is the free space wavelength. In this case a 2-SI calculated bistatic radar cross-section result based on relatively fine mesh used as a reference solution. The 4-SI results obtained using a coarser mesh are validated against this 2-SI result, obtained using 7390 unknowns.

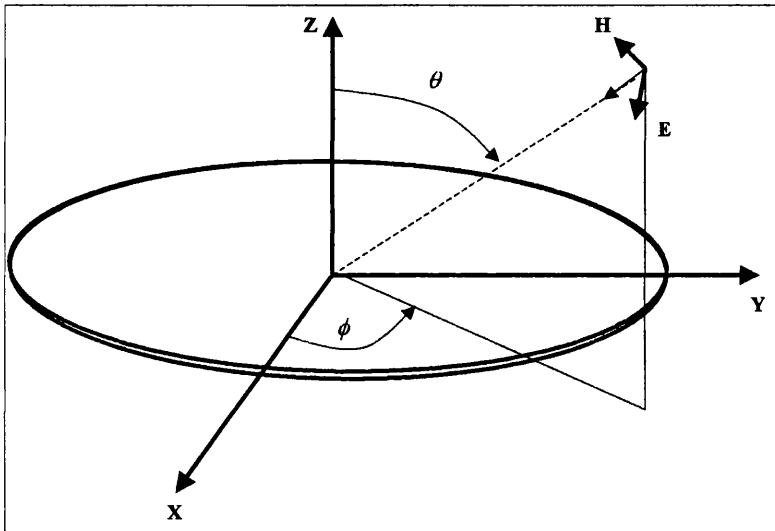


Figure 3.16 Scattering by a thin metallic disc for wave incidence
at an angle

The wave is incident on the disc at $\theta^i = 60^\circ$ with the \mathbf{E} -field parallel to the surface of the disc. At this angle of incidence, more surface waves are generated than at normal incidence. The graph denoted by 2-SI(a) in Figure 3.17 and Figure 3.18 and denotes the bistatic scattering for the 2-SI method when the

disc is coarsely meshed such that the maximum triangular patch edge is $0.38\lambda_o$. The corresponding graph for the 4-SI scheme is denoted by 4-SI(a). When the mesh is increased to 7390 edges, nearly the maximum possible allowed by the computer memory, the 2-SI scheme result given by 2-SI(b) converges towards the 4-SI generated results using 4863 unknowns. The two results are in good agreement. The maximum edge length for the 4-SI mesh is $0.26\lambda_o$ whereas it is $0.14\lambda_o$ for the 2-SI mesh. It is observed that for a mesh with a maximum edge length of $0.38\lambda_o$ corresponding to 2364 unknowns, the 2-SI result shown by 2-SI(b) deviates significantly from the reference solution of 2-SI(a), particularly for values of θ^i approaching grazing angles. However, for the same mesh, the 4-SI results shown by 4-SI(a) show a better comparison with the reference solution although it also shows deviations for values of θ^i approaching grazing angles as well. The graphs for both cases can be seen converging towards the reference solution, thus indicating convergence. The maximum number of unknowns for the 4-SI formulation was limited to 5000 by the computing resources.

Table 3.2 summarises the computation times of the two schemes. For the data shown, the 4-SI is six times faster and uses a far less number of unknowns than the 2-SI scheme. From Figure 3.17 it can also be observed that the 2-SI scheme requires more meshing to converge to the 4-SI graph. This problem demonstrates that the 4-SI formulation is more capable in coping with the effects of surface waves on a flat disc than the 2-SI formulation.

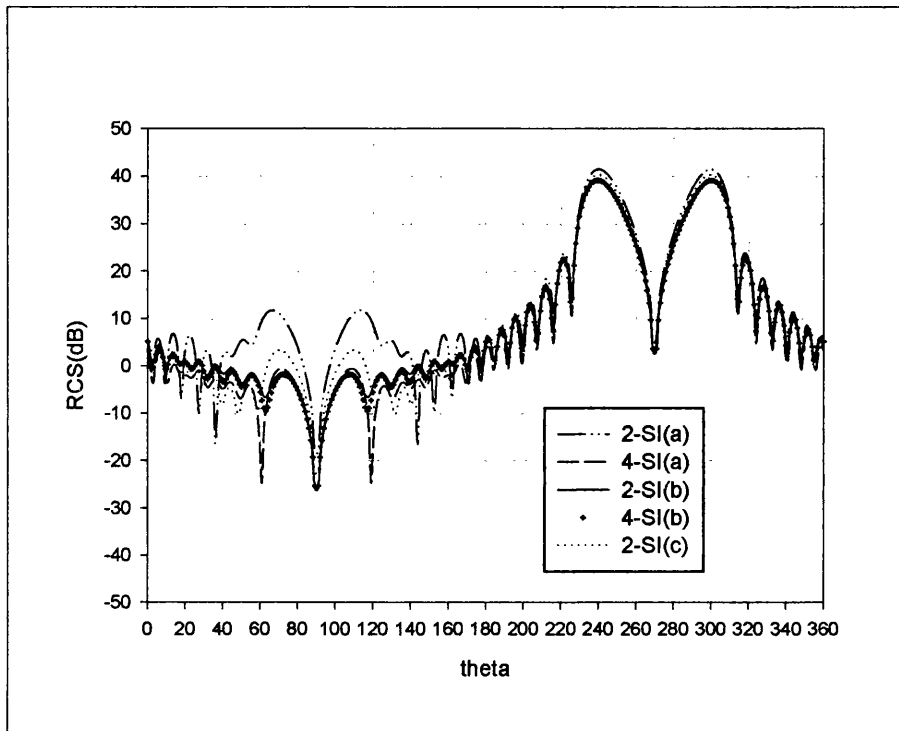


Figure 3.17 The bistatic scattering for a metallic disc of radius 4λ in the plane $\phi = 0^\circ$ for an incident angle $\theta_i = 60^\circ$ with $\alpha = 0^\circ$

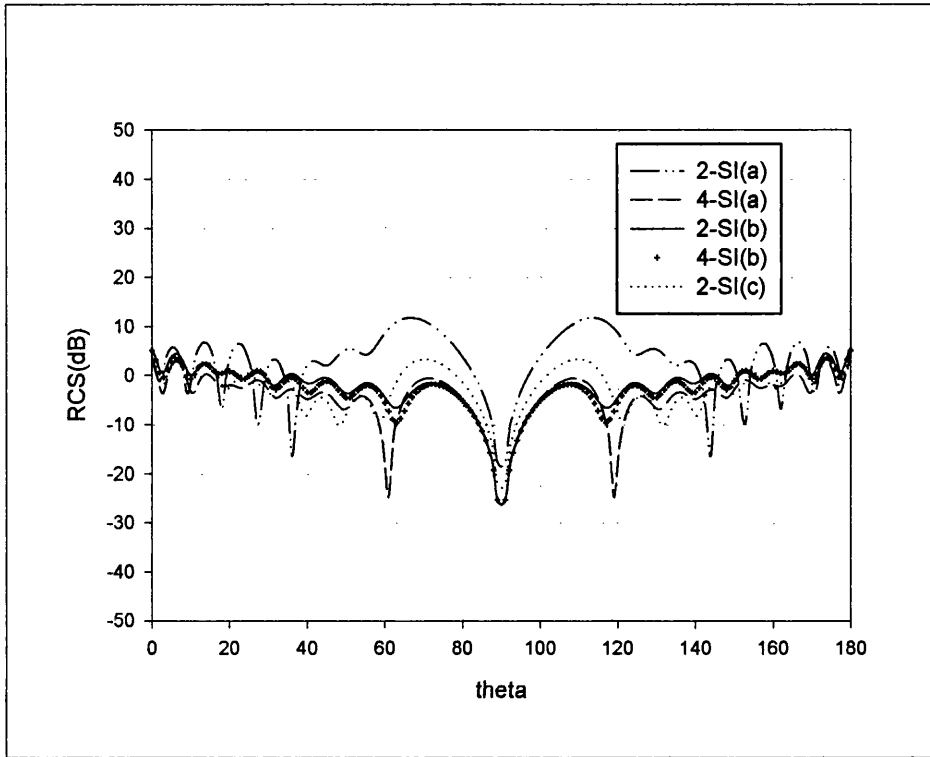


Figure 3.18 The RCS in Figure 5.17 shown for $0^\circ \leq \theta \leq 180^\circ$ to highlight the differences between the graphs.

The 2-SI suffers from the limitation that the maximum length for a triangle patch's edge length should not exceed $0.15\lambda_o$, where λ_o is the free space wavelength if accurate results are to be obtained. This limitation inhibits the use of the 2-SI method for analysing electromagnetic scattering by electrically large objects due to large computer secondary memory requirements and long run times.

Table 3.2 – Performance indicators for the 2-SI and 4-SI schemes for the scattering from a disc.

| Scheme | Number of triangular patches | Number of unknowns | Maximum edge length | Matrix fill time (sec) | Solve time (sec) | Total computation time (sec) | Memory (MB) |
|-----------------------------|------------------------------|--------------------|---------------------|------------------------|------------------|------------------------------|-------------|
| 2-SI(a) | 1602 | 2364 | 0.38 | 156.9 | 197.3 | 354.3 | 9.78 |
| 2-SI*(b) (With symmetry) | 4995 | 7390 | 0.142 | 2395.7 | 9881.3 | 12277.1 | 95.175 |
| 2-SI(c) | 3282 | 4863 | 0.257 | 596.0 | 1721.0 | 2317.0 | 41.05 |
| 4-SI(a) | 1602 | 2364 | 0.38 | 1708.5 | 407.7 | 2116.2 | 19.58 |
| 4-SI(b) | 3282 | 4863 | 0.257 | 9700.0 | 5086.0 | 14786.0 | 82.1 |

3.5.4 Scattering from a metallic plate at nearly grazing incidence

The next example demonstrates the 4-SI scheme can handle scattering from a metallic plate with fewer numbers of unknowns than the 2-SI method. This is a more challenging problem than the scattering by a conducting sphere. The horizontally polarised plane wave impinges at the metallic plate at almost grazing angle ($\theta^i = 70^\circ$), causing the excitation of very strong waves along the edges of the metallic plate. These waves contribute to the scattering process and need to be resolved to accurately predict the far field scattering.

The dimensions of the square plate are $4\lambda_o \times 4\lambda_o$. The bistatic RCS is calculated with the incident plane wave at a nearly grazing angle of incidence ($\theta_i = 70^\circ$). The results are shown in Figure 3.19. Figure 3.20 and Figure 3.21 show the RCS results for the bistatic angles of $0^\circ \leq \theta_i \leq 45^\circ$ and $45^\circ \leq \theta_i \leq 90^\circ$ to clearly show the differences between the results for the 2-SI and 4-SI formulations when

compared with reference solution [132]. The maximum length of the triangular edges is varied from $0.3\lambda_0$ to $0.11\lambda_0$ and the 2-SI and 4-SI results are compared with the results obtained by Poirier *et al.* [132] using the method of moments. The 2-SI method gives good agreement only when the maximum edge length is $0.15\lambda_0$ and less as shown by the plots labelled 2-SI(b) and 2-SI(c). For meshes with maximum edge lengths of $0.25\lambda_0$ and $0.3\lambda_0$, the results of which are shown by plots 2-SI(a) and 2-SI(d) respectively, it is observed that the results are not in agreement with the reference solution for the region $\theta_i < 70^\circ$. The corresponding results for the 4-SI formulation shown by plots 4-SI(a) and 4-SI(c) show good agreement with the reference solution for the whole observation region, i.e. $0 \leq \theta_i \leq 90^\circ$. The 4-SI method gives very good agreement with the reference solution even with a mesh having a maximum edge length of $0.3\lambda_0$.

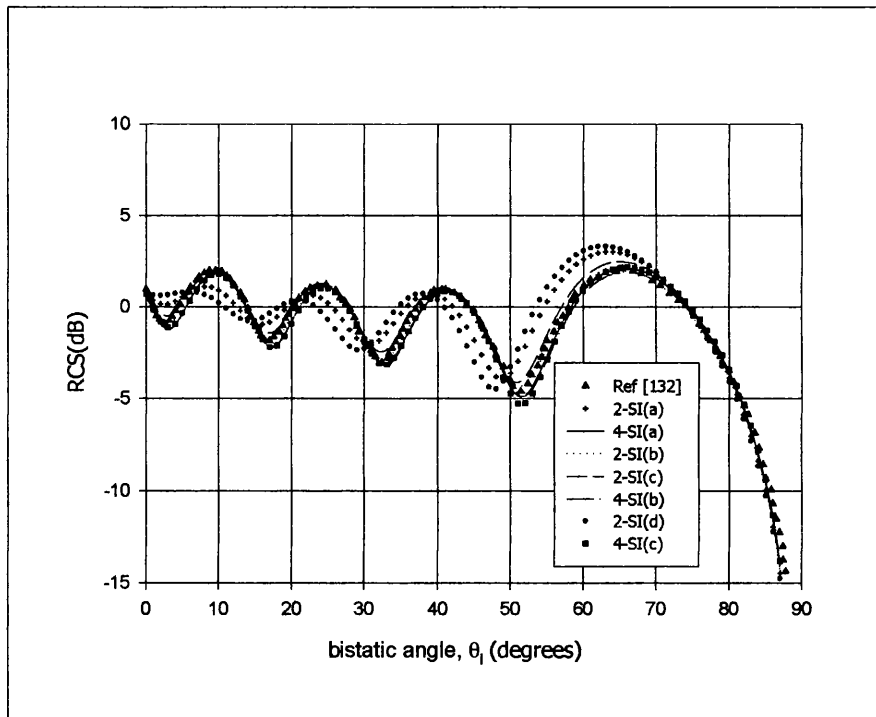


Figure 3.19 Bistatic scattering diagram for the $4\lambda_0 \times 4\lambda_0$ plate

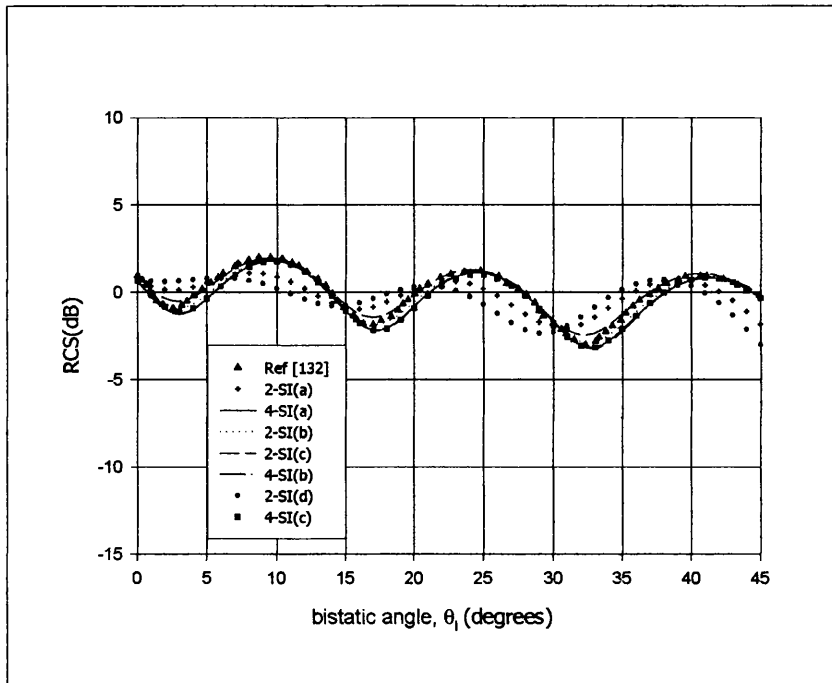


Figure 3.20 Bistatic scattering diagram for the $4\lambda_0 \times 4\lambda_0$ plate
for $0^\circ \leq \theta_i \leq 45^\circ$.

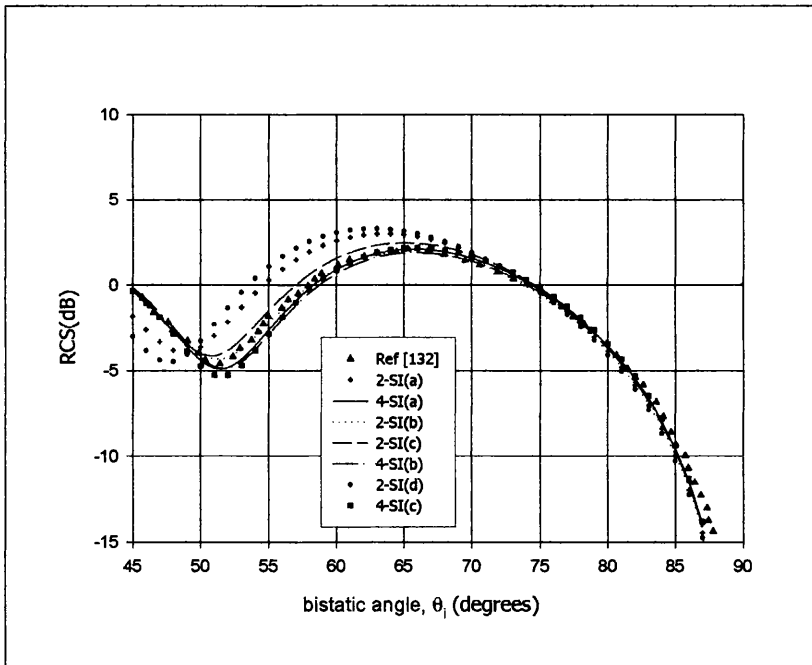


Figure 3.21 Bistatic scattering diagram for the $4\lambda_0 \times 4\lambda_0$ plate
for $45^\circ \leq \theta_i \leq 90^\circ$.

This problem demonstrates the advantage of the 4-SI method over the 2-SI method in handling electromagnetic scattering at nearly grazing angles of incidence.

Table 3.3 shows the performance indicators for the 2-SI and 4-SI formulations for the electromagnetic scattering by the $4\lambda_0 \times 4\lambda_0$ square plate.

Table 3.3– Performance indicators for the 2-SI and 4-SI schemes for the $4\lambda_0 \times 4\lambda_0$ metallic plate.

| Scheme | Number of triangular patches | Number of Edges | Maximum edge length (λ_0) | Matrix fill time (sec) | Solve time (sec) | Total computation time (sec) | Memory (MB) |
|---------|------------------------------|-----------------|-------------------------------------|------------------------|------------------|------------------------------|-------------|
| 2-SI(a) | 1058 | 1541 | 0.25 | 473.1 | 54.2 | 527.3 | 9.1 |
| 2-SI(b) | 5000 | 7400 | 0.11 | 1481.4 | 9898.2 | 11379.6 | 210.0 |
| 2-SI(c) | 2888 | 4256 | 0.15 | 474.0 | 1133 | 1607 | 69.1 |
| 2-SI(d) | 722 | 1045 | 0.3 | 230.0 | 17.0 | 247.0 | 4.2 |
| 4-SI(a) | 1058 | 1541 | 0.25 | 845.5 | 110.0 | 955.5 | 18.11 |
| 4-SI(b) | 2888 | 4256 | 0.15 | 7013.0 | 3623.0 | 10636.0 | 138.0 |
| 4-SI(c) | 722 | 1045 | 0.3 | 459.0 | 34.0 | 493.0 | 8.3 |

The 4-SI method shows computational gains in both computation time and memory requirements as shown in Table 3.3. Results for plot 2-SI(b), which gives an excellent comparison with the reference solution, are compared with the results for 4-SI(a), which also agrees well with the reference solution. From Table 3.3, it is noted that the 4-SI is nearly 12 times as fast as the 2-SI formulation and saves on memory requirements by a factor of eleven.

3.5.5 Scattering from a metallic rectangular Trihedral

In this section, the backscattered fields from a rectangular trihedral are computed using the 2-SI and 4-SI formulations and the results compared with

the results by Al-hekail and Burnside [133]. Al-Hekail and Burnside used a hybrid method based on the Uniform Theory of Diffraction (UTD) to compute the backscattered fields from the trihedral structure and the results compared very well those they obtained using the method of moment. The reference results from [133] are those based on the method of moments. The number of unknowns used is not mentioned. The trihedral corner reflector is an interesting target in that the RCS of several objects such as trucks, tanks or other vehicles have significant trihedral corner reflector scattering effects. Metal trihedrals are also commonly used as radar chaff constituents by the military.

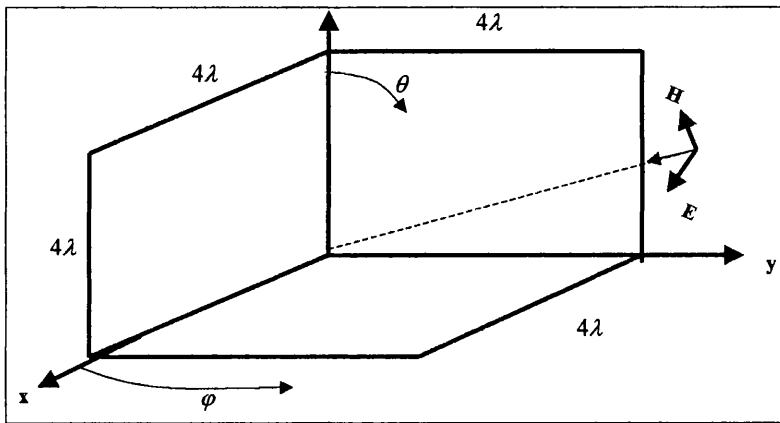


Figure 3.22 Rectangular Trihedral

Figure 3.22 shows a rectangular trihedral consisting of three identical plates with each side of length $4\lambda_0$. The frequency is 1.2 GHz. This structure is particularly interesting in that it is not only electrically large but there exist strong interactions between the different parts of the structure.

The electromagnetic scattering by rectangular trihedrals has been investigated by other authors. Taflove and Umashankar [134] used the finite-difference time-domain method to analyse the scattering from an electrically

large metallic trihedral. Baldauf *et al.* [135] used the shooting and bouncing ray method (SBR) method and the geometrical optics theory to compute the backscattered far fields from a rectangular trihedral.

Figure 3.23 shows the backscattered fields taken in $\theta = 54.7^\circ$ plane for an incident plane wave in the $\theta = 90^\circ$ plane and polarized in the ϕ – direction. Figure 3.24 shows the results but only for $0^\circ \leq \phi \leq 180^\circ$, so as to clearly show the differences between the results for the 2-SI and 4-SI formulations.

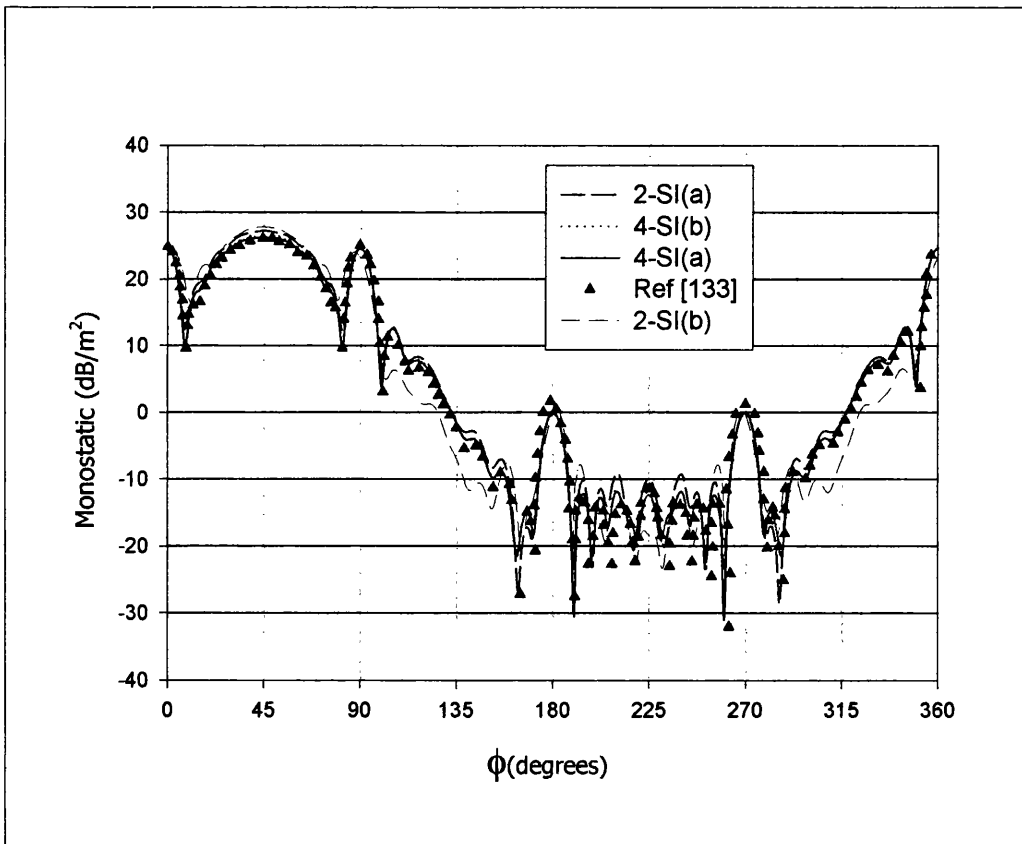


Figure 3.23 Monostatic RCS from the rectangular trihedral at 1.2 GHz in the plane $\theta = 54.7^\circ$

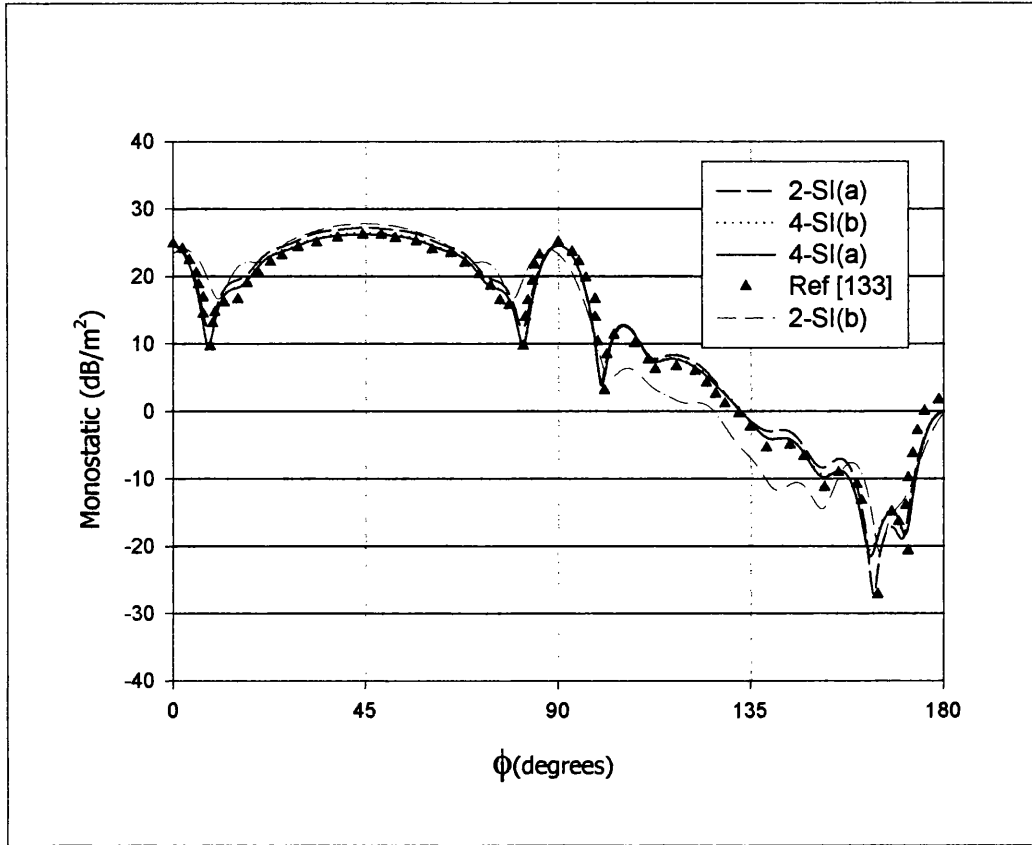


Figure 3.24 Monostatic RCS from the rectangular trihedral

at 1.2 GHz in the plane $\theta = 54.7^\circ$ for $0^\circ \leq \phi \leq 180^\circ$

Figure 3.23 and Figure 3.24 show the backscattered fields from the trihedral at 1.2 GHz in the plane $\theta = 54.7^\circ$. The electric field is polarised in the phi direction.

The graphs show good agreement between the reference solution [133] and the 4-SI when the maximum mesh edges are $0.24\lambda_0$ and $0.28\lambda_0$ as shown by the plots 4-SI(a) and 4-SI(b) respectively. For the same meshing, the 2-SI method shows large deviations from the reference solution when the maximum edge length is $0.28\lambda_0$ as expected but shows some improvement when the maximum mesh edge is $0.24\lambda_0$. Still, its accuracy is not as good as either plot 4-SI(a) or 4-SI(b). This demonstrates the capability of the 4-SI method to model scattering

of electromagnetic fields from electrically large bodies with a far fewer number of unknowns than the 2-SI method. As for the 2-SI, a very fine mesh with a very large number of unknowns would be needed to match the 2-SI accuracy to that of the 4-SI and the reference solution. The 4692 unknowns used to generate plots 2-SI(a) and 4-SI(a) were the maximum possible due to the limitation on memory by the available computing resources. The 2-SI formulation is known to produce very good results if the maximum mesh edge lengths are of the order of one-tenth of a wavelength. The number of unknowns and the total computation times and memory requirements are summarised in Table 3.4.

Table 3.4– Performance indicators for the 2-SI and 4-SI formulations for the rectangular trihedral with each edge of length $4\lambda_0$.

| Scheme | Number of triangular patches | Number of Edges | Maximum edge length (λ) | Matrix fill time (sec) | Solve time (sec) | Total computation time (sec) | Memory (MB) |
|---------|------------------------------|-----------------|-----------------------------------|------------------------|------------------|------------------------------|-------------|
| 2-SI(a) | 3174 | 4692 | 0.24 | 580.0 | 2353.2 | 2933.2 | 84.0 |
| 2-SI(b) | 2400 | 3540 | 0.28 | 230.9 | 1915 | 2145.9 | 47.8 |
| 4-SI(a) | 3174 | 4692 | 0.24 | 9937.0 | 6467.7 | 16404.7 | 168.0 |
| 4-SI(b) | 2400 | 3540 | 0.28 | 5004.8 | 4410.2 | 9415.0 | 95.6 |

3.5.6 Scattering from a cavity

This example shows the scattering by a $2.5\lambda_0 \times 2.5\lambda_0 \times 3.75\lambda_0$ open cavity. See Figure 3.25. The opening is in the direction of $\theta = 0^\circ$ and is closed at the bottom. The monostatic RCS patterns for the $\theta\theta$ - and $\phi\phi$ - polarisation are computed using 2-SI and 4-SI formulations using triangular patches with maximum edge lengths of $0.37\lambda_0$ and $0.24\lambda_0$. An additional 4-SI result, i.e. plot 4-SI(c), see Table 3.5, was later obtained using a different computer from the one used to

compute the rest of the results. The results are shown in Figure 3.26 - Figure 3.29 and are compared with the results by Donepudi *et al.* [136].

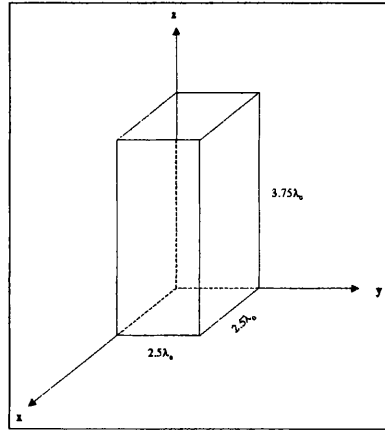


Figure 3.25 Diagram of the $2.5\lambda_0 \times 2.5\lambda_0 \times 3.75\lambda_0$ cavity

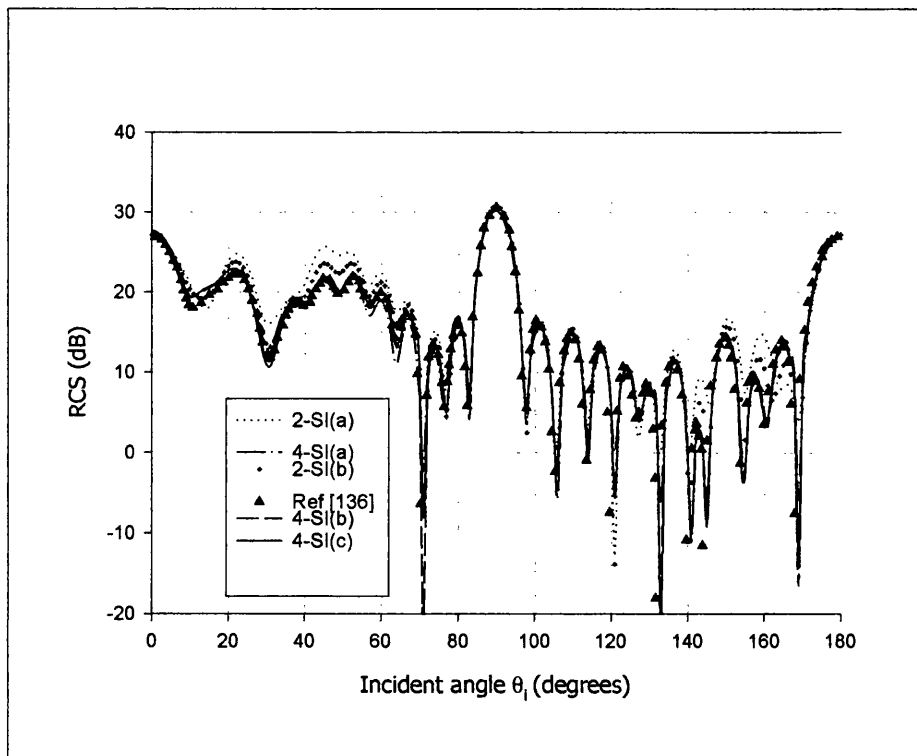


Figure 3.26 Monostatic RCS of an $2.5\lambda \times 2.5\lambda \times 3.75\lambda$ open cavity for $\theta\theta$ polarisation.

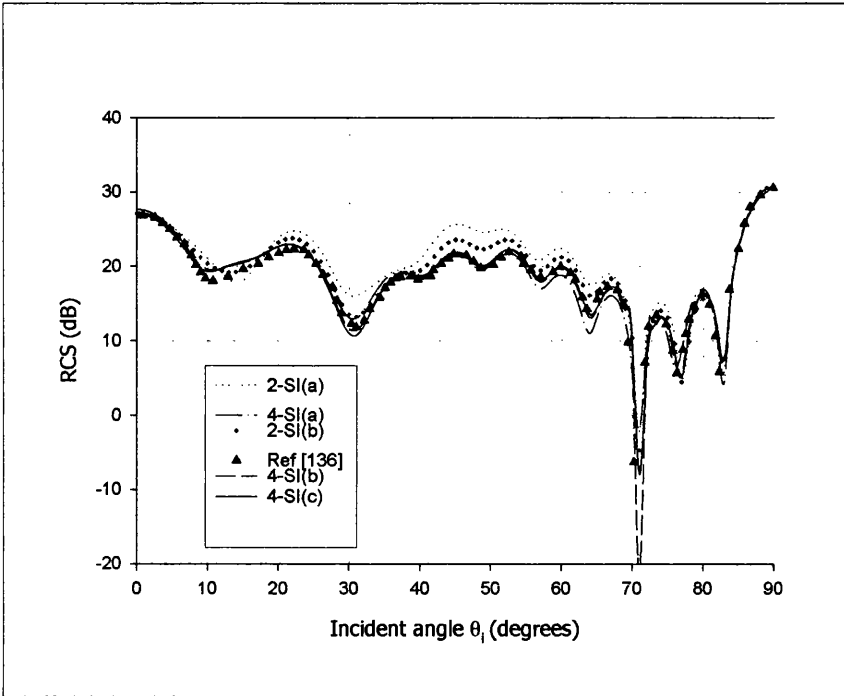


Figure 3.27 Monostatic RCS of an $2.5\lambda \times 2.5\lambda \times 3.75\lambda$ open cavity for $\theta\theta$ polarisation for $0^\circ \leq \theta_i \leq 90^\circ$.

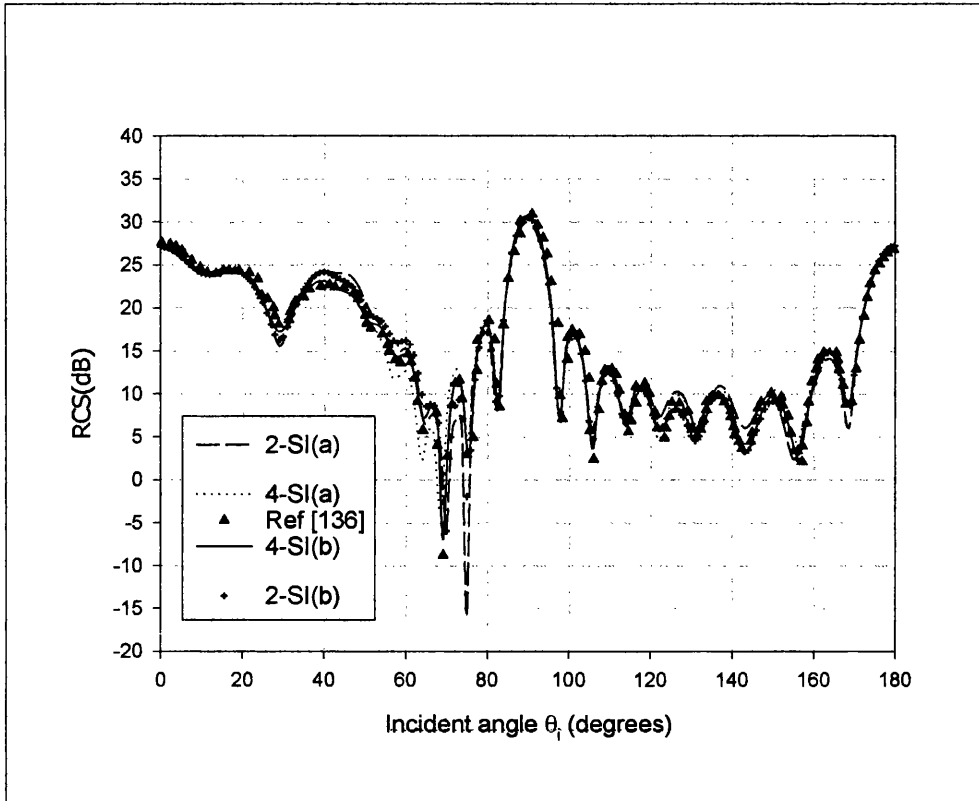


Figure 3.28 Monostatic RCS of an $2.5\lambda \times 2.5\lambda \times 3.75\lambda$ open cavity for $\phi\phi$ polarisation.

Ling *et al.* [137] obtained the RCS of an electrically large open-ended rectangular cavity using the waveguide modal approach and the shooting-and-bouncing ray (SBR) method. The comparison between the two approaches was very good. Rius *et al.* [138] presented a spectral iterative algorithm for RCS computation in electrically large open-ended conducting cavities. Good agreement with method of moments and hybrid modal solutions and with experimental data was obtained.

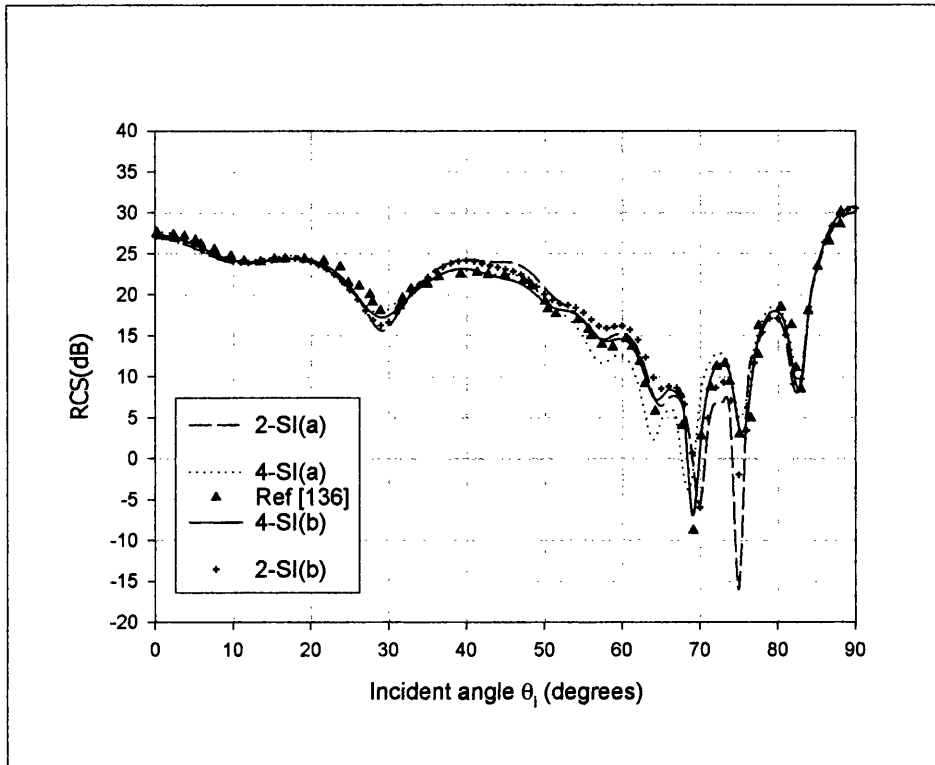


Figure 3.29 Monostatic RCS of an $2.5\lambda \times 2.5\lambda \times 3.75\lambda$ open cavity for $\phi\phi$ polarisation for $0^\circ \leq \theta_i \leq 90^\circ$.

Donepudi *et al.* [136] used a higher order multilevel fast multipole algorithm (MLFMA) for solving integral equations of electromagnetic wave scattering by the open-ended conducting cavity. Their scheme leads to a significant reduction in the mesh density, thus the number of unknowns, without compromising the accuracy of geometry modelling. The thrust of this method is similar to the theme of this work, which seeks to reduce the number of unknowns when modelling electrically large bodies without compromising the accuracy of the method.

As can be seen in Figure 3.26 and Figure 3.27 showing the monostatic RCS for the $\theta\theta$ -polarisation, the RCS levels predicted by the 4-SI formulation are in better agreement with the RCS levels predicted by the reference result in [136] than corresponding results obtained using the 2-SI formulation. The 4-SI(b) plot is almost indistinguishable from the 4-SI(c) result (obtained using a finer mesh as shown in Table 3.5) and the reference results, apart from the null around $\theta = 71^\circ$ where it underpredicts the level of the reference result by about 12 dB. Plot 4-SI(b), obtained a mesh possessing a maximum edge length of $0.24\lambda_o$, corresponding to 4768 unknowns, is in excellent agreement with the reference solution, unlike corresponding result of plot 2-SI(b).

Figure 3.28 and Figure 3.29 show the computed 2-SI and 4-SI monostatic results for the $\phi\phi$ polarisation. Figure 3.29 shows the same results as shown by Figure 3.28, but only for $0^\circ \leq \theta \leq 90^\circ$ to highlight the differences between the results. The results were obtained using the same meshes as those used to obtain the monostatic RCS $\theta\theta$ -polarisation results as shown in Table 3.5. As can be seen in Figure 3.28 and Figure 3.29, the 4-SI results, i.e. plots 4-SI(a) and 4-SI(b) produce better comparisons with the reference solution than does the results for the 2-SI formulation, i.e. plots 2-SI(a) and 2-SI(b). The agreement between the 4-SI result, 4-SI(b) and the reference solution is very good. The same can be not said for the corresponding result for the 2-SI formulation, i.e. plot 2-SI(b).

To produce the same level of accuracy as that given by the plot 4-SI(b), the 2-SI formulation would need the cavity mesh to have maximum edge length of the order of $0.1\lambda_o$. This would require about 24000 unknowns. The 4-SI formulation requires only 4768 unknowns. The 4-SI formulation's savings in computation time and computer storage are huge.

Table 3.5 summarises the computational requirement for the 2-SI and the 4-SI schemes.

Table 3.5– Computation and memory requirements for an open cavity

with dimensions $2.5\lambda_0 \times 2.5\lambda_0 \times 3.75\lambda_0$.

| Scheme | Number of triangular patches | Number of Edges | Maximum edge length (λ) | Matrix fill time (sec) | Solve time (sec) | Total computation time (sec) | Memory (MB) |
|----------|------------------------------|-----------------|-----------------------------------|------------------------|------------------|------------------------------|-------------|
| 2-SI(a) | 1320 | 1960 | 0.37 | 121.6 | 186.8 | 308.4 | 14.6 |
| 2-SI(b) | 3200 | 4768 | 0.24 | 605.5 | 2020.2 | 2625.7 | 87.4 |
| 4-SI(a) | 1320 | 1960 | 0.37 | 1456.3 | 299.7 | 1756.0 | 29.5 |
| 4-SI(b) | 3200 | 4768 | 0.24 | 9942.7 | 4135.8 | 15078.5 | 173.4 |
| 4-SI(c)* | 6400 | 9520 | 0.18 | 6654.2 | 5709.9 | 11364.1 | 691.5 |

4-SI(c)* - problem run on a faster computer

3.6 Conclusion

A formulation based on the EFIE using the MoM and the RWG basis functions has been presented. The technique presented evaluates the impedance matrix more accurately than the 2-SI method. The scheme has been applied to the electromagnetic scattering problems by electrically large objects. The results have shown that the 4-SI is an efficient scheme to analyse the RCS of electrically large objects with a high level of accuracy. In the results that were presented, a coarse mesh with a maximum edge length of about 0.38λ has been used and the comparisons between the 4-SI and published materials or between the 4-SI and the 2-SI scheme with a fine level of discretisation have been good. The examples that were given in this Chapter demonstrate that the 4-SI method can be applied to objects of a variety of sizes and shapes.

In the formulation presented in this chapter, two surface integrals appearing in the tested EFIE are evaluated with a higher order Gaussian quadrature scheme for closely coupled objects, which is a very time consuming process. The

impedance elements due to the coupling between closely spaced triangular patches dominate the second level in terms of magnitude of the impedance matrix after the diagonal elements. Hence an accurate evaluation of these terms also determines the overall accuracy of the final solution, i.e. the surface currents. The overall accuracy and the numerical efficiency of the 4-SI scheme depends largely on the speed and accurate evaluation of the integrals in the tested EFIE. This requires the evaluation of two surface integrals over both the observation and source triangles. For electrically large objects, this involves many pairs of triangles and thus many unknowns. It then becomes critical that a good compromise be struck between accuracy, the evaluation of the double surface integrals and the total computation time.

For nearby terms a 7-point Gaussian integration is used. For loosely coupled triangles, a one-point Gaussian quadrature scheme is used without compromising the accuracy of the evaluation of the surface integrals. This also helps to speed up the computation process.

The scheme has been shown to possess advantages over the 2-SI scheme when analysing electrically large conducting objects. It uses fewer unknowns than the 2-SI method to analyse a particular electrically large problem. That in turn translates to less computer storage space and total computation time. Thus the 4-SI scheme can be applied to the electromagnetic scattering from electrically large objects, providing satisfactory results at less computation costs when compared with the usual 2-SI method.

This new approach not only results in improved accuracy in the computation of the impedance matrix elements, but in fewer triangular meshing patches for the same scatterer as a result of the improved averaging process of the tested EFIE. The latter result translates to larger edge lengths of the triangular patches on the surface of the scatterer. However, it must be noted that this scheme

possesses more complex integrals that inevitably require more computational time and storage space if not handled properly. Computational improvements over the RWG formulation exist only if the scheme is applied to electrically large scatterers where a very large number of triangle patches are needed to define the geometry of the scatterer.

CHAPTER 4

FOUR-SI FORMULATION FOR ELECTROMAGNETIC SCATTERING FROM DIELECTRIC OBJECTS

| | |
|---|-----|
| 4.1 INTRODUCTION | 110 |
| 4.2 4-SI FORMULATION FOR DIELECTRIC OBJECTS | 112 |
| 4.2.1 Introduction | 112 |
| 4.2.2 CFIE Matrix Equation | 121 |
| 4.2.3 Optimisation of the number of Gaussian Points for the $1/R^3$ | 125 |
| 4.2.4 Numerical Implementation | 134 |
| 4.3 RESULTS AND DISCUSSIONS | 135 |
| 4.3.1 Scattering by dielectric spheres | 136 |
| 4.3.2 Scattering by a dielectric cylinder | 142 |
| 4.3.3 Scattering by a dielectric box | 144 |
| 4.3.4 Scattering by a dielectric plate | 150 |
| 4.3.4 Scattering by a dielectric disc | 153 |
| 4.4. CONCLUDING REMARKS | 160 |

4.1 INTRODUCTION

The previous chapter dealt with the electromagnetic scattering by perfect electric conductors using the 4-SI method. This chapter extends the applicability of the 4-SI scheme to scattering by homogeneous dielectric objects.

A Galerkin formulation based on the Rao-Wilton-Glisson (RWG) basis functions [6] is used. The same RWG basis functions reviewed in chapter 2 are used in the formulation to be presented in this chapter. As in chapter 3, the technique to be employed is to evaluate more accurately the double surface integrals appearing in the tested integral equation, particularly for the case of closely coupled triangular patches. The modified formulation for the electromagnetic scattering by dielectric conductors presented in this chapter builds up on the work of Umashankar *et al.* [53]. Umashankar *et al.* [53] extended the work done by Rao *et al.* [6] to calculate the scattered electromagnetic field from a three-dimensional lossy dielectric object of arbitrary shape illuminated by an incident plane wave. In their approach, the object was approximated by planar triangular patches and the same basis functions developed by Rao *et al.* [6] for conducting bodies were used. In their formulation, Umashankar *et al.* [53] used a CFIE instead of the EFIE used by Rao *et al.* [6] for scattering by conducting bodies.

The underlying theory for scattering of electromagnetic waves by dielectric objects was discussed in chapter 2. The surface integral equations are formulated in terms of equivalent electric and magnetic currents over the dielectric's surface. The RWG basis functions are both used for testing and current expansion. The application of the boundary conditions leads to a set of

four integral equations that are linearly combined to yield the combined field integral equation (CFIE). As with the case of perfectly conducting objects discussed in chapter 3, the double surface integrals arising from the tested integral equation are evaluated more accurately using an n-point Gaussian quadrature scheme, particularly for closely coupled triangular patches. The use of higher order n-point Gaussian quadrature is relaxed when the triangular patches are loosely coupled. Instead, a 1-point Gaussian quadrature scheme, which is identical to the 2-SI scheme, is implemented. No accuracy is lost by performing this 1-point Gaussian integration because the Green's function is slowly varying for loosely coupled triangles. The accuracy of this new formulation is studied with respect to the computation of the RCS for dielectric objects of various shapes. The technique is then applied to the study of radar cross-sections of electrically large dielectric objects. The accuracy and computation costs of the 4-SI method are then compared with those of the 2-SI method. Published data is also used to validate the accuracy of the 4-SI method.

Several papers have analysed the electromagnetic scattering by homogeneous dielectric objects and some of the methods used are the T-matrix [139,140] and unimoment [141], Fredholm integral equation approach [142] and the method of moments for the surface integral formulation [53,118,143-145].

Also the finite-difference method [146,147], the finite-element method (FEM) [148,149] and the volume integral equation (VIE) formulation [150,151] have been found to be very versatile in dealing with arbitrary shaped dielectric bodies. The FEM is an efficient method for modelling electromagnetic scattering from dielectric objects, either homogeneous or inhomogeneous objects. This is due to the fact that the resulting impedance matrix is sparse.

However, when analysing electrically large objects, the VIE technique has been accelerated by fast solvers since the number of unknowns increases very rapidly

with the size of the dielectric objects. The most commonly used acceleration technique is the Conjugate Gradient Fast Fourier Transform (CGFFT) [152]. This has the effect of reducing both the computation time and computer storage.

However, these methods all suffer the disadvantage that they yield very large matrices for three-dimensional problems. The surface integral equation formulation is often preferred for homogeneous dielectric objects because it limits the discretisation of the unknown quantity to the surface of the object. This results in a comparatively smaller matrix.

This chapter is divided into three sections. Section 4.1 is the introduction, section 4.2 discusses the theory of the 4-SI pertaining to dielectric objects and most of it has been discussed in Chapter 2. Section 4.3 presents the numerical results and comparison of the 4-SI results are made those of the 2-SI and those of published papers. Finally, section 4.4 presents the concluding remarks.

4.2 4-SI FORMULATION FOR DIELECTRIC OBJECTS

4.2.1 Introduction

The RWG formulation for dielectric bodies was reviewed in section 2.6. The derivation of the CFIE and its MoM solution for dielectric objects was discussed in the same section. It was pointed out that the integral terms of the tested CFIE containing the scalar/vector potentials, curl of the vector potentials and the gradient of the scalar potentials over the observation triangles are evaluated by approximating them by their values at the centroids of the observation triangles. This simplifies the evaluation of the integrals greatly resulting in a fast and

accurate algorithm. However, the requirement that the maximum edge length be of the order $\lambda/10$ for the 2-SI formulation so as to prevent erroneous solutions leads to many unknowns when analysing electrically large dielectric objects. The formulation to be presented allows the edges of the triangular patches to exceed $\lambda/10$ leading to fewer triangular patches to define the geometry. Fewer triangles translate to fewer unknowns for a given problem. This is achieved by evaluating the two surface integrals accurately, particularly for closely coupled pairs of source and observation triangles.

The starting point are the two equations (2.67) and (2.68) in chapter 2. These are repeated here for clarity:

$$\begin{aligned} \langle \mathbf{E}^{inc}, \mathbf{f}_m \rangle = & \langle j\omega [\mathbf{A}_1 + \mathbf{A}_2], \mathbf{f}_m \rangle + \langle [\nabla\Phi_1 + \nabla\Phi_2], \mathbf{f}_m \rangle \\ & \text{on surface S} \quad (4.1) \\ & + \langle \nabla \times \left[\frac{\mathbf{F}_1}{\epsilon_1} + \frac{\mathbf{F}_2}{\epsilon_2} \right], \mathbf{f}_m \rangle \end{aligned}$$

$$\begin{aligned} \langle \mathbf{H}^{inc}, \mathbf{f}_m \rangle = & \langle j\omega [\mathbf{F}_1 + \mathbf{F}_2], \mathbf{f}_m \rangle + \langle [\nabla\Psi_1 + \nabla\Psi_2], \mathbf{f}_m \rangle \\ & \text{on surface S} \quad (4.2) \\ & - \langle \nabla \times \left[\frac{\mathbf{A}_1}{\mu_1} + \frac{\mathbf{A}_2}{\mu_2} \right], \mathbf{f}_m \rangle \end{aligned}$$

The testing of the magnetic vector potential \mathbf{A} and the gradient of the electric scalar potential Φ has already been treated in detail in section 3.2. The testing of the electric vector potential \mathbf{F} and the magnetic scalar potential Ψ is similar to the testing of the magnetic vector potential \mathbf{A} and the electric scalar potential Φ respectively. It is observed in equations (4.1) and (4.2) that the application of

the method of moments with Galerkin method (the RWG basis functions are also used as testing functions) to solve the electromagnetic integral equations requires the calculation of double surface integrals. However, the review of the RWG formulation in chapter 2 has shown how the evaluation of the double surface integrals is avoided by approximating the integral over the observation triangle and evaluating only the surface integral over the source triangle.

Since the inner product is linear, the first term on the right hand side of (4.1) can be written as:

$$\langle j\omega[\mathbf{A}_1 + \mathbf{A}_2], \mathbf{f}_m \rangle = j\omega \langle \mathbf{A}_1(\mathbf{r}'), \mathbf{f}_m(\mathbf{r}) \rangle + j\omega \langle \mathbf{A}_2(\mathbf{r}'), \mathbf{f}_m(\mathbf{r}) \rangle \quad (4.3)$$

Using (3.2), the left hand side terms of equation (4.3) can be written as

$$\langle j\omega \mathbf{A}_i, \mathbf{f}_m \rangle = j\omega \frac{\mu_i}{4\pi} \frac{l_m}{2A_m^\pm} \frac{l_n}{2A_n^\pm} \iint_{(T_m^+ + T_m^-)} \iint_{(T_n^+ + T_n^-)} \rho_n^\pm(\mathbf{r}') \cdot \rho_m^\pm(\mathbf{r}) \frac{e^{-jk_r R}}{R} dS' dS \quad (4.4)$$

where the terms in equation (4.4) have been defined in Chapter 2 , $i = 1, 2$ and denotes the region in which the source and the field position vectors \mathbf{r} and \mathbf{r}' are located. The primed and unprimed quantities refer to the source and observation terms respectively.

Similarly, using (4.4), the terms containing the tested terms for the electric vector potential in (4.2) can be written as

$$\langle j\omega \mathbf{F}_i, \mathbf{f}_m \rangle = j\omega \frac{1}{4\pi\epsilon_i} \frac{l_m}{2A_m^\pm} \frac{l_n}{2A_n^\pm} \iint_{(T_m^+ + T_m^-)} \iint_{(T_n^+ + T_n^-)} \rho_n^\pm(\mathbf{r}') \cdot \rho_m^\pm(\mathbf{r}) \frac{e^{-jk_i R}}{R} dS' dS \quad (4.5)$$

The evaluation of the integrals in (4.4) and (4.5) follows exactly the same steps presented in equations (3.16) – (3.33) and inserting the relative permeability and permittivity of the respective media where appropriate.

The evaluation of the tested gradients of the electric scalar and magnetic scalar potentials follows directly from equation (3.37).

For the tested gradient of the electric scalar potential, the expression becomes:

$$\langle \nabla \Phi_i, \mathbf{f}_m \rangle = \frac{l_m l_n}{2\pi j\omega\epsilon_i} \sum_{j=1}^{N_g} w_j \left[\int_0^1 \int_0^{1-b'} G_i(\mathbf{r}_j^o, \mathbf{r}') da' db' \right] \quad \text{for } i = 1, 2 \quad (4.6)$$

where N_g is the number of Gaussian points for the outer integral, and w_j is the weight.

The expression for the tested gradient of the magnetic scalar potential is similar to (4.6) except for the floating constants:

$$\langle \nabla \Psi_i, \mathbf{f}_m \rangle = \frac{\mu_i l_m l_n}{2\pi j\omega} \sum_{j=1}^{N_g} w_j \left[\int_0^1 \int_0^{1-b'} G_i(\mathbf{r}_j^o, \mathbf{r}') da' db' \right] \quad (4.7)$$

Now consider the third term on the right hand side of equation (4.2) which contains the tested curl of the magnetic vector potential.

Now, using equation (2.59), the expression for the magnetic vector potential takes the form

$$\mathbf{A}_{inn}^{\pm} = \frac{\mu_i}{4\pi} \iint_{(T_n^+ + T_n^-)} \mathbf{f}_n(\mathbf{r}') G_i(\mathbf{r}_m, \mathbf{r}') dS(\mathbf{r}') \quad (4.8)$$

so that

$$\begin{aligned} \nabla \times \mathbf{A}_{inn} &= \frac{\mu_i}{4\pi} \iint_{(T_n^+ + T_n^-)} \mathbf{f}_n(\mathbf{r}') \times \nabla' G_i(\mathbf{r}_m, \mathbf{r}') dS(\mathbf{r}') \\ &= \frac{\mu_i}{4\pi} \frac{l_n}{2A_n^{\pm}} \iint_{(T_n^+ + T_n^-)} \rho_n(\mathbf{r}') \times \nabla' G_i(\mathbf{r}_m, \mathbf{r}') dS(\mathbf{r}') \end{aligned} \quad (4.9)$$

using the definition of the RWG basis function in (2.24) and ∇' denotes the surface divergence with respect to the source (primed) coordinates, \mathbf{r}_m is the observation point vector.

Hence the tested form of (4.9) becomes

$$\begin{aligned}
& \langle \nabla \times \mathbf{A}_i, \mathbf{f}_m \rangle \\
&= \frac{\mu_i}{4\pi} \frac{l_m}{2A_m^\pm} \frac{l_n}{2A_n^\pm} \iint_{(T_m^+ + T_m^-)} \left[\iint_{(T_n^+ + T_n^-)} \rho_{i_q} \times \nabla' G_i(\mathbf{r}, \mathbf{r}') dS' \right] \cdot \rho_{i_p} dS
\end{aligned} \tag{4.10}$$

$$= \frac{\mu_i}{4\pi} \frac{l_m}{2A_m^\pm} \frac{l_n}{2A_n^\pm} \iint_{(T_m^+ + T_m^-)} \iint_{(T_n^+ + T_n^-)} (\mathbf{r}^o - \mathbf{r}_{i_p}) \cdot \left((\mathbf{r}' - \mathbf{r}_{i_q}) \times \nabla' G_i(\mathbf{r}, \mathbf{r}') \right) dS' dS$$

where use has been of the expressions for the position vectors in equations (3.12) and (3.13).

Now, substituting the expression

$$\nabla' G_i(\mathbf{r}, \mathbf{r}') = (\mathbf{r}^o - \mathbf{r}') (1 + jk_i R) \frac{e^{-jk_i R}}{R^3} \tag{4.11}$$

in (4.10) and manipulating the cross-product term gives

$$\begin{aligned}
& \langle \nabla \times \mathbf{A}_i, \mathbf{f}_m \rangle \\
&= \frac{\mu_i}{4\pi} \frac{l_m}{2A_m^\pm} \frac{l_n}{2A_n^\pm} \iint_{(T_m^+ + T_m^-)} \iint_{(T_n^+ + T_n^-)} (\mathbf{r}^o - \mathbf{r}_{i_p}) \cdot \left[(\mathbf{r}' - \mathbf{r}_{i_q}) \times (\mathbf{r}^o - \mathbf{r}') (1 + jk_i R) \right] \frac{e^{-jk_i R}}{R^3} dS' dS \\
&= \frac{1}{4\pi} \frac{l_m}{2A_m^\pm} \frac{l_n}{2A_n^\pm} \iint_{(T_m^+ + T_m^-)} \iint_{(T_n^+ + T_n^-)} (\mathbf{r}^o - \mathbf{r}_{i_p}) \cdot \left[(\mathbf{r}^o \times \mathbf{r}_{i_q}) + (\mathbf{r}_{i_q}' - \mathbf{r}^o) \times \mathbf{r}' \right] (1 + jk_i R) \frac{e^{-jk_i R}}{R^3} dS' dS
\end{aligned} \tag{4.12}$$

Rearranging the equation (4.12) to a form that can easily be numerically integrated leads to

$$\langle \nabla \times \mathbf{A}_i, \mathbf{f}_m \rangle = \frac{\mu_i l_m l_n}{4\pi 2A_m^\pm} \iint_{(T_m^+ + T_m^-)} (\mathbf{r}^o - \mathbf{r}_{i_p}) \cdot \left[(\mathbf{r}^o \times \mathbf{r}_{i_q}) \mathbf{J} + (\mathbf{r}_{i_q}' - \mathbf{r}^o) \times (\mathbf{r}_1' \mathbf{J}_a + \mathbf{r}_2' \mathbf{J}_b + \mathbf{r}_3' \mathbf{J}_c) \right] dS^o \quad (4.13)$$

where

$$\mathbf{J} = \int_0^1 \int_0^{1-b'} (1 + jk_i R) \frac{e^{-jk_i R}}{R^3} da' db' \quad (4.14)$$

$$\mathbf{J}_a = \int_0^1 \int_0^{1-b'} a' (1 + jk_i R) \frac{e^{-jk_i R}}{R^3} da' db' \quad (4.15)$$

$$\mathbf{J}_b = \int_0^1 \int_0^{1-b'} b' (1 + jk_i R) \frac{e^{-jk_i R}}{R^3} da' db' \quad (4.16)$$

and

$$\mathbf{J}_c = \int_0^1 \int_0^{1-b'} c' (1 + jk_i R) \frac{e^{-jk_i R}}{R^3} da' db' \quad (4.17)$$

After several manipulations the following expressions are obtained for the dot and vector product terms for the position vectors in equation (4.13):

$$(\mathbf{r}^o - \mathbf{r}_{i_p}) \cdot (\mathbf{r}^o \times \mathbf{r}_{i_q}) = \left[a_o (\mathbf{r}_1^o \times \mathbf{r}_{i_p}) \cdot \mathbf{r}_{i_q} + b_o (\mathbf{r}_2^o \times \mathbf{r}_{i_p}) \cdot \mathbf{r}_{i_q} + c_o (\mathbf{r}_3^o \times \mathbf{r}_{i_p}) \cdot \mathbf{r}_{i_q} \right] \quad (4.18)$$

$$\begin{aligned}
(\mathbf{r}_{i_q} - \mathbf{r}^o) \times \mathbf{r}_1' &= [a_o(\mathbf{r}_1' \times \mathbf{r}_1^o \cdot \mathbf{r}_{i_q} + \mathbf{r}_1^o \times \mathbf{r}_1' \cdot \mathbf{r}_{i_p}) + b_o(\mathbf{r}_1' \times \mathbf{r}_2^o \cdot \mathbf{r}_{i_q} + \mathbf{r}_2^o \times \mathbf{r}_1' \cdot \mathbf{r}_{i_p}) \\
&\quad + c_o(\mathbf{r}_1' \times \mathbf{r}_3^o \cdot \mathbf{r}_{i_q} + \mathbf{r}_3^o \times \mathbf{r}_1' \cdot \mathbf{r}_{i_p}) + \mathbf{r}_{i_p} \times \mathbf{r}_1' \cdot \mathbf{r}_{i_q}]
\end{aligned} \tag{4.19}$$

$$\begin{aligned}
(\mathbf{r}_{i_q} - \mathbf{r}^o) \times \mathbf{r}_2' &= [a_o(\mathbf{r}_2' \times \mathbf{r}_1^o \cdot \mathbf{r}_{i_q} + \mathbf{r}_1^o \times \mathbf{r}_2' \cdot \mathbf{r}_{i_p}) + b_o(\mathbf{r}_2' \times \mathbf{r}_2^o \cdot \mathbf{r}_{i_q} + \mathbf{r}_2^o \times \mathbf{r}_2' \cdot \mathbf{r}_{i_p}) \\
&\quad + c_o(\mathbf{r}_2' \times \mathbf{r}_3^o \cdot \mathbf{r}_{i_q} + \mathbf{r}_3^o \times \mathbf{r}_2' \cdot \mathbf{r}_{i_p}) + \mathbf{r}_{i_p} \times \mathbf{r}_2' \cdot \mathbf{r}_{i_q}]
\end{aligned} \tag{4.20}$$

$$\begin{aligned}
(\mathbf{r}_{i_q} - \mathbf{r}^o) \times \mathbf{r}_3' &= [a_o(\mathbf{r}_3' \times \mathbf{r}_1^o \cdot \mathbf{r}_{i_q} + \mathbf{r}_1^o \times \mathbf{r}_3' \cdot \mathbf{r}_{i_p}) + b_o(\mathbf{r}_3' \times \mathbf{r}_2^o \cdot \mathbf{r}_{i_q} + \mathbf{r}_2^o \times \mathbf{r}_3' \cdot \mathbf{r}_{i_p}) \\
&\quad + c_o(\mathbf{r}_3' \times \mathbf{r}_3^o \cdot \mathbf{r}_{i_q} + \mathbf{r}_3^o \times \mathbf{r}_3' \cdot \mathbf{r}_{i_p}) + \mathbf{r}_{i_p} \times \mathbf{r}_3' \cdot \mathbf{r}_{i_q}]
\end{aligned} \tag{4.21}$$

Using the equations from (4.18) to (4.21) in (4.13) gives

$$\begin{aligned}
& \langle \nabla \times \mathbf{A}_i, \mathbf{f}_m \rangle \\
&= \frac{\mu_i}{4\pi} \frac{l_m l_n}{2} \left[\sum_{j=1}^{N_g} w_j a_j^o (\mathbf{r}_1^o \times \mathbf{r}_{i_p} \cdot \mathbf{r}_{i_q}) J(a_j^o, b_j^o, c_j^o, a_i^i, b_i^i, c_i^i) \right. \\
&+ \sum_{j=1}^{N_g} w_j b_j^o (\mathbf{r}_2^o \times \mathbf{r}_{i_p} \cdot \mathbf{r}_{i_q}) J(a_j^o, b_j^o, c_j^o, a_i^i, b_i^i, c_i^i) \\
&+ \sum_{j=1}^{N_g} w_j c_j^o (\mathbf{r}_3^o \times \mathbf{r}_{i_p} \cdot \mathbf{r}_{i_q}) J(a_j^o, b_j^o, c_j^o, a_i^i, b_i^i, c_i^i) \\
&+ \sum_{j=1}^{N_g} w_j a_j^o (\mathbf{r}_2^i \times \mathbf{r}_1^o \cdot \mathbf{r}_{i_q} + \mathbf{r}_1^o \times \mathbf{r}_2^i \cdot \mathbf{r}_{i_p}) J_a(a_j^o, b_j^o, c_j^o, a_i^i, b_i^i, c_i^i) \\
&+ \sum_{j=1}^{N_g} w_j b_j^o (\mathbf{r}_2^i \times \mathbf{r}_2^o \cdot \mathbf{r}_{i_q} + \mathbf{r}_2^o \times \mathbf{r}_2^i \cdot \mathbf{r}_{i_p}) J_a(a_j^o, b_j^o, c_j^o, a_i^i, b_i^i, c_i^i) + \\
&+ \sum_{j=1}^{N_g} w_j c_j^o (\mathbf{r}_2^i \times \mathbf{r}_3^o \cdot \mathbf{r}_{i_q} + \mathbf{r}_3^o \times \mathbf{r}_2^i \cdot \mathbf{r}_{i_p}) J_a(a_j^o, b_j^o, c_j^o, a_i^i, b_i^i, c_i^i) \\
&+ \mathbf{r}_{i_p} \times \mathbf{r}_2^i \cdot \mathbf{r}_{i_q} J_a(a_j^o, b_j^o, c_j^o, a_i^i, b_i^i, c_i^i) + \\
&+ \sum_{j=1}^{N_g} w_j a_j^o (\mathbf{r}_2^i \times \mathbf{r}_1^o \cdot \mathbf{r}_{i_q} + \mathbf{r}_1^o \times \mathbf{r}_2^i \cdot \mathbf{r}_{i_p}) J_b(a_j^o, b_j^o, c_j^o, a_i^i, b_i^i, c_i^i) \\
&+ \sum_{j=1}^{N_g} w_j b_j^o (\mathbf{r}_2^i \times \mathbf{r}_2^o \cdot \mathbf{r}_{i_q} + \mathbf{r}_2^o \times \mathbf{r}_2^i \cdot \mathbf{r}_{i_p}) J_b(a_j^o, b_j^o, c_j^o, a_i^i, b_i^i, c_i^i) \\
&+ \sum_{j=1}^{N_g} w_j b_j^o (\mathbf{r}_2^i \times \mathbf{r}_3^o \cdot \mathbf{r}_{i_q} + \mathbf{r}_3^o \times \mathbf{r}_2^i \cdot \mathbf{r}_{i_p}) J_b(a_j^o, b_j^o, c_j^o, a_i^i, b_i^i, c_i^i) \\
&+ \mathbf{r}_{i_p} \times \mathbf{r}_2^i \cdot \mathbf{r}_{i_q} J_b(a_j^o, b_j^o, c_j^o, a_i^i, b_i^i, c_i^i) \\
&+ \sum_{j=1}^{N_g} w_j a_j^o (\mathbf{r}_3^i \times \mathbf{r}_1^o \cdot \mathbf{r}_{i_q} + \mathbf{r}_1^o \times \mathbf{r}_3^i \cdot \mathbf{r}_{i_p}) J_c(a_j^o, b_j^o, c_j^o, a_i^i, b_i^i, c_i^i) \\
&+ \sum_{j=1}^{N_g} w_j b_j^o (\mathbf{r}_3^i \times \mathbf{r}_2^o \cdot \mathbf{r}_{i_q} + \mathbf{r}_2^o \times \mathbf{r}_3^i \cdot \mathbf{r}_{i_p}) J_c(a_j^o, b_j^o, c_j^o, a_i^i, b_i^i, c_i^i) \\
&+ \mathbf{r}_{i_p} \times \mathbf{r}_3^i \cdot \mathbf{r}_{i_q} J_c(a_j^o, b_j^o, c_j^o, a_i^i, b_i^i, c_i^i) \left. \right] \tag{4.22}
\end{aligned}$$

The tested curl of the magnetic vector potential is now in a form that can be programmed.

In (4.22), the integrals J , J_a , J_b and J_c over the source triangles T_n^\pm are evaluated using Patterson's rule [124]. Each complete integration over T_n^\pm is performed for each observation point inside observation triangle T_m^\pm . The Gaussian quadrature scheme is then used to complete the integration over the observation triangle. This is represented by the summation signs in (4.22).

The expression for the tested curl of the electric vector potential is obtained in the same way used to come up with (4.22). The integrals for the tested curl of the vector potential are evaluated in exactly the same way as for the tested curl of the magnetic vector potential. The only difference is in the floating constants.

4.2.2 CFIE Matrix Equation

To obtain the moment matrix the equivalent surface currents \mathbf{J} and \mathbf{M} are expanded with the RWG basis functions, \mathbf{f}_n , such that

$$\mathbf{J} \simeq \sum_{n=1}^{N_d} \alpha_n \mathbf{f}_n \quad (4.23)$$

$$\mathbf{M} \simeq \sum_{n=1}^{N_d} \beta_n \mathbf{f}_n \quad (4.24)$$

where N_d is the number of edges on the triangular mesh approximating the geometry of the dielectric scatterer and the quantities α_n and β_n are the unknown expansion coefficients of the currents on the dielectric mesh edges.

Equations (4.23) and (4.24) are substituted into the tested equations (4.1) and (4.2) to yield $2N_d \times 2N_d$ simultaneous equations and a square impedance matrix Z . These equations can be written in matrix form as

$$\begin{bmatrix} [Z_{mn}^{JJ}] & [Z_{mn}^{JM}] \\ [Z_{mn}^{MJ}] & [Z_{mn}^{MM}] \end{bmatrix} \begin{bmatrix} [\alpha_n] \\ [\beta_n] \end{bmatrix} = \begin{bmatrix} [V_m] \\ [H_m] \end{bmatrix} \quad (4.25)$$

where the first superscript of the matrix element indicates the field current type, the second superscript denotes the source current type, m and n are give the edge number for the observation and source triangles respectively, i.e. $m = 1, 2, 3, \dots, N_d$ edges and $n = 1, 2, 3, \dots, N_d$ edges. The right side column vector contains tested excitation vectors, V_m for electric fields and H_m for magnetic fields.

The Z matrix is shown in (4.25) partitioned into square matrices. The elements of the diagonal submatrix for the electric current are given by:

$$\begin{aligned}
Z_{mn}^{JJ} = l_m l_n & \left[\sum_{i=1}^2 (j\omega\mu_i) \mathbf{A}_{i_{mn}}^+ + \sum_{i=1}^2 (j\omega\mu_i) \mathbf{A}_{i_{mn}}^- \right. \\
& \left. + \sum_{i=1}^2 \left(-\frac{1}{j\omega\epsilon_i} \right) \{ \Phi_{i_{mn}}^- - \Phi_{i_{mn}}^+ \} \right]
\end{aligned} \tag{4.26}$$

The elements for the diagonal submatrix, $[Z_{mn}^{MM}]$, for the magnetic current are given by:

$$\begin{aligned}
Z_{mn}^{MM} = l_m l_n & \left[\sum_{i=1}^2 (j\omega\epsilon_i) \mathbf{F}_{i_{mn}}^+ + \sum_{i=1}^2 (j\omega\epsilon_i) \mathbf{F}_{i_{mn}}^- \right. \\
& \left. + \sum_{i=1}^2 \left(-\frac{1}{j\omega\mu_i} \right) \{ \Psi_{i_{mn}}^- - \Psi_{i_{mn}}^+ \} \right]
\end{aligned} \tag{4.27}$$

The elements for the off-diagonal submatrix are given by

$$Z_{mn}^{JM} = \left[\sum_{i=1}^2 P_{i_{mn}}^+ + \sum_{i=1}^2 P_{i_{mn}}^- \right] \tag{4.28}$$

$$Z_{mn}^{MJ} = \left[\sum_{i=1}^2 Q_{i_{mn}}^+ + \sum_{i=1}^2 Q_{i_{mn}}^- \right] \tag{4.29}$$

The elements for the excitation vectors are:

$$\mathbf{V}_m = \frac{l_m}{2} \left[\mathbf{E}^{inc+} \cdot \boldsymbol{\rho}_{i_p}^+(\mathbf{r}, \mathbf{r}_{i_p}) + \mathbf{E}^{inc-} \cdot \boldsymbol{\rho}_{i_p}^-(\mathbf{r}, \mathbf{r}_{i_p}) \right] \quad (4.30)$$

$$\mathbf{H}_m = \frac{l_m}{2} \left[\mathbf{H}^{inc+} \cdot \boldsymbol{\rho}_{i_p}^+(\mathbf{r}, \mathbf{r}_{i_p}) + \mathbf{H}^{inc-} \cdot \boldsymbol{\rho}_{i_p}^-(\mathbf{r}, \mathbf{r}_{i_p}) \right] \quad (4.31)$$

The tested vector potential integrals take the form

$$\begin{aligned} \mathbf{A}_{i_{mn}}^{\pm} &= \frac{1}{4\pi} \frac{1}{2A_m^{\pm}} \frac{1}{2A_n^{\pm}} \left[\iint_{(T_m^+ + T_m^-)} \iint_{(T_n^+ + T_n^-)} \boldsymbol{\rho}_n^{\pm}(\mathbf{r}') \cdot \boldsymbol{\rho}_m^{\pm}(\mathbf{r}) G_i(\mathbf{r}, \mathbf{r}') dS' dS \right] \\ &= \mathbf{F}_{i_{mn}}^{\pm} \end{aligned} \quad (4.32)$$

The tested scalar potentials and scalar take the form

$$\begin{aligned} \Phi_{i_{mn}}^{\pm} &= \frac{1}{4\pi} \frac{1}{A_m^{\pm}} \frac{1}{A_n^{\pm}} \iiint_{T_m^{\pm} T_n^{\pm}} G_i(\mathbf{r}, \mathbf{r}') dS' dS \\ &= \Psi_{i_{mn}}^{\pm} \end{aligned} \quad (4.33)$$

and the tested curl of the vector potentials take the form

$$\begin{aligned}
P_{i_{mn}}^{\pm} &= \frac{1}{4\pi} \frac{1}{2A_m^{\pm}} \frac{1}{2A_n^{\pm}} \iint_{(T_m^+ + T_m^-)} \left[\iint_{(T_n^+ + T_n^-)} \rho_{i_q} \times \nabla' G_i(\mathbf{r}, \mathbf{r}') dS' \right] \cdot \rho_{i_p} dS \\
&= Q_{i_{mn}}^{\pm}
\end{aligned} \tag{4.34}$$

Equations (4.32) and (4.33) are evaluated as shown in section 3.2.2. The evaluation of (4.34) is shown in (4.10) through (4.22). In all cases, the two surface integrals are evaluated accurately and are not approximated.

With the current expansion coefficients α_n and β_n determined from (4.25), the scattered fields and hence the RCS, can be calculated using the usual expressions [153]. The electric and magnetic currents on the surface of other regions are calculated using the relationships in (4.23) and (4.24).

4.2.3 Optimisation of the number of Gaussian Points for the $1/R^3$ integral

A nearness factor (NF) was introduced in Chapter 3, Section 3.3.2.2, as a normalised parameter to specify the separation between source and observation triangles. It was observed that the larger the NF becomes, i.e. the closer the observation points get to the source triangle, the more computational effort is required for the $1/R$ integral. However, as the NF gets smaller, i.e. as the observation points recede from the source triangle, less computational effort is required to compute the $1/R$ integrals. Numerical experiments were performed to determine the optimum number of Gaussian points needed for the observation triangles for the numerical integration process. Graphs of the variations of the matrix impedance elements, calculated using a 1-point, 4-point, 7-point and a

13-point Gaussian quadrature scheme, with the NF were plotted and the point of intersection of the graphs for low NF values determined. This gave the values of the NF below which a 1- Gaussian quadrature scheme could be used in the 4-SI method without losing accuracy but saving computation time. This is necessary to strike a good compromise between accuracy and computation time for the 4-SI method. In this section, the same procedure is repeated for the $1/R^3$ integrals. These integrals are encountered when dielectrics are present in the scattering problem. The value for the relative permittivity used in the numerical experiments was 4.

CASE 1

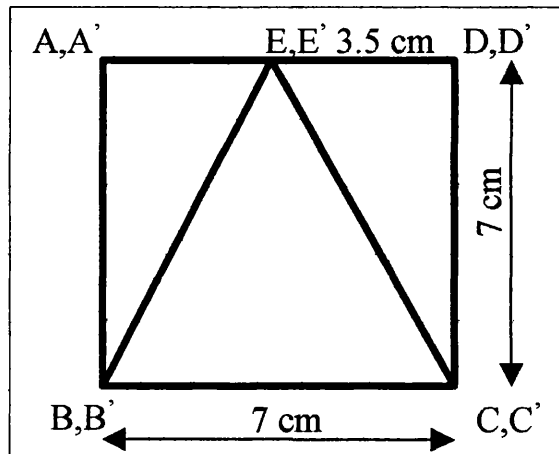


Figure 4.1 Triangles used to generate graph in Figure 4.2

Figure 4.1 shows two dielectric plates, ABCD and A'B'C'D', each meshed into three triangles with the dimensions shown. The vertical distance between the plates is varied, with plate ABCD fixed, and each time the impedance element for particular source/observation triangles is calculated using 1-point, 4-point, 7-

point and 13-point Gaussian quadrature. Triangles BCE and B'CE' were used as the source and observation triangles respectively. All the dimensions shown in Figure 4.1 are in centimetres and the frequency used was 300 MHz. The values for the impedance elements were plotted against the nearness factor as shown in Figure 4.2.

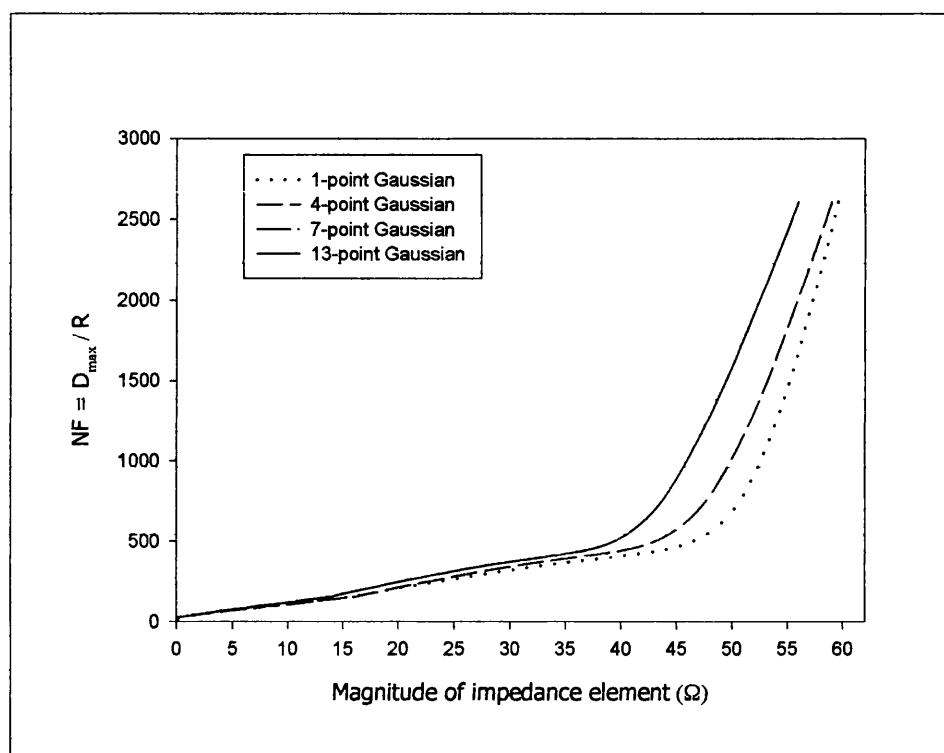


Figure 4.2 Case 1 - Variation of impedance element with nearness factor for Figure 4.1.

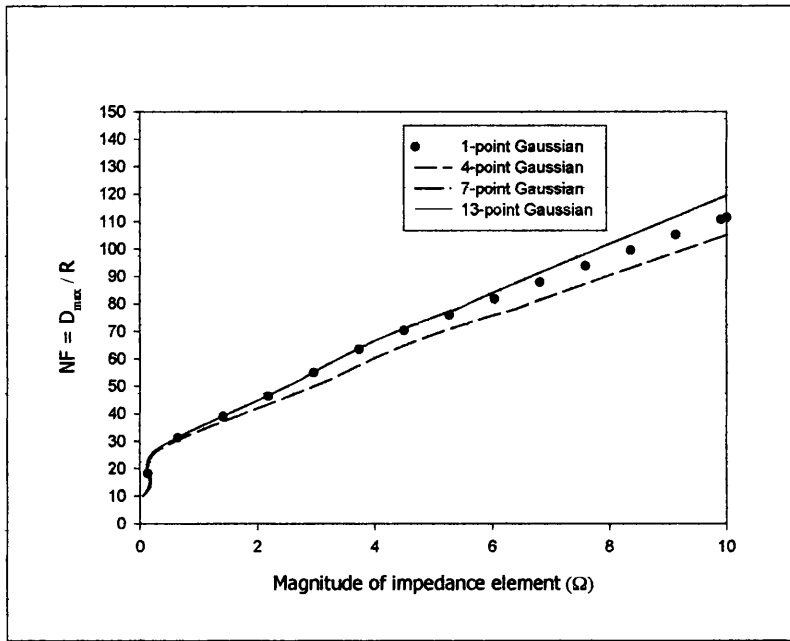


Figure 4.3 Graph in Figure 4.2 redrawn to show the intersection of the curves for low NF values

The same procedure was repeated for three other cases and the triangle shapes varied as shown below.

CASE 2

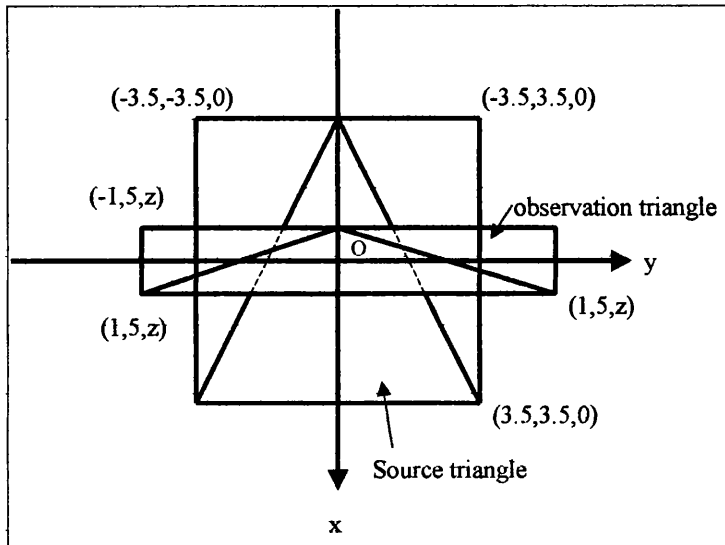


Figure 4.4 Mesh used to generate graph in Figure 4.5

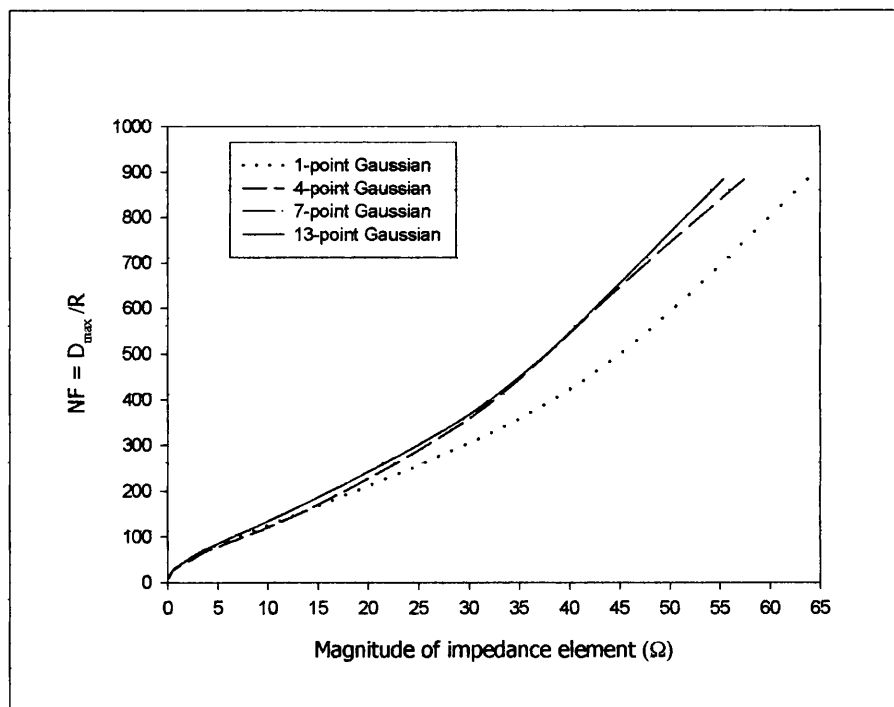


Figure 4.5 Case 2 - Variation of impedance element with nearness factor for Figure 4.4

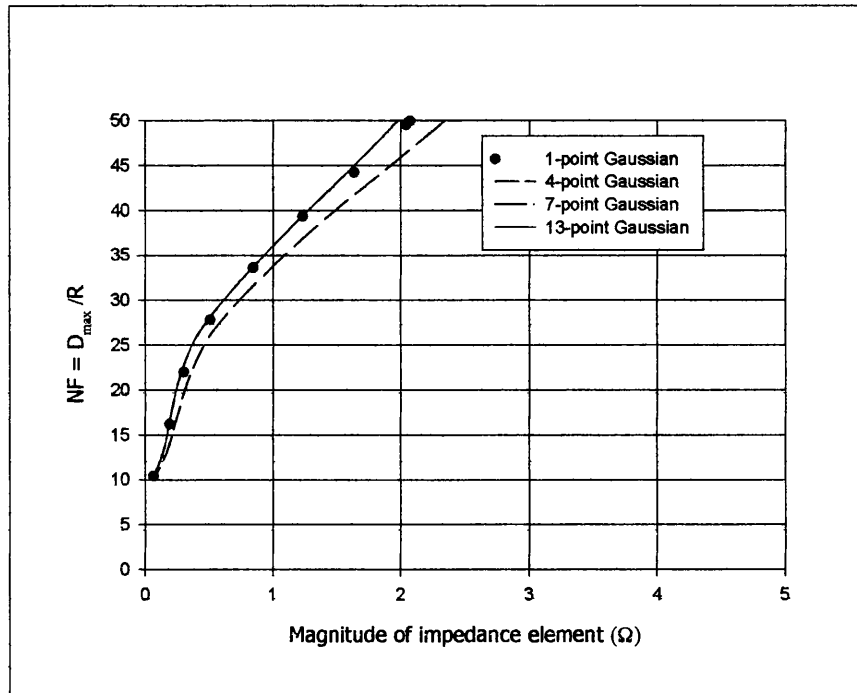


Figure 4.6 Redrawn Figure 4.5 showing clearly the intersection for the n-point curves.

CASE 3

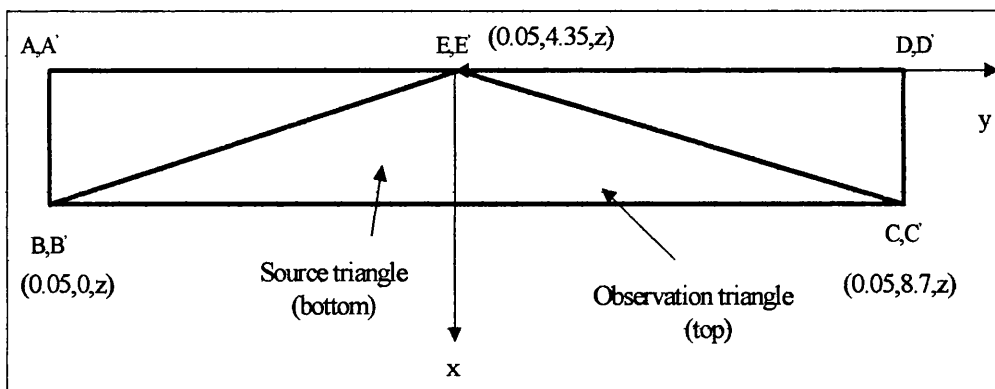


Figure 4.7 Mesh used to generate Figure 4.8

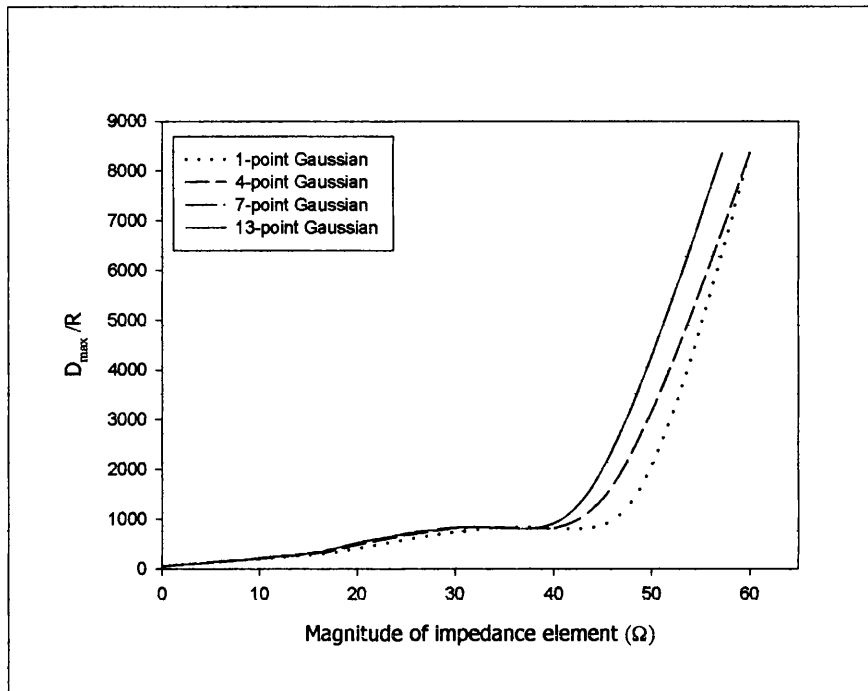


Figure 4.8 Case 3: Variation of impedance element with nearness factor for Figure 4.7.

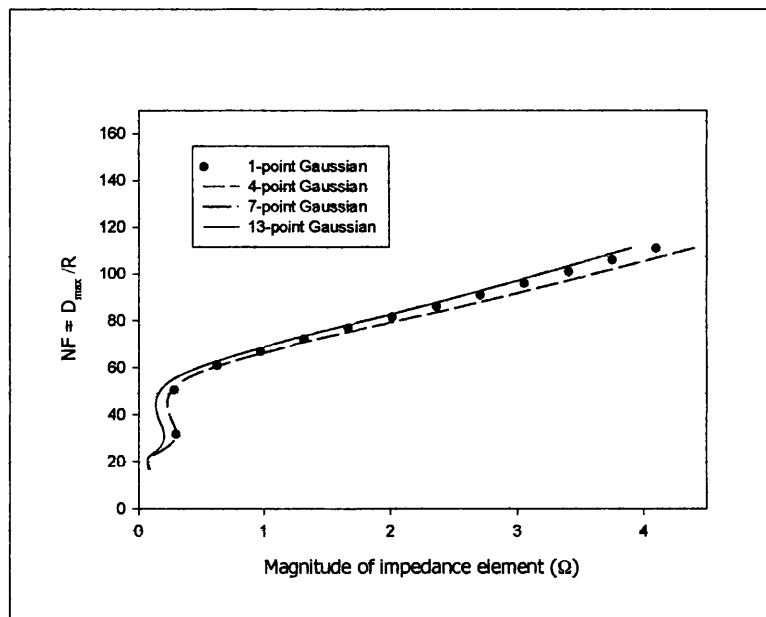


Figure 4.9 Graph in Figure 4.8 redrawn to show the intersection of the curves for low NF values.

CASE 4

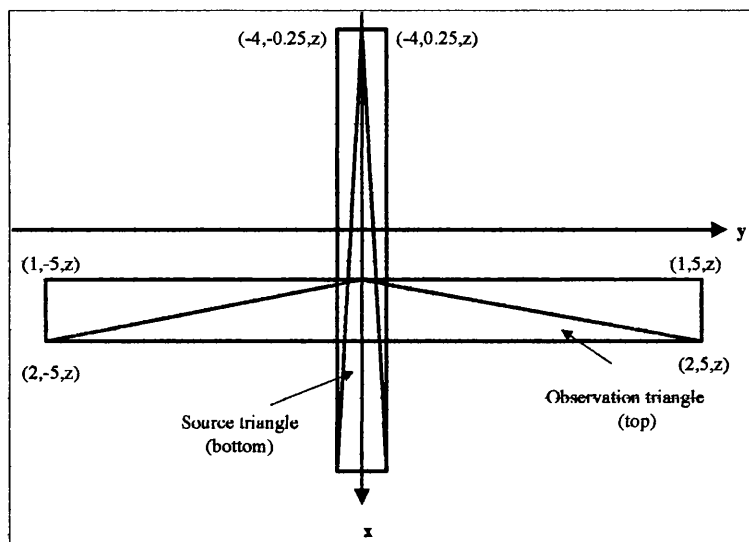


Figure 4.10 Mesh used to generate Figure 4.11.

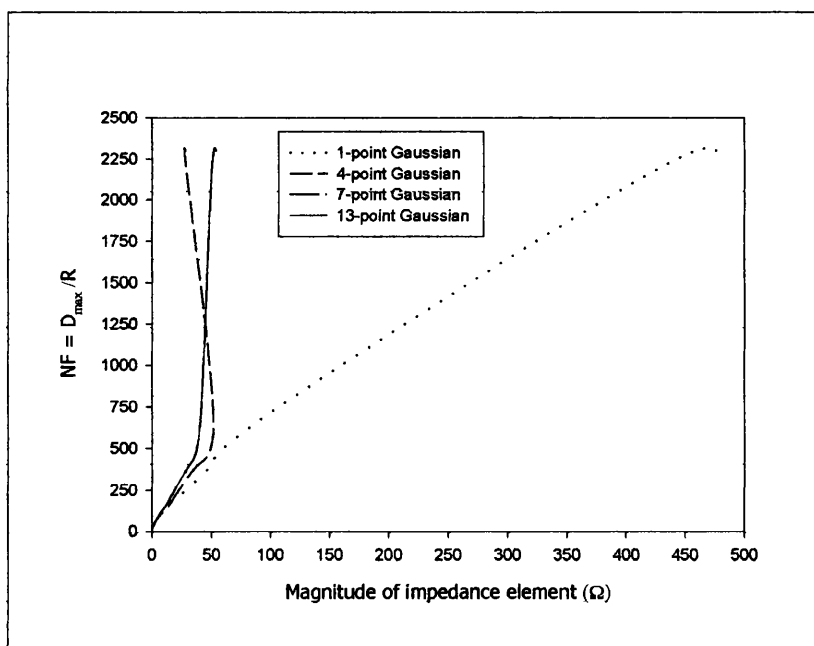


Figure 4.11 Case 3: Variation of impedance element with nearness factor for Figure 4.10.

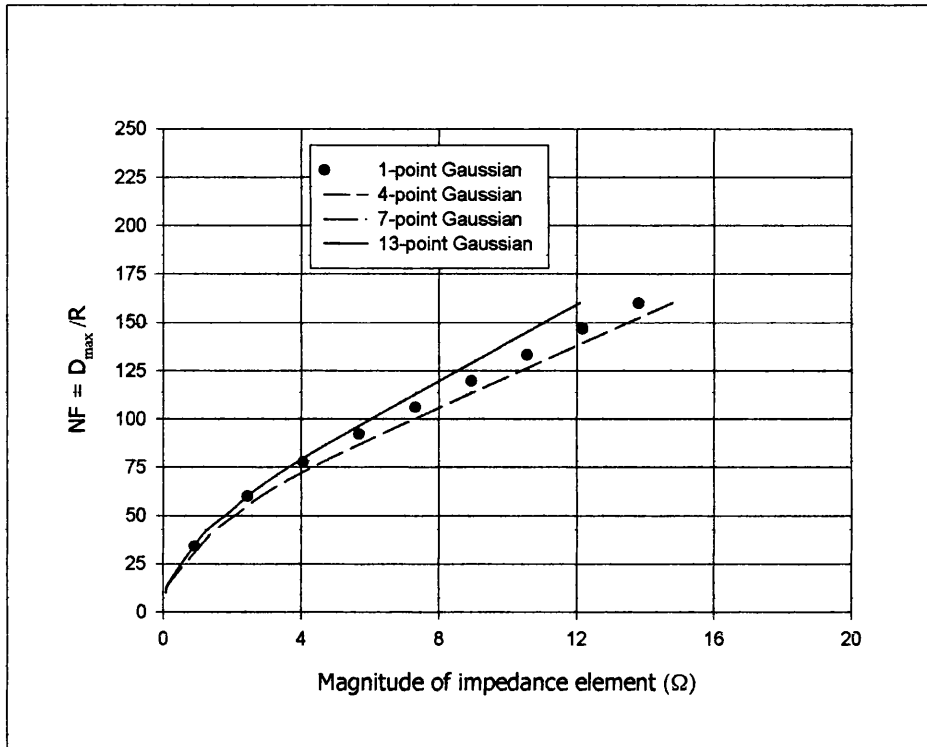


Figure 4.12 Graph in Figure 4.11 redrawn to show the intersection of the curves for low NF values.

As the above Figures demonstrate, a distinct improvement in the impedance element calculations was observed by increasing the number of quadrature points from 1 to 13 for closely coupled triangles. However, no appreciable improvements were observed by increasing the number of quadrature points from 7 to 13. Graphs for the 7-point and 13-point Gaussian quadrature schemes are virtually indistinguishable. It was on this basis that the 7-point Gaussian was chosen in preference to the 4-point Gaussian integration. There is a marked difference between the one-point and the higher order Gaussian schemes for when the source and observation triangles are in close proximity, i.e. when the NF is large. This proves that the higher order Gaussian schemes calculate the impedance matrix elements more accurately than the one-point scheme for closely spaced triangles. It is also observed that for large distances between the source and observation triangles, the one-point scheme is just as accurate as any

higher order scheme. This is observed to occur for a NF value of 40 and below. happens when the nearness factor is about 20 or less. This is the value of NF at which the 1-point curve converges with the higher order scheme curves as shown in the above graphs. Hence beyond a certain separation distance between the source and observation triangles, a one-point Gaussian scheme is sufficient. This translates to very fast computation times for the evaluation of the impedance elements.

The 4-point is seen to be less accurate than the 7-point or the 13-point schemes, particularly for closely coupled triangles. It is on this basis that the 4-point scheme was not used. As it was observed that there is little difference between the 7-point and the 13-point schemes, the 7-point Gaussian quadrature scheme was used for closely coupled triangular patches ($NF > 40$) and the 1-point Gaussian quadrature scheme used for loosely coupled triangular patches.

4.2.4 Numerical Implementation

Consider the evaluation of the integrals in (4.22). If the observation triangle, T_m^\pm and the source triangle, T_n^\pm are not closely coupled, then the integrals in (4.22) are regular and can be calculated numerically using the Gaussian quadrature scheme for the outer integral, and Patterson's rule [124] for the inner triangle. Following the procedure in Chapter 3, a one-point Gaussian quadrature scheme is used for loosely coupled triangles and a seven-point Gaussian quadrature scheme for closely coupled objects. This is equivalent to employing the 2-SI scheme. In fact, as was illustrated in Chapter 3, the numerical solutions for the higher order n-point Gaussian quadrature scheme are the same as the one-point Gaussian quadrature scheme. The only difference is in the computation time

where the higher order Gaussian scheme takes many orders of magnitude longer than the one-point solution.

When the triangles T_m^\pm and T_n^\pm are close to each other the evaluation of the double surface integrals are evaluated using a 7-point Gaussian quadrature scheme.

From (4.10), it is observed that $\langle \nabla \times \mathbf{A}_i, \mathbf{f}_m \rangle$ is zero if the triangles T_m^\pm and T_n^\pm lie on the same plane. The cross product of the gradient of the Green's function and the basis function results in a vector that is perpendicular to the testing function. For the case when T_m^\pm and T_n^\pm are not in the same plane but are very close to each other, $\langle \nabla \times \mathbf{A}_i, \mathbf{f}_m \rangle$ has a near singularity of the order of $1/R^3$. This is evaluated using the seven-point Gaussian quadrature scheme.

4.3 RESULTS AND DISCUSSIONS

This section presents some performance data on the 4-SI method for dielectric objects based on the theory given in the above sections. The 4-SI results are compared with those of the 2-SI and published material. The performance of the 4-SI is measured in terms of the number of unknowns, computer storage space required and the total computation time needed to solve a particular problem with good accuracy. These parameters are then compared principally against those of the 2-SI method. Published papers are also used to check the accuracy of the 4-SI method.

4.3.1 Scattering by dielectric spheres

This section presents the radar cross-section results for scattering by a lossless and a lossy dielectric sphere. The lossless dielectric sphere is considered first. The incident wave is travelling in the negative z -direction and the electric field is polarised in the positive x -direction. For reference, the Mie-series results are used. Figure 4.13 shows the bistatic radar cross-section results of a lossless dielectric sphere whose relative permittivity is $\epsilon_r = 3$ and permeability $\mu_r = 1$. Figure 4.14 shows the same results but for $0 \leq \theta_i \leq 90^\circ$ to highlight the differences between the two methods. The size of the sphere is $ka = 5.3$, where k is the free space wave number and a is the radius of the sphere. There are three types of results shown in Figure 4.13 and Figure 4.14, a Mie series solution result, 4-SI results and 2-SI results obtained for different triangular patch meshing of the dielectric sphere. Figure 4.14 shows the same results as Figure 4.13 but only for the region $0^\circ \leq \theta_i \leq 90^\circ$, so as to show clearer the differences between the results of the three approaches. The 4-SI results, i.e. 4-SI(a) and 4-SI(b) with maximum edge lengths of $0.38\lambda_d$ and $0.27\lambda_d$ respectively, compare very well with the Mie series solution result. The wavelength in the dielectric is denoted by λ_d . This is despite the course mesh used to obtain the 4-SI(a) result. The slight discrepancies between the 4-SI(a) and the Mie series solution could be explained by the surface geometry being not defined accurately enough by the large triangular patches used. A radius correction factor would need to be introduced. The analytic Mie series solution uses the exact radius of the sphere in calculating radar cross-section results. The 2-SI result shown by curve 2-SI(b), uses a mesh with a maximum edge of $0.27\lambda_d$, fails to track the reference Mie series solution result as accurately as the 4-SI results. However, on reducing the maximum edge length to $0.24\lambda_d$, the 2-SI result, shown by curve 2-SI(a),

compares well with the reference Mie series solution. The mesh is still very coarse for the 2SI scheme but the result is very remarkable in that it shows maximum deviations of only about 1dB from the Mie series at some values of θ .

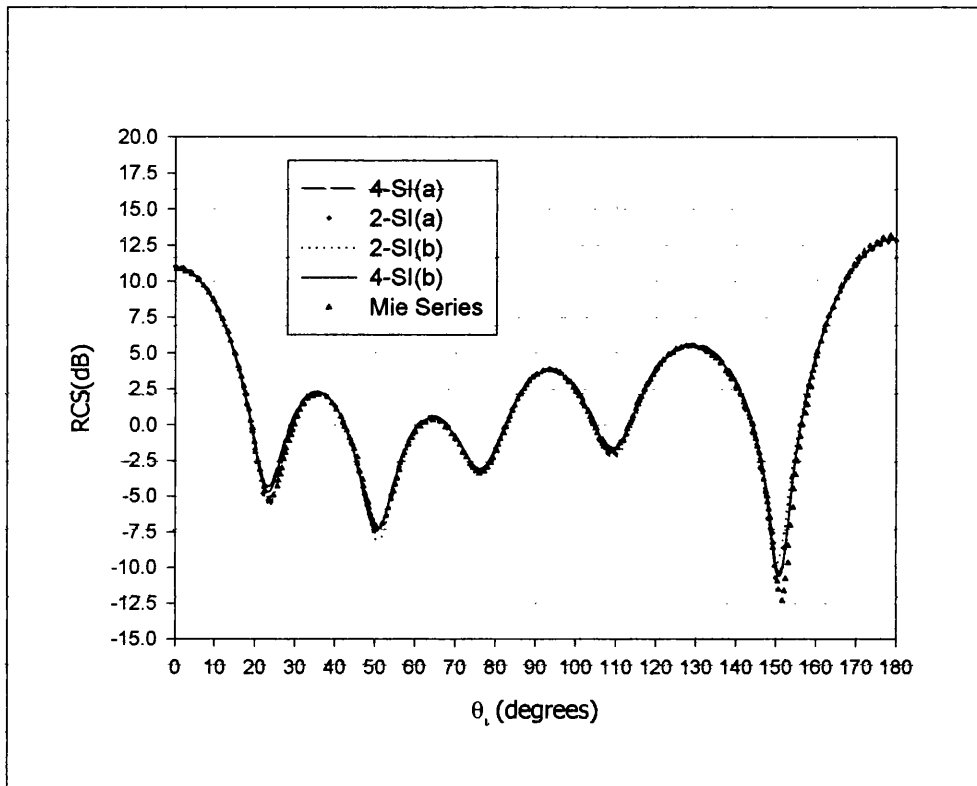


Figure 4.13 Bistatic scattering by a dielectric sphere $ka = 5.3$, $\epsilon_r = 3$, $\mu_r = 1$

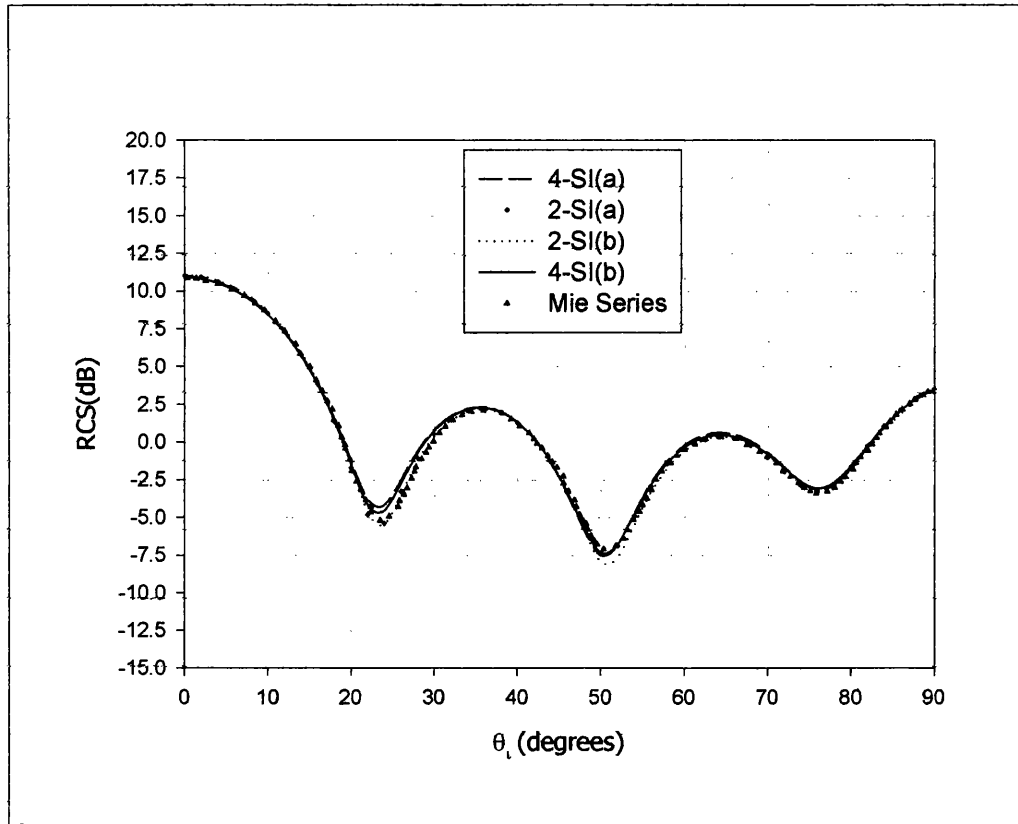


Figure 4.14 Bistatic scattering by a dielectric sphere for $0 \leq \theta_i \leq 90^\circ$.

In order to produce accurate results, the maximum triangular patch edge should be of the order of $0.1\lambda_d$ for the 2-SI formulation. This would require the total number of unknowns exceeding 28000. The computation time and the computer memory requirement would therefore be many magnitudes higher than that for the 4-SI to achieve the equivalent accuracy. Table 4.1 summarises the CPU and memory requirements for the 2-SI and 4-SI methods. The computing resources limited the number of unknowns to 7500 and 5000 for the 2-SI formulation when calculating the bistatic radar cross-section and monostatic radar cross-section bistatic results respectively. The limitation for the 4-SI formulation was 5000 unknowns.

Table 4.1– Computation time and computer memory requirements for

a $ka = 5.3$ dielectric sphere

| Scheme | Number of triangular patches | Number of unknowns | Maximum edge length (λ_d) | Matrix fill time (sec) | Solve time (sec) | Total computation time (sec) | Memory (MB) |
|---------|------------------------------|--------------------|-------------------------------------|------------------------|------------------|------------------------------|-------------|
| 2-SI(a) | 2292 | 6876 | 0.24 | 1632.5 | 8659.1 | 10291.598 | 180.3 |
| 2-SI(b) | 1596 | 4788 | 0.27 | 860.5 | 1619.0 | 2479.5 | 87.4 |
| 4-SI(a) | 876 | 2628 | 0.38 | 6706.9 | 1484.4 | 8191.23 | 52.7 |
| 4-SI(b) | 1596 | 4788 | 0.27 | 11965.2 | 5955.0 | 17920.2 | 174.9 |

Its worth noting that the data given for the 2-SI scheme in Table 4.1 is not representative of the 2-SI requirements for the given problem. The mesh would need to have a maximum triangular patch edge length of the order of one-tenth of the dielectric results. What is clear though from Table 4.1 is the fact that given a proper mesh, the CPU time and memory requirements for the 2-SI method would exceed that for the 4-SI method.

The electromagnetic scattering by a $2\lambda_0$ diameter sphere of lossy dielectric, $\epsilon_r = 2.0 - j2.0$, is presented next. Figure 4.15 and Figure 4.16 show the bistatic radar cross-section for the H-plane and E-plane respectively for the $2\lambda_0$ diameter lossy sphere. Good agreement is obtained between the 2-SI, the 4-SI results with those by McCowen and Tran [154] and Zhu *et al.* [155]. Two mesh structures were employed, one with a maximum edge length of $0.38\lambda_d$ and the other with a maximum edge length of $0.25\lambda_d$. As in the lossless sphere case discussed above, one would not normally use a mesh structure with an edge length exceeding about $0.15\lambda_d$ with the 2-SI formulation.

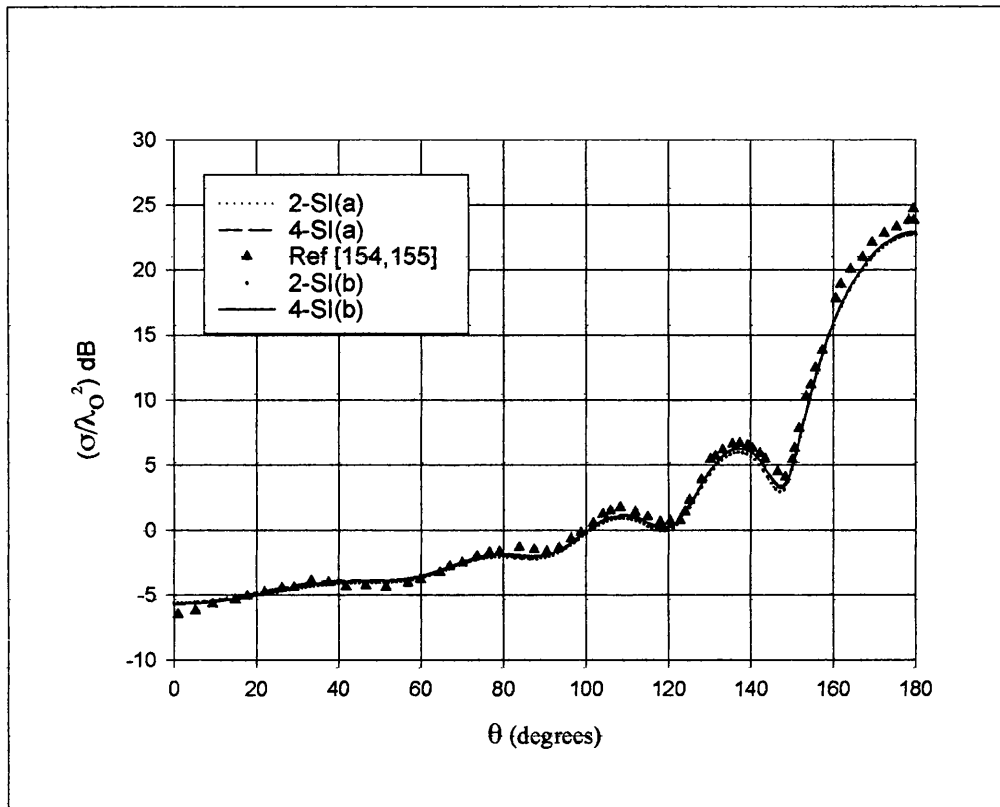


Figure 4.15 The bistatic radar cross-section of a lossy sphere in the H-plane

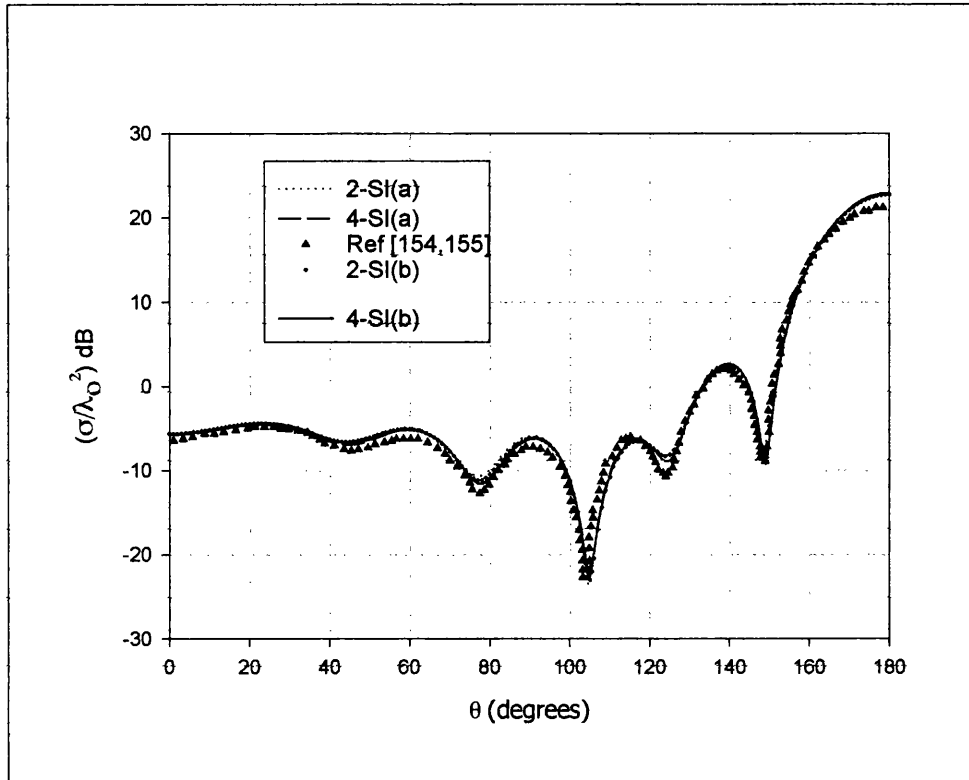


Figure 4.16 The bistatic radar cross-section of a lossy sphere in the E-plane

Table 4.2 gives the computation requirements for the two methods. No definite conclusions can be drawn from the 2-SI results when compared with the 4-SI results because of the coarseness of the mesh. Judging from the data in Table 4.2, the computation time and storage space for the 2-SI formulation would exceed that of the 4-SI(b) if a suitably fine mesh were to be used.

Table 4.2– Computation time and memory requirements for a lossy dielectric sphere of radius $1.0\lambda_0$ and relative permittivity $\epsilon_r = 2.0 - j2.0$.

| Scheme | Number of triangular patches | Number of unknowns | Maximum edge length (λ_d) | Matrix fill time (sec) | Solve time (sec) | Total computation time (sec) | Memory (MB) |
|---------|------------------------------|--------------------|-------------------------------------|------------------------|------------------|------------------------------|-------------|
| 2-SI(a) | 1012 | 3036 | 0.38 | 392.1 | 420.6 | 812.7 | 35.15 |
| 2-SI(b) | 1596 | 4788 | 0.25 | 2416.0 | 3647.6 | 6063.6 | 87.4 |
| 4-SI(a) | 1012 | 3036 | 0.38 | 9439.8 | 842.9 | 10282.7 | 70.3 |
| 4-SI(b) | 1596 | 4788 | 0.25 | 21340. | 3663.9 | 25003.9 | 175 |

4.3.2 Scattering by a dielectric cylinder

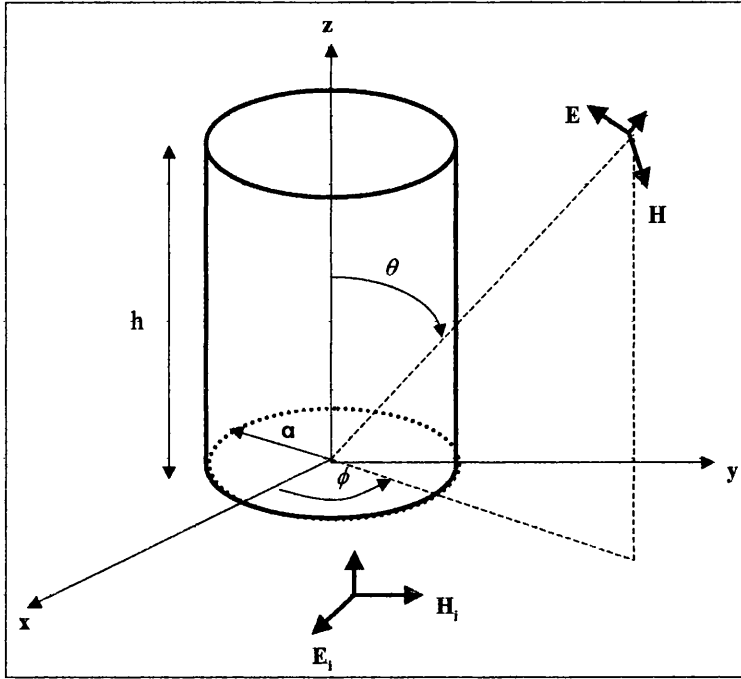


Figure 4.17 Homogeneous dielectric cylinder excited by a plane wave

This example considers the bistatic scattering by a homogeneous lossless dielectric cylinder of relative permittivity $\epsilon_r = 2$. The dielectric cylinder is excited by a plane wave as shown in Figure 4.17 and its height is given by $h = 2a = 0.7733\lambda_o = 1.093\lambda_d$, where λ_o and λ_d are the free space and dielectric wavelengths respectively. Shown in Figure 4.18 are the bistatic scattering cross-section results of the 2-SI and 4-SI formulations for the dielectric cylinder in the plane $\phi = 0^\circ$. The 2-SI and 4-SI computed results are compared with the results by Notaros and Popovic [156]. Three different mesh structures were used to obtain the 2-SI results, i.e. 2-SI(a), 2-SI(b) and 2-SI(c) as shown in Figure 4.18. For the first mesh with a maximum edge length of $0.36\lambda_d$, the 2-SI fails to agree with the reference solution. However, the corresponding 4-SI result given by curve 4-SI(a) compares well with the reference solution in [156]. This is despite

the coarse mesh which distorts the surface area of the modelled cylinder. There is an improvement in the comparison of the 2-SI result, 2-SI(c), when the meshing density is increased such the maximum edge length is $0.2\lambda_d$. Still, the corresponding 4-SI result, curve 4-SI(b), compares better with the reference solution. For a fine mesh such that the maximum edge length is $0.1\lambda_d$, the 2-SI result, curve 2-SI(b), is in excellent agreement with the reference solution. For this result, the 2-SI formulation requires 7494 unknowns, 11655 sec and 214 Mb of memory. This is compared with the 4-SI result, 4-SI(b), which requires 1860 unknowns, 5746 and about 26.4 MB to produce the same levels of accuracy as that of the 2-SI(b) result and the reference solution.

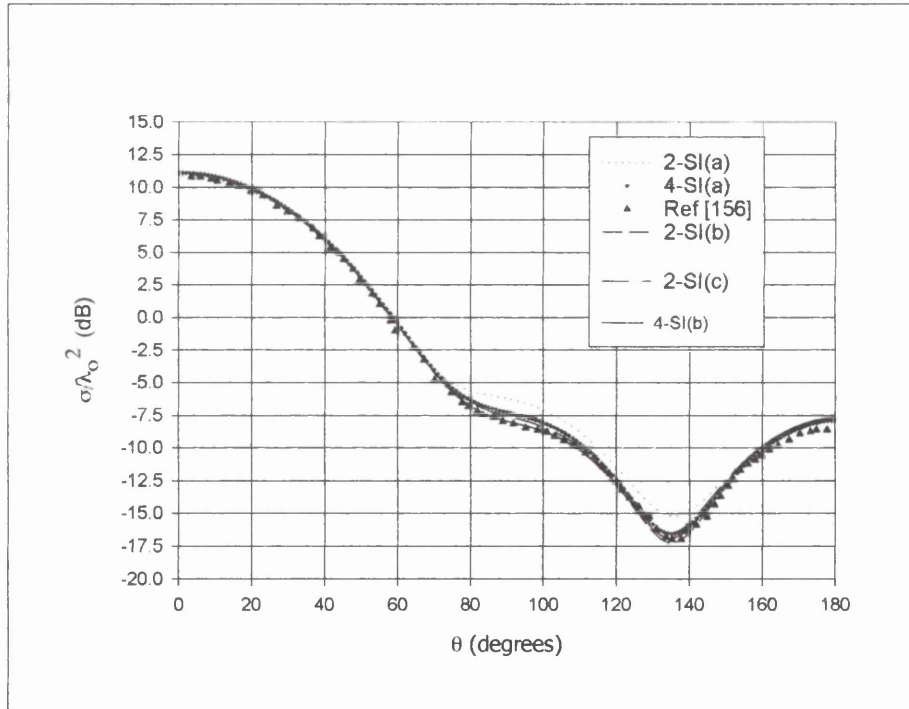


Figure 4.18 Bistatic cross-section of a homogeneous lossless dielectric cylinder in the plane $\phi = 0^\circ$

The 4-SI(a) solution generated with a mesh with a maximum edge length of $0.36\lambda_d$ is in fairly good agreement with the reference solution. For a mesh with a

maximum edge length of $0.2\lambda_d$, the 4-SI method gives the same accuracy as that achieved by the 2-SI scheme with a mesh with a maximum edge length of $0.1\lambda_d$. The performance indicators of the 2-SI and the 4-SI formulations in analysing the electromagnetic scattering by the dielectric cylinder are summarised in Table 4.3.

Table 4.3– Computation time and memory requirements for a dielectric cylinder
with height $0.7733\lambda_o$ and radius $0.38665\lambda_o$

| Scheme | Number of triangular patches | Number of unknowns | Maximum edge length (λ_d) | Matrix fill time (sec) | Solve time (sec) | Total computation time (sec) | Memory (MB) |
|---------|------------------------------|--------------------|-------------------------------------|------------------------|------------------|------------------------------|-------------|
| 2-SI(a) | 204 | 612 | 0.36 | 24.1 | 3.6 | 27.7 | 1.44 |
| 2-SI(b) | 2498 | 7494 | 0.1 | 1971.0 | 9683.5 | 11654.5 | 214 |
| 2-SI(c) | 620 | 1860 | 0.2 | 187.7 | 94.7 | 282.4 | 13.2 |
| 4-SI(a) | 204 | 612 | 0.36 | 506.3 | 6.9 | 513.2 | 2.86 |
| 4-SI(b) | 620 | 1860 | 0.2 | 5220.3 | 525.8 | 5746.1 | 26.4 |

It is observed from Table 4.3 that with a fine mesh of $0.1\lambda_d$, the 2-SI method takes nearly 22 times more time than the 4-SI to achieve the same accuracy. This despite the fact that a coarse mesh was used with the 4-SI method. Furthermore, the 2-SI requires 99 times more memory to achieve good accuracy for this particular problem.

4.3.3 Scattering by a dielectric box

This example considers the bistatic scattering by a dielectric box shown in Figure 4.19. The box has dimensions $5.0\lambda_o \times 1.0\lambda_o \times 0.6\lambda_o$ and relative permittivity, $\epsilon_r = 1.75 - j0.3$.

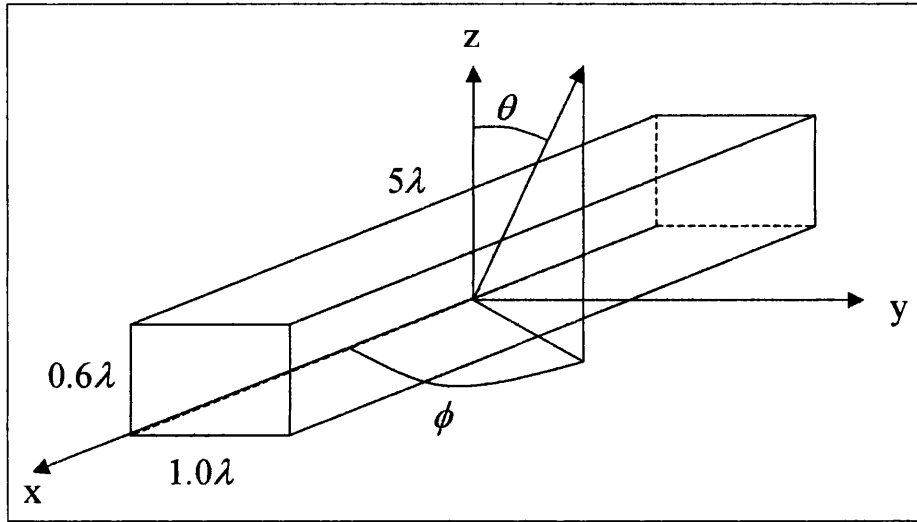


Figure 4.19 Geometry of the dielectric box

The excitation is a plane wave along the z -axis. The resulting bistatic radar cross-section curves are given in Figure 4.20- Figure 4.23 for the $\theta\theta$ and $\phi\phi$ polarisations. Initially, the box is discretised with 1290 edges resulting in a maximum edge length of $0.38\lambda_d$. As can be seen in Figure 4.20 - Figure 4.23, the 4-SI results, shown by the curves 4-SI(a) are in almost complete agreement with the results obtained by Topsakal *et al.* [157] apart from the instances when $55^\circ < \theta < 75^\circ$ when the 4-SI differs from the reference solution for the E_θ scattering. The corresponding results for the 2-SI formulation, given by curves 2-SI(a), are not agreement with the results in [157] by Topsakal *et al.* [157] which used an adaptive integral method [158] with 5500 unknowns. The meshing density was increased to 1608 triangular patches, corresponding to 4824 unknowns. There was marginal improvement in the 4-SI results, shown by the curves 4-SI(b). However, the 2-SI result showed a great improvement by converging towards the reference but still the agreement with the reference solution was poor. When the meshing density was further increased to 2496 triangular patches, i.e. 7488 unknowns, the 2-SI result, shown in Figure 4.20 and

Figure 4.21 by curves 2-SI(c), showed an improvement over the previous results with coarser mesh. The levels of accuracy predicted by the 2-SI results are still different from those of the results in [157], particularly for the region $20^\circ \leq \theta_i \leq 110^\circ$.

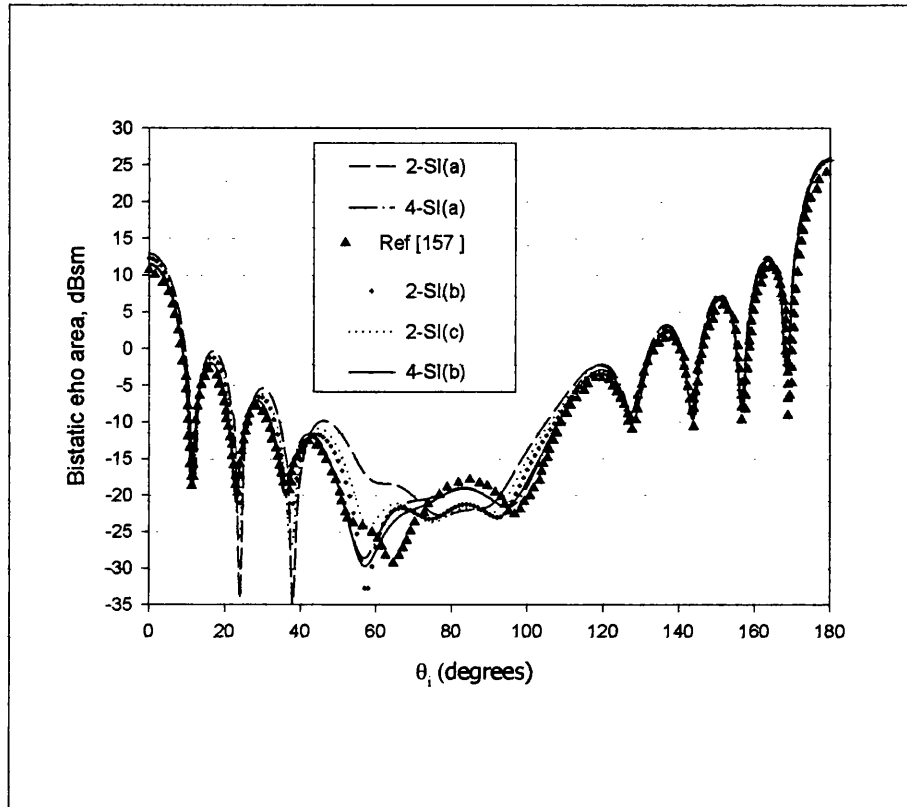


Figure 4.20 Bistatic radar cross-section for the E_θ component for the the scattering by the dielectric box.

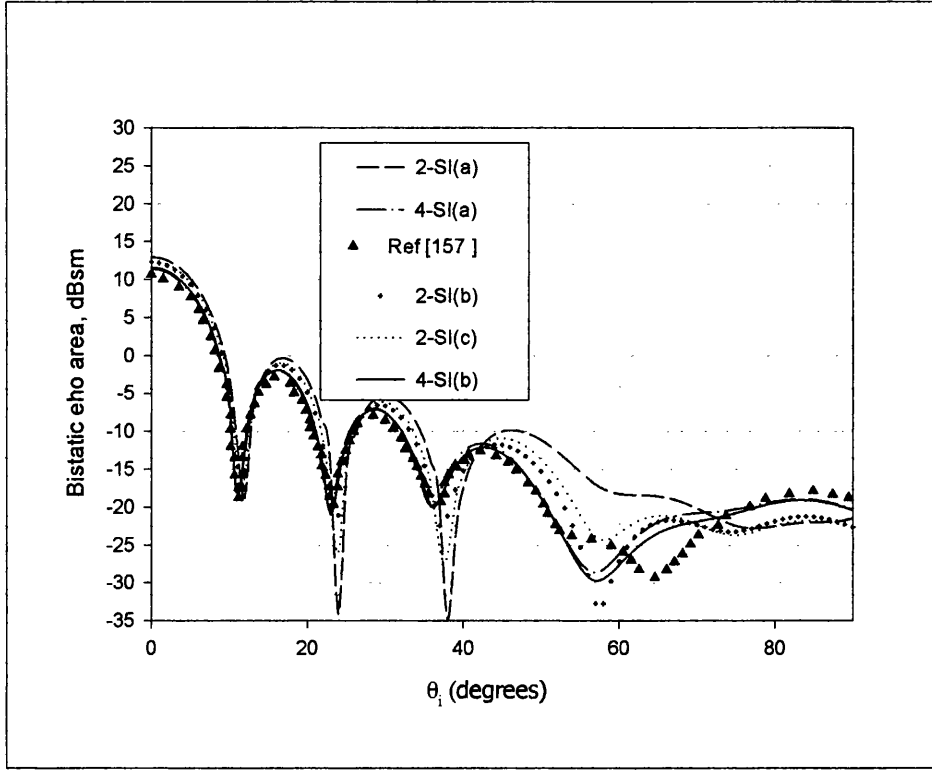


Figure 4.21 Bistatic radar cross-section for the E_θ component shown for

$$0 \leq \theta_i \leq 90^\circ.$$

With more edges such that the maximum patch edge length is of the order of $0.1\lambda_d$, the 2-SI result would eventually compare very well with the reference curve. This would require a mesh with 3350 triangular patches, corresponding to 10050 unknowns. This would certainly result in higher computational costs for the 2-SI formulation over those of the 4-SI formulation shown in Table 4.4. The computational costs for the 2-SI and 4-SI formulations for the results presented in this section are summarised in Table 4.4.

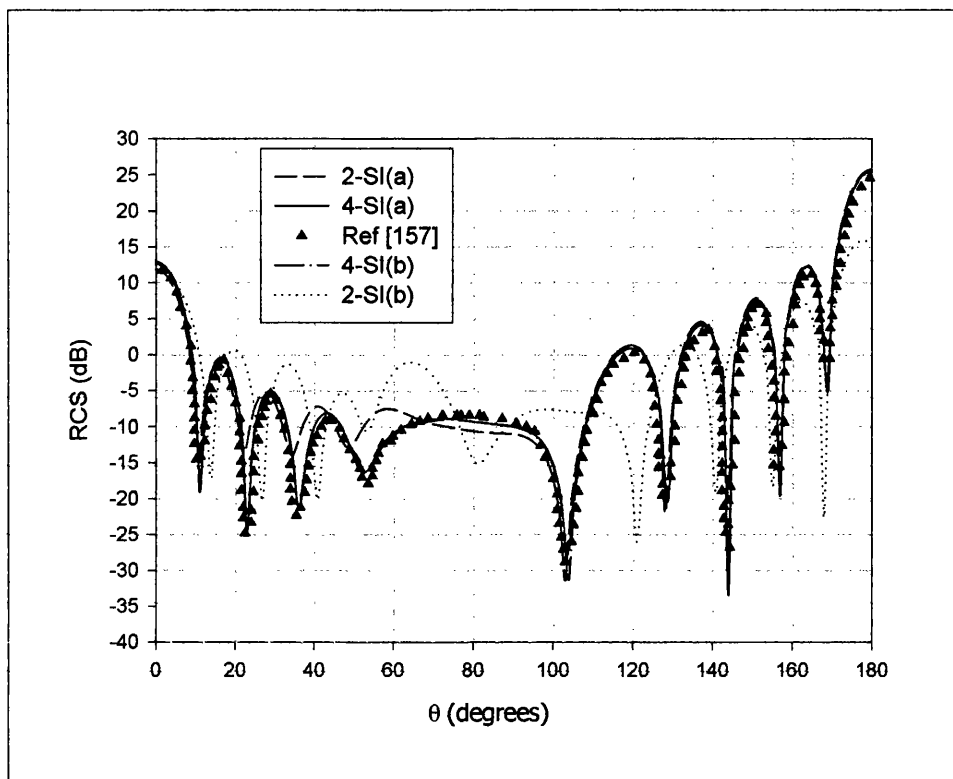


Figure 4.22 Bistatic radar cross-section for the E_ϕ component for the scattering by the dielectric box.

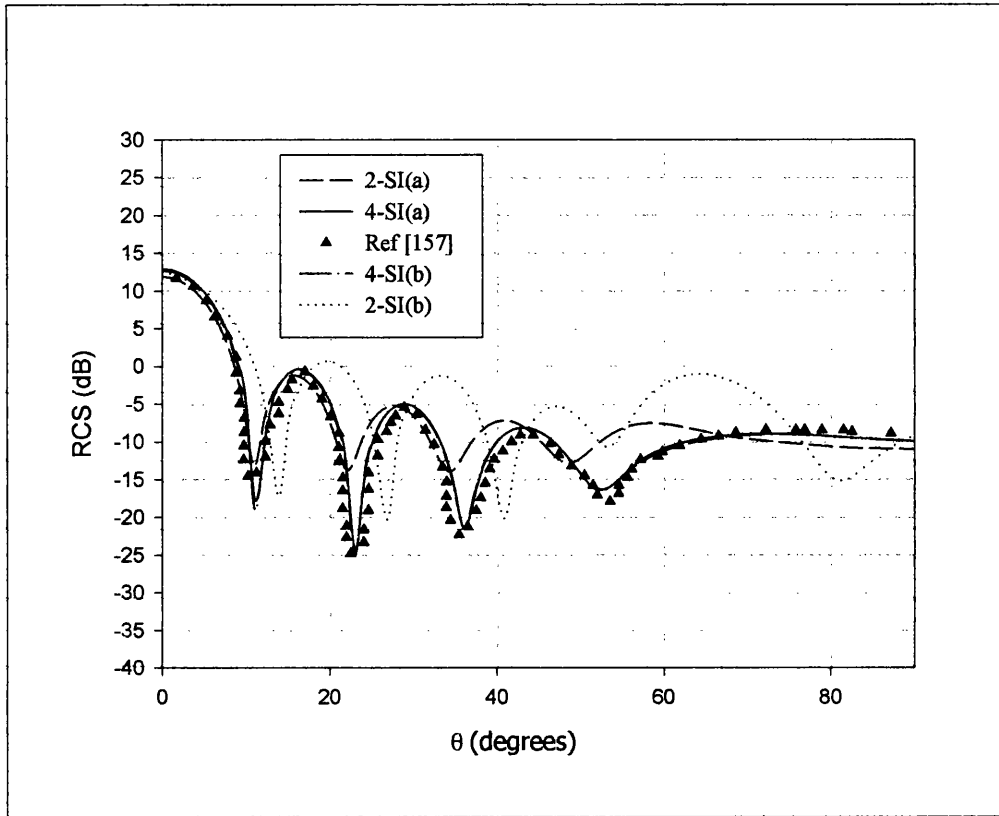


Figure 4.23 Bistatic radar cross-section for the E_θ component shown for $0 \leq \theta_i \leq 90^\circ$.

Table 4.4— Computation costs for the dielectric box in Figure 4.19

| Scheme | Number of triangular patches | Number of unknowns | Maximum edge length (λ_d) | Matrix fill time (sec) | Solve time (sec) | Total computation time (sec) | Memory (MB) |
|---------|------------------------------|--------------------|-------------------------------------|------------------------|------------------|------------------------------|-------------|
| 2-SI(a) | 860 | 2580 | 0.38 | 269.8 | 257.8 | 527.6 | 25.4 |
| 2-SI(b) | 2496 | 7488 | 0.22 | 1976.7 | 10148.90 | 12125.6 | 214 |
| 2-SI(c) | 1608 | 4824 | 0.28 | 835.9 | 1684.8 | 2520.7 | 88.8 |
| 4-SI(a) | 860 | 2580 | 0.38 | 8147.0 | 1212.7 | 9359.7 | 50.8 |
| 4-SI(b) | 1608 | 4824 | 0.28 | 20336.8 | 7212.0 | 27548.8 | 177.5 |

4.3.4 Scattering by a dielectric plate

This section considers the monostatic radar cross section of a $2\lambda_o \times 2\lambda_o$ dielectric slab with a thickness of $0.0254\lambda_o$, $\epsilon_r = 7.4 - j1.11$ and $\mu_r = 1.4 - j0.672$. The dielectric slab could only be meshed with a maximum number of triangular patches of 1596 corresponding to 4799 unknowns. The computing resources limited the maximum number of unknowns to 5000. The results computed using the 2-SI and 4-SI formulations are shown in Figure 4.24 and Figure 4.25 for H-polarisation and E-polarisation cases respectively. The computed results are compared with the results by Shen [159] who used the discrete Fourier transform numerical technique to evaluate the differential-integral arising from the electromagnetic scattering problem. He validated his results with those of Peters and Volakis [160]. As seen in Figure 4.24, there is excellent agreement between the 4-SI results and those of Peters and Volakis for the H-polarisation case. This is despite the fact that the dielectric plate was discretised with 1596 triangles whose maximum edge lengths were $0.4\lambda_d$. This was the smallest possible edge length due to the computer's memory resources. However, this type meshing is too coarse for the 2-SI method as is evident in Figure 4.24.

Figure 4.25 compares the 2-SI, 4-SI and the results in [159] for the E-polarisation case. The comparison is good except for $60^\circ < \theta < 67^\circ$ where there is a large discrepancy between the 4-SI results and those in [159]. Elsewhere, the 4-SI result compares very well with there reference solution and fares better than the 2-SI. The differences in the radar cross-section levels are explained by the fact that the mesh is too coarse. However, the results demonstrate that the 4-SI formulation can still produce accurate results for scattering by dielectric objects with lower levels of discretisations than the 2-SI formulation.

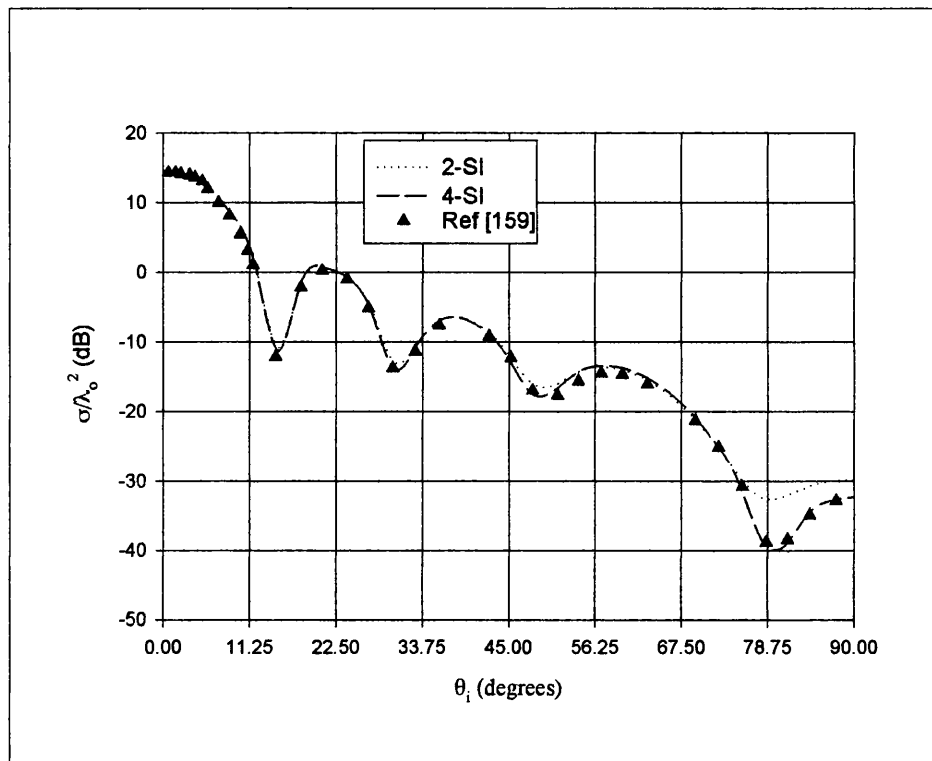


Figure 4.24 Monostatic RCS of a square dielectric slab: H-polarisation

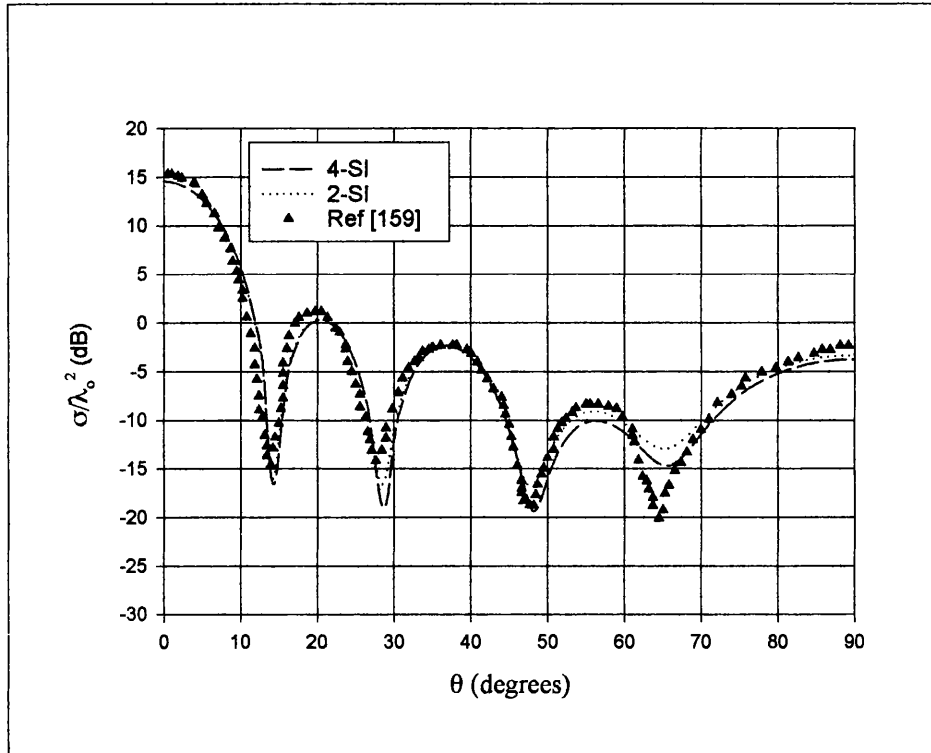


Figure 4.25 Monostatic RCS of a square dielectric slab: E-polarisation

Table 4.5 shows the trend in the computational costs for the dielectric plate problem.

Table 4.5 – Computation costs for the dielectric box in Figure 4.19

| Scheme | Number of triangular patches | Number of unknowns | Maximum edge length (λ_d) | Matrix fill time (sec) | Solve time (sec) | Total computation time (sec) | Memory (MB) |
|--------|------------------------------|--------------------|-------------------------------------|------------------------|------------------|------------------------------|-------------|
| 2-SI | 1596 | 4788 | 0.40 | 807.9 | 3027.00 | 3834.9 | 87.4 |
| 4-SI | 1596 | 4788 | 0.40 | 19395.2 | 8013.8 | 27409.0 | 175 |

However, Table 4.5 cannot be used for a direct comparison between the 2-SI and the 4-SI methods for this particular problem because the “correct”

discretisation was not used for this problem for the 2-SI because of lack of enough computer memory. For an edge resolution in the order of $0.1\lambda_d$, there would be 66240 unknowns. Using symmetry would reduce this to 33120 unknowns, which is a massive problem. This would certainly take far longer than the 4-SI to run and would require massive computer memory space.

The next section presents the last example for electromagnetic scattering by a dielectric disc.

4.3.4 Scattering by a dielectric disc

The last example is a dielectric disc of radius λ_o , thickness of $0.01\lambda_o$, relative permittivity $\epsilon_r = 2.0 - j10.0$ and a relative permeability $\mu_r = 1.0$. The monostatic radar cross-section is computed using the 2-SI and 4-SI methods and the results compared with the results by Peters and Volakis [160].

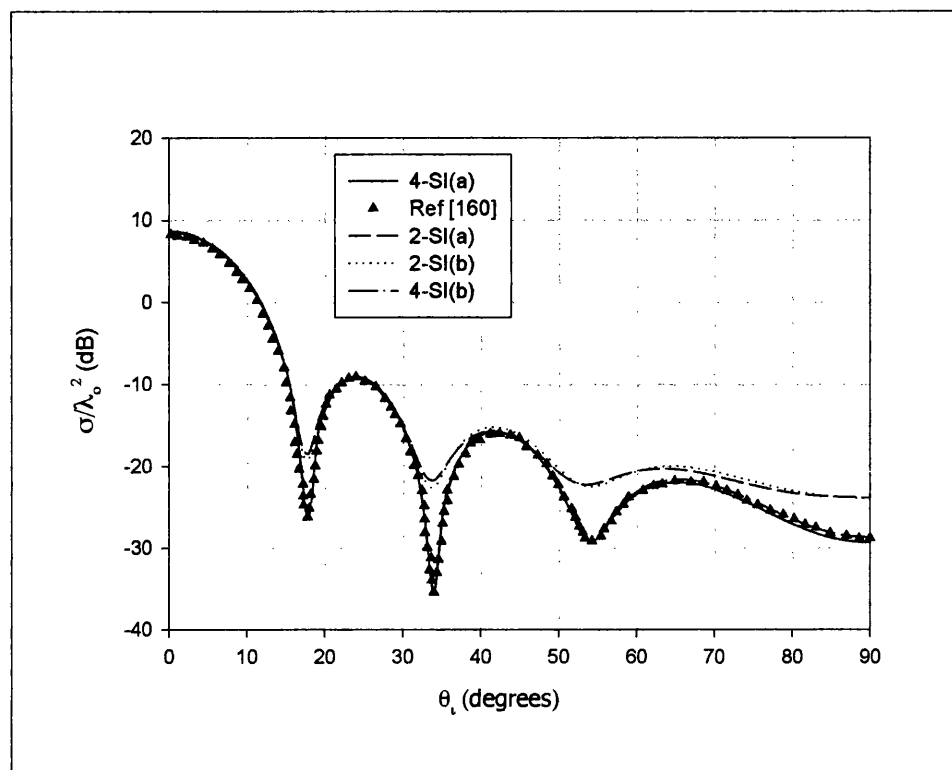


Figure 4.26 Monostatic RCS for a dielectric disc: $\epsilon_r = 2.0 - j10.0$,
thickness = $0.01\lambda_o$ (E-polarisation)

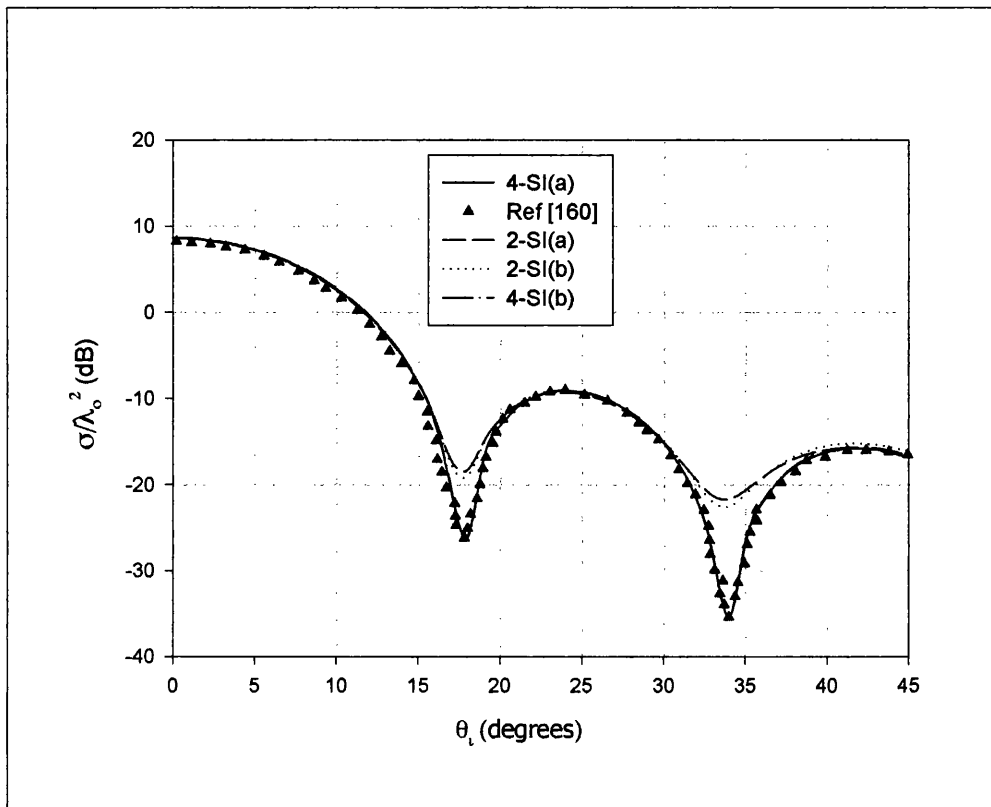


Figure 4.27 Monostatic RCS for a dielectric disc (E-polarisation) for $0 \leq \theta \leq 45^\circ$.

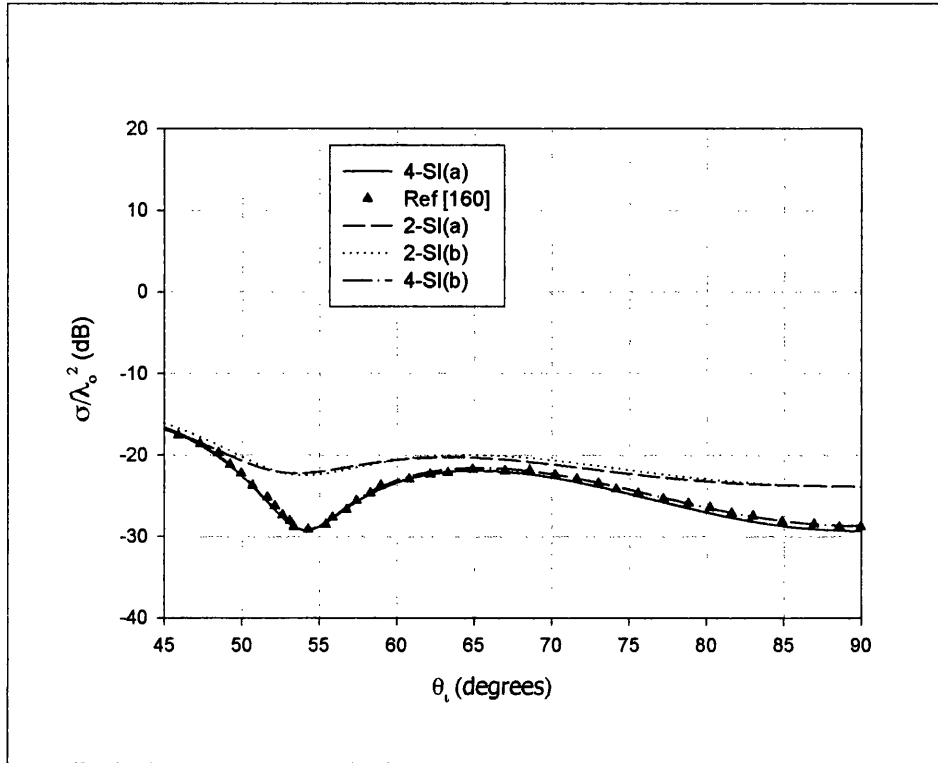


Figure 4.28 Monostatic RCS for a dielectric disc (E-polarisation) for $45^\circ \leq \theta \leq 90^\circ$.

Peters and Volakis solved the integrals in the dielectric scattering problem using the combined conjugate gradient-fast Fourier transform (CG-FFT) method. For the 4-SI method, the dielectric disc is discretised with 1200 triangles and 1632 triangles such that the maximum edge lengths are $0.38\lambda_d$ and $0.32\lambda_d$ respectively. For the E-polarisation case shown in Figure 4.26, Figure 4.27 and Figure 4.28, the 4-SI curve shows excellent agreement with Peters and Volakis' results [160], despite the coarse mesh. For both mesh cases of 1200 triangles and 1632 triangles, the 2-SI results was in agreement with the reference solution for certain values of theta, on a section basis as shown in Figure 4.26, Figure 4.27 and Figure 4.28. Nevertheless, this shows that the 2-SI method fails to produce accurate results for the same number of triangles as for the 4-SI method, if the mesh is coarse.

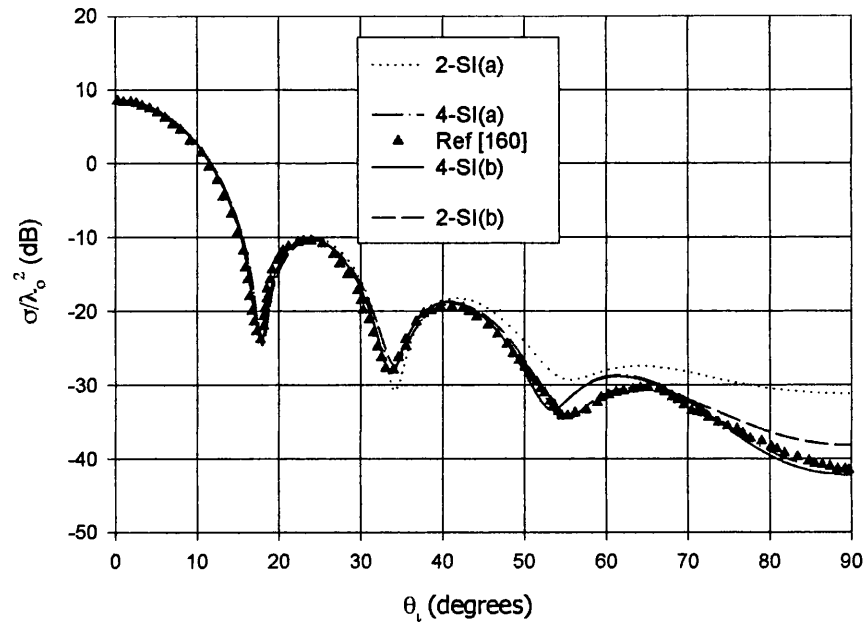


Figure 4.29 Monostatic RCS for a dielectric disc: $\epsilon_r = 2.0 - j10.0$,
thickness = $0.01\lambda_0$ (H-polarisation)

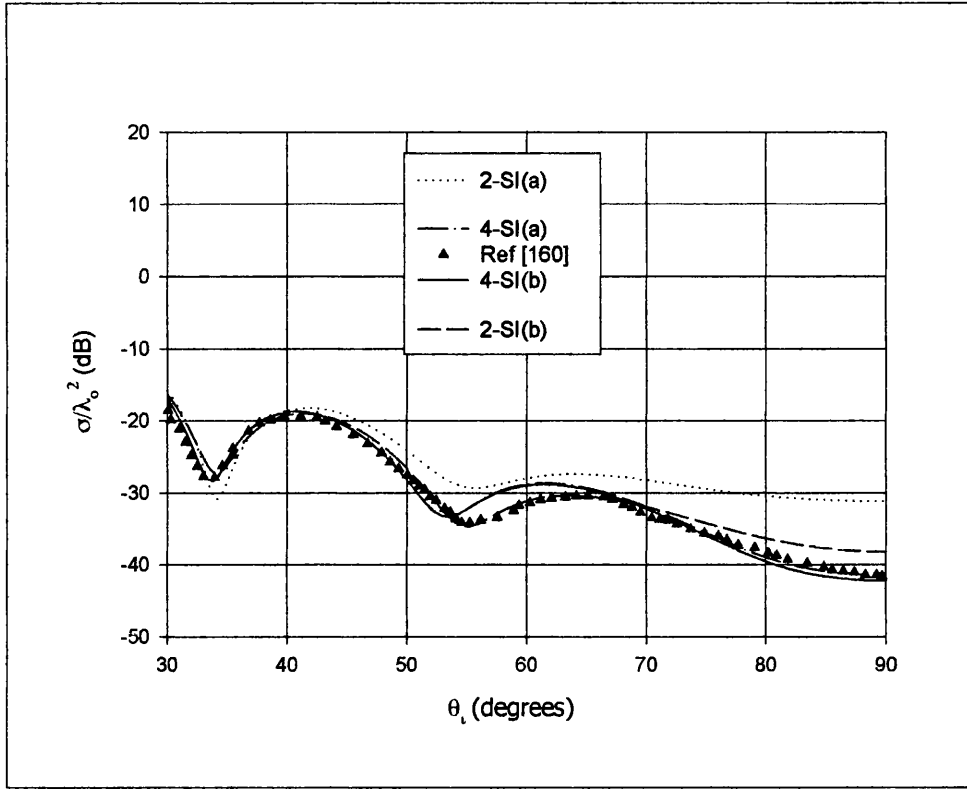


Figure 4.30 Monostatic RCS for a dielectric disc (H-polarisation)
for $30^\circ \leq \theta_i \leq 90^\circ$.

For the H-polarisation case shown in Figure 4.29 and Figure 4.30, the 4-SI results exhibit good agreement with Peters and Volakis' results except when $55^\circ < \theta < 65^\circ$, in which case relatively large discrepancies from the reference solution are observed. However, the two meshes of 1200 and 1632 triangles give almost indistinguishable results. A slight increase in meshing should remove these discrepancies. However, this is not the case with the 2-SI method. A mesh with 1200 triangles (curve 2-SI(a)) exhibits a large deviation from the reference solution whereas for a mesh of 1632 triangles, very good agreement is achieved for theta up to 70° . Thereafter, the agreement between the 2-SI and the reference solution is poor, unlike the results of the 4-SI method. It appears the 2-SI fails to cope when the incidence angle approaches grazing angles. A large

increase in the discretisation of the dielectric disc such that the maximum edge length is of the order $0.1\lambda_d$ would clear these errors. However, this increase in accuracy would come with a very huge computation cost when compared with the 4-SI method.

A comparison of the memory and CPU requirements for this example is shown in Table 4.6.

Table 4.6– Computation costs for the dielectric box in Figure 4.19

| Scheme | Number of triangular patches | Number of unknowns | Maximum edge length (λ_d) | Matrix fill time (sec) | Solve time (sec) | Total computation time (sec) | Memory (MB) |
|---------|------------------------------|--------------------|-------------------------------------|------------------------|------------------|------------------------------|-------------|
| 2-SI(a) | 1200 | 3600 | 0.38 | 486.6 | 820.9 | 1307.5 | 49.4 |
| 2-SI(b) | 1632 | 4896 | 0.32 | 819.0 | 1973.4 | 2792.4 | 91.4 |
| 4-SI(a) | 1200 | 3600 | 0.38 | 7945.7 | 1520.1 | 9465.8 | 100 |
| 4-SI(b) | 1632 | 4896 | 0.32 | 21007.4 | 7635.9 | 28643.3 | 182.9 |

The figures given for the 2-SI method in Table 4.6 are not representative of the actual performance of the 2-SI in tackling this dielectric problem. The mesh is too coarse and the maximum edge length should be of the order of $0.1\lambda_d$. This would require 8040 triangular patches resulting in 24100 unknowns. Computation times and demand for computer memory would therefore exceed those of the 4-SI by several orders of magnitude.

4.4. CONCLUDING REMARKS

The 4-SI formulation of the CFIE for dielectric objects has been presented and implemented. The 4-SI implementation for the CFIE was validated using reference data for dielectric objects of different geometrical shapes. Where the available computer memory allowed, the presented results have shown that the 4-SI formulation is accurate and possesses computational advantages over the 2-SI formulation in calculating the scattered fields by dielectric objects. However, the computational advantages are not as impressive as those obtained for the 4-SI implementation of the EFIE for perfectly conducting objects.

The 4-SI formulation was applied to obtain the radar cross-section for several dielectric objects of different geometrical shapes. The 4-SI formulation results were compared with results calculated using the 2-SI formulation and the results from published material. In some cases, the numerical results for the 4-SI were found to be in good agreement with the results from published material despite the course mesh with maximum triangular patch edges as large as $0.4\lambda_d$. This was achieved with a very reduced value of the number of unknowns for several geometrical dielectric objects' shapes when compared with the 2-SI method. In addition, the CPU time was also reduced significantly despite the evaluation of the computationally time demanding double surface integrals. The accuracy of the 4-SI results was justified by comparing the 4-SI results with analytical solutions and published data for several dielectric objects of different geometrical shapes.

The integral equations and method of moment technique generates a dense impedance matrix with complex valued elements. For the traditional matrix solution, the required computer storage is $\mathcal{O}(N^2)$ and execution time $\mathcal{O}(N^2)$ to

$134\mathcal{O}(N^3)$, where N is the number of triangular surface patches. With the 2-SI method, the required computer storage is $\mathcal{O}(N^2/2)$ because of the matrix folding and only the upper matrix is stored. For large dielectric scatterers N becomes very large. Hence a method that solves a particular problem with a reduced value of N without compromising accuracy is desired. The results that were presented have demonstrated that the 4-SI method is a more efficient method than the 2-SI for solving the electromagnetic scattering problems by electrically large dielectric objects.

From the results presented in section 4.3, the 2-SI's results are not very accurate for monostatic RCS as the incidence angle approaches grazing angles. This is probably because the surface waves are not being modelled properly because of the approximation made in the evaluation of the integral equations. The 4-SI method appears to cope very well with grazing angles of incidence.

The 4-SI CFIE formulation for electromagnetic scattering by homogenous dielectric using the RWG basis functions as both the expansion and testing functions objects. The double surface integrals appearing in the tested CFIE are evaluated more accurately than in the original RWG formulation. This accuracy enables the size of the triangular patches to be larger than in the 2-SI formulation because of the improved averaging process in the calculation of the impedance matrix elements.

CHAPTER 5

FOUR-SI FORMULATION FOR ELECTROMAGNETIC SCATTERING FROM CONDUCTING/DIELECTRIC COMPOSITE OBJECTS

| | |
|--|-----|
| 5.1 Introduction | 163 |
| 5.2. 4-SI Formulation for Composite problems | 165 |
| 5.2.1 Integral Equations | 165 |
| 5.2.2 Testing of the Integral Equations | 167 |
| 5.3 RESULTS | 171 |
| 5.3.1 Scattering by a metallic plate coated with a dielectric | 172 |
| 5.3.2 Scattering by a prism with multiple metallic and dielectric regions | 178 |
| 5.3.3 Scattering by a dielectric disc coated with conducting material at both ends | 181 |
| 5.4 Concluding Remarks | 183 |

5.1 Introduction

This Chapter presents the MoM solution of the CFIE [50] for scattering by three-dimensional dielectric and perfectly conducting objects using the 4-SI formulation. Like in the previous chapters 3 and 4, the scatterers' surfaces are modelled by triangular patches. The RWG basis functions are both used as the expansion and testing functions to convert the EFIE and MFIE into matrix equations.

A number of authors have applied the RWG basis functions in addressing the problem of scattering by composite objects [50,118,120,161,162]. Rao *et al.* [118] used a method based on basis functions defined over triangular patches, which was an extension of the method previously developed for metallic structures [6], for the analysis of conducting bodies coated with lossy materials. Rao *et al.* later extended the method in [6] to handle combined metallic and dielectric structures separated by infinitesimally distances but never touching [50]. Soudais [161] analysed the scattering from arbitrary shaped conducting and dielectric objects using a hybrid boundary integral method/finite element method. Salman and McCowen [120] used the method of moments (and the RWG basis functions) applied to CFIE to determine far-field scattering from resonant size objects comprising dielectric material and perfect electric

conducting surfaces. Kolundzija [162] analysed the scattering by composite objects using a method based on the formulation in [163].

As was observed in chapters 3 and 4, as the size of the scatterer increases, the computational resources required to solve the scattering problem increases. When the problem consists of both the conducting and dielectric materials, the number of unknowns grows very rapidly, thereby restricting the size of the problem that can be analysed. This is so because the dielectric doubles the number of unknowns. The material presented in chapters 3 and 4 for analysing the electromagnetic scattering by perfect electric conductors and dielectrics respectively demonstrated that the 4-SI formulation handles an electrically large scatterer with a fewer number than the conventional 2-SI technique. The decrease in memory requirements and computation time was particularly pronounced for electrically larger scatterers.

This chapter extends the application of the 4-SI method to the electromagnetic scattering from problems having both dielectric and perfect electric conductors. The dielectric and conducting objects may or may not be in contact. As in previous chapters, the conducting and the dielectric structures are both modelled by planar triangular patches and by using a Galerkin procedure with the RWG basis functions, the method of moments is used to solve the combined field integral equation (CFIE).

The composite objects comprising the dielectric and the conducting objects can take various configurations: it can consist of conductive body coated with a thin layer of dielectric material or a dielectric body partially coated with a thin layer of conducting material, a combination of both or three dimensional dielectric and conducting objects in contact. The problem of electromagnetic scattering from composite problems has been analysed by several authors [50,162,164,165,166].

A formulation to the scattering problem in terms of the equivalent dielectric and magnetic currents on the surface of the dielectric scatterer and equivalent electric currents on the surface of the conducting scatterer is used, leading to surface integral equations which are solved using the method of moments. The RWG formulation for mixed dielectric and conductor problems was reviewed in chapter 2.

The 4-SI formulation is applied to the investigation of scattering from composite materials and the results compared with published data. This chapter is organised as follows. In the next section, the 4-SI formulation for composite materials is presented. The numerical results are presented in section 5.3 and section 5.4 presents the concluding remarks for the chapter.

5.2. 4-SI Formulation for Composite problems

5.2.1 Integral Equations

The derivation of the RWG formulation for mixed problems, i.e. consisting of dielectric and conductors, was reviewed in section 2.7. For the purpose of deriving the equations for the 4-SI formulation, the starting points are the equations (2.85) – (2.87). They are repeated here for the sake of continuity.

$$\mathbf{E}_{\text{tan}}^{\text{inc}} = -\left[\mathbf{E}^s(\mathbf{J}_c) + \mathbf{E}^s(\mathbf{J}_d, \mathbf{M}_d)\right]_{\text{tan}} \quad \text{on } S_c \quad (5.1)$$

$$\mathbf{E}_{\text{tan}}^{\text{inc}} = -[\mathbf{E}^s(\mathbf{J}_c) + \mathbf{E}^s(\mathbf{J}_d, \mathbf{M}_d)]_{\text{tan}} \quad \text{on } S_d \quad (5.2)$$

$$\mathbf{H}_{\text{tan}}^{\text{inc}} = -[\mathbf{H}^s(\mathbf{J}_c) + \mathbf{H}^s(\mathbf{J}_d, \mathbf{M}_d)]_{\text{tan}} \quad \text{on } S_d \quad (5.3)$$

The electric and magnetic surface currents produce the electric and magnetic fields which radiate into the unbounded medium. These fields are given by

$$\mathbf{E}^s(\mathbf{r}) = -j\omega\mathbf{A}(\mathbf{r}) - \nabla\Phi - \frac{1}{\varepsilon}\nabla \times \mathbf{F}(\mathbf{r}) \quad (5.4)$$

$$\mathbf{H}^s(\mathbf{r}) = -j\omega\mathbf{F}(\mathbf{r}) - \nabla\Psi + \frac{1}{\mu}\nabla \times \mathbf{A}(\mathbf{r}) \quad (5.5)$$

where the magnetic vector potential, \mathbf{A} , the electric vector potential, \mathbf{F} , the electric scalar potential, Φ , and the magnetic scalar potential, Ψ , are given by equations (2.18), (2.19), (2.20) and (2.21) respectively.

Substituting (5.4) and (5.5) into (5.1), (5.2) and (5.3) and making use of equations (2.18), (2.19), (2.20) and (2.21) yields

$$j\omega [\mathbf{A}_e(\mathbf{J}_c) + \mathbf{A}_e(\mathbf{J}_d)] + [\nabla\phi_e(\rho_c^e) + \nabla\phi_e(\rho_d^e)] \quad (5.6)$$

$$+ \frac{1}{\epsilon_e} \nabla \times \mathbf{F}_e(\mathbf{M}_d) = \mathbf{E}_{\tan}^{inc} \quad \text{on } S_c$$

$$j\omega \mathbf{A}_e(\mathbf{J}_c) + \nabla\phi_e(\rho_c^e) + j\omega [\mathbf{A}_e(\mathbf{J}_d) + \mathbf{A}_i(\mathbf{J}_d)] + \quad (5.7)$$

$$[\nabla\phi_e(\rho_d^e) + \nabla\phi_i(\rho_d^e)] + \nabla \times \left[\frac{\mathbf{F}_e(\mathbf{M}_d)}{\epsilon_e} + \frac{\mathbf{F}_i(\mathbf{M}_d)}{\epsilon_i} \right] = \mathbf{E}_{\tan}^{inc} \quad \text{on } S_c$$

$$- \frac{1}{\mu_e} \nabla \times \mathbf{A}_e(\mathbf{J}_c) + j\omega [\mathbf{F}_e(\mathbf{M}_d) + \mathbf{F}_i(\mathbf{M}_d)] + \quad (5.8)$$

$$[\nabla\Psi_e(\rho_d^m) + \nabla\Psi_i(\rho_d^m)] - \nabla \times \left[\frac{\mathbf{A}_e(\mathbf{J}_d)}{\mu_e} + \frac{\mathbf{A}_i(\mathbf{J}_d)}{\mu_i} \right] = \mathbf{H}_{\tan}^{inc} \quad \text{on } S_d$$

where ρ_c^e , ρ_d^e and ρ_d^m represent the surface charge densities associated with the current densities \mathbf{J}_c , \mathbf{J}_d , \mathbf{M}_d respectively.

The subscripts on the field quantities represent the unbounded medium in which the sources radiate, e for external and i for internal. The bracketed currents for the field quantities represent the source of that field.

5.2.2 Testing of the Integral Equations

The integral equations (5.6) - (5.8) are solved numerically using the method of moments [5]. The unknown electric current density, \mathbf{J}_c and the unknown dielectric current density, \mathbf{J}_d flowing on the surfaces of the conductor and the

dielectric respectively and the unknown magnetic current density \mathbf{M}_d on the dielectric's surface are expanded using the RWG basis functions such that:

$$\mathbf{J}_c = \sum_{n=1}^{N_c} \alpha_n \mathbf{f}_n \quad (5.9)$$

$$\mathbf{J}_d = \sum_{n=1}^{N_d} \beta_n \mathbf{f}_n \quad (5.10)$$

$$\mathbf{M}_d = \sum_{n=1}^{N_d} \gamma_n \mathbf{f}_n \quad (5.11)$$

where α_n , β_n and γ_n are the unknown current expansion coefficients to be determined using the method of moments and are for the electric, dielectric and magnetic currents respectively. N_c and N_d are the number of non-boundary edges on the electric conductor and dielectric respectively.

To solve for the unknown current coefficients, the equations (5.6) - (5.8) are tested using the RWG basis functions and reduced to a set of $(N_c + 2N_d) \times (N_c + 2N_d)$ linear algebraic equations which can be written in matrix form as:

$$\begin{bmatrix} \begin{bmatrix} Z^{J_c J_c} \end{bmatrix} & \begin{bmatrix} Z^{J_c J_d} \end{bmatrix} & \begin{bmatrix} Z^{J_c M_d} \end{bmatrix} \\ \begin{bmatrix} Z^{J_d J_c} \end{bmatrix} & \begin{bmatrix} Z^{J_d J_d} \end{bmatrix} & \begin{bmatrix} Z^{J_d M_d} \end{bmatrix} \\ \begin{bmatrix} Z^{M_d J_c} \end{bmatrix} & \begin{bmatrix} Z^{M_d J_d} \end{bmatrix} & \begin{bmatrix} Z^{M_d M_d} \end{bmatrix} \end{bmatrix} \begin{bmatrix} \begin{bmatrix} \alpha_n \end{bmatrix} \\ \begin{bmatrix} \beta_n \end{bmatrix} \\ \begin{bmatrix} \gamma_n \end{bmatrix} \end{bmatrix} = \begin{bmatrix} \begin{bmatrix} E_c^{inc} \end{bmatrix} \\ \begin{bmatrix} E_d^{inc} \end{bmatrix} \\ \begin{bmatrix} H_d^{inc} \end{bmatrix} \end{bmatrix} \quad (5.12)$$

where $(N_c + 2N_d)$ is the total number of unknowns.

E_c^{inc} and E_d^{inc} are the voltages due to the incident electric fields on the conductor and dielectric surfaces respectively and H_d^{inc} is the magnetic field incident on the dielectric surface.

The impedance matrix is shown in (5.12) partitioned into nine sub matrices. For each sub matrix, the first superscript indicates that the observation edge m is on a conducting surface, if the first superscript is J_c or on a dielectric surface if the first superscript is J_d or M_d . The second superscript denotes the location of the source point.

Sub matrix $Z^{J_c J_c}$ is an $N_c \times N_c$ matrix and its elements are given by equation (4.27), noting that there is only one region, i.e. the perfect electric conductor. This expression is the same as the impedance for a perfect electric conductor treated in chapter 3.

The sub matrix $Z^{J_c J_d}$ is an $N_c \times N_d$ matrix and its elements are also given by equation (4.27). The elements result from the testing with f_m of the electric field on the surface of an electric conductor produced by the dielectric current on the dielectric. The source points are on the dielectric and the correct constitutive parameters of the dielectric object are

inserted in equation (4.27).

The submatrix $Z^{J_c M_d}$ is an $N_c \times N_d$ matrix and its elements $Z^{J_c M_d}(m, n)$ are given in equation (4.29). It is the result of the testing with \mathbf{f}_m of the electric field on the electric conductor's surface produced by a magnetic current on the surface of the dielectric.

The sub matrix $Z^{J_d J_c}$ is an $N_d \times N_c$ matrix. The element $Z^{J_d J_c}(m, n)$ is equal to the testing of the electric field on the dielectric's surface produced by a surface current on the surface of the electric conductor. The expression for element $Z^{J_d J_c}(m, n)$ is given by equation (4.27) with the correct constitutive parameters for inserted for each region.

The sub matrix $Z^{J_d J_d}$ is an $N_d \times N_d$ and its elements are given by (4.27). The observation and source points are all on the dielectric materials. The sub matrix $Z^{J_d M_d}$ is an $N_d \times N_d$ and its elements are also given by (4.27) but this time the tested fields are due to the magnetic current on the surface of the dielectric. The observation and source points are all on the dielectric materials.

An element of the $N_d \times N_c$ sub matrix $Z^{M_d J_c}$ is equal the negative of that of $Z^{J_c M_d}$.

The elements of the $N_d \times N_d$ sub matrix $Z^{M_d J_d}$ are given by (4.30).

Lastly, the elements of the $N_d \times N_d$ sub matrix $Z^{M_d M_d}$ are given by (4.28).

The 4-SI evaluation of the elements of the sub matrices in (5.12) has been presented in detail in Chapters 3 and 4 and hence will not be repeated here. The

strategy of the computation is the accurate evaluation of the double surface integrals appearing the sub matrices for closely coupled observation and source triangular patches. For loosely coupled triangular patches, an evaluation of the elements is done in a manner identical to the RWG formulation.

Once the matrix equation (5.12) is solved for the unknown current coefficients, any other parameters of interest such the radar cross-section can easily be calculated.

The potential integrals in the evaluation of the impedance elements have a singularity of the order of $(1/R^3)$ when the dielectric is in contact with the perfect electric conductor. The calculation of the singular terms follows the analytical approach developed in [167].

5.3 RESULTS

The modified CFIE formulation is applied to scattering of electromagnetic by mixed objects comprising conducting and dielectric objects. The RCS results computed using the 4-SI formulation developed in Chapters 3 and 4 but applied to mixed objects are presented. These results are compared with those based on the 2-SI formulation and published material. Three examples will be considered in the following sections.

5.3.1 Scattering by a metallic plate coated with a dielectric

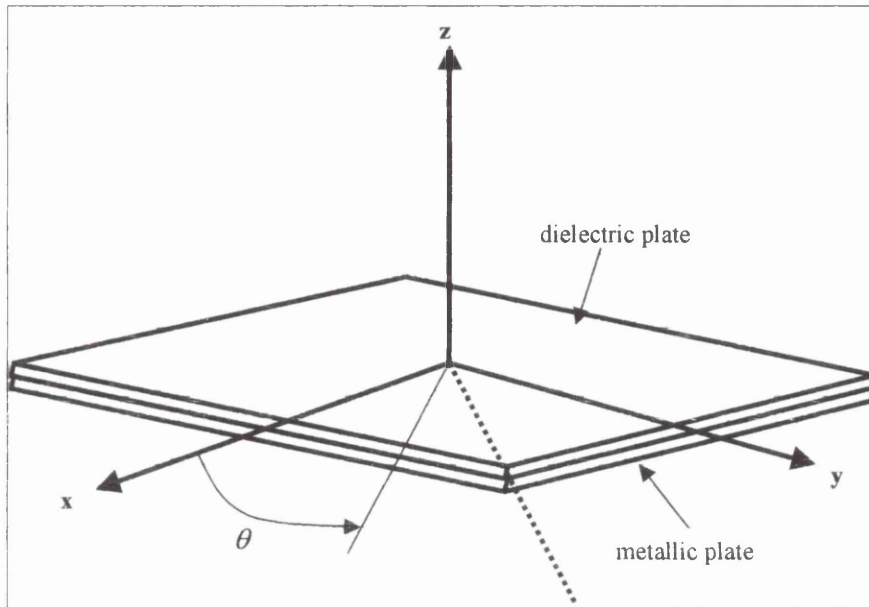


Figure 5.1 Perfectly conducting plate coated at the top with a dielectric

Figure 5.1 shows a perfectly conducting plate with dimensions $20 \times 20 \times 1$ cm, coated on one side with a dielectric. The dielectric material with $\epsilon_r = 3.15 - 0.1j$ and $\mu_r = 1.0$, is 3 mm thick. The frequency is 3.2 GHz. The monostatic RCS of the coated conducting plate is studied at grazing incidence for two polarisation cases, the $\theta\theta$ -polarisation and the $\phi\phi$ -polarisation.

The grazing incidence makes it a difficult problem because of the generation of surface waves that must be modelled properly. The total scattering is a combination of the scattering from the edges, corners and the junction between the conducting and dielectric materials.

The monostatic RCS results generated using the 2-SI and of 4-SI schemes are compared with the results of Soudais *et al.* [168] in Figure 5.2 - Figure 5.5. Soudais *et al.* [168] modelled the electromagnetic scattering from the composite dielectric and conducting structure by hybrid partial differential equation - integral equation formulations. Their method entailed solving for both surface and volume unknowns for the exterior and interior regions of the structure.

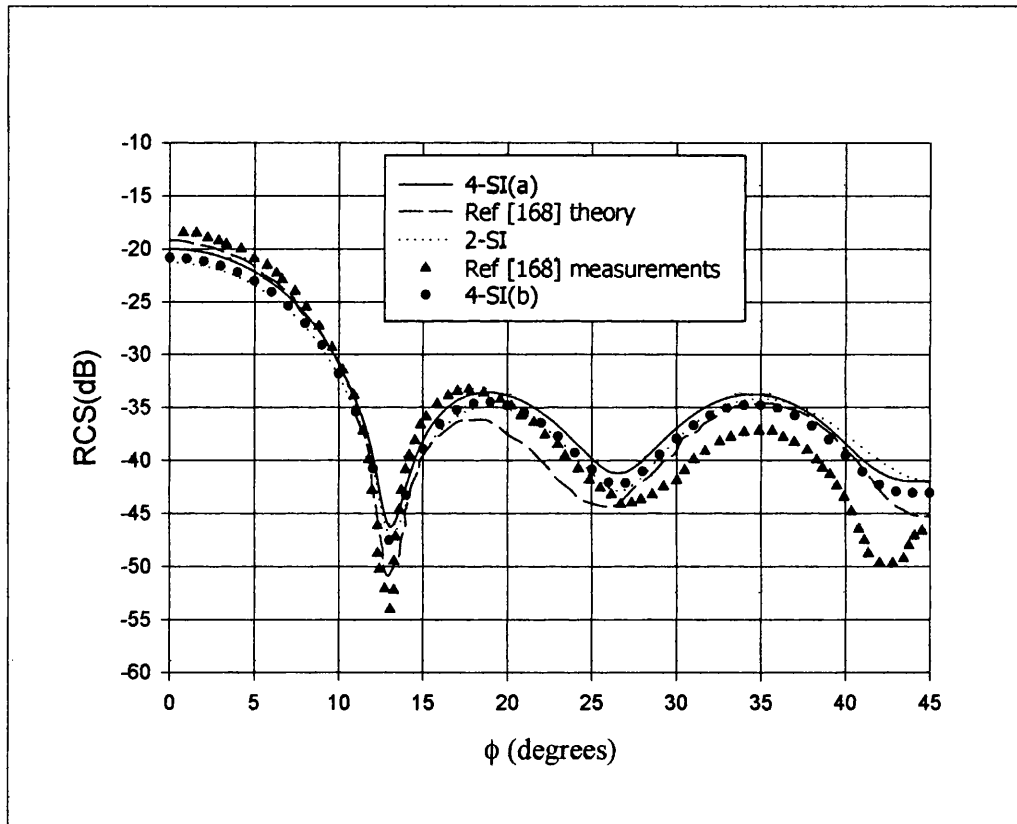


Figure 5.2 Comparison of the monostatic RCS of a conducting plate of size $20 \times 20 \times 1$ cm coated on one side with a dielectric. Grazing incidence at 3.2 GHz, $\phi\phi$ polarisation.

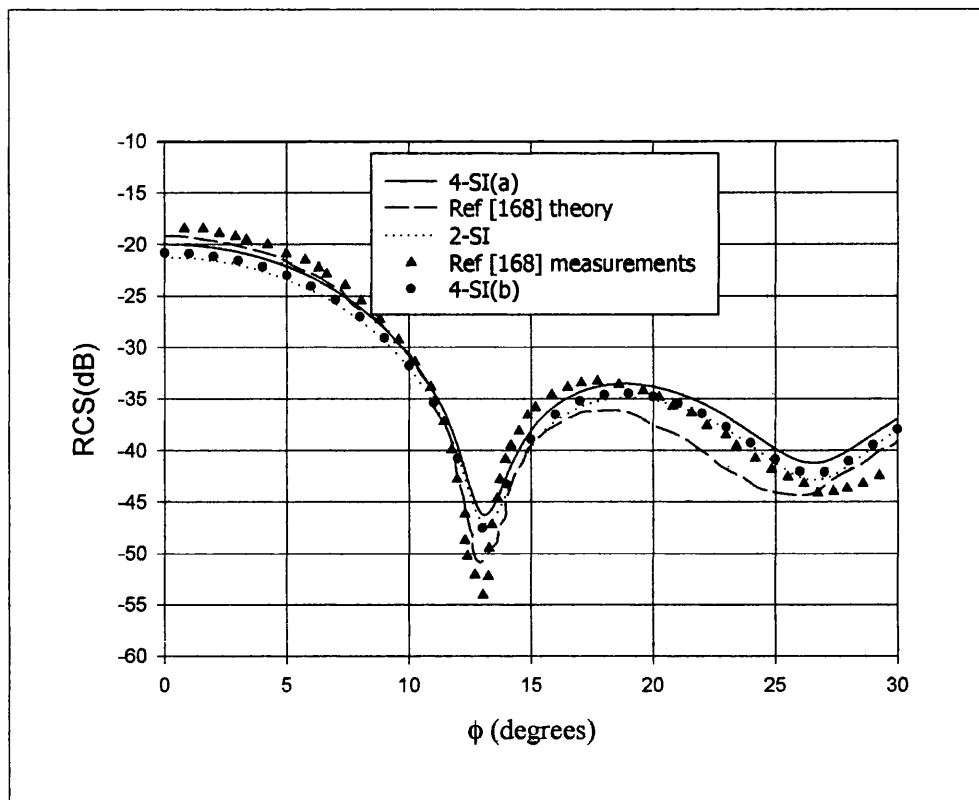


Figure 5.3 Monostatic RCS in Figure 5.2 shown with θ up to 30° to highlight the differences in the results. Grazing incidence, 3.2 GHz, $\phi\phi$ polarisation.

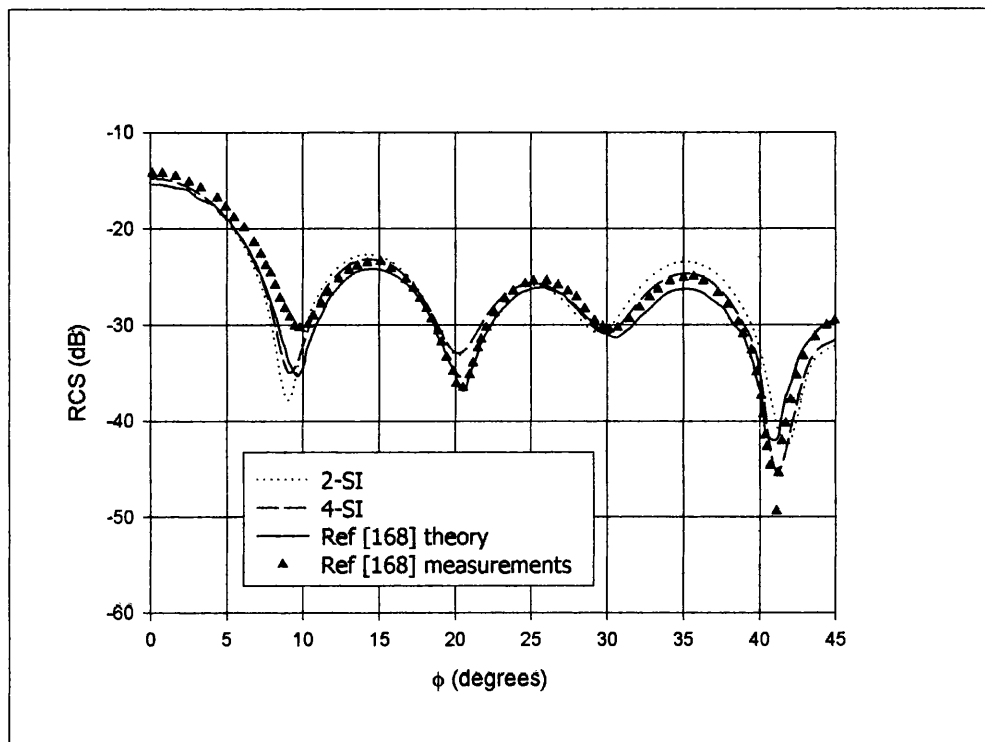


Figure 5.4 Comparison of the monostatic RCS of a conducting plate of size 20 x 20 x 1 cm coated with a dielectric layer of thickness 3 mm. Grazing incidence, 3.2 GHz, $\theta\theta$ polarisation.

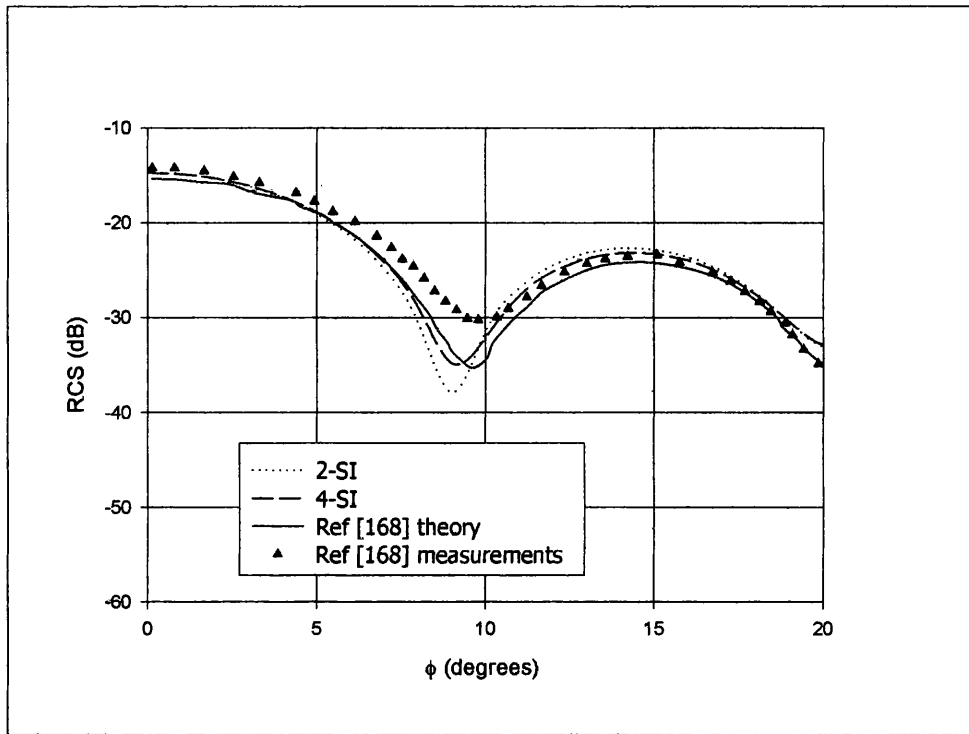


Figure 5.5 The monostatic RCS in Figure 5.2 shown with θ up to 20° to highlight the differences in the results. Grazing incidence, 3.2 GHz, $\theta\theta$ polarisation.

Table 5.1 Computation costs for the coated conducting plate for $\phi\phi$ -polarisation and the $\theta\theta$ -polarisation.

| Scheme | Number of pec patches | Number of dielectric patches | Total Number of unknowns | Maximum edge length (λ_o, λ_d) | Matrix fill time (sec) | Solve time (sec) | Total computation time (sec) | Memory (MB) |
|----------|-----------------------|------------------------------|--------------------------|--|------------------------|------------------|------------------------------|-------------|
| 2-SI | 1020 | 1020 | 4590 | 0.20,0.36 | 2570 | 3585 | 6175 | 80.4 |
| 4-SI(a) | 1020 | 1020 | 4590 | 0.20,0.36 | 17853.7 | 6861 | 24714.7 | 160.7 |
| 4-SI(b)* | 1932 | 1932 | 8694 | 0.14,0.25 | 13508.7 | 5372 | 18880.7 | 576.7 |

* results modelled on a different pc

For the monostatic RCS results for the $\phi\phi$ -polarisation, the results are shown in Figure 5.2 and Figure 5.3, (Figure 5.3 shows the same results as in Figure 5.2,

but for only for $0^\circ \leq \phi \leq 30^\circ$). Both the 2-SI and 4-SI results are better than the theoretical results in [168], assuming that the measurements are more accurate than the calculated results. However, in all cases, the measurement results differ significantly from the calculated results save for the region $0^\circ \leq \phi \leq 15^\circ$, where the contribution from the scattering by the corners of the structure is not very significant. Significant differences appear between the calculated results and the measurement results for ϕ greater than 15° , where the scattering by the corners is important. Of particular concern is the little difference between the 4-SI(a) and 4-S(b) results and the 2-SI results. The corresponding meshing and computation times are shown in Table 5.1. The 4-SI(a) and 2-SI results have the same and the dielectric material is very undermeshed. It was expected that the 4-SI method would produce better results than the 2-SI method, as was the case in Chapter 3 with scattering by perfectly conducting materials. It appears that scattering from the edges is not being modelled properly. When the meshing density is nearly doubled, the 4-SI method results, shown by curve 4-SI(b), are almost the same as the 2-SI method with nearly half the meshing density.

For the case of $\theta\theta$ -polarisation, the results are shown in Figure 5.4 and Figure 5.5. Figure 5.4 shows the results for $0^\circ \leq \phi \leq 45^\circ$ and Figure 5.5 shows the results for $0^\circ \leq \phi \leq 20^\circ$, to highlight the differences between the results. The mesh and computation times for the 2-SI and 4-SI methods in Figure 5.4 and Figure 5.5 are the same as those shown for 2-SI and 4-SI(a) in Table 5.1. Using the measurement results as reference for the case of $\theta\theta$ -polarisation in [168], the 4-SI results compare very well with the theoretical results in [168] apart from the small region around $\phi = 20^\circ$. The 2-SI results differ significantly from the measurement and theoretical results in [168] in certain regions. The number of unknowns for this problem was limited to 4590 for both the 2-SI and 4-SI formulations. Soudais *et. al* [168] used 9175 surface unknowns and 15 079

volume unknowns. This difference in the number of unknowns partly explains the difference between the 2-SI, 4-SI and the results in [168]. The comparison between the computational requirements for the 2-SI and 4-SI is difficult to make considering the very coarse mesh used for the dielectric.

5.3.2 Scattering by a prism with multiple metallic and dielectric regions

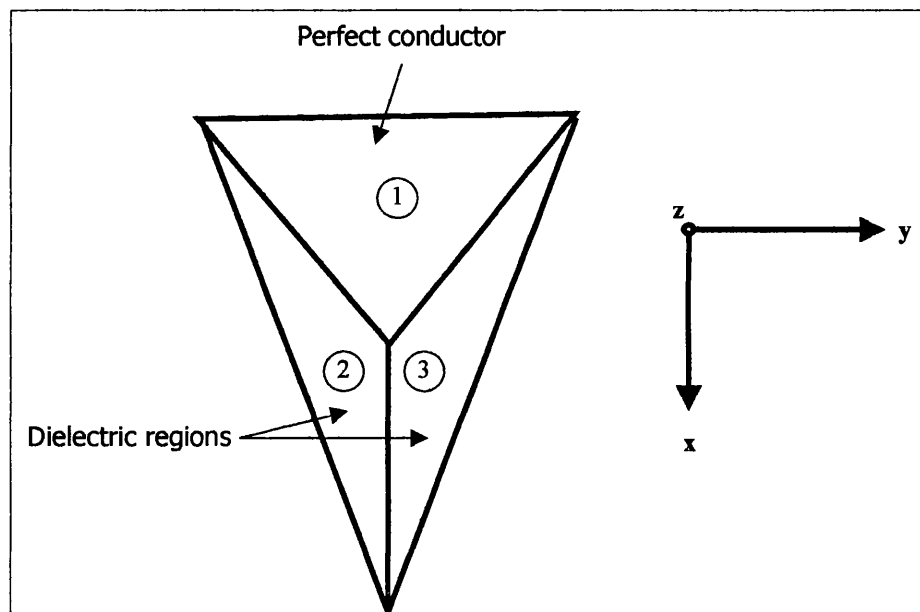


Figure 5.6 Cross-section of the prism with one metallic and two dielectric regions.

The result presented in this section consists of a prism comprising a metallic and two dielectric regions. This structure is important due to the presence of two

junctions formed by the metallic region and the two dielectric regions. The cross-section of prism in the x-y plane, shown in Figure 5.6, is an isosceles triangle whose medians divide it into three regions of different constitutive parameters. The length of the two equal triangle sides is λ_0 , the angle between them is 40° and the height of the prism is λ_0 , where λ_0 is the free space wavelength. The constitutive parameters of the two dielectric regions are: $\epsilon_{r1} = 1.4 - j0.7$, $\mu_{r1} = 1$, $\epsilon_{r2} = 4.0 - j0.3$ and $\mu_{r1} = 1.2 - j0.6$. The subscripts 1 and 2 denote the position of the dielectric region as shown in Figure 5.6. The prism is excited by a plane wave such that the electric field vector is given by $\mathbf{E}_i = e^{j\beta_0(x\cos\phi + y\sin\phi)}\mathbf{i}_z$ V/m.

Figure 5.7 shows the monostatic RCS normalized by wavelength squared in decibels versus angle phi. The 2-SI and 4-SI results are compared with those obtained by Soudais [161] using a finite element method. Kolundzija [162] later analysed the same problem using a general method based on the PMCHW formulation [163] for analysis of scattering by arbitrary composite metallic and dielectric structures., and obtained good comparison with the results in [168].

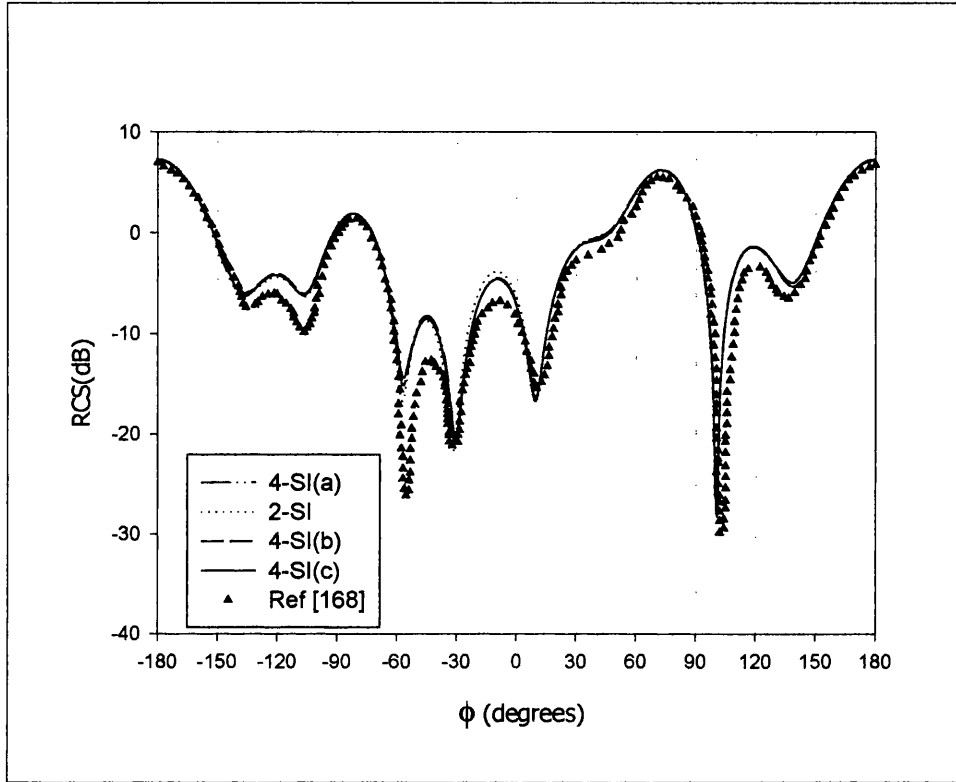


Figure 5.7 Monostatic RCS of a 3-D prism with conducting and dielectric regions in contact.

The prism scattering problem was analysed using the meshing data shown in Table 5.2. It is seen in Figure 5.7 that the results obtained by the both the 2-SI and 4-SI methods appear to have converged. Apart from slight variations, all the 4-SI results are almost coincident, despite the fact the number of unknowns ranges from 3357 to 9570. The 2-SI results, with 3357 unknowns, practically coincides with the 4-SI result generated with 9570 unknowns.

Although the general shapes of the graphs for the 2-SI and 4-SI methods is the same as that of the reference solution, the comparison is not good except when the electromagnetic wave is incident on the conducting side of the prism.

Table 5.2 Computation costs for the composite prism in Figure 5.6

| Scheme | Number of pec patches | Number of dielectric patches | Total Number of unknowns | Maximum edge length (λ_d) | Matrix fill time (sec) | Solve time (sec) | Total computation time (sec) | Memory (MB) |
|----------|-----------------------|------------------------------|--------------------------|-------------------------------------|------------------------|------------------|------------------------------|-------------|
| 2-SI | 350 | 944 | 3357 | 0.28 | 1125 | 1005 | 2130 | 43 |
| 4-SI(a)* | 1100 | 2640 | 9570 | 0.14 | 12437 | 6099 | 18536 | 699 |
| 4-SI(b) | 350 | 944 | 3357 | 0.28 | 12134 | 3878 | 16012 | 86 |
| 4-SI(c) | 612 | 1940 | 6738 | 0.19 | 7826 | 2249 | 10075 | 347 |

*results generated with a PC with higher specifications

The next example is on the electromagnetic scattering by a dielectric disk coated with a conducting material at both ends.

5.3.3 Scattering by a dielectric disk coated with conducting material at both ends

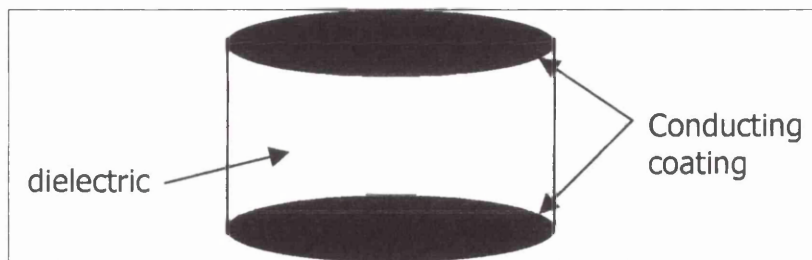


Figure 5.8 Geometry for dielectric disk for which $ka = 6.37, h = 0.4a$, coated with a conducting material at both ends.

Figure 5.8 shows the geometry for a dielectric disk with $ka = 6.37$, height $h = 0.4a$ and $\epsilon_r = 3.17$. The dielectric disk is coated on both ends only. The results for the 2-SI and 4-SI formulations are compared in Figure 5.9 with measurements and calculated results in [166]. The theoretical results in [166] were calculated using a numerical scheme based on surface integral equations solved using the method of moments. This numerical scheme can only be applied to objects with circumferential symmetry.

It is observed in Figure 5.9 that the comparison of the both the 2-SI and the 4-SI results and the reference solutions in [166] is not good.

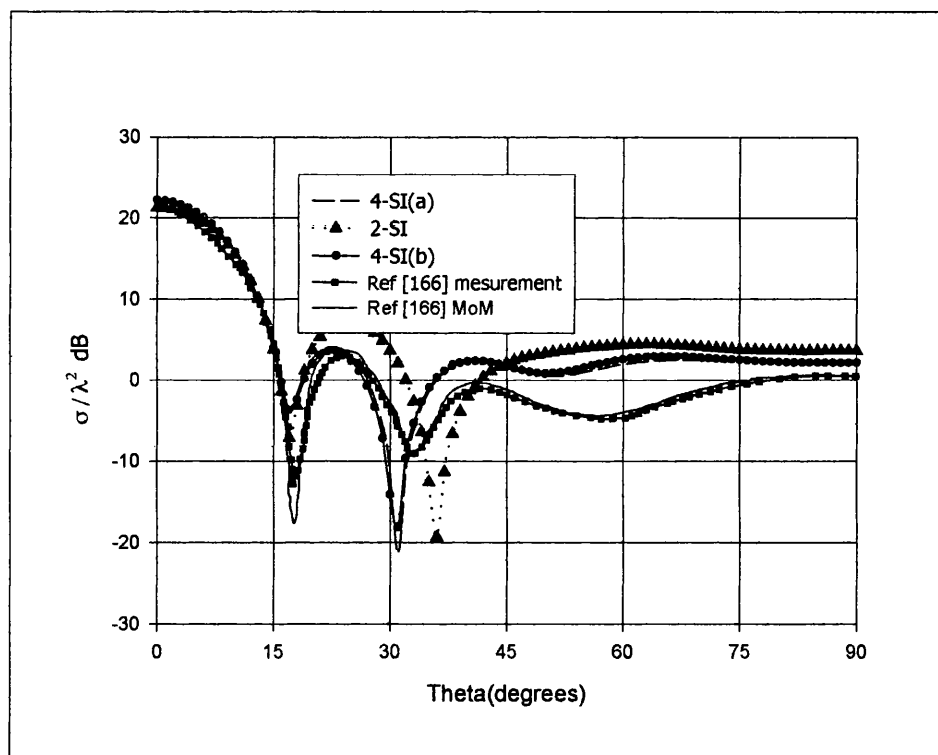


Figure 5.9 Monostatic RCS for a dielectric disk coated with a conducting film at both ends.

However, although the general shape for the 4-SI graphs are almost similar to the reference solutions. This discrepancy is attributed to the very coarse mesh used, particularly for the dielectric medium, as shown in Table 5.3. There is no mention of the number of unknowns used in [166]. The computing resources limited the number of unknowns used that could be used.

Table 5.3 Computation costs for the metallic coated dielectric disk

| Scheme | Number of pec patches | Number of dielectric patches | Total Number of unknowns | Maximum edge lengths λ_d, λ_o | Matrix fill time (sec) | Solve time (sec) | Total computation time (sec) | Memory (MB) |
|----------|-----------------------|------------------------------|--------------------------|---|------------------------|------------------|------------------------------|-------------|
| 2-SI | 840 | 1240 | 4940 | 0.32 0.184 | 2664 | 4942 | 7606 | 93 |
| 4-SI(a) | 840 | 1240 | 4940 | 0.32 0.184 | 15137 | 5648 | 20785 | 186 |
| 4-SI(b)* | 1580 | 2380 | 9284 | 0.25 0.14 | 11137 | 5044 | 16181 | 657.59 |

The results for plot 4-SI(b) shown with an asterisk in Table 5.3 were generated on a faster computer.

5.4 Concluding Remarks

A 4-SI formulation has been presented to solve the CFIE for the electromagnetic scattering problem by mixed objects of arbitrary shapes. The procedure is based on the method of moments solution technique and the surfaces of the conductors and the dielectric surfaces are modelled by planar triangular patches. In all the examples presented in this section, it is observed that there is almost no discernable improvement of the 4-SI formulation over that of the 2-SI formulation.

The results obtained using the 2-SI and 4-SI formulations are not as good as the reference solutions from published papers. This can be attributed partly to the coarse mesh in all the examples presented. However, for the same mesh, the 4-SI's results are seen to be slightly closer to the reference solutions than the 2-SI results.

In all the examples presented in this section, it is observed that there is almost no discernable improvement of the 4-SI formulation over that of the 2-SI formulation. Some of the plausible reasons are: the 4-SI formulation does not work very well for composite objects or that the code developed from the 4-SI formulation for composite objects has a bug somewhere which causes this unexpected under performance. It is also noted that the mesh density in all the three examples presented was not as fine as that normally used for such problems for the 2-SI formulation. The performance of the two formulations could not therefore be investigated for a wide range of mesh densities due to the limitation on the available computer memory.

CHAPTER 6

SUMMARY AND CONCLUSIONS

| | |
|------------------------------|-----|
| 6.0 Summary and conclusions | 186 |
| 6.1 Introduction | 186 |
| 6.2 Chapter summaries | 186 |
| 6.3 Future Work | 190 |

6.0 Summary and conclusions

6.1 Introduction

This chapter presents the conclusion of the thesis and proposes suggestions for future research.

A frequency-domain MoM approach using the RWG basis functions to calculate electromagnetic scattering from 3-D objects was presented. The 4-SI formulation implementation has been compared with results from the 2-SI formulation and validated with results from published papers. The 4-SI formulation results for dielectric and conducting objects are found to be in good agreement with the analytical solutions and other numerical techniques' results. The results show that with the 4-SI formulation for scattering from perfectly conducting objects, the mesh density is reduced considerably when compared with the results from the 2-SI formulation. This reduction in the mesh density results in significant savings in computational time and memory requirements. It has been demonstrated that 4-SI is more efficient in analysing electrically larger problems than the 2-SI formulation. This is attributed to the more accurate evaluation of the surface integrals in the tested integral equations.

It has been demonstrated that the 4-SI formulation offers an alternative to the 2-SI and has a faster computation time, uses less computer memory storage space and possesses improved accuracy with increasing electrical size of the object(s). Computational efficiency is very important when scattering evaluation is required for numerous cases of electrically large objects. This, in fact, motivated the development of the 4-SI method.

6.2 Chapter summaries

An approach based on the MoM and the RWG basis functions to scattering by 3-D objects has been developed and validated.

Chapter 1 presented an introduction to the main topics of this thesis. Also included was the literature review covering the commonly used numerical techniques used to model electromagnetic scattering from conducting and dielectric objects.

In chapter 2, the review of the RWG formulation, upon which the formulation presented in this thesis is based, was done. The integral formulations for the scattering by perfectly conducting objects, dielectric objects and composite objects as is currently used by the many cited papers were reviewed. The chapter clearly outlined the way the RWG formulation approximates the integrals of the impedance matrix. The proposed formulation addresses the shortcomings the 2-SI formulation.

Chapter 3 presented the 4-SI formulation for scattering by perfectly conducting bodies. The EFIE for the 4-SI formulation for scattering by conducting bodies was derived. The approach was to evaluate the four-dimensional integrals $j\omega\langle\mathbf{A},\mathbf{f}_m\rangle$ and $\langle\nabla\phi,\mathbf{f}_m\rangle$ directly and accurately with no arbitrary simplifications, particularly for closely coupled triangular patches. This is different from the 2-SI formulation where the observation point is always placed at the centre of the observation triangle to avoid the evaluation of the four-dimensional integrals. Convergence tests were performed to determine a good compromise between computation speed and the accuracy of the solution. These tests yielded the optimum number of Gaussian quadrature points needed to evaluate coupling triangular patches depending on the distance between the source and the observation triangles. Performance of the 4-SI scheme against the 2-SI method was examined by considering computer execution time, the required computer

memory storage space the number of unknowns needed to solve a particular problem with good accuracy. The 4-SI and 2-SI results were compared with results from the published literature.

By examining the comparison between the results of the 4-SI, 2-SI and published results in Chapter 3, it is apparent that the 4-SI scheme is more computational efficient when analysing scattering by electrically larger perfectly conducting bodies. Less computation times, less computer memory and fewer unknowns are needed by the 4-SI method than with the 2-SI method to solve a particular problem. In addition, the 4-SI scheme can handle remarkably coarser meshes than the 2-SI method, i.e. edge lengths of the order of 0.25λ are acceptable. This translates to fewer unknowns with the 4-SI method. In fact some results have shown that edge lengths of the order of 0.38λ yield surprisingly good results.

Chapter 4 presented the 4-SI formulation for electromagnetic scattering by dielectric objects only. The expression for the evaluation of the impedance matrix terms were derived and presented in a format suitable for program coding. The same concepts used for the evaluation of the impedance matrix integrals in chapter 3 were used. The results for scattering by dielectric objects were presented. These were compared with the 2-SI results and results from published literature. The same conclusions drawn from chapter 3 apply to chapter 4. The 4-SI method also works for dielectric objects and that the 4-SI is a computationally more efficient method than the 2-SI for solving electrically larger dielectric objects with a large radius of curvature. Less computation time and fewer unknowns is needed to converge to a solution. As in chapter 3, the 4-SI tolerates edge lengths larger than $0.25\lambda_d$, where λ_d is the wavelength of the

electromagnetic wave inside the dielectric. This explains the decrease in the number of unknowns in the 4-SI method compared to the 2-SI method.

Chapter 5 presented the formulation for the scattering by mixed problems, comprising dielectric and conducting objects. Most of the theory meant for this chapter was covered in chapters 3 and 4. Electromagnetic scattering results for mixed objects were presented and compared with the results obtained using the 2-SI method and published literature. Again, the same trend observed in results presented in chapters 3 and 4 were observed, i.e. the 4-SI requires less number of unknowns and takes less computation time when dealing with electrically larger problems when compared with the 2-SI method.

From the results presented in chapters 3, 4 and 5, it is obvious that the 4-SI scheme works. The examples that have been presented clearly show that the 4-SI, when compared to the conventional 2-SI method as proposed by Rao *et. al* [6], reduces the number of unknowns without compromising the accuracy of the solution. This translates to improved computation times and lower computer storage space. However, these gains can only be achieved if the object under test is electrically large, otherwise the conventional 2-SI MoM approach is superior to the 4 fold scheme. From the results presented in chapters 3, 4 and 5, it can be seen that the 4-SI method improves the computational efficiency in the sense of both memory and CPU time over that of the 2-SI method. However, this is only possible for objects whose dimensions exceed the order of a λ , the wavelength of the incident wavelength in the case of conducting objects, or it is the wavelength inside the dielectric object. Electrically smaller objects or objects with high radius of curvature or fine detail need very fine mesh so that the geometrical surface is described more accurately than with a coarser mesh. In those cases, the advantages of the 4-SI method no longer apply.

It was also observed that the 4-SI is better equipped to handle electromagnetic scattering problems at or near grazing angles of incidence. In such cases, more surface waves are generated and the 2-SI scheme struggles to converge to solution even with very fine mesh densities.

A 4-SI method has been used to analyse scattering from conducting and dielectric objects. This is achieved by testing the full surface integrals of the impedance matrix without making any assumptions. Gaussian quadrature is used to solve the integrals for closely coupled triangular patches leaving the one point Gaussian quadrature rule for the loosely coupled patches.

6.3 Future Work

More work is needed to validate the 4-SI scheme against other examples. The 4-SI scheme has been demonstrated to work well for dielectrics and conducting objects. The 4-SI numerical results for the electromagnetic scattering by dielectrics and conducting objects are encouraging for the investigation of this procedure for the solution of electrically larger problems where the advantage of the 4-SI is expected to be more pronounced. The results for the mixed objects have been inconclusive, mainly because of the limitations imposed by the computing resources.

Although not reported in the thesis, the current distribution on the edges of thin dielectric slabs (thickness typically less than $0.01\lambda_d$) is not being modelled properly. This is probably due to the source and observation points being very close each other, resulting in near singularity terms in the impedance matrix terms. This needs further investigation.

This work demonstrates that 4-SI scheme has an advantage over the standard 2-SI formulation in the RCS prediction of dielectric and conducting objects.

The conventional MoM technique leads to fully populated impedance matrices. This limits the electrical size of the problem that can be solved on a given computer with limited memory. The application of fast solution methods such the fast multipole method [38] to the MoM leads to reduced memory and CPU requirements. Very recently, McCowen [169] demonstrated the effectiveness of applying the FMM to the CFIE by reducing the matrix-fill time and the computer storage of the original CFIE by over 80%. Because of the improved accuracy demonstrated for the 4-SI formulation, particularly for scattering from perfectly conducting objects and to a less extent scattering from dielectric objects, there is scope to carry over the 4-SI to the fast-multiple method with view to further enhancing the effectiveness of the fast-multiple method's applications.

7

APPENDICES

| | | |
|-------------------|--|-----|
| Appendix A | A Normalized Local Area Coordinate System and numerical integration over a triangle | 193 |
| Appendix B | Definition of Scattering Angles | 197 |

Appendix A

A Normalized Local Area Coordinate System and numerical integration over a triangle

The integral considered in Chapters 3, 4 and 5 for numerical of a function f over a triangle is performed by a Gaussian quadrature rule such that:

$$I = \iint_T f(\alpha, \beta, \gamma) dA = A \sum_{i=1}^{ng} w_i f(\alpha_i, \beta_i, \gamma_i) \quad (A.1)$$

where the i^{th} Gaussian point of location $(\alpha_i, \beta_i, \gamma_i)$, there corresponds a Gaussian weight w_i and functional evaluation $f(\alpha_i, \beta_i, \gamma_i)$. T is a flat triangle of area A . The error in quadrature is zero if the number of points ng is of sufficient magnitude. The values of the constants $w_i, \alpha_i, \beta_i, \gamma_i$ are listed in Table A.1 for the various formulas. The most convenient way to evaluate the integral is to transform coordinates to a local system of area coordinates [127] within triangle T . The triangle T is divided into three regions of area A_1, A_2 , and A_3 which are constrained to satisfy $A_1 + A_2 + A_3 = A$, as shown in Figure (A.1).

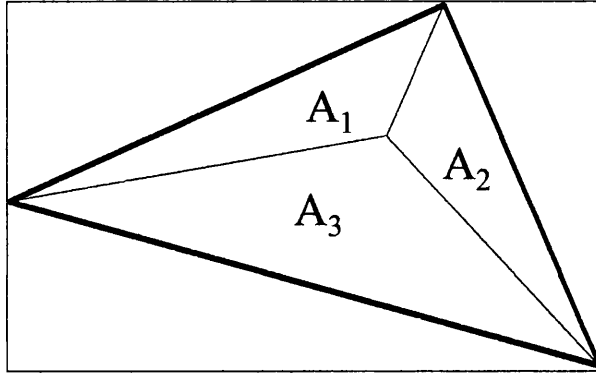


Figure A.1 Definitions of areas used in defining area coordinates.

The normalised area coordinates are defined as

$$\begin{aligned}\alpha &= \frac{A_1}{A} \\ \beta &= \frac{A_2}{A} \\ \gamma &= \frac{A_3}{A}\end{aligned}\tag{A.2}$$

which, because of the area constraint, must satisfy

$$\alpha + \beta + \gamma = 1\tag{A.3}$$

Some of the quadrature rules are listed in Table A.1. A multiplication factor M indicates the number of permutations associated with an evaluation point having a weight w_i . For example, $M = 1$ is associated with an evaluation point at the triangle's centroid $(\frac{1}{3}, \frac{1}{3}, \frac{1}{3})$, $M = 3$ indicates a point on a median line and $M = 6$ indicates an arbitrary point in the interior of the triangle. The factor p indicates the order of the quadrature rule.

It can be shown that [169] :

$$dA = 2A d\alpha d\beta \quad (\text{A.4})$$

It can easily be shown that the surface integral over T in (A.1) transforms as follows:

$$I = \iint_T f(\alpha, \beta, \gamma) dA = 2A \int_{\alpha=0}^1 \int_{\beta=0}^{1-\alpha} f(\alpha, \beta, \gamma) d\alpha d\beta \quad (\text{A.5})$$

Equation (A.5) is used to evaluate the integral over the source triangle.

Table A.1 Weights and evaluation points for integration on triangles.

| n | w_i | α | β, γ | M | p |
|-----------|--|--|--|--|-----------------------|
| 1 | 1.000000000000000 | 0.333333333333333 | 0.333333333333333 0.333333333333333 | 1 | 1 |
| 3 | 0.333333333333333 | 0.666666666666667 | 0.166666666666667 0.166666666666667 | 3 | 2 |
| 4 | -0.562500000000000 | 0.333333333333333 0.333333333333333 0.600000000000000 | 0.333333333333333 0.333333333333333 0.200000000000000 0.200000000000000 | 1 3 | 3 |
| 6 | 0.109951743655322 0.223381589678011 | 0.816847572980459 0.108103018168070 | 0.091576213509771 0.091576213509771 0.445948490915965 0.445948490915965 | 3 3 | 4 |
| 7 | 0.225000000000000 0.125939180544827 0.132394152788506 | 0.333333333333333 0.797426985353087 0.059715871789770 | 0.333333333333333 0.333333333333333 0.101286507323456 0.101286507323456 0.470142064105115 0.470142064105115 | 1 3 3 | 5 |
| 12 | 0.050844906370207 0.116786275726379 0.082851075618374 | 0.873821971016996 0.501426509658179 0.636502499121399 | 0.063089014491502 0.063089014491502 0.249286745170910 0.249286745170910 0.310352451033785 0.053145049844816 | 3 3 6 | 6 |
| 13 | -0.149570044467670 0.175615257433204 0.053347235608839 0.0771133760890257 | 0.333333333333333 0.479308067841923 0.869739794195568 0.638444188569809 | 0.333333333333333 0.333333333333333 0.260345966079033 0.260345966079033 0.065130102902216 0.065130102902216 0.312865496004875 0.486903154253160 | 1 3 3 6 | 7 |

Appendix B

Definition of Scattering Angles

The azimuth angle and the elevation angle used in the RCS plots are defined in Figure B.1, where ϕ denotes the azimuth angle, θ denotes the elevation angle, and α denotes the polarization of the incident wave. Figure B.1 shows the case where the plane wave is incident on a flat plate. The E-polarisation is defined when $\alpha = 90^\circ$ and the H-polarisation occurs when $\alpha \equiv 0^\circ$.

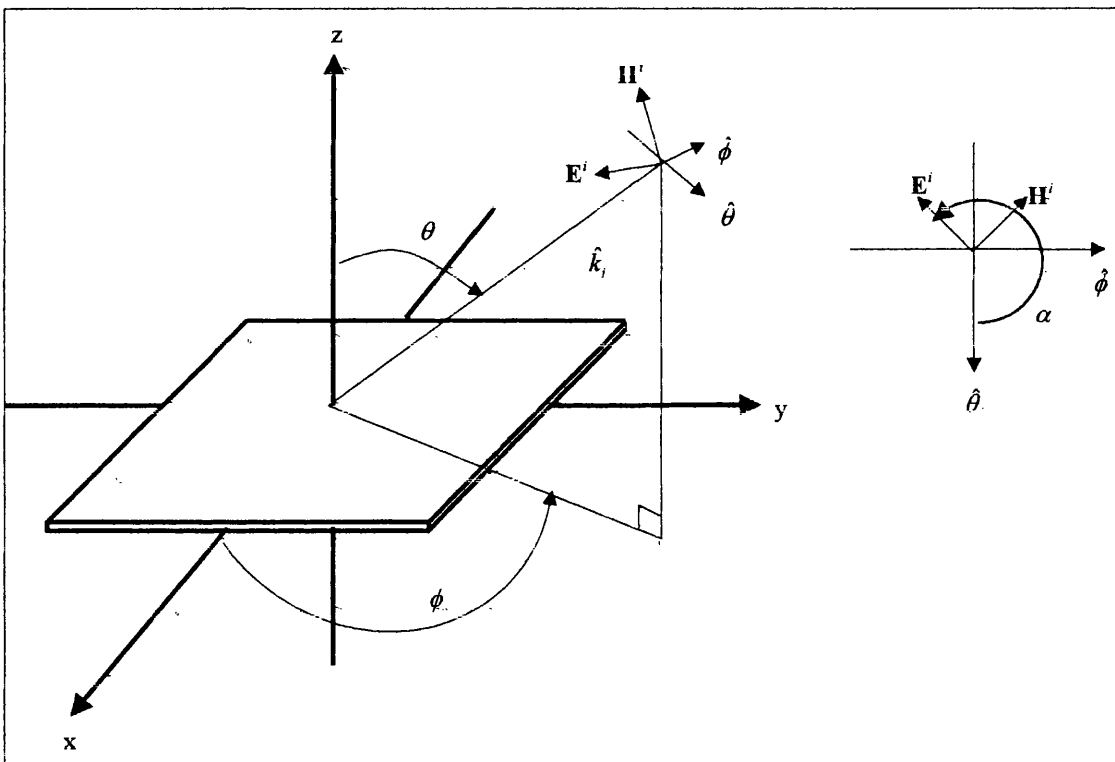


Figure B.1 Definition of the azimuth, elevation and polarisation angles used in the calculation of RCS.

The incident electric field is usually specified with unity amplitude and may be written as :

$$\mathbf{E}^i = [(\hat{\alpha} \cdot \hat{\theta})\hat{\theta} + (\hat{\alpha} \cdot \hat{\phi})\hat{\phi}]e^{-j\hat{k}_i \cdot \mathbf{r}} = [E_{x0}\hat{x} + E_{y0}\hat{y} + E_{z0}\hat{z}] \quad (\text{B.1})$$

where

$$\hat{k}_i \cdot \mathbf{r} = -k_o \sin(\theta_i)[\cos(\phi_i)x + \sin(\phi_i)y] \quad (\text{B.2})$$

and k_i is the propagation constant in the medium under consideration.

REFERENCES

1. K. S. Yee, "Numerical solution of initial boundary value problems involving Maxwell's equations in isotropic media", *IEEE Trans. Antennas Propagat.*, vol. 14, pp. 302-307, 1966.
2. S. S. Zivanovic, K. S. Lee and K. K. Mei, "A subgridding for the time-domain finite-difference method to solve Maxwell's equations," *IEEE Trans. Microwave Theory Tech.*, vol. 39, pp. 471-479, 1991.
3. P. P. Silvester and R. L. Ferrari, *Finite elements for electrical engineers*, Cambridge University Press, Cambridge, 1990.
4. J. M. Jin, J. L. Volakis and J. D. Collins, "A finite element-boundary integral method for scattering and radiation by two- and three boundary-dimensional structures", *IEEE Trans. Antennas Propagat. Mag.*, vol. 33, pp. 22-32, June 1991.
5. R. F. Harrington, *Field Computation by Moment Methods*. New York: Macmillan Company, 1968.
6. S. M. Rao, D. R. Wilton and A. W. Glisson, "Electromagnetic scattering by surfaces of arbitrary shape", *IEEE Trans. Antennas Propagat.*, vol. 30, pp. 409-418, May 1982.
7. D. R. Lynch and K. D. Paulsen, "Time-domain integration of the Maxwell equations on finite elements," *IEEE Trans. Antennas Propagat.*, vol. 38, pp. 1933-1942, Dec 1990.
8. F. Bost, L. Nicolas, G. Rojat, "A time-domain integral formulation for the scattering by thin wires," *IEEE Trans. Magnetics*, vol. 36, pp. 868-871, Jul. 2000.

9. T. K. Sarkar, L. Wonwoo, S. M. Rao, "Analysis of transient scattering from composite arbitrarily shaped complex structures," *IEEE Trans. Antennas Propagat.*, vol. 48, pp. 1625-1634, Oct. 2000.
10. D. Jiao, Lu Mingyu, E. Michielssen, Jin Jian-Ming, "A fast time-domain finite element-boundary integral method for electromagnetic analysis," *IEEE Trans. Antennas Propagat.*, vol. 49, pp. 1453-1461, Oct. 2001.
11. S. M. Rao, T. K. Sarkar, "Numerical solution of time domain integral equations for arbitrarily shaped conductor/dielectric composite bodies," *IEEE Trans. Antennas Propagat.*, vol. 50, pp. 1831-1837, Dec. 2002.
12. K. S. Yee and J. S. Chen, "Conformal hybrid finite difference time do-main and finite volume time domain," *IEEE. Trans. Antennas Propagat.*, vol. 42, pp. 1450-1455, Oct. 1994.
13. K. L. Shlager and J. B. Schneider, "A selective survey of the finite-difference time-domain literature," *IEEE Antennas Propagat. Mag.*, vol. 37, pp. 39-56, Aug. 1995.
14. A. Taflove, ed., *Advances in computational electrodynamics: the finite-difference time-domain method*, Boston: Artech House, 1998.
15. A. Taflove and K. Umashankar, "The Finite-Difference Time-Domain(FDTD) Method for electromagnetic scattering and interaction problems," *J. Electromag. Waves Appl.*, vol.1, pp. 243-267, 1987.
16. A. Taflove and M. E. Brodwin, "Numerical solution of steady-state electromagnetic scattering problems using the time-dependent," *IEEE Trans. Microwave Theory Tech.*, vol. 23, pp. 623-630, Aug. 1975.
17. K. Umashankar and A. Taflove, "A novel method to analyze electromagnetic scattering of complex objects," *IEEE Trans. Electromagn. Compat.*, vol. EMC-24, pp. 397-405, Nov. 1982.
18. D. M. Sullivan, D. T. Borup, O. P. Gandhi, "Use of the finite-difference time-domain method in calculating EM absorption in human tissues," *IEEE Trans. Biomed. Eng.*, vol. 34, pp. 148-157, 1987.

19. D. M. Sheen, S. M. Ali SM, M. D Abouzahra, J. A. Kong , "Application of the three-dimensional finite-difference time-domain method to the analysis of planar microstrip circuits," *IEEE Trans. Microwave Theory Tech.*, vol. 38, pp. 849 –857, Jul. 1990.
20. W. V. Andrew, C. A. Balanis, P. A. Tirkas, J. Peng , C. R. Birtcher, "Finite-difference time-domain analysis of HF antennas on helicopter airframes," *IEEE Trans. Electromagn. Compat.*, vol. 39, pp. 100-117, May 1997.
21. A. K. Shaw and K. Naishadham, "ARMA-based time-signature estimator for analysing resonant structures by the FDTD method," *IEEE Trans. Antennas Propagat.*, vol. 49, pp. 327-339, Mar. 2001.
22. A. Taflove, K. R. Umashankar and T. G. Jurgens, "Validation of FDTD modelling of the radar cross-section of three-dimensional structures spanning up to 9 wavelengths," *IEEE Trans. Antennas Propagat.*, vol. 33, pp. 662-666, June 1985.
23. R. J. Luebbers, K. S. Kunz, M. Schneider, F. Hunsberger, "A finite-difference time-domain near zone to far zone transformation," *IEEE Trans. Antennas Propagat.*, vol. 39, pp. 429-433, Apr 1991.
24. M. A. Fusco, M. V. Smith, L. W. Gordon, "A three-dimensional FDTD algorithm in curvilinear," *IEEE Trans. Antennas Propagat.*, vol. 39, pp. 1463-1471, Oct 1991.
25. R. De Leo, A. Schiavoni, "FDTD evaluation of scattering by metallic objects in GTEM cells," *IEE Proceedings-Science, Measurement and Technology*, vol. 141, pp. 287-292, Jul 1994.
26. S. Dey, R. Mittra, "A locally conformal finite-difference time-domain (FDTD) algorithm for modeling three-dimensional perfectly conducting objects ," *IEEE Microwave and Guided Wave Lett.*, vol. 7, pp. 273-275, Sep 1997.
27. R. Holland, L. Simpson and K. Kunz, "Finite difference analysis of EMP coupling to lossy dielectric structures," *IEEE Trans. Electromagn. Compat.*, vol. 22, pp. 203-209, Aug. 1980.

28. R. Luebbers, "Lossy dielectrics in FDTD," *IEEE Trans. Antennas Propagat.*, vol. 41, pp. 1586-1588, Nov 1993.
29. C. L. Britt, "Solution of electromagnetic scattering problems using time domain techniques," *IEEE Trans. Antennas Propagat.*, vol. 37, pp. 1181-1192, Sep 1989.
30. P. Leveque, A. Reineix, B. Jecko, "Modelling of dielectric losses in microstrip patch antennas: application of FDTD method," *Electron. Lett.*, vol. 28, pp. 539-541, Mar 1992.
31. L .K. Wu, L. T. Han, "E-polarized scattering from a conducting rectangular cylinder with an infinite axial slot filled by a resistively coated dielectric strip," *IEEE Trans. Antennas Propagat.*, vol. 40, pp. 731-733, Jun 1992.
32. M. A. Morgan, K. K. Mei, "Finite-element computation of scattering by inhomogeneous penetrable bodies of revolution," *IEEE Trans. Antennas Propagat.*, vol. 27, pp. 202-214, Mar 1979.
33. R. E. White, *An introduction to the finite element method with applications to nonlinear problems*, New York:Wiley, 1985.
34. P. P. Silvester, R. L. Ferrari, *Finite elements for electrical engineers*, New York: Cambridge Univ Press, 1996.
35. R. Coccioli, T. Itoh, G. Pelosi, P. P. Silvester, "Finite-elements methods in microwaves: a selected bibliography," *IEEE Antennas Propagat. Mag.*, vol. 38, pp. 34-48, Dec 1996.
36. C. A. Balanis, *Advanced Engineering Electromagnetics*, New York: John Wiley & Sons, Inc., 1989.
37. De Moerloose, and D. De Zutter, "Surface integral representation radiation boundary condition for the FDTD method," *IEEE Trans. Antennas and Propagat.*, vol. 41, pp. 890-896, Jul. 1993.
38. X. Q. Sheng, J. M. Jin, J. M. Song, C. C. Lu, W. C. Chu, "On the formulation of hybrid finite-element and boundary-integral methods for 3-D scattering," *IEEE Trans. Antennas Propagat.*, vol. 46, pp. 303-311, Mar 1998.

39. T. G. Moore, J. G. Blaschak, A. Taflove, and G. A. Kriegsmann, "Theory and application of radiation boundary operators," *IEEE Trans. Antennas Propagat.*, vol. 36, pp. 1797-1812, 1988.
40. J. J. AngeAlini, C. Soize, P. Soudais, "Hybrid numerical method for harmonic 3-D Maxwell equations: Scattering by a mixed conducting and inhomogeneous anisotropic dielectric medium", *IEEE Trans. on Antennas and Propagat.*, vol., 44, pp. 66-76, Jan. 1993.
41. W. Sun and C. A. Balanis, "Edge-based FEM solution of scattering from inhomogeneous and anisotropic objects," *IEEE Trans. Antennas Propagat.*, vol. 42, pp. 627-632, May 1994.
42. M. W. Ali, T. H. Hubing, J. L. Dreniak, "A hybrid FEM/MOM technique for electromagnetic scattering and radiation from dielectric objects with attached wires," *IEEE Trans. Electromagn. Compat.*, vol. 39, pp. 304-314, Nov 1997.
43. F. Bocquet, L. Pichon, A. Razek, "3D FEM analysis of electromagnetic wave scattering from a dielectric sheet in EMC problems," *IEEE Trans. Magnetics*, vol. 34, pp. 2791-2794, Sep 1998.
44. J. Park, H. Chae, S. Nam, "Study of efficient FEM-based iteration method for open region problem and its application to scattering from a three-dimensional cavity-backed aperture," *Electron. Lett.*, vol. 36, pp. 1529-1530, Aug 2000.
45. E. Newman and P. Tulyathan, "Wire antennas in the presence of a dielectric/ferrite inhomogeneity," *IEEE Trans. Antennas Propagat.*, vol. 26, pp. 587-593, Jul. 1978.
46. J. Shaeffer, and L. Medgyesi-Mitschang, "Radiation from wire antennas attached to bodies of revolution: The junction problem," *IEEE Trans. Antennas Propagat.*, vol. 29, pp. 479-487, May 1981.
47. L. Medgyesi-Mitschang and J. Putnam, "Electromagnetic scattering from extended wires and two- and three-dimensional surfaces," *IEEE Trans. Antennas Propagat.*, vol. 33, pp. 10190-1100, Oct. 1985.

48. I. Tekin and E. H. Newman, "Method of moments solution for a wire attached to an arbitrary faceted surface," *IEEE Trans. Antennas Propagat.*, vol. 46, pp. 559-562, Apr 1998.
49. J. R. Rogers, "Moment-method scattering solutions to impedance boundary condition integral equations," *IEEE AP-S Int. Symp.*, Boston, MA, pp. 347-350, 1984.
50. S. M. Rao, T. K. Sarkar, P. Midya and A. R. Djordevic, "Electromagnetic radiation and scattering from finite conducting and dielectric structures: surface/surface formulation," *IEEE Trans. Antennas Propagat.*, vol. 36, pp. 1034-1037, Jul. 1991.
51. A. McCowen, "Efficient 3-D moment-method analysis for reflector antennas using a far-field approximation technique," *IEE Proc. Microwaves, Antennas Propagat.*, vol. 146, pp. 7-12, Feb. 1999.
52. J. M. Rius, E. Ubeda and J. Parron, "On the testing of the magnetic field integral equation with RWG basis functions in method of moments," *IEEE Trans. Antennas Propagat.*, pp. 1550-1553, vol. 49, Nov 2001.
53. K. Umashankar, A. Taflove, S. Rao, "Electromagnetic scattering by arbitrary shaped three-dimensional homogeneous lossy dielectric objects," *IEEE Trans. Antennas Propagat.*, vol. 34, pp. 758-766, Jun. 1986.
54. A. McCowen, "A Far-Field Approximation for the Fast-Multipole Method applied to the Combined Field Integral Equation," *To be published in IEEE Trans. Magnetics*.
55. W. Ko, R. Mittra, "A new approach based on a combination of integral equation and asymptotic techniques for solving electromagnetic scattering problems," *IEEE Trans. Antennas Propagat.*, vol. 25, pp. 187-197, Mar. 1977.
56. R. Mittra and V. Varadarajan, "A technique for solving the 2-D method of moments problems involving large scatterers," *Microwave Opt. Technol. Lett.*, vol. 8, pp. 132-136, Feb. 1995.

57. E. Michielssen and A. Boag, "Multilevel evaluation of electromagnetic fields for the rapid solution of scattering problems," *Microwave Opt. Technol. Lett.*, vol. 7, pp. 790-795, Dec. 1995.
58. C. SU and T. P. Sarkar, "Adaptive Multiscale Moment Method (AMMM) for Analysis of Scattering From Three-Dimensional Perfectly Conducting Structures," *IEEE Trans. Antennas Propagat.*, vol. 50, pp. 444-450, April 2002.
59. A. Kas, E. Yip, "Preconditioned conjugate gradient methods for solving electromagnetic problems," *IEEE Trans. Antennas Propagat.*, vol. 35, pp. 147-152, Feb 1987.
60. G. A. Thiele, "Overview of selected hybrid method in radiating system analysis," *Proc. IEEE*, vol. 80, pp. 67-78, Jan. 1992.
61. F. X. Canning, "Improved impedance matrix localization method," *IEEE Trans. Antennas Propagat.*, vol. 41, pp. 659-667, May 1993.
62. A. Heldring, J. M. Rius, L. Ligthart, "New block ILU preconditioner scheme for numerical analysis of very large electromagnetic problems," *IEEE Trans. Magnetics*, vol. 38, pp. 337-340, Mar. 2002.
63. F. X. Canning, "The impedance matrix localisation (IML) method for moment-method calculations," *IEEE Trans. Antennas Propagat. Mag.*, vol. 32, pp. 18-30, Oct. 1990.
64. Z. Altman, R. Mittra, "Combining an extrapolation technique with the method of moments for solving large scattering problems involving bodies of revolution," *IEEE Trans. Antennas Propagat.*, vol. 44, pp. 548-553, Apr 1996.
65. S. C. Wu, Y. L. Chow, "An Application of the Moment Method to Waveguide Scattering Problems," *IEEE Trans. Microwave Theory Tech.*, vol. 20, pp. 744-749, Nov. 1972.
66. A. McCowen, B. G. Salman, "Efficient modelling of finite-size ungrounded PCBs with a full wave 3D moment-method analysis," *Electronics Lett.*, vol. 35, pp. 1410-1412, Aug 1999.

67. A. A. Kucharski, "A method of moments solution for electromagnetic scattering by inhomogeneous dielectric bodies of revolution," *IEEE Trans. Antennas Propagat.*, vol. 48, pp. 1202-1210, Aug. 2000.
68. G. A. Thiele, "Overview of selected hybrid method in radiating system analysis," *Proc. IEEE*, vol. 80, pp. 67-78, Jan. 1992.
69. D. P. Bouche, F. A. Molinet and R. Mittra, "Asymptotic and hybrid techniques for electromagnetic scattering," *Proc. IEEE*, vol. 81, pp. 1658-1684, Dec. 1993.
70. C. Su, "Progress in Electromagnetics Research", *PIER* vol. 21, pp. 71-89, 1999.
71. F. X. Canning, "The impedance matrix localization method (IML) uses," *Proc. IEEE*, vol.41, pp. 1659-1667, 1993.
72. R. Coifman, V. Rohklin and S. Wandzura, "The fast multipole method for the wave equation: pedestrian prescription," *IEEE Antennas Propagat. Mag.*, vol. 35, pp. 7-12, 1 Jun 1993.
73. C. C. Lu and W. C. Chew, "A Fast Algorithm for Solving Hybrid Integral equation," *IEE Proceedings-H*, vol. 140, pp. 455-460, Dec. 1993.
74. A. Boag and R. Mittra, "Complex multipole beam approach to electromagnetic scattering problems," *IEEE Trans. Antennas Propagat.*, vol. 42, pp. 366-372, Mar. 1994.
75. W. C. Chin, J. Jin, C. Lu, E. Michielssen and J. M. Song "Fast Solution Methods in Electromagnetics," *IEEE Trans. Antennas Propagat.*, vol. 45, pp. 533-543, Mar. 1997.
76. J. M. Song, C. C. Lu and W. C. Chew "Multilevel Fast Multipole Algorithm for electromagnetic Scattering by Large Complex Objects," *IEEE Trans. Antennas Propagat.*, vol. 5, pp. 1488-1493, Oct. 1997.
77. T. T. Chia, R. J. Burkholder, R. Lee, "The application of FDTD in hybrid methods for cavity scattering analysis," *IEEE Trans. Antennas Propagat.*, vol. 43, pp. 1082-1090, Oct. 1995.

78. G. Cerri, P. Russo, A. Schiavoni, G. Tribellini, P. Bielli, "MoM-FDTD hybrid technique for analysing scattering problems," *Electronics Lett.*, vol. 34, pp. 438-440, Mar 1998.
79. R. Lee and T. T. Chia, "Analysis of electromagnetic scattering from a cavity with a complex termination by means of a hybrid ray-FDTD method," *IEEE Trans. Antennas Propagat.*, vol. 41, pp. 1560-1569, Nov. 1993.
80. T. Rylander, A. Bondeson, "Application of stable FEM-FDTD hybrid to scattering problems," *IEEE Trans. Antennas Propagat.*, vol. 50, pp. 141-144, Feb. 2002.
81. 73. A. C. Cangellaris and R. Lee, "The bymoment method for two-dimensional electromagnetic scattering," *IEEE Trans. Antennas Propagat.*, vol. 38, pp. 1429-1437, Sep 1990.
82. 74. S. D. Gedney, R. Mittra, "Analysis of the electromagnetic scattering by thick gratings using a combined FEM/MM solution," *IEEE Trans. Antennas Propagat.*, vol. 39, pp. 1605-1614, Nov 1991.
83. D. J. Hoppe, L. W. Epp, J. F. Lee, "A hybrid symmetric FEM/MOM formulation applied to scattering by inhomogeneous bodies of revolution," *IEEE Trans. Antennas Propagat.*, vol. 42, pp. 798-805, Jun 1994.
84. Y. Lu; J. Xu; J. S. Fu, "Analysis of microstrip antennas with complex and anisotropic substrate by a hybrid FEM/BEM approach," *IEEE Trans. Magnetis*, vol. 34, pp. 3300-3303, Sep 1998.
85. A. W. Glisson and D. R. Wilton, "Simple and Efficient Numerical Methods for Problems of Electromagnetic Radiation and Scattering from Surfaces", *IEEE Trans. Antennas Propagat.*, vol. 28, pp. 593-603, Sept. 1980.
86. A. W. Glisson, "On the development of numerical techniques for treating arbitrarily-shaped surfaces," Ph.D. dissertation, Univ. Mississippi, 1978.
87. J. J. H. Wang, "Numerical analysis of three-dimensional arbitrarily-shaped conducting scatterers by trilateral surface cell modelling", *Radio Sc.*, vol. 13, pp. 947-952, Nov-Dec 1978.

88. B. P. Rynne, "Time domain scattering from arbitrary surfaces using the electric field integral equation," *J. Electromagn. Waves Applicat.*, vol. 5, pp. 93–112, Jan. 1991.
89. D. A. Vechinski and S. M. Rao, "Transient scattering from dielectric cylinders—E-field, H-field, and combined field solutions," *Radio Sci.*, vol. 27, pp. 611–622, Sept./Oct. 1992.
90. B. G. Salman and A. McCowen, "Application of the FFA technique for efficient near-field evaluation for electrically large PEC structures", *IEEE Trans. Magnetics*, Vol. 34, pp. 2684-2687, Sep 1998.
91. C. J. Leat, N. V. Shuley and G. F. Stickley, "Triangular-patch model of bowtie antennas: validation against Brown and Woodward," *IEE Proc.-Microw. Antennas Propag.*, vol. 145, pp. 465-470, Dec 1998.
92. P. J. Cullen, L. Rossi, "On the fully numerical evaluation of the linear-shape function times the 3D Green's function on a plane triangle", *IEEE Trans. Microwave Theory Tech.*, Vol. 47, pp. 398-402, Apr 1999.
93. J. Gulick, M. Kowolski, L. Kempel, and J. Jin, "Experimental Results for Implementing a Combination of AP and RWG Basis Functions Using MoM to Solve the EFIE," *IEEE AP-S Int. Symp. and URSI Radio Sci. Meeting, Boston, Massachusetts*, July 8-13, 2001.
94. S. Chaowei, T. K. Sarkar, "Adaptive multiscale moment method (AMMM) for analysis of scattering from three-dimensional perfectly conducting structures", *IEEE Trans. Antennas Propagat.*, vol. 50, pp. 444-450, Apr 2002.
95. N. N. Wang, J. H. Richmond and M. C. Gilreath, "Sinusoidal Reaction Formulation for Radiation and Scattering from Conducting Surfaces", *IEEE Trans. Antennas Propagat.*, vol. 23, pp. 376-382, May 1975.
96. E. H. Newman and P. Tulyatha, "A Surface Patch Model for Polygonal Plates", *IEEE Trans. Antennas Propagat.*, vol. 30, pp. 588-593, July 1982.
97. E. H. Newman, P. Alexandroupoulos and E. K. Walton, "Polygonal Plate Modelling of Realistic Structures", *IEEE Trans. Antennas Propagat.*, vol. 32, pp. 742-747, July 1984.

98. D. L. Wilkes and C.-C. Cha, "Method of moments solution with parametric curved triangular patches," *IEEE AP-S Int. Symp. Dig.*, London, ON, Canada, pp. 1512–1515, 1991.
99. N. Y. Zhu, F. M. Landstorfer, "Application of curved parametric triangular and quadrilateral edge elements in the moment method solution of the EFIE", *IEEE Microwave and Guided Wave Letters*, pp. 319-321, Sep 1993.
100. K. W. Brown, A. Prata (Jr.), "Simple meshing and efficient numerical analysis of curved surfaces using a new quadrilateral basis function", *IEEE AP-S Int. Symp. Dig.*, Atlanta, GA, USA, pp. 290-293, Jun 1998.
101. C. Wei, Y. Tiejun, W. Han and Y. Yihun, " High-Order Mixed RWG Basis Functions for Electromagnetic Applications", *IEEE Trans. Antennas Propagat.*, vol. 49, pp. 1295-1303, Jul 2001.
102. James Clerk Maxwell, " A dynamical theory of the electromagnetic field," *Royal Society Transactions*, CLV, 1864.
103. J. Van Bladel, *Electromagnetic Fields*, New York, McGraw-Hill, 1964.
104. R. F. Harrington, *Time-Harmonic Electromagnetic Fields*, Piscataway, NJ: IEEE Press, 1994.
105. C.-C. Lu, W. C Chew and Ji-Ming Song, "A study of disparate grid sizes for an irregular-shape scatterer on EFIE, MFIE, and CFIE," *IEEE AP-S Int. Symp. Dig.*, Baltimore, MD , USA, pp. 1746-1749, vol. 3, 21-26 July, 1996.
106. I. K. Sendur and L. Gurel, "Solution of radiation problems using the fast multipole method," *IEEE AP-S Int. Symp. Dig.*, Montreal, Que. , Canada, vol.1, pp. 88-91, 13-18 Jul 1997.
107. G. H. Brown and O. M. Woodward, "Experimentally determined radiation characteristics of conical and triangular antennas", *RCA Rev.*, pp. 425-452, 1952.
108. B. G. Salman and A. McCowen, "Application of the FFA technique for efficient near-field evaluation for electrically large PEC structures", *IEEE Trans. Magnetism*, Vol. 34, pp. 2684-2687, Sep. 1998.

109. L. Rossi, P. J. Cullen, C. Brennan, "Implementation of a multilevel fast far-field algorithm for solving electric-field integral equations", *IEE Proc.-Microw. Antennas Propagat.*, Vol. 147, pp. 19-24, Feb. 2000.
110. J. M. Song and W. C. Chew, "Large scale computations using FISC", *IEEE AP-S Int. Symp. Dig.*, Salt Lake City, UT , USA, vol. 4, pp. 1856-1859, July 2000 .
111. M. A. Carr, J. L. Volakis and D. C. Ross, "Acceleration of moment method solutions for discrete bodies of revolution in free space", *IEEE Trans. Antennas Propagat.*, vol. 50, pp. 1319-1322, Sep 2002.
112. P. Huddleston, L. Medgyesi-Mitschang, J. Putnam, "Combined field integral equation formulation for scattering by dielectrically coated conducting bodies," *IEEE Trans. Antennas Propagat.*, vol. 34, pp. 510-520, Apr 1986.
113. T. K. Sarkar, E. Arvas, S. Ponnappalli, "Electromagnetic scattering from dielectric bodies ", *IEEE Trans. Antennas Propagat.*, vol. 37, pp. 673-676, May 1989.
114. E. N. Opp, S. L. Geyer, R. Thomas, M. S. Willet, K. Umashankar, "Numerical computation of electromagnetic scattering on the Connection Machine using the method of moments", *IEEE Trans. Magnetics*, vol. 25, pp. 2907-2909, Jul 1989.
115. X. Q. Sheng, J-M. Jin, J. Song, W. C. Chew and C-C. Lu, "Solution of Combined-Field Integral Equation Using Multilevel Fast Multipole Algorithm for Scattering by Homogeneous Bodies", *IEEE Trans. Antennas Propagat.*, vol. 46, pp. 1718-1726, Nov. 1998.
116. T. K. Sarkar, S. M. Rao and A. R. Djordjevic, " Electromagnetic Scattering and Radiation from Finite Microstrip Structures", *IEEE Trans. Microwave Theory Tech.*, vol. 38, pp. 1568-1575, Nov. 1990.
117. E. Arvas, A. A. Rahhal, A. Sadigh, S. M. Rao, "Scattering from multiple conducting and dielectric bodies of arbitrary shape", *IEEE Antennas and Propagat. Mag.*, vol. 33, pp. 29-36 Apr. 1991.

118. S. M. Rao, C.-C. Cha, R. L. Cravey, D. L. Wilkes, "Electromagnetic scattering from arbitrary shaped conducting bodies coated with lossy materials of arbitrary thickness", *IEEE Trans. Antennas Propagat.*, vol 39, pp. 627-631, May 1991.
119. B. G. Salman, A. McCowen, "The CFIE technique applied to finite-size planar and non-planar microstrip antenna", *Third International Conference on Computation in Electromagnetics*, Bath, UK, pp. 338-341, Apr. 1996.
120. B. G. Salman, A. McCowen, "A comparative study of the computation of near-field scattering from resonant dielectric/PEC scatterers", *IEEE Trans. Magnetism*, vol. 32, pp. 866-869 May 1996.
121. F. Ling; C. -Fu. Wang; J. -M. Jin, "An efficient algorithm for analysing large-scale microstrip structures using adaptive integral method combined with discrete complex image method", *IEEE International Conference on Microwave and Millimetre Wave Technology Proceedings*, Beijing, China, pp. 953-956, 1998.
122. M. G. Andreason, "Scattering from bodies of revolution", *IEEE Trans. Antennas Propagat.*, vol. AP-13, no. 2, pp. 303-310, Mar. 1965.
123. K. Kalbasi, K. R. Demarest, "A multilevel formulation of the method of moments", *IEEE Trans. Antennas Propagat.*, vol. 41 pp. 589-599, May 1993.
124. T. N. L. Patterson, "The Optimum addition of points to quadrature formulae", *Math. Comput.*, Vol. 22, pp. 847 – 856, 1968.
125. The MoM 3D Code, Department of Electrical and Electronic Engineering, University of Wales Swansea, UK, 1997.
126. O. C. Zienkiewicz, *The Finite Element Method*, McGraw-Hill, 1977.
127. D. A. Dunavant, "High Degree Efficient Symmetrical Gaussian Quadrature Rules for the Triangle", *Int. J. for Numer. Meth. Engng.*, Vol. 21, pp. 1129-1148, 1985.
128. J. S. Savage, A. F. Peterson, "Quadrature rules for numerical integration over triangles and tetrahedra", *IEEE Antennas Propagat. Mag.*, vol. 38, pp. 100-102, Jun 1996.

129. D. Wilton, S. M. Rao, A. Glisson, D. Schaubert, O. Al-Bundak, C. Butler, "Potential integrals for uniform and linear source distributions on polygonal and polyhedral domains", *IEEE Trans. Antennas Propagat.*, vol. 32, pp. 276-281, Mar. 1984.
130. M. Abramowitz and I. Stegun, *Handbook of Mathematical Functions*, New York, Dover, 1974.
131. P. C. Hammer, O. P. Marlowe and A. H. Stroud, "Numerical integration over simplexes and cones", *Math. Tables Aids Comput.*, vol. 10, pp. 130-137, 1956.
132. J. -R. Poirier, A. Bendali, P. Borderies, "A macro-element compression for the moment method", *IEEE Trans. Antennas Propagat.*, vol. 49, pp. 1485-1490, Oct. 2001.
133. Z. O. Al-Hekail, W. D. Burnside, "A hybrid method for computing the scattered fields from complex structures", *IEEE Trans. Antennas Propagat.*, vol. 42, pp. 847-852, Jun. 1994.
134. A. Taflov, K. R. Umashankar, "The finite-difference time-domain (FD-TD) method for numerical modeling of electromagnetic scattering", *IEEE Trans. Magnetism*, vol. 25, pp. 3086-3091, Jul. 1989.
135. J. Baldauf, S.-W. Lee, L. Lin, S.-K Jeng, S. M. Scarborough, C. L. Yu, "High frequency scattering from trihedral corner reflectors and other benchmark targets: SBR versus experiment", *IEEE Trans. Antennas Propagat.*, vol. 39, pp. 1345-1351, Sep. 1991.
136. K. C. Donepudi, J. Jian-Ming, S. Velamparambil, J. Song, C. C. Weng, "A higher order parallelized multilevel fast multipole algorithm for 3-D scattering", *IEEE Trans. Antennas Propagat.*, vol. 49, pp. 1069-1078, Jul. 2001.
137. H. Ling, S.-W. Lee, R. -C. Chou, "High-frequency RCS of open cavities with rectangular and circular cross sections", *IEEE Trans. Antennas Propagat.*, vol. 37, pp. 648-654, May 1989.
138. J. M. Rius, A. Lozano, L. Jofre, A. Cardama, "Spectral iterative algorithm for RCS computation in electrically large or intermediate perfectly

- conducting cavities", *IEEE Trans. Antennas Propagat.*, vol. 42, pp. 790-797, Jun. 1994.
139. S. Strom, "T matrix for electromagnetic scattering from an arbitrary number of scatterers with continuously varying electromagnetic properties", *Phys. Rev. D*, vol. 10, pp. 2585-2600, 1974.
 140. P. W. Barber and C. Yeh, "Scattering of EM waves by arbitrarily shaped dielectric bodies", *Applied. Opt.*, vol. 14, 2864-2872, 1975.
 141. S. K Chang, K. Mei, "Application of the unimoment method to electromagnetic scattering of dielectric cylinders", *IEEE Trans. Antennas Propagat.*, vol. 24, pp. 35-42, Jan. 1976.
 142. A. R. Holt, "The scattering of electromagnetic waves by single hydrometeors", *Radio. Sci.*, vol. 17, pp. 929-945, 1982.
 143. A. A. Kishk and L. Shafai, "On the accuracy limits of different integral equation formulations for numerical solution of dielectric bodies of revolution", *Can. J. Phys.*, vol. 63, pp. 1532-1539.
 144. A. Jostingmeier, A. S. Omar, "Analysis of the scattering by dielectric bodies using the SIE formulation", *IEEE Trans. Microwave Theory Tech.*, vol. 42, pp. 471-480, March 1994.
 145. A. W. Glisson, D. Kajfez, J. James, "Evaluation of Modes in Dielectric Resonators Using a Surface Integral Equation Formulation", *IEEE Trans. Microwave Theory Tech.*, vol. 31, pp. 1023-1029, Dec 1983.
 146. G. Mur, "A Finite Difference Method For The Solution Of Electromagnetic Waveguide Discontinuity Problems", *IEEE Trans. Microwave Theory Tech.*, vol. 22, pp.54-57, Jan. 1974.
 147. K. Bierwirth, N. Schulz, F. Arndt, "Finite-Difference Analysis of Rectangular Dielectric Waveguide Structures", *IEEE Trans. Microwave Theory Tech.*, vol. 34, pp. 1104-1114, Nov. 1986.
 148. B. M. A. Rahman, J. B. Davies, "Finite-Element Analysis of Optical and Microwave Waveguide Problems", *IEEE Trans. Microwave Theory Tech.*, vol. 32, pp. 20-28, Jan 1984.

149. T. Angkaew, M. Matsuhara, N. Kumagai, "Finite-Element Analysis of Waveguide Modes: A Novel Approach that Eliminates Spurious Modes", *IEEE Trans. Microwave Theory Tech.*, vol.35, pp. 117-123, Feb. 1987.
150. A. Jostingmeier, A. S. Omar, "Analysis of inhomogeneously filled cavities coupled to waveguides using the VIE formulation", *IEEE Trans. Microwave Theory Tech.*, vol. 41, pp. 1207-1214, Jun/Jul 1993.
151. A. A. Kucharski, "Resonances in heterogeneous dielectric bodies with rotational symmetry-volume integral-equation formulation", *IEEE Trans. Microwave Theory Tech.*, vol. 48, pp. 766-770, May 2000.
152. M. F. Catedra, E. Gago, L. Nuno, "A numerical scheme to obtain the RCS of three-dimensional bodies of resonant size using the conjugate gradient method and the fast Fourier transform", *IEEE Trans. Antennas Propagat.*, vol. 37, pp. 528-537, May 1989.
153. Balanis, A. A. Zaporozhets, M. F. Levy, "Bistatic RCS calculations with the vector parabolic equation method", *IEEE Trans. Antennas Propagat.*, vol. 47, pp. 1688-1696, Nov. 1999.
154. A. McCowen, T. V. Tran, "Matrix interpretation of the spectral iteration technique for 3D dielectric scatterers in the resonance region", *IEE Proceedings-H*, vol. 138, pp. 219-224, Jun 1991.
155. X. Zhu, Y. Geng, X. Wu, "Application of MoM-CGM-FFT to 3D dielectric scatterers", *ISAPE Proceedings*, pp. 293-296, Aug. 2000.
156. B. M. Notaros, B. D. Popovic, "General entire-domain method for analysis of dielectric scatterers", *IEE Proceedings-H*, vol. 143, pp. 498-504, Dec 1996.
157. E. Topsakal, M. Carr, J. Volakis, M. Bleszynski, "Galerkin operators in adaptive integral method implementations", *IEE Proceedings-H*, vol. 148, pp. 79-84, Apr 2001.
158. E. Bleszynski, M. Bleszynski and T. Jaroszewicz, "AIM: adaptive integral method compression algorithm for solving large scale electromagnetic scattering and radiation problems", *Radio Sci.*, vol. 31, pp. 1225-1251, 1996.

159. C. Y. Shen, "Application of the discrete Fourier transform method to thin dielectric structures", *IEEE Trans. Antennas Propagat.*, vol. 37, pp. 1277-1283, Oct 1989.
160. T. J. Peters, J. L. Volakis, "Application of a conjugate gradient FFT method to scattering from thin planar material plates", *IEEE Trans. Antennas Propagat.*, vol. 36, pp. 518-526, Apr 1988.
161. P. Soudais, "Iterative solution of a 3-D scattering problem from arbitrary shaped multidielectric and multiconducting bodies," *IEEE Trans. Antennas Propagat.*, vol. 42, pp. 954-959, Jul. 1994.
162. B. M. Kolundzija, "Electromagnetic modeling of composite metallic and dielectric structures," *IEEE Trans. Microwave Theory Tech.*, vol. 47, pp. 1021-1032, Jul 1999.
163. T. K. Wu and L. L. Tsai, "Scattering from arbitrarily-shaped lossy dielectric bodies of revolution," *Radio Sci.*, vol. 12, no. 5, pp. 709-718, 1977.
164. T. K. Sarkar, E. Arvas, "An integral equation approach to the analysis of finite microstrip antennas: volume/surface formulation," *IEEE Trans. Antennas Propagat.*, vol. 38, pp. 305-312, Mar 1990.
165. J. J. Angelini, C. Soize, P. Soudais, "Hybrid numerical method for harmonic 3-D Maxwell equations: scattering by a mixed conducting and inhomogeneous anisotropic dielectric medium," *IEEE Trans. Antennas Propagat.*, vol. 41, pp.66-76, Jan 1993.
166. Y. M. M. Antar, A. A. Kishk, L. Shafai, L. E. Allan, "Radar backscattering from partially coated targets with axial symmetry," *IEEE Trans. Antennas Propagat.*, vol. 37, pp. 564-575, May 1989.
167. B. G. J. Salman, "Electromagnetic modelling of resonant structures using the method of moments," Phd Thesis, Dept. of Electrical and Electronic Engineering, University of Wales Swansea, UK, 1997.
168. P. Soudais, H. Steve, F. Dubois, " Scattering from several test-objects computed by 3-D hybrid IE/PDE methods," *IEEE Trans. Antennas Propagat.*, vol. 47, pp. 646-653, Apr 1999.

169. A. McCowen, "A far-field approximation for the fast-multipole method applied to the combined field integral equation," *IEEE Trans. Magnetics*, vol. 39, pp. 1254-1256, May 2003.